DEVELOPMENT AND APPLICATION

OF MOLECULAR AND COMPUTATIONAL TOOLS

TO IMAGE COPPER IN CELLS

Martin Priessner

Department of Chemistry
Centre for Neurotechnology
Imperial College London

This dissertation is submitted for the degree of
Doctor of Philosophy

January 2022

DECLARATION

Declaration of Originality

I declare that the work described herein was carried out by myself, and that any contribution from others has been clearly identified in print at the relevant sections. Furthermore, I hereby confirm that this thesis was written by myself and that all references are listed in the bibliography.

Signed: Martin Priessner

Date: 17.01.2021

"PhD journey is like a box of chocolates.
You never know what you're gonna get (in the end)."
By Martin Priessner

ABSTRACT

Copper is a trace element which is essential for many biological processes. A deficiency or excess of copper(I) ions, which is its main oxidation state of copper in cellular environment, is increasingly linked to the development of neurodegenerative diseases such as Parkinson's and Alzheimer's disease (PD and AD). The regulatory mechanisms for copper(I) are under active investigation and lysosomes which are best known as cellular "incinerators" have been found to play an important role in the trafficking of copper inside the cell. Therefore, it is important to develop reliable experimental methods to detect, monitor and visualise this metal in cells and to develop tools that allow to improve the data quality of microscopy recordings. This would enable the detailed exploration of cellular processes related to copper trafficking through lysosomes. The research presented in this thesis aimed to develop chemical and computational tools that can help to investigate concentration changes of copper(I) in cells (particularly in lysosomes), and it presents a preliminary case study that uses the here developed microscopy image quality enhancement tools to investigate lysosomal mobility changes upon treatment of cells with different PD or AD drugs.

Chapter I first reports the synthesis of a previously reported copper(I) probe (**CS3**). The photophysical properties of this probe and functionality on different cell lines was tested and it was found that this copper(I) sensor predominantly localized in lipid droplets and that its photostability and quantum yield were insufficient to be applied for long term investigations of cellular copper trafficking. Therefore, based on the insights of this probe a new copper(I) selective fluorescent probe (**FLCS1**) was designed, synthesized, and characterized which showed superior photophysical properties (photostability, quantum yield) over **CS3**. The probe showed selectivity for copper(I) over other physiological relevant metals and showed strong colocalization in lysosomes in SH-SY5Y cells. This probe was then used to study and monitor lysosomal copper(I) levels via fluorescence lifetime imaging microscopy (FLIM); to the best of my knowledge this is the first copper(I) probe based on emission lifetime.

Chapter II explores different computational deep learning approaches for improving the quality of recorded microscopy images. In total two existing networks were tested (fNET, CARE) and four new networks were implemented, tested, and benchmarked for their capabilities of improving the signal-to-noise ratio, upscaling the image size (GMFN, SRFBN-S, Zooming SlowMo) and interpolating image sequences (DAIN, Zooming SlowMo) in z- and t-dimension of multidimensional simulated and real-world datasets. The best performing networks of each category were then tested in combination by sequentially applying them on a low signal-to-noise ratio, low resolution, and low frame-rate image sequence. This image enhancement workstream for investigating lysosomal mobility was established. Additionally, the new frame interpolation networks were implemented in user-friendly Google Colab notebooks and were made publicly available to the scientific community on the ZeroCostDL4Mic platform.

Chapter III provides a preliminary case study where the newly developed fluorescent copper(I) probe in combination with the computational enhancement algorithms was used to investigate the effects of five potential Parkinson's disease drugs (rapamycin, digoxin, curcumin, trehalose, bafilomycin A1) on the mobility of lysosomes in live cells.

ACKNOWLEDGEMENTS

Five years is a long time, but it feels like a blink of an eye that this amazing time of my life has passed, and I am ready for the next adventure that is waiting for me. But before I move on and look back with a thought of nostalgia, I want to take the opportunity to thank some of the very important people that I have met along that way and that have helped me to make the past 5 years an unforgettable experience.

First, I would like to thank the **EPSRC - Centre for Doctoral Training** for giving me the unique opportunity to do a cutting-edge research MRes/PhD at Imperial College London, one of the best universities in the world. This also includes the administrative support from this program which was done by my CDT coordinator **Kate Hobson**. She always had an open ear for all the challenges that came up during the different phases of the MRes and PhD and with her happy attitude she always found ways to cheer us up in moments of difficulties.

Next, I would like to thank all my four amazing supervisors **Ramon Vilar, Ying Liming, Magdalena Sastre** and **Alfonso de Simone**. They helped me to re-find myself in my research work by giving me the freedom to shape my project in a way that I thought could lead to success. They tolerated my stubbornness in some decisions and encouraged me with their trust which made me push myself not to disappoint them. Amongst them I want to point out my main supervisor **Ramon Vilar**, who supported me in the difficult situations where other PIs confronted my research project. With his always positive attitude, and his sense for correctness he combined for me the perfect combination of a researcher that want to push the limits of knowledge without intimidating others. I learnt a lot from him, and I am very thankful to be supervised by such a nice and intelligent person.

Also, I want to thank my collaborators Marina Kuimova and Romain Laine who helped me in the process of publishing my two papers as well as all my fellow PhD and PostDoc colleagues from the different research groups (Rainbow, Tiffany, Tim, Carmen, Caitlin, Florian, Phil, Ajesh, Aaron, Raju, Nicola, Bibiana, Xiangyu, Alastair, Bogachan etc.) who helped me in several situations throughout my PhD, gave me good advice in difficult situations and made my working hours in the lab and generally my time in London richer.

Furthermore, I would like to thank all the people that I could call friends starting from my flat mates (Sebastian & Gabby, Thomas & Marina, Matias & Valerio) followed by my CDT student colleagues and friends from the Imperial College Dance Club (Wenlan, Mik, Erica, Oz, Mamun and many more). They made my time in London unique and I will never forget them.

Next to all the acknowledgements directed to London my biggest expression of thanks is directed to **my parents Alfons and Sigrid Prießner**. They always supported me throughout my life in doing the things that I like. They gave me the opportunity to study, to reinvent myself and to follow my heart in whatever direction it was pulling me. In moments where I thought I cannot find a solution for the challenges that I was facing they were the people who gave me strength and encouraged me in all possible ways.

Finally, I would like to thank my “Bro”, **brother Alfons jun. Prießner**, who always had an open ear for everything I wanted to talk about. Also, for his honesty and for his mentoring throughout my career. He was the one who told me the things I needed to hear to make the best possible decisions in my life.

CONTENTS

LIST OF ABBREVIATIONS AND ACRONYMS

2PM Two-photon microscopy
AB Amyloid-beta
ACN Acetonitrile
ALP Autophagy-lysosome pathway
ANN Artificial neural network
AS Alpha-synuclein
AU Airy units
BCS 2,9-Dimethyl-4,7-diphenyl-1,10-phenantrolinedisulfonic acid disodium salt
BETA bis(2-((2-(Ethylthio) ethyl)thio)ethyl)amine
BIC Bicubic
BIL Bilinear
BODIPY 4,4-Difluoro-4-bora-3*a*,4*a*- diaza-*s*-indacen
BSA Bovine serum albumin
CARE Content-aware image restoration
$CDCl_3$ Deuterated chloroform
CHCA α-Cyano-4-hydroxycinnamic acid
CLEAR Coordinated lysosomal expression and regulation
CNN Convolutional neural networks
CT Charge transfer
DAIN Depth-aware video frame Interpolation
DBN Deep belief networks
DCM Dichloromethane
DDQ 2,3-Dichloro-5,6-dicyano-1,4-benzoquinone
DIEA *N,N*-Diisopropylenthylamine
DL Deep learning
DLS Dynamic light scattering
DMEM Dulbecco's modified eagle medium
DMF Dimethylformamide
DNN Dense neural network
DMSO Dimethyl sulfoxide
DTDP 2,2'-Dipyridyldisulfide
DMCP Dimethyl 4-chlorophenyl thiophosphate
EA Ethyl acetate
EDC 1-Ethyl-3-(-3-dimethylaminopropyl) carbodiimide hydrochloride
ESI-MS Electrospray ionization mass spectrometry
EtOH Ethanol
Eq. Equivalents
ER Endoplasmic reticulum
ESET Excited state electron transfer
FBS Fetal bovine serum
FC Flash chromatography
FLIM Fluorescence lifetime imaging microscopy
GAN Generative adversarial network
GB Gigabyte
GFM Gated feedback module
GFP Green fluorescent protein
GMFN Gated multiple feedback network
GSH Glutathione
HEPES 4-(2-Hydroxyethyl)-1-piperazineethanesulfonic acid
HOMO Highest occupied molecular orbital
HR High resolution
ICP-MS Inductively coupled plasma mass spectrometry
IRF Instrument response function
ISC Inter system crossing
K_d Dissociation constant
LD Lipid droplets
LDA Lifetime determination algorithms
LSD Lysosomal storage disorders
LSTM Long short-term memory
LR Low resolution
LUMO Lowest unoccupied molecular orbital
MALDI Matrix-assisted laser desorption/ionization
MeOH Methanol
ML Machine learning
MLE Maximum likelihood estimation
mTORC1 Mammalian target of rapamycin complex 1

Nano-SIMS Nano-secondary ion mass spectrometry
NIR Near infrared
NMR Nuclear magnetic resonance
NN Neural network
PBS Phosphate-buffered saline
PD Parkinson's disease
PET Photoinduced electron transfer
PFA Paraformaldehyde
PSNR Peak-signal-to-noise ratio
PSSR Point-scanning super-resolution
QE Quantum efficiency
RB Reconstruction block
RDB Residual dense block
ReLU Rectified linear unit
RIPA Radioimmunoprecipitation assay
Rh 6G Rhodamine 6G
RNN Recurrent neural networks
RMSE Root-mean-square error
ROS Reactive oxygen species
RT Room temperature
SDS Sodium dodecyl sulfate
SGD Stochastic gradient descent
SIM Structured illumination microscopy
SISR Single image super-resolution imaging
SNR Signal-to-noise ratio
SPT Single-particle tracking
SRFBN-S Super-resolution feedback network
SSIM Structural similarity index metric
TCSPC Time-correlated single photon counting
TEA Triethylamine
TFA Trifluoroacetic acid
TFEB Transcription factor EB
TGN *trans*-Golgi-network
THF Tetrahydrofuran
TLC Thin-layer chromatography
TRIS Tris(hydroxymethyl) aminomethane
UPS Ubiquitin-proteasome system
VFI Video frame interpolation
VSR Video super-resolution
WF Wide-field microscopy
XFM X-ray fluorescence microscopy
ZS Zooming SlowMo

INTRODUCTION

Metal ions such as copper(I)/copper(II), iron(II)/iron(III) and zinc(II) amongst others play a fundamental role in biology by serving as essential cofactors in processes such as respiration, growth, gene transcription, enzymatic reactions, cell proliferation and immune function. Some estimates suggest that at least one third of all proteins interact with metal ions[1] and half of all enzymes require them to perform their functions.[2]

The unique chemical reactivity of metal ions allow for many essential biological processes to take place, but can also be responsible for a wide range of detrimental effects which makes a tight regulation of metal ion metabolism necessary to ensure that unwanted processes are minimal. The process of import, trafficking and availability, and export of metal ions is called homeostasis and because of the potential of metals to act as toxins the homeostasis must be tightly regulated.

In the last few decades, several diseases have been identified to be related to a malfunction of metal homeostasis, such as neurodegenerative diseases[3], cancer[4] and diabetes.[5] In particular, the abnormal accumulation of copper ions has been increasingly connected to the development of neurodegenerative abnormalities such as Parkinson's disease, Alzheimer's disease, and Wilson's disease. Generally, it is believed that in the diseased state the copper ion homeostasis is disrupted which results in a reduced control of the potentially toxic form of the metal ions.

Copper(I) and copper(II) ions participate in the cascade of Fenton reactions that can lead to reactive oxygen species (ROS) generation. These reactions can turn relatively stable hydrogen

peroxide into hydroxyl radicals which induce oxidative stress to the neurons. Those radicals are very reactive and can damage lipids, proteins and nucleic acids.[6]

Another reported copper-damaging mechanism in the case of Parkinson's disease (PD) is linked to the oligomerization of the protein alpha-synuclein (AS).[7] Copper supports the oligomerization and facilitates the fibrilization of this protein in the brain which leads to the formation of Lewy Bodies, the hallmarks of PD.

Lysosomes have been found to play an important role in the trafficking of copper inside the cell as well as being involved in the process of dismantling cellular alpha-synuclein. This cellular organelle is mostly known as a cellular "incinerator" because of its function for the degradation and recycling of cellular waste. More recently a growing body of evidence has linked its function to the role of regulating the metabolism/homeostasis of metals inside cells. Through a web of transporter proteins (dyneins and kinesins) the lysosomes can move within the cells and specific transporter proteins on the lysosomal membrane allow metal ions to be moved into or out of this organelle. This allows the organelle to direct metal fluxes to cellular compartments where it is needed. If an excess of metal is present in the cell the lysosomal content can be sequestered outside the cell to lower cellular metal levels.

The exact roles of metals and the regulatory mechanisms of lysosomes in the context of disease development is still unclear. Their intricate interactions with many proteins, their small catalytic concentrations inside biological systems and their complex regulatory cellular mechanism have limited their study. Therefore, it is of great importance to develop chemical and computational tools that allow us to gain deeper insights into the location, concentration, and trafficking of metal ions in biological systems.

Fluorescent probes are the technology of choice to investigate *in vivo* cellular metal distributions and trafficking. Through their ability to selectively bind to target metals they show changes in their fluorescence intensity, fluorescence lifetime or/and their wavelength excitation or emission and have been widely used to study the cellular behaviour of metals. The vast majority of optical probes are intensity-based and a powerful tool/technique that is used to visualize them to study cellular structures and investigate dynamic cellular processes are point-scanning microscopy techniques such as confocal microscopes. They can capture spatiotemporal organization of biological micro-environments and provide the advantages of higher resolution, 3D information, and good signal-to-noise ratio (SNR).

Although fluorescence intensity-based imaging microscopy is the most common technology used to investigate cellular processes, as will be discussed in subsequent chapters of this

thesis, fluorescence lifetime imaging microscopy (FLIM), can provide additional insights, and has several advantages over traditional fluorescence microscopy techniques.

However, these point-scanning systems suffer from an effect called the “eternal triangle of compromise” which states that at a given SNR, improving any of the three, i.e. resolution, system sensitivity or imaging speed, comes at the cost of one of the others. Therefore, the speed, sample preservation, and SNR of point-scanning systems are difficult to optimize simultaneously. This becomes especially problematic if computational tracking of objects over time is performed such as movements of cellular organelles in 4D (3D + time). If the travelled distance of an object from one image at a certain timepoint to the next image is too large the tracking algorithm will make mistakes. Therefore, it is important to find methods to overcome the limitations of imaging speed and image quality and signal by artificially increasing the image resolution, the image frequency and SNR.

One such computational technology that has the potential to stretch these limitations is called “deep learning”. It has gained strong momentum in the field of computer vision and more recently it has also found its way into the biological sciences by applying these algorithms also to microscopy images. In the context of the limitations of point-scanning microscopy, deep learning algorithms have the potential to *artificially upscale* the image resolution, *improve the signal-to-noise ratio* of a given image and to *synthetically increase the image frequency* in 4-dimensional image timeseries, where the capturing of fast cellular processes are sometimes limited by a too low frame rate of the microscopy setup.

These image improvements have beneficial consequences when e.g. performing computational tracking of small organelles which is of great importance to unveil their role and function for metal homeostasis.

Aims and Objectives

The three broad aims of this PhD research were to: (i) develop new fluorescent probes for imaging cellular copper(I) levels, (ii) implement computational deep learning tools to enhance the quality of confocal microscopy images and (iii) investigate the influence of Parkinson’s disease drugs on lysosomal mobility in a neuroblastoma cell-line using the new fluorescence probe and the implemented image enhancement algorithms.

To achieve the first aim, an existing probe from the literature (**CS3**) was resynthesized, characterized, and tested for its cellular application. Subsequently, some biological

experiments with alpha-synuclein (AS) were carried out to investigate the role of copper(I) in Parkinson's disease. Based on the knowledge gained from this first probe a novel selective fluorescent copper(I) probe was designed, synthesized, and spectroscopically characterized. The new probe demonstrated a selective binding to copper(I) and showed superior photophysical properties compared to the previously synthesized copper(I) probes from the literature. The new copper probe was then used in cellular studies to investigate the cellular localization of copper(I) in particular in organelles such as lysosomes. Finally, the effect of copper transporter molecules such as bis(thiosemicarbazonato)-copper complex (Cu-GTSM) on cellular copper levels was investigated using fluorescence lifetime imaging microscopy.

For the second aim, the fluorescent copper(I) probe was used to monitor the trafficking of copper containing lysosomes over time. To overcome the physical limitations of speed, signal-to-noise ratio and resolution of point-scanning microscopy systems ("eternal triangle of compromise"), the aim was to implement several neural networks to improve each of the three limitation corners. The focus of the first deep learning tool was to artificially increase the resolution, the second neural network was to tackle the limitations of low SNRs and the third tool was applied to improve the recording frame rate of the microscopy image series. Each tool should be benchmarked with state-of-the-art mathematical interpolation or upscaling techniques and should be used on several different datasets to test their capabilities.

The third aim was achieved by utilization of the new fluorescent copper(I) probe to investigate the effect of different Parkinson's disease drugs on the mobility and movement behaviour of copper-containing organelles in the neuroblastoma cell line (SH-SY5Y) using confocal microscopy. The recorded low resolution and low frame rate image timeseries data was enhanced by the computational deep learning algorithms developed and implemented previously.

Structure of the Thesis

Chapter I gives a detailed literature review on the topics related to the first aim including the mechanism of fluorescence, the role of copper in biology, BODIPY fluorescent probes and technologies used for investigating copper(I) with a strong focus on the development on fluorescent copper(I) probes. It then describes the synthesis of fluorescent probes and their ability to detect copper(I) *in vitro* and in cells.

Then **Chapter II** transitions into the topics of computational tool development for microscopy. It gives an introduction into deep learning for microscopy, and it explains the algorithms that were implemented in this thesis. Furthermore, it presents the findings of the implemented deep learning image enhancement algorithms, including the results of benchmarking studies of three categories of neural networks implemented and tested (SNR enhancement, resolution upscaling, image interpolation).

Chapter III provides the biological background on the importance of lysosomes in the context of neurodegenerative diseases. Then several Parkinson's disease drugs that have previously shown positive effects on *in vivo* animal experiments are presented and discussed in the context of lysosomes. It then shows and discusses the results of the lysosomal copper tracking experiments and the observed influences of the different Parkinson's disease drugs on the movement dynamics of lysosomes.

The thesis ends with a summary **Chapter IV** which concludes the findings of the thesis and provides ideas for improvements and future research ideas for each of the targeted aim.

CHAPTER I

1.1. Theoretical Background

1.1.1. Luminescence

Luminescence is “a spontaneous emission of radiation from an electronically excited species (or from a vibrationally excited species) not in thermal equilibrium with its environment”.[8] There are different types of luminescence that are categorized following their mode of excitation such as chemical reactions (chemiluminescence and bioluminescence), recrystallization (crystalloluminescence), and electrical current (electroluminescence), amongst others. Fluorescence and phosphorescence are forms of photoluminescence whose differences are determined by the nature of the electronic excited state. After the introduction of the term fluorescence by G. G. Stokes[9] in the mid-19th century, the distinction between fluorescence and phosphorescence was based on duration of emission after the end of excitation. At that time, every emission that disappeared immediately after excitation was considered to be fluorescence, whereas phosphorescence was identified if the emitted light persisted after the end of excitation. However, this definition was modified later because of discoveries of several exceptions to the rules such as long-lived fluorescence (e.g. divalent europium salts) or short-lived phosphorescence (e.g. violet luminescence of zinc sulfide).

1.1.2. Mechanism of fluorescence and phosphorescence

The mechanisms involved in fluorescence and phosphorescence are schematically explained in the Jablonski diagram (see Figure 1). This describes the different internal energy pathways and general electronic states of a molecule involved in fluorescence and phosphorescence and the transitions between them.[10]

In the case of fluorescence, a molecule in the electric ground state S_0 is excited by absorption of a photon to the first excited state S_1 where the electron has an opposite spin compared to the remaining electron in the ground state. The electron first gets to a higher vibrational state, which undergoes vibrational relaxation processes by mechanisms such as intermolecular collisions with solvent molecules.[11] When the electron returns to the ground state the loss of energy results in the emission of a photon. For fluorescence, this process happens very fast and the time that a fluorophore spends in the excited state (fluorescence lifetime) is in a range of 1 – 20 ns. The Born-Oppenheimer approximation[12] demands that the nuclear motion of the molecules can be neglected for such short time frames which results in the emission spectrum mirroring the corresponding absorption spectrum. This process of excitation with spontaneous emission is competing with other processes such as intersystem crossing (ISC). For phosphorescence, the presence of heavy atoms within a molecule can result in a spin-orbit coupling, which allows the excited singlet state electron to be transferred via ISC to an excited triplet state by changing the spin direction of the excited electron (which has the same spin as the electron in the ground state orbital). The transition of the electron back to the ground state is therefore forbidden. This kinetic hindrance of the relaxation process results in an increased timescale, making the process of relaxation much slower and it can take between 10^{-3} to 10^{3} seconds.

Fluorescence is typically observed in molecules which exhibit some aromaticity or have big conjugated systems. Phosphorescence occurs usually in molecules that have heavy atoms in their structure. When molecules have both aromatic systems and heavy atoms it can be difficult to distinguish phosphorescence from fluorescence.

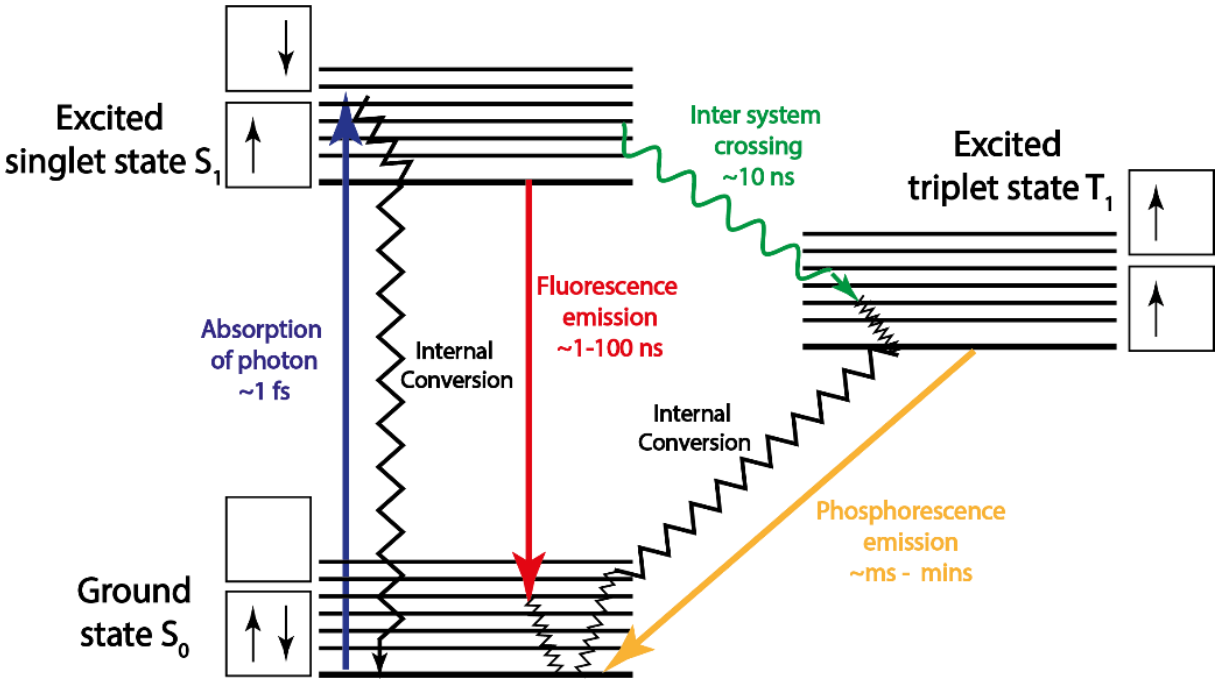

Figure 1: Jablonski diagram showing the energy pathways of a molecule from the ground state S_0 to the excited singlet state S_1 after absorption of a photon (blue) and the possible transitions of internal conversion (black), fluorescence emission (red), intersystem crossing between excited singlet state and triplet state (green) and phosphorescence back to the ground state (yellow).

1.1.3. Fluorescence parameters for sensing

The most common parameter for fluorescence sensing is the *fluorescence emission intensity (F)*. The intensity strongly depends on many physical variables such as temperature, concentration of the dye, excitation light intensity, solvent type, and presence of quenching agents, among others. The emission spectrum's shape is usually independent of the excitation wavelength which is explained by the fast relaxation of the excited molecule to the lowest vibrational state S_1. This is also the reason why the fluorescence spectrum usually is a "mirror image" of the absorption spectrum. For most fluorophores, the energy levels of the vibrational states S_1 and S_0 are usually not significantly altered which explains the symmetry of the mirrored emission and absorbance spectrum. Some exceptions for this symmetry can occur for two photon excitation or in the case of dimer formation of the measured dye molecule. There the emission spectrum can show significant differences compared to the absorbance spectrum.

Other important parameters of the spectroscopic measurements are the *absorption and emission maximum* (λ_{abs}, λ_{em}). The peak of fluorescence emission usually shows a bathochromic redshift in comparison to the absorption spectrum. This is commonly caused by a loss of energy through the non-radiative vibrational relaxations of the higher vibrational

levels, complex formation or also by solvent stabilization of the excited state.[13] The difference between λ_{abs} and λ_{em} was first discovered in 1852 and is called Stokes shift.[9]

The *anisotropy* (*I)* and *polarization* (*P)* of fluorescence are two more parameters that can provide information on the immediate environment of the fluorophore which were found to be a useful metric for investigating biological systems. When fluorophores get irradiated with polarized light, only the molecules with a parallel transition dipole moment can absorb light. When recording fluorescence in environments with low viscosity the polarization of the light gets lost because of the high rotation rate of the molecules. However, when the molecule is in a highly viscous environment such as in polymers or lipid membranes the rotation is hindered, and this leads to a polarized emission. When this polarized fluorescence is measured at two different angles, one can calculate the fluorescence anisotropy.

The efficiency of a fluorophore to emit light after excitation is characterized by its *fluorescence quantum yield (Φ)*. It describes the ratio between emitted photons to absorbed photons where fluorophores with Φ values close to 1 are the most efficient converters of absorbed light and for non-fluorescent compounds the Φ value approaches 0. This value is also strongly dependent on conditions like temperature, solvent polarity, type of substituents on the fluorophore, amongst others. The definition of fluorescence quantum yield in terms of the rates of excitation state decay is as follows $\Phi_F = k_f / \sum_i k_i$ where Φ_F is the quantum yield; k_f the rate of spontaneous emission of radiation and $\sum_i k_i$ the sum of all types of excited state decay from the lowest vibrational state S_1. The term $\sum_i k_i$ can also be split into $(k_r + k_{nr})$, where k_{nr} represents the rate constant for all non-radiative decay processes that occur for that particular system.

The last parameter for fluorophores presented is the *fluorescence lifetime* τ. This describes the average time that a molecule spends in the excited state before returning to the ground state. For fluorescence, this relaxation time is normally in the range of several nanoseconds and for phosphorescence it can take from several milliseconds up to minutes. The process of fluorescence lifetime includes both relaxation pathways, radiative and non-radiative. Fluorescence lifetime can be influenced by many factors such as the environment of the dye and the introduction of heavy atoms which increases the non-radiative decay and therefore increases the fluorescence lifetime.

1.3.1. Principles of fluorescence lifetime

The fluorescence with organic molecules is generally understood as the process of a radiative transition from a first excited singlet state S_1 to the ground state S_0. This transition is called molecular fluorescence and can be characterized by the following three parameters: i) the fluorescence spectrum I(λ) which is defined as the intensity as a function of the wavelength; ii) the fluorescence quantum yield Φ, which is the ratio between the total number of emitted photons released after excitation to the total number of absorbed photons and iii) the fluorescence lifetime τ, which is seen as a kinetic parameter. The fluorescence lifetime is described as the inverse of the sum of all rate constants including the radiative and the non-radiative processes, k_r and k_{nr} respectively (see Equation 1).

$$\tau = \frac{1}{k_r + k_{nr}} \qquad \text{(Equation 1)}$$

The non-radiative rate constant k_{nr} is the sum of rate constant for internal conversion k_{ic} and rate constant for intersystem crossing k_{isc} to an excited triplet state k_{isc}(see Equation 2).

$$k_{nr} = k_{ic} + k_{isc} \qquad \text{(Equation 2)}$$

Following the so-called Kasha's rule[11] the fluorescence emission always occurs from the lowest excited vibrational level S_1.

$$\tau_0 = \frac{1}{k_r} \qquad \text{(Equation 3)}$$

The natural or radiative lifetime τ_0 is the inverse of the radiative rate constant (see Equation 3) and is related to the fluorescence lifetime via the fluorescence quantum yield Φ which is the ratio of the number of photons emitted to the number of photons absorbed by a fluorescence compound (see Equation 4).

$$\Phi = \frac{\tau}{\tau_0} = \frac{k_r}{k_r + k_{nr}} = \frac{1}{1 + (k_{nr}/k_r)} \qquad \text{(Equation 4)}$$

The fluorescence quantum yield can have a value between 0 and 1. Following the logic of the equation $\Phi \times \tau_0 = \tau$; τ_0 can be seen as the fluorophore's longest possible lifetime which is achieved if the non-radiative rate constant k_{nr} approaches zero.

The two parameters, fluorescence lifetime τ and the fluorescence quantum yield Φ, are seen as key spectroscopic parameters because they make it possible to calculate the radiative rate constant k_r and the non-radiative rate constant k_{nr}.

From a mechanistic point of view the time-dependent depopulation of the excited state can be explained with the following Equation 5.

$$dN = (k_r + k_{nr}) \times N(t) \times dt \qquad \text{(Equation 5)}$$

This equation describes the time it takes for dN number of fluorophores to return to the ground state S_0 after excitation of N fluorophores to the excited state S_1. The integration of this equation in aspect of time t by taking into account that the fluorescence intensity $F(t)$ is proportional to the number of excited fluorophores $N(t)$ results in Equation 6

$$F(t) = F_0 \times e^{-\frac{t}{\tau}} \qquad \text{(Equation 6)}$$

where F_0 is the fluorescence intensity at time t=0 and τ is the calculated fluorescence lifetime. According to this, the fluorescence lifetime has an exponential decay and τ describes the time it takes for the maximum fluorescence intensity to decay to a value $e^{-1} \sim 37\%$. The easiest way of analysing the fluorescent decay curves is by plotting it on a logarithmic fluorescence intensity scale. During a measurement with a time-correlated single photon counting unit (TCSPC), the signal shows initially a steep increase caused by the instrument response function (IRF) (see Figure 2 red signal). For a mono-exponential decay the increase is followed by a linear signal decrease when plotted on a logarithmic scale. At longer lifetimes when the signal approaches zero the curve flattens out because of background signal collected (Figure 2). This way of plotting the data allows for easy visual inspection and provides quick insights into the fluorescence decay behaviour. For the extraction of the real fluorescence lifetime the measured signal needs to be deconvoluted from the IRF signal.

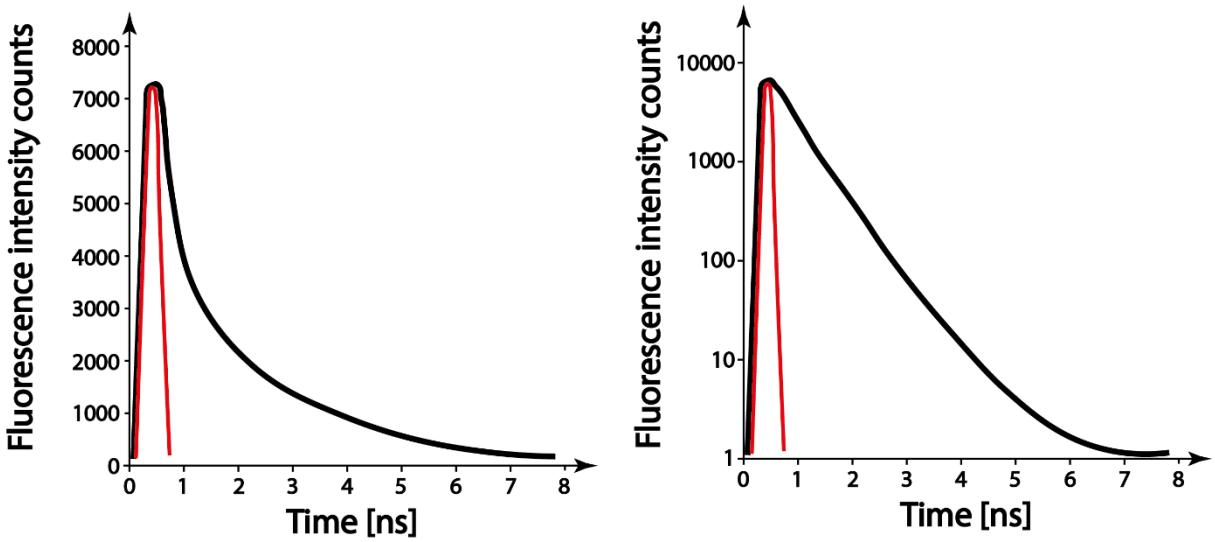

Figure 2: Example TCSPC lifetime trace with normal and logarithmic intensity count scales. The black signal line shows the collected photon count distribution, and the red signal line shows the instrument response function (IRF) which needs to be considered in a deconvolution process for extracting the correct fluorescence lifetime value from the measured decay curve.

A linear decay in the logarithmic plot indicates that the measured fluorescence decay curve follows a first order relationship. In that case the measured fluorescence lifetime value τ is numerically equivalent to the average lifetime τ_{avg}.

However, fluorophores with several different conformational states display more complicated lifetime decay curves because of several different fluorescent decays that contribute to the measured lifetime. This can be seen if the goodness of fit parameter χ^2 gets larger and deviates from unity (χ^2 > 1.5). Then a multiexponential decay and a more complex fluorescence decay mechanism with multiple fluorescence components must be considered.[14]

In that case, the fluorescence lifetime is defined as the arithmetic mean $\bar{\tau}$ of each individual lifetime component (τ_i) and their fractional contribution (f_i) (see Equation 7).

$$\bar{\tau} = f_1\tau_1 + f_2\tau_2 + \cdots \qquad \text{(Equation 7)}$$

The parameters of individual lifetimes and fractional contributions are obtained by mathematical lifetime determination algorithms (LDA) on the measured decay curve. Two common fitting algorithms traditionally used for LDAs are the least square method (LSM) or maximum likelihood estimation (MLE)[15] and a reduced chi-squared criterion is used to determine the goodness of the model fittings.

In practice the two fitting LDA methods introduce some problems. In complex biological processes it is often difficult to categorize the fluorescence emission into a certain exponential model. Often a fitting routine with bi- or a tri-exponential models result in equal fits based on reduced chi-square tests[16] but lead to totally different interpretation of the molecular mechanism. To verify the chosen models, and to ensure the accuracy a long acquisition time and a high photon count is needed, which is often not feasible for FLIM settings. Therefore, two alternative forms of average lifetimes have been found useful: the intensity-weighted (Equation 8) and amplitude-weighted (Equation 9) average fluorescence lifetime

$$\tau_I = \frac{\sum_{i=1}^{p} f_i \tau_i^{\,2}}{\sum_{i=1}^{p} f_i \tau_i} \qquad \text{(Equation 8)}$$

$$\tau_A = \frac{\sum_{i=1}^{p} f_i \tau_i}{\sum_{i=1}^{p} f_i} \qquad \text{(Equation 9)}$$

where p is the number of exponentials used for fitting the decay curve.[17] A thorough investigation on the two types of average lifetimes and associated case studies of when which one should be used can be found in the following review.[18]

1.3.2. Photophysical mechanisms of fluorescence sensing

In this section the most important photophysical processes and principles involved in fluorescence sensing are discussed.

1.1.3.1. Fluorescence quenching

Fluorescence quenching is seen as one of the most important mechanisms of a fluorescent molecule. It describes any process that leads to a decrease of fluorescence intensity of a fluorophore by processes such as excited state reaction, molecular rearrangement, energy transfer, ground-state complex formation and collision quenching, amongst others. In the case of collisional quenching direct contact between quencher molecules and fluorophores are required and it occurs when the quencher diffuses to the fluorophore during the time-period where the fluorophore is in an excited state. This contact results in a return of the fluorophore to the ground state without emission of a photon. This process can be described by the Stern-Volmer equation (Equation 10) which allows to explore the kinetics of photophysical intermolecular deactivation processes.

$$\frac{F_0}{F} = 1 + k \times \tau \times c(Q) \qquad \text{(Equation 10)}$$

F_0 and F are the fluorescence intensities in absence and presence of quenchers, respectively; k is the bimolecular quenching constant; τ is the fluorescence lifetime of the fluorescent dye in the absence of quenchers, and $c(Q)$ is the concentration of the quenching substance. The equation is usually used to determine the diffusion coefficient of a quencher in a given environment. Molecules that can act as quenchers are e.g. molecular oxygen, heavy halogens and aromatic or aliphatic amines.

1.1.3.2. Photoinduced electron transfer

For the design of optical probes, the photoinduced electron transfer (PET) also needs to be considered. PET occurs when excited electrons of a donor get transferred to an acceptor down an energy gradient. Since the PET mechanism is much faster (often < 1ps) than the excited state relaxation of a fluorophore (ca. 2-5 ns), a system that incorporates a PET mechanism will undergo quenching which turns-off the fluorescence. In the context of molecular fluorescent probes, the fluorophore is designed in a way that the PET donor and acceptor are both within the same molecule and connected by some linker.

The PET mechanism can take place in two directions determined by the redox potential of the two involved parts of the molecule. The PET mechanism can be visualized with a simplified molecular orbital scheme (see Figure 3).

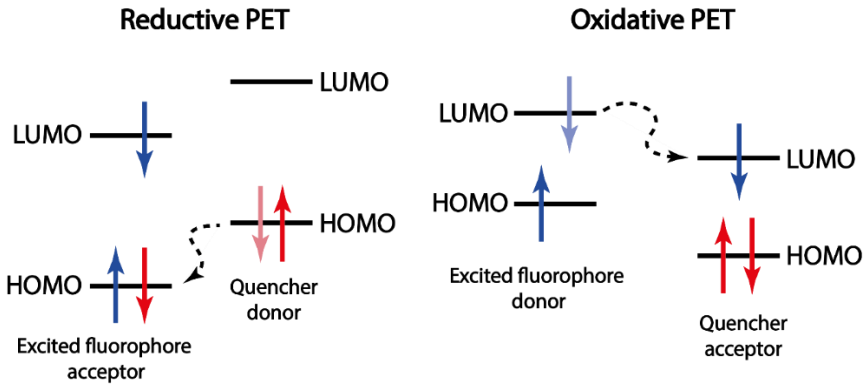

Figure 3: Reductive (left) and oxidative (right) PET mechanism.

PET can take place in two directions: from a donor to the excited-state fluorophore (reductive PET), or from an excited-state fluorophore to a receptor (oxidative PET). Both events are accompanied by a quenching of the fluorophore emission. If the molecule is designed such that the photoexcitation promotes an electron of the fluorophore from HOMO to LUMO the mechanism is called "reductive PET". The donor part of the molecule which is in a higher-energy HOMO can then transfer its electron from the ground state to the ground state of the acceptor and occupies the vacant HOMO orbital. This in turn prevents the relaxation through photon emission and therefore the molecule is in a quenched state. On the other hand, if the LUMO electron of a donor fluorophore is transferred to the LUMO of the acceptor part of the molecule it is called "oxidative PET" mechanism which also leads to a quenching of the molecule. The effectivity of the PET mechanism can be tuned by chemically altering the electronic state of the receptor by changing coordination of analyte or by oxidation or reduction which changes the energy of the receptor's HOMO and LUMO. A reductive PET mechanism usually results in a "turn-on" probe and oxidative PET in a "turn-off" type sensor.

1.1.4. Biological role of copper

1.1.4.1. The essential role of copper

Copper ions play an important role in many biological processes. The electron configuration of elemental copper is $[Ar]3d^{10}4s^{1}$ and it can occur in the oxidation states +1, +2 and +3 of which the preferred biological oxidation state is +2 but due to the reducing environment

inside cells its prevalent oxidation state is +1. The metal is an essential trace nutrient that plays both catalytic and structural roles in proteins and enzymes.[19] A surprising fact is that the ionic radius of copper(I) and copper(II) cations are very similar even though they have different numbers of electrons, which allows them to coordinate to similar sized binding pockets and carry out many electron-transition tasks frequently found in biochemical cellular processes.

Copper(I) is a soft Lewis acid and copper(II) is a borderline hard/soft Lewis acid. This is reflected in a different affinity for ligands. Copper(I) prefers soft ligands such as thiols, and copper(II) prefers hard ligands such as amines.[20]

The copper ions found in biological systems can be divided into a static pool where the ions are tightly bound by proteins and other macromolecules, and a labile pool where the metal is bound relatively weakly to cellular ligands, including proteins and low molecular weight ligands[21] (see Figure 4). The total metal pool of the cell can therefore be considered as the sum of the protein-bound metal pool and the labile metal pool.

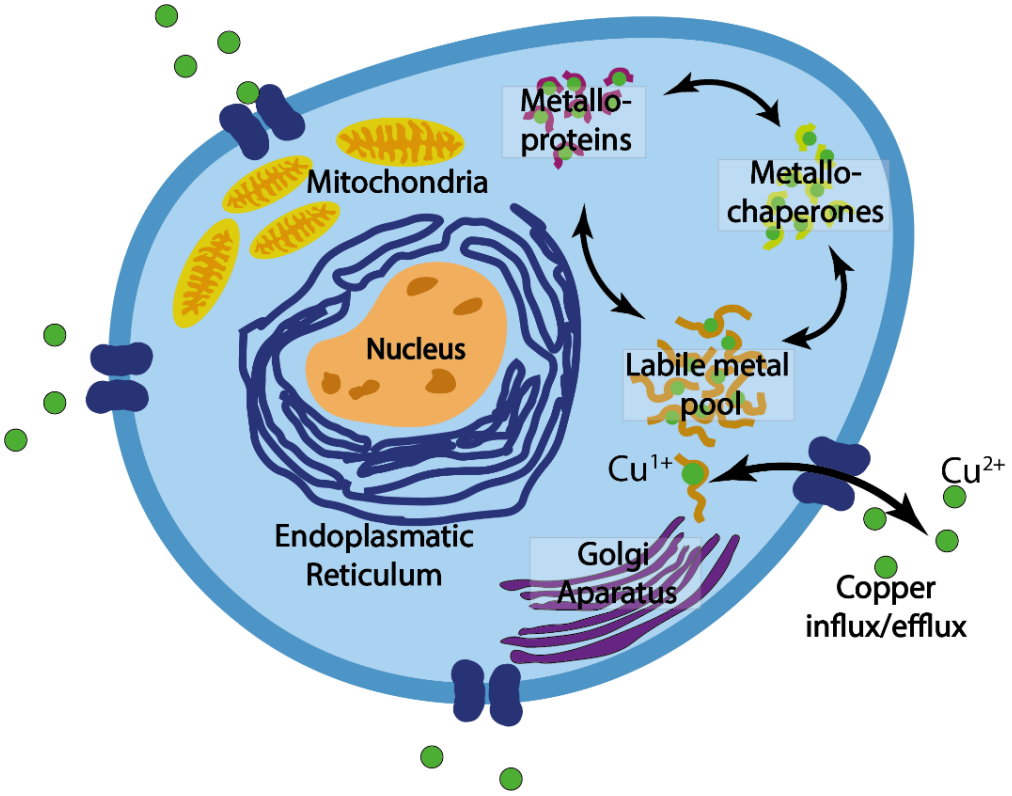

Figure 4: Simplified model of cellular copper homeostasis.

The formation of copper(II) is tightly regulated by a system of intracellular chaperones and transporters (e.g. CTR-1, ATOX-1, GSH).[21] The ability of copper to cycle between copper(I) and copper(II) during enzymatic processes, enables it to adapt to the enzyme's conformation.

Alternatively, it induces global morphological changes to the enzyme where the enzyme adapts itself to form a better ligand for the metal ion.

In cellular biochemistry copper plays important roles in physiological processes and is a key component of a wide range of redox enzymes that react with dioxygen and its reduced derivatives like superoxide ($O^{2-\bullet}$).[22,23] Copper related enzymes are involved in many biological processes such as respiration (e.g. cytochrome c oxidase),[24] electron transfer/substrate oxidation and iron uptake,[58] pigmentation,[25] antioxidant defence,[26] neurotransmitter synthesis, and metabolism.[27]

1.1.4.2. Toxicity of ROS caused by copper ions

Copper is usually tightly regulated in biological systems. Misregulation of copper metal homeostasis in the brain leads to oxidative stress which interrupts the cells detoxification of reactive oxygen species (ROS). This can produce irreparable cellular damage by degrading lipids, nucleic acids and can cause misfolding of proteins that could damage neuronal cells.[28–32] Some of the most common ROS species are superoxide radical ($O_2^{\bullet-}$), hydrogen peroxide (H_2O_2), and hydroxyl radical ($OH^{\bullet}$), among others.[33–35] Copper and iron ions can participate in Fenton-like reactions (see Equation 11) where copper(I) or iron(II) reacts with H_2O_2 to produce $OH^{\bullet}$ and OH^- and form the corresponding oxidized metal centres copper(II) or iron(III).[36]

$$M^{n+} + H_2O_2 \rightarrow M^{(n+1)+} + HO^{\bullet} + HO^- \qquad \text{(Equation 11)}$$

At the same time redox active ions such as copper and iron can also use their ability to change redox states to scavenge ROS. Some known antioxidant metalloenzymes are superoxide dismutase or catalase that are actively involved in cell defence mechanisms against ROS.[37] Furthermore, thiols like glutathione (GSH) help to maintain a healthy redox balance by scavenging superfluous oxidant species. GSH concentration and antioxidant enzymes are also established markers for diseased systems. They are used to indicate that the cellular equilibrium is favouring an oxidative environment where levels of ROS are elevated. To maintain optimal metal levels for function without causing damage, organisms maintain highly coordinated and regulated levels of both redox-active and redox-inactive metal ions.

1.1.4.3. Copper homeostasis in biology

The cellular uptake of copper is achieved by membrane reductases which import extracellular copper(II) into the cell by reducing its oxidation state.[38] Once inside the cell there are two main mechanisms in place to ensure the delivery of copper(I) to the right place in the right

amount and at the right time. One being i) subcellular compartmentalization and ii) the usage of metallochaperone proteins.

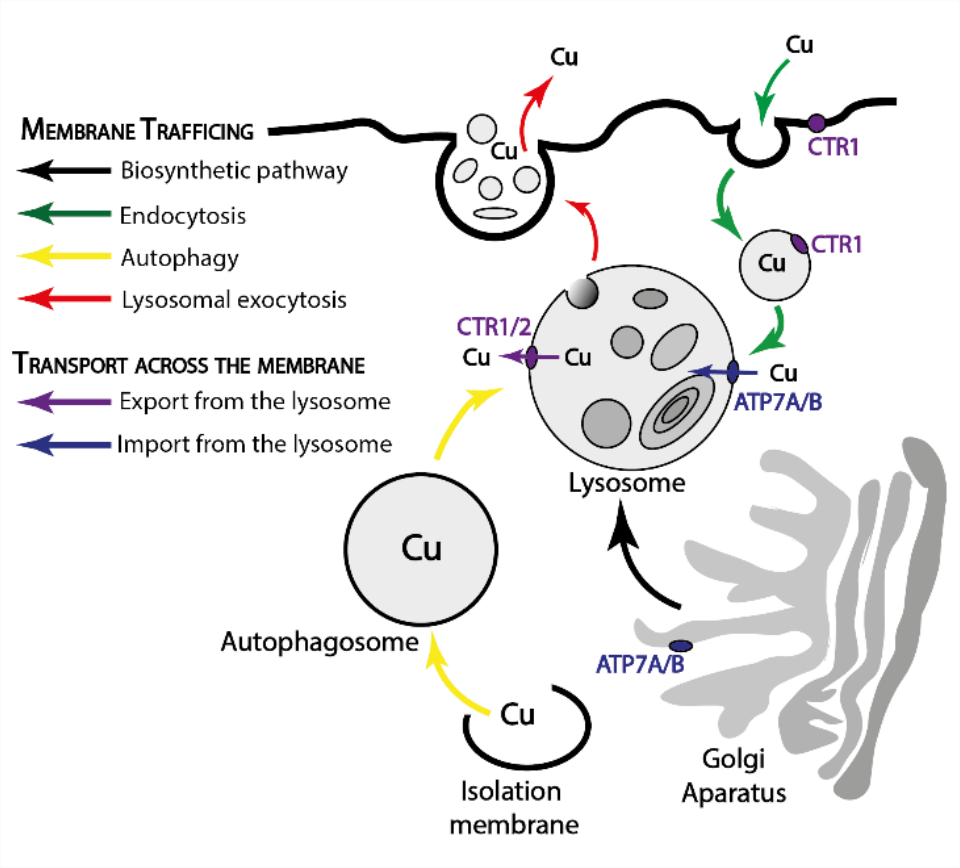

Figure 5: Copper trafficking within the lysosomal pathway. CTR1 and CTR2 are high/low affinity transporter proteins that are located largely on the plasma membrane and are responsible for copper influx in mammalian cells.[39] ATP7A and ATP7B are proteins that function as copper transporter pumps across lipid bilayers by using energy obtained from ATP hydrolysis.[40]

In the first strategy, cellular organelles like lysosomes are used for regulating and distributing the metals inside the cell. In this process metal-containing components are directed through incoming membrane flows, while numerous transporters such as CTR1/2 and ATP7A/B allow metal ions to move across the lysosome membrane.[41] With this mechanism the lysosomes direct the metal fluxes to the sites where metal ions are either used by cellular components or in the case of a metal overload the lysosomal content is sequestered through the cell membrane to maintain a healthy metal concentration inside the cell (see Figure 5).

In the second strategy, metallochaperones are used to selectively bind and safely escort the specific metal ion to various subcellular destinations. When reaching a target protein in need of such metal the ion gets transferred by protein–protein interactions.[42]

The determined binding affinity and dissociation constant of the metal proteins involved in this copper trafficking process vary widely depending on the methods used for the

analysis.[43–45] Some studies suggest that these metallochaperones bind copper(I) with dissociation constants in the femtomolar to attomolar concentration range,[44] other research suggests that the binding affinity is in the order of picomolar affinity[46] but the common ground of the different theories is that the metal downstream transfer to the recipient occurs with rapid kinetics.[47]

Many studies suggest that the copper affinity to proteins follow a gradient from relatively low affinity ligation at the point of uptake, higher affinity for the metallochaperones and highest affinity at its ultimate destination.[46] There are several arguments that suggest that the intracellular environment is devoid of free copper ions because at acidic pH aqueous copper(I) would either spontaneously disproportionate into copper(II) and copper(0) or form precipitates in the form of cuprous oxide (Cu_2O) under neutral or basic conditions. These processes become thermodynamically unfavourable at low nanomolar concentrations. Since there is the necessity for biological systems to exchange metal ions between different metalloprotein pathways and the requirement for a supply of metal ions to nascent metalloproteins, in addition to the strongly-chelated metal in proteins, there must also be a labile pool of metal ions that is less tightly bound, and can be sequestered upon demand.[48] Glutathione (GSH) with its millimolar concentrations in the cytosol is proposed to serve as a cellular copper(I) buffer.[49]

1.1.4.4. Copper related diseases

Misregulation of copper has been shown to have significant implications for health and disease. Excess amounts of copper causes toxicity and compromises the redox homeostatic mechanisms of cells. The toxicity of a copper overload becomes particularly clear in Wilson's disease, a pathological condition caused by a mutation in the ATP7B gene.[50] With a correctly functioning ATP7B gene excess copper is transported from the *trans*-Golgi network to the endo-lysosomal organelles where ATP7B facilitates the metal excretion via a tightly regulated exocytic processes.[51] However, a mutation on this gene disturbs this process and causes a build-up of copper in the liver and several other tissues.[52]

On the other hand, Menkes disease is the best-known disorder of copper deficiency, which is caused by a genetic disorder associated with impaired copper efflux from enterocytes into the blood and inadequate transport of copper to the brain.[53] Furthermore, copper has been proposed to play a crucial role for several other neurogenerative diseases such as Parkinson's disease,[54]Alzheimer's disease[55] and Huntington disease.[56]

In Parkinson's disease a misregulation of copper is proposed to lead to a faulty folding of the protein alpha-synuclein (AS). This protein is believed to play an important role in the outbreak of the disease by forming clusters of oligomers and consequently bigger accumulations forming fibrils inside the cells. Those fibrils can be found in post mortem brains in the so called Lewy bodies, which are the histopathological hallmark of PD (see Figure 6).[57]

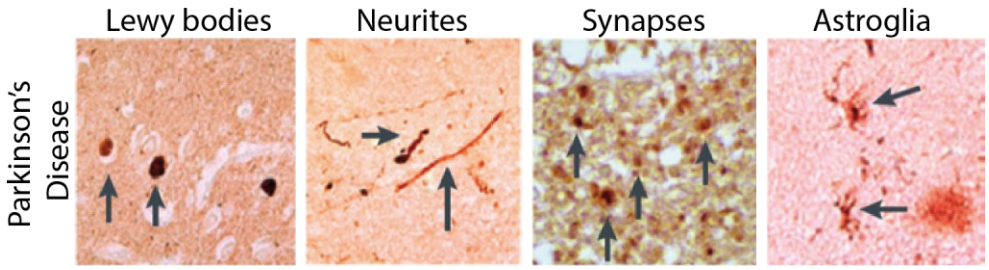

Figure 6: Alpha-synuclein spots as histopathological hallmark of Parkinson's disease in examples of Lewy bodies, neurites, synapses and astroglia cells highlighted by black arrows. Figure taken with permission from publisher from the following reference.[57]

In vitro studies have shown that even at physiological concentration divalent copper may accelerate the rate of AS aggregation.[58] AS is mainly located in the cytosol of the presynaptic neuron. However, small amounts of AS monomers as well as aggregates might be secreted outside the cell, e.g. to plasma and cerebrospinal fluid,[59,60] thus creating conditions that might favour copper(II) binding. These copper-bound forms may promote production of reactive oxygen species (ROS) which leads to oxidative cell damage.[61] Additionally, it is believed that copper(II)-bound to extracellular protein oligomers is responsible for protein toxicity in PD.[62] The interest in elucidating the pathological roles of copper motivates the development of new technologies that enable monitoring of metal content in biological specimens and investigate the influence of external stimuli or genetic modifications on the metal content of cells.

1.1.5. Technologies for measuring copper

The physiological and pathological roles of copper and its delicate cellular regulation mechanisms have led to significant interest and motivated the development of new technologies to measure cellular metal levels.

Technologies to measure the total cellular metal content have formed the basis of bioinorganic studies for more than half a century specifically through the development of absorption spectroscopy and mass spectrometry. Although there have been many advances made on measuring the total metal pool of cells, current research studies have a stronger focus

on investigating the effects of external influences on the cellular metal levels. This sets a demand for technologies that can detect changes in metal level rather than the absolute metal concentrations. Furthermore, there is an interest in observing the redistribution of metal pools within the cell which demands spatially resolved techniques. This demands a sufficient resolution to discriminate between distinct sub cellular regions which is achieved by microscopy technologies.

In general, the technological tools to investigate cellular copper can be categorized in two groups i) technologies which investigate the total metal content of a cell and ii) tools that investigate just the cellular labile copper pool.

1.1.5.1. Techniques to measure total metal content

The total metal pool can be defined as all metal ions within the cell, regardless of oxidation state or coordination environment. Quantification of the total metal pool is therefore of value in reporting the occurrence of metal movements into or out of a cell in response to an external stimulus.

Traditional techniques for the measurement of total metal content, such as flame atomic absorption spectroscopy (FAAS) or inductively coupled plasma mass spectrometry (ICP-MS), require the digestion of cells prior to analysis, and can therefore report only on total changes in intracellular metal concentration for a population of cells, without sub-cellular spatial information. Amongst these techniques, ICP-MS, in particular, has advanced to the stage where it can now detect concentrations below 1 ppt for most elements.[48] Laser ablation ICP-MS is a modified form of this technology that uses a laser and allows for scanning for metal content of tissues.[63]

Another commonly used technique is X-ray fluorescence microscopy (XFM).[64] This synchrotron-based method[65] has the advantage of greater sensitivity and spatial resolution for elemental analysis of single cells. It enabled the visualization of elemental distribution of chemically or cryofixed samples by detection of the characteristic fluorescence emission signatures. Nano-secondary ion mass spectrometry (Nano-SIMS)[66] has similar capabilities to XFM but detects mass rather than fluorescence. It uses an imaging technique which measures secondary ions ejected from a solid sample and provides subcellular resolution. Example images of these techniques are shown in Figure 7.

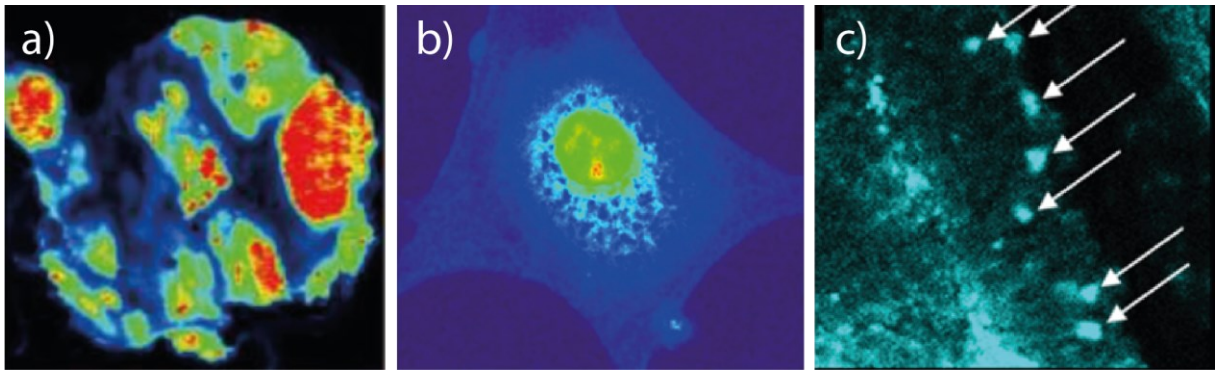

Figure 7: Example images of copper distribution with a) LA-ICP-MS of a mouse brain section; b) S-XRF elemental of 3T3 mouse fibroblast cell; c) NanoSIMS image of megamitochondria of a zebrafish retina. Figures taken with permission of publisher from the following references.[67–69]

The techniques mentioned have their advantages, however they are not capable of measuring and tracking cellular copper levels in living cells and do not make distinctions between labile or static copper pools. For that purpose, fluorescent probes offer a powerful alternative for mapping specifically the labile metal pools with high spatial and temporal resolution.

1.1.5.2. Techniques to measure labile copper content

Analytical methods such as fluorescent probes can complement the suite of techniques to investigate metal ions by assessing the labile metal pools of cells.[70,71]

Since metals in the labile pool are weakly bound to intracellular ligands, they can be rapidly removed or exchanged by competing metal chelators and can therefore also undergo exchange with small molecule fluorescent probes which offers similar binding affinities to the target metal as the cellular ligands. In that case, the small molecule fluorescent probe can bind with an intracellular metal and change its fluorescence response by increasing or decreasing its emission signal. The most common approach is a turn-on of the fluorescence after binding to the analyte where the emission of the bound molecule is measured against a dark background. This response allows for metal detection in live cells with high spatial but also temporal resolution which allows metal distribution to be monitored over time.[32]

However, this technology comes with its own limitations, requirements, and challenges as discussed below.

1.1.6. Basic criteria for an effective fluorescence probe

To successfully utilize small molecules as fluorescent probes for cellular processes several criteria need to be met to get meaningful results in experimental measurements. In general, it is important that the probe shows cellular compatibility which requires the molecule to be

water soluble, non-toxic and cell permeable. Furthermore it should minimally perturb cellular homeostasis, should not cross-react with other sub-cellular species and the subcellular localization of the specimen should be understood.[32] Those probes cannot report on the absolute copper ion concentration but rather provide relative information on the availability and distribution changes of labile copper pools in living or fixed cells. Since this approach is dependent on the chemical properties and the structure of the analyte, rather than the physical properties of the metal, it creates the challenge of sensitivity and selectivity of the formed complex in the heterogeneous environment of the cell. This also requires the development of independent analytical and chemical controls to properly validate the probe's function for the biological context.

Therefore, there are several important chemical design criteria to consider when developing an effective metal targeting fluorescent probe.

1.1.6.1. Selectivity

The metal ion probe needs to selectively bind to only one metal ion over other commonly found ions in cellular systems. There are several ways to ensure that the binding is specific for the ligand by considering the ligand denticity and geometry, the hardness or softness of the donor atoms, and the size of the metal ion.[32]

1.1.6.2. Sensitivity (extinction coefficient and quantum yield)

High sensitivity of a molecular sensor is a key requirement for studying cellular events. This is especially important because the local concentration of the particular analyte may be in the low nanomolar or picomolar range inside the cell. Furthermore, the signal needs to be distinguishable from autofluorescence (which is the natural emission of light after excitation) produced by highly conjugated molecules naturally occuring in cells. Autofluorescence makes it more difficult to distinguish background from weak fluorescence intensity signals produced by the fluorescent molecule. Therefore, the fluorescent probe should display a high extinction coefficient and quantum yield. By definition, compounds with large extinction coefficients strongly absorb light at a given wavelength and in case of a high quantum yield the molecule can efficiently convert the absorbed energy into emitted photons.[32,72]

1.1.6.3. Equilibrium dissociation constant K_d

The dissociation constant (K_d) of a metal ligand binding describes the affinity between the probe and the metal ion of interest. The smaller the K_d value is the more tightly bound is the metal to the ligand. For a successful application of the fluorescent probe the metal chelating ligand should possess a dissociation constant that is within the same order of magnitude as the concentration of the metal ion of interest within a particular cellular location. In case of a too weak binding affinity, the sensor would not be able to detect the intracellular metal pools; conversely, if it is too strong it could disturb the physiological balance of the metal being detected and could cause unwanted cytotoxicity.[32]

1.1.6.4. Excitation wavelength and photostability

An excitation wavelength close to the UV-light spectrum usually results in more pronounced autofluorescence because several cellular components absorb light well in this range.[72] Therefore, fluorophores with visible-light or even further red-shifted excitation and emission wavelengths are preferred. A red-shifted excitation wavelength provides the additional benefit of better tissue permeability and allows the application of the fluorescent probe for fluorescence imaging in tissues. Furthermore, photobleaching effects due to limited photostability must be considered when the fluorophore is illuminated. Besides the reduced signal-to-noise ratio due to photobleaching, it produces toxic compounds and harms the cellular functions and therefore, potentially influences the investigated biological mechanisms.

1.1.6.5. Turn-on/off sensors and ratiometric sensors

Generally, “turn-on” and ratiometric probes are preferred for intracellular applications over “turn-off” probes that undergo emission quenching upon analyte binding. Ratiometric probes provide the advantage that the intensity is measured at two wavelengths, which makes it possible to normalize the background interference due to photobleaching.[32] Such probes are often used to sense environmental parameters such as pH, viscosity, or polarity.

Most sensors described in the literature do not fulfil all the criteria described above. This highlights the difficulty for optimal probe development and points out the need to develop probes with better and improved properties. One promising molecular platform that has been investigated thoroughly as fluorescent probes are the very bright and chemically stable compound platform of 4,4-difluoro-4-bora-3a,4a-diaza-s-indacen or in short BODIPY.

1.1.7. BODIPY

Over the past few decades BODIPY based fluorescent probes have seen a strong focus of research interest. The backbone compound was first synthesized by Kreuzer and Treibs in 1968[73] where they tried to conduct an acylation of 2,4-dimethylpyrrole by acetic anhydride in the presence of BF_3 as a Lewis acid. Instead of the desired 2-acetyl-3,5-dimethylpyrrole they obtained the first highly fluorescent BODIPY compound (see Scheme 1).

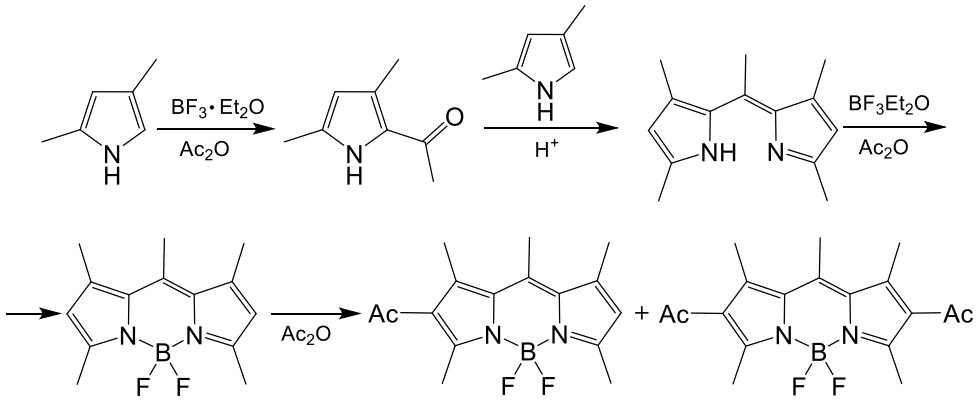

Scheme 1: Synthetic scheme of the first BODIPY compound by Kreuzer and Treibs[73]

BODIPY compounds saw their rise in popularity in chemistry in the mid 1990's due to their synthetic versatility and outstanding spectroscopic properties. The feature that make BODIPY molecules such interesting compounds and target fluorophores are their very high chemical stability. They only decompose under very strong acidic or basic conditions and therefore allow a wide range of reactions on the fluorescent core of the molecule. The reason for BODIPY's high chemical stability can be explained by the fact that all three heteroatoms (boron, fluorine, and nitrogen) are first row elements that enable an efficient delocalization of the π-orbitals. This allows for tuning their spectroscopic properties across a broad spectral range from the visible to the near infrared (NIR), by introduction of different groups into the BODIPY core structure. They have therefore found many applications in science and technology fields such as for chemical sensing,[70,74–76] biological imaging,[77,78] as well as more recently in photodynamic therapy,[79,80] and organic photovoltaics.[81,82]

1.1.7.1. Structure of BODIPY

The BODIPY core has, similar to many other fluorescent organic dyes, a mostly planar structure; except for the two fluorine atoms, that lie on the perpendicular bisecting plane. The BF_2 unit restricts the flexibility of the dipyrrin structure which results in an enhanced fluorescent response. The molecular structure of BODIPY dyes can be described by two

equivalent ionic resonance structures shown in Scheme 2. To simplify the notation the positive and negative isomeric charges on the boron and nitrogen atoms are omitted. The notation for the numbering of each atom follows the rules set for s-indacene where the position 8 of the BODIPY core can also be referred as *meso*-position which is similar to the notation of porphyritic systems.

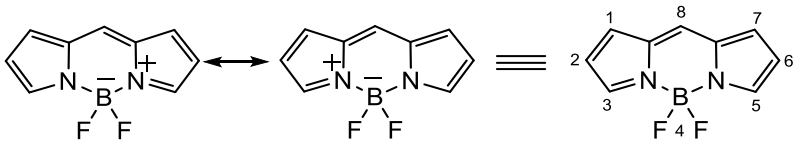

Scheme 2: The two resonance structures of BODIPY (left); IUPAC atom numbering convention (right).

1.1.7.2. Synthesis of BODIPY core structure

Most BODIPY synthetic routes are based on well-established pyrrole condensation reactions with electrophile reagents inspired by porphyrin research which lead to the formation of symmetrical BODIPY molecules.[83,84] Also the synthesis of BODIPY molecules from aromatic aldehydes are well established and widely used.[85,86] Dipyrrolomethanes are formed from acid-catalysed condensation reactions of pyrroles with aldehydes where the pyrroles should be used in large excess to prevent polymerization. The intermediate dipyrrolemethanes are not very stable and are normally not isolated but immediately oxidized *in-situ* to dipyrromethenes or dipyrrins with DDQ or *p*-chloranil (Scheme 3)

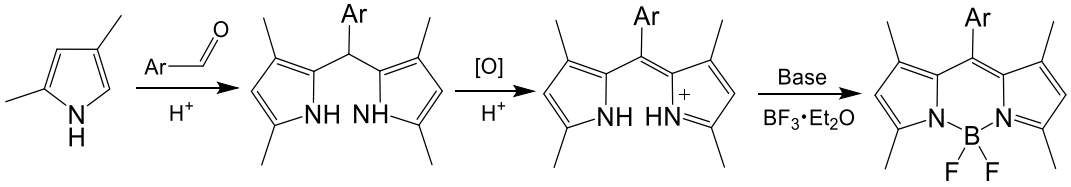

Scheme 3: Synthetic route to BODIPY by condensation of pyrroles with aromatic aldehydes.

The deprotonation of the formed dipyrrins and complexation with boron trifluoride diethyl etherate leads to the BODIPY product. Some reports demonstrated that in the case of introduction of different substituents at the *meso*-position the oxidation of dipyrrolemethanes fails with DDQ or *p*-chloranils.[87]

Alternatively other acylium equivalents such as anhydrides,[88] acid chlorides,[89] or orthoesters,[90] are used as electrophilic agents for which the reaction does not form the intermediate acylated pyrrole product. Instead under these acidic conditions, the 2-acylpyrrole immediately reacts with a second pyrrole molecule to form the dipyrrin. This reaction pathway does not require the oxidation step and under basic conditions and after addition of

BF_3 provides the BODIPY compounds in high yields (see Scheme 4). This reaction procedure has the additional advantage that it allows for the synthesis of alkyl-substituted dyes in *meso*-position which in the previous procedure with the acylium equivalent would not be possible.

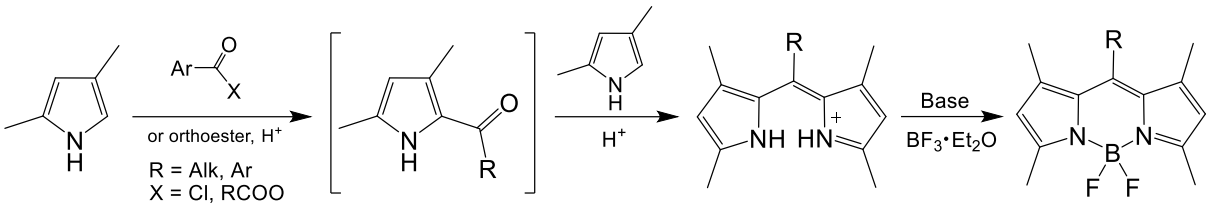

Scheme 4: Synthetic route to BODIPY by condensation reaction of pyrroles with acylium equivalents.

These are the most common general synthetic steps for the formation of the BODIPY structure which are at the core of any further modification of this molecule structure. Many alterations and substitutions on the BODIPY core have been reported and two exhaustive reviews provide further details on that.[91,92]

Because of their stability and easily tuneable properties BODIPY molecules have been widely used as platform for several selective fluorescent metal probes. In the next section the attention is focused on the field of fluorescent copper(I) probes which saw a rise of popularity over the past 15 years. Several of the reported probes have BODIPY as a core structure, but also other fluorescent dyes demonstrated some advantages in certain aspects.

1.3.3. Fluorescent copper(I) probes

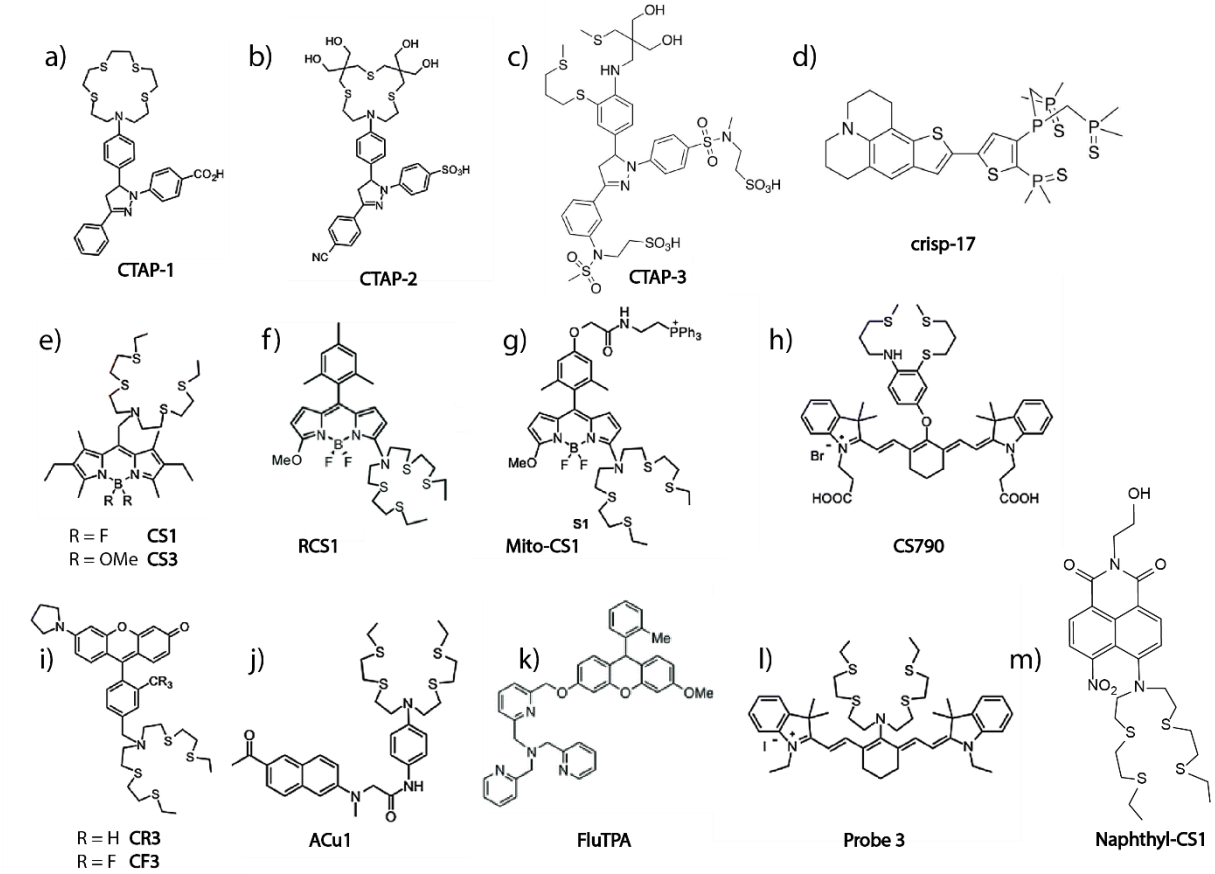

Figure 8: Chemical structure of fluorescent copper(I) probes. Taken with permission from the journals of references.[93,46]

Over the last two decades several fluorescent copper(I) probes were reported in the literature (Figure 8). These chemical tools were designed to sense the labile copper(I) pools in live cells by molecular imaging, allowing for real-time detection of changes in copper(I) levels. Furthermore, next to the cellular metal distribution also movement patterns of the metal containing organelles can be investigated with high spatial and temporal resolution.[94–96]

The fluorescence switching mechanism of most of the available turn-on fluorescent sensors for copper(I) is dependent on a photoinduced electron transfer (PET) process or a related charge transfer (CT) pathway.[97] Two exhaustive reviews show greater details of these developments.[46,93]

In brief, the group of Fahrni developed the first small-molecule fluorescent probe **CTAP-1**[98] (Figure 8a) to detect copper(I) which is comprised of a 1,3-diarylpyrazoline fluorophore linked to a tetrathiazacrown ether receptor (NS_4) which has high selectivity for copper(I). This probe was then further improved with **CTAP-2**[99] (Figure 8b) in which the hydrophilicity of **CTAP-1** was increased by adding four hydroxymethyl groups to the tetrathiazacrown

receptor. **CTAP-3**[99] (Figure 8c) represents the third generation of these copper(I) probes and has improved the optical properties over the previous generations by introducing strong electron withdrawing groups such as sulfonamide and anionic sulfonate moieties into the structure which made it also nicely water soluble. This third-generation copper(I) probe overcomes the problem of aggregation and accumulation in lipid environments, which is a common challenge for many fluorescent dyes. However, it has not been applied to cells as it was done for the previous generations of probes. More recently Fahrni's group developed a new probe with a sulfide-stabilized phosphine copper(I) binding site, **crisp-17**[143] (Figure 8d), which allows for cytosolic copper(I) detection which is buffered at very low attomolar concentrations.

Over those years in parallel the group of Chang developed several other copper(I) probes. Their first copper(I) probe was based on acyclic form of the NS_4 receptor connected to a BODIPY based fluorophore named **CS1**[100] (Figure 8e). The optical properties of this probe was further improved by exchanging the fluoride substituents of the boron centre for more electron-rich methoxy groups in **CS3**[101] (Figure 8e). The Chang laboratory also modified the BODIPY core structure to develop the ratiometric copper sensor **RCS1**[96] (Figure 8f) and another version that specifically targets mitochondrial copper(I) **Mito-CS1**[102] (Figure 8g). In later generations different dye platforms were investigated such as Cy5-base in **CS790**[103] (Figure 8h) or fluorescein-base probes in **CR3** and **CF3**[104] (Figure 8i) while keeping the binding site of the NS_4 receptor the same. However, **CS1** and **CS3** were the most widely used probes to tackle biological questions. Even though both compounds have been successfully used for detecting intensity changes after copper supplementation in HEK293 cells this could not be repeated in SH-SY5Y, M17, U87MG, and CHO cell lines. In those cell lines the dye mainly localized in lysosomes and did not show changes in intensity signals upon supplementation of copper.[105] Furthermore, it has been shown that the free copper(I) levels in the cytosol of eukaryotic cells are modulated at attomolar levels ($\sim 10^{-18}$ mol L^{-1})[106,107,108] due to copper metallochaperone proteins such as Atox1 or GSH[44] which bind copper(I) with orders of magnitude lower than the binding affinity of the acyclic tetrathiaza-receptor (K_d $\sim 10^{-13}$ mol L^{-1}).[101] At a neutral physiological pH, as it is present in the cytosol of the cell, it has been shown that the high GSH levels can remove the copper(I) from the tetrathiaza binding site of **CS1** and **CS3**. However, at acidic pH 4.0, which is present in lysosomes[109] **CS1** could successfully compete with GSH for copper(I).[105]

Since it is well established that lysosomes play a key role in the regulation of copper[110,111] it could well be that the probe is gaining access to copper(I) made available *via* recycling of nutrient copper in the acidic lysosome, as it was hypothesized for **CS1** in [105].

Other research groups added some more selective copper(I) probes such as **ACu1**[112] (Figure 8j) which is a two-photon fluorescent copper(I) probe that has successfully been used for detecting copper(I) in brain tissue. **FluTPA**[113] (Figure 8k) is a fluorescent copper(I) probe based on a fluorescein platform that turns-on irreversibly upon cleavage of an ether bridge by interaction with copper(I) ions. A tricarbocyanine dye backbone in combination with the NS_4 copper(I) binding site was used for **Probe 3**[114] (Figure 8l) a NIR turn-on copper(I) probe which has been used to detect copper(I) changes in living MG63 cells and the ratiometric naphthalimide based copper(I) sensor **Naphthyl-CS1**[115] (Figure 8m) was published by the group of Satriano which was able to monitor changes in copper(I) levels by fluorescence intensity changes in SH-SY5Y cells.

1.1.8. Fluorescence lifetime imaging microscopy (FLIM)

Besides the detection of metal ions such as copper by intensity-based sensing, the last few decades showed the gaining popularity of an alternative *in vivo* fluorescence sensing method based on the fluorescence lifetime property of fluorescent dyes. The idea of time-resolved fluorescence measurements with a microscope was first mentioned in the 1950s[116] but the actual breakthrough for FLIM came in 1989 when the first reports about the use of fluorescence lifetime for imaging were published.[117,118] Specifically in the last two decades FLIM saw an increasing rise of popularity because of its high sensitivity to the molecular environment and changes in molecular conformations which allowed the visualisation of phenomena that could not be studied using intensity based methods. Therefore FLIM established itself as a key technology to image the interaction and environment of fluorescent probes in living cells.[14,119,120]

What makes FLIM stand out from all the other fluorescence microscopy techniques is that it can report on photophysical events that are difficult or impossible to observe with fluorescence intensity imaging. One big advantage of FLIM is that it is independent of the fluorophore concentration.[115] This is especially beneficial in context of cellular imaging since sensory probe molecules are not distributed uniformly throughout a cell.[70,95,121]

Compared to fluorescence intensity, fluorescence lifetime provides an absolute measurement which, is less susceptible to artefacts arising from scattered light, photobleaching, non-

uniform illumination of the sample or excitation intensity variations.[72] The FLIM signal can monitor changes in the immediate microenvironment of the molecules and is capable at reporting molecular processes with high sensitivity. This technique allows for semi-quantitative analysis by monitoring systematic signal changes at subcellular locations as a function of time or analyte concentration.[122] FLIM has been shown to be useful for sensing parameters such as viscosity[123] and temperature of different parts of the cell.[124] Furthermore, this technique has been used to visualize cellular uptake and release of ions.[120,119] However, the measured lifetime needs to be considered with caution due to the dependency of both the local concentration of the analyte and the sensor, on the average radiative lifetime. Therefore, two different cellular regions can have the same measured lifetime, but very different overall concentrations in the aspect of the measured analyte.[122] Additionally, varying cellular (local) environments (such as polarity, rigidity etc.) can show strong sensitivity on the average radiative lifetimes and the resulting observed multi-exponential decay can be difficult to interpret.[120,121,125]

1.1.8.1. Fluorescence lifetime imaging microscopy for copper

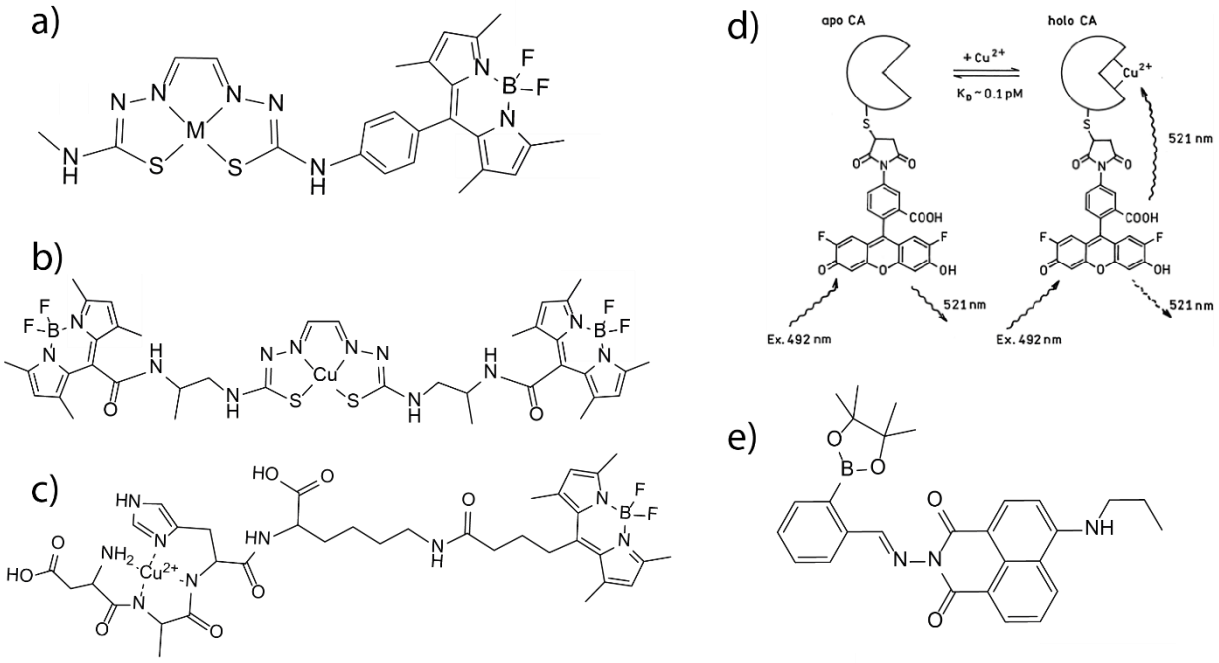

Figure 9: Examples of copper(II) probes used for FLIM. Taken with permission from the journal of references.[126–130]

FLIM has been used in several different ways to investigate the behaviour and function of intracellular copper(II). Fluorescently labelled copper(II) bis(thiosemicarbazonato) complexes

were used to monitor the release and substitution of copper(II) with zinc(II) of in neuroblastoma cells and primary cortical neurons with FLIM (Figure 9a, b).[126,127] Jung *et al.,* developed a high-affinity copper(II) probe based on a peptide binding site connected to a BODIPY molecule for fluorescence lifetime correlation spectroscopy (Figure 9c). This system, however, has not been used in live cells.[128] Another concept for measuring copper(II) at very low femtomolar concentrations in cells with FLIM was proposed by Thompson *et al.,* where they used the protein human carbonic anhydrase II labelled with the dye Oregon Green to monitor differences of copper(II) concentrations based on the frequency-domain of fluorescence lifetime microscopy (Figure 9d).[129] Another approach to measure copper(II) with FLIM was with a ditopic boronic acid and an imine-based naphthalimide fluorescence turn-off probe (Figure 9e)[130] and the quenching effect of copper(II) on GFP was used in cells to monitor release and uptake of copper(II) with FLIM in plant cells.[119]

Although there are several examples where FLIM has been used to investigate copper(II) in live cells, there is no reported compound in the literature that is able to do that with copper(I). Therefore, it was attempted to design a new selective fluorescent copper(I) probe that aims to perform FLIM measurements to sense fluctuations of copper(I) levels in live cells.

1.2. Aims and Objectives

The first aim of this PhD project was to develop a detection toolset for visualizing and studying copper(I) *in cellulo* in different cell lines and to investigate its localization pattern in relation to alpha-synuclein and amyloid-beta. The technology of choice was the use of selective fluorescent copper(I) probes and fluorescently labelled proteins. With this combined toolset at hand their localization/colocalization with AS and AB would then be investigated.

The milestones of the first phase of this aim are:

- resynthesize an already existing and well-established probe from the literature which is capable of detecting cellular copper(I) via fluorescence microscopy;
- test the photophysical properties and the abilities of the selected target molecule to sense copper(I) *in vitro* and in cells;
- perform localisation studies of copper(I) in cells;
- find a fluorescent labelling strategy for AS proteins which enables the *in cellulo* localization of AS and to perform a colocalization study with the copper(I) probe in SH-SY5Y, N27, HEK293 cell lines and primary hippocampal neurons;

- perform a control experiment with overexpressed AS by transfecting cells with a plasmid and visualize AS by immunohistochemistry staining with an AS antibody;
- investigate the potential of the copper(I) probe for sensing copper(I) based on fluorescence lifetime changes.

In the next phase of the project, based on the knowledge gained from the synthesized probe from the literature, a new copper(I) selective fluorescent "turn-on" probe should be designed with improved properties and its qualities should be compared with the previously synthesized one. The properties should be tuned for improved photostability for a potential use of the new probe in fluorescence lifetime imaging microscopy.

1.3. Results and Discussion

1.3.1. Copper Sensor 3 (CS3)

For the selection process of the existing probes in the literature, a thorough literature research was carried out and the copper(I) probe **CS3** developed in C. Chang's laboratory was identified as a potentially suitable first target probe.[101] The small molecule probe consists of a BODIPY core structure connected to a NS_4 copper(I) binding ligand linked via a carbon bridge to the *meso* position of the BODIPY dye. A PET mechanism from the NS_4 ligand causes quenching of **CS3** in the unbound state. When binding to copper(I) a 40-fold fluorescence "turn-on" response was reported. **CS3** selectively binds to copper(I) over many other biological relevant metal ions, and it has been successfully used for cellular imaging (in HEK293 cells and primary hippocampal neurons). The K_d of **CS3** was determined to be 13×10^{-14} mol×L^{-1}. Furthermore, a control ligand **Ctrl-CS3** without the copper(I) binding abilities was used to confirm the functionality of the probe. Since the properties of this probe sounded promising this ligand was chosen as a first target molecule to synthesize and perform experiments to investigate copper(I) in cells.

1.3.1.1. Synthesis of CS3

The synthesis of the two compounds copper(I) ligand **CS3** and control ligand **Ctrl CS3** was performed following an already existing procedure from the literature.[100,101,131] The synthetic scheme of the selected molecule and its control counterpart are shown in Scheme 5.

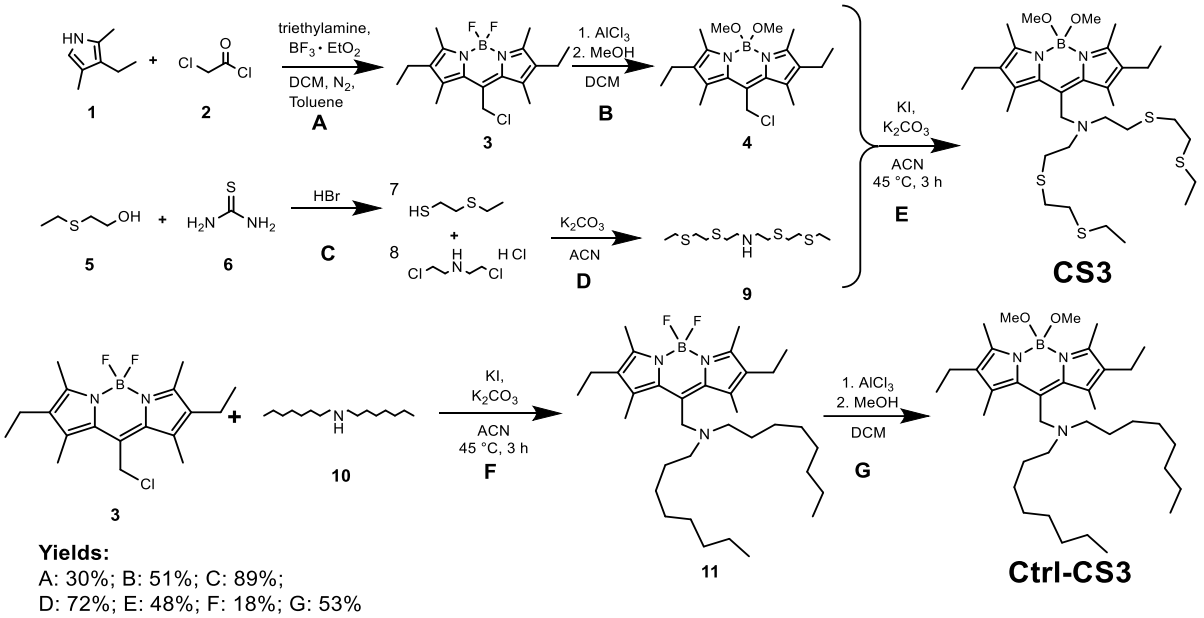

Scheme 5: Synthetic scheme for the synthesis of fluorescent copper(I) ligand **CS3** and control ligand **Ctrl-CS3**

In the reaction step **A** the basic structure of the BODIPY dye was synthesized. The pyrrole derivate **1** and the acid halide **2** were mixed in a 2:1 ratio in degassed DCM and heated up. After changing the solvent to toluene, boron trifluoride was added to the mixture. The ^{1}H-NMR spectrum gave very clear evidence that the right product was formed showing one triplet and one quartet which indicated that the ethyl group was attached onto the pyrroles and the three singlet peaks indicated the two methyl groups on the pyrrole and the slightly upshifted chlorinated methyl group in the *meso* position between the two pyrrole rings. (Figure 10a). The exchange of the fluorine moiety to methoxy groups had shown to have a positive effect on the fluorescent properties of the dye by increasing the electron density in the system.[132] The methoxylated form of the BODIPY **4** from reaction **B** was easily identified by an additional peak at 2.8 ppm in the ^{1}H-NMR spectrum which was not present in the fluorinated form of the BODIPY **3** (Figure 10b). For reasons that were not known this signal showed a small split with a coupling constant of 5.1 Hz which became a normal singlet in the reaction steps following to that.

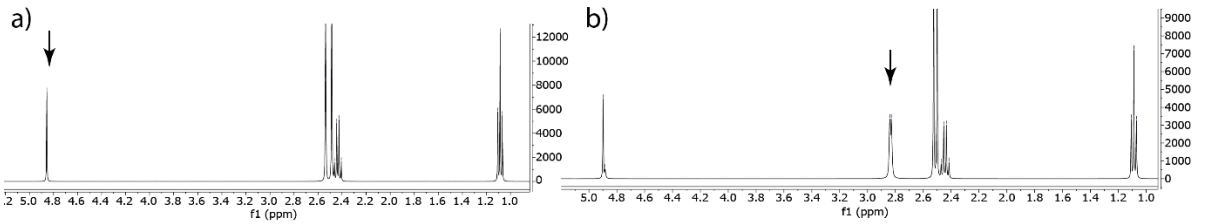

Figure 10: ^{1}H-NMR spectra of (a) compound **3** with arrow indicating the chlorinated methyl group in the *meso* position of BODIPY; b) compound **4** with arrow on the peak of the newly formed methoxy-groups in the product.

The methoxylated BODIPY had a short shelf life, was very unstable to light exposure and was used immediately after its preparation for the next reaction step. The synthesis of the copper(I) binding ligand tetrathia-monoazaheptadecan **9** was performed in a two-step synthesis (reaction **C** and **D** in Scheme 5). The first reaction step yielded product **7** as a very smelly oil which was not further purified and used crude for the reaction with bis(chloroethyl)amine **8** to form compound **9**. This product was characterized by ^{1}H-NMR spectroscopy which showed a triplet and a quartet, corresponding to the two terminal ethyl groups, and two multiplets corresponding to the four symmetric ethyl linkers. Furthermore, the hydrogen from the nitrogen was visible as a broad peak in the aliphatic region of the spectrum (see Figure 11).

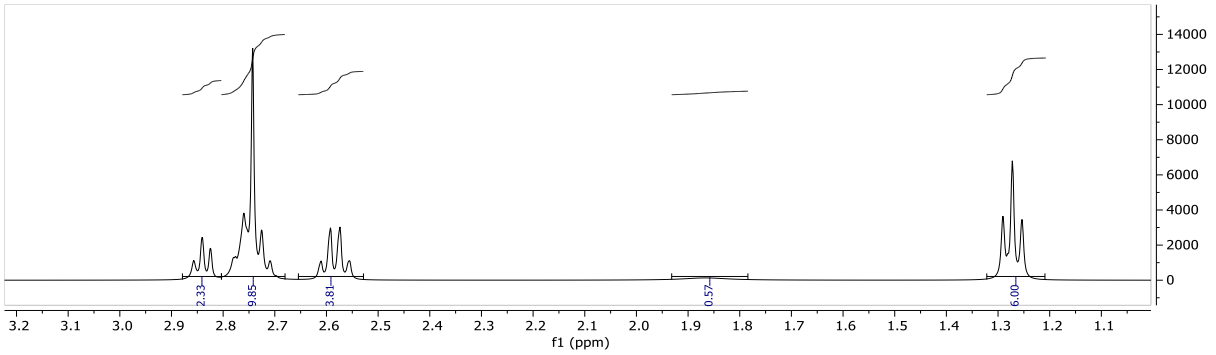

Figure 11: ^{1}H-NMR spectrum of copper(I) binding site tetrathia-monoazaheptadecan.

The final reaction step **E** was the reaction of the amine **9** with the chloride of the BODIPY dye **4**. In this reaction, KI and K_2CO_3 were used as activating agent for reaction of the amine of **9** with the chloride residue of the BODIPY dye **4**. This reaction was also kept under a strict nitrogen atmosphere. The pure product **CS3** was obtained after column chromatography using ethyl acetate as solvent resulting in a clear separation of the product from side products. The product was characterized by ^{1}H-NMR spectroscopy which shows a slightly shifted overlap of the two starting materials. The synthesis of the **Ctrl-CS3** ligand was performed following analogous procedures to those used to prepare **CS3**. Reaction **F** followed the procedure of

reaction step **E** and reaction **G** followed the procedure of reaction step **B**. The formation of both final products was confirmed using ^{1}H-NMR and ESI-MS.

1.3.1.2. Spectroscopic characterization of CS3

After the synthesis of ligand **CS3** and control ligand **Ctrl-CS3** some spectroscopic measurements were performed to confirm the properties which were reported in the literature.[101]

The absorption spectrum of **CS3** with 1 equivalent of copper(I) shows a characteristic intense peak at 540 nm with a weaker shoulder at around 500 nm. In the fluorescence spectrum, after excitation of the HEPES buffer solution at 525 nm, the fluorescence shows a stock shift of around 10 nm (see Figure 12a) and the fluorescence copper(I) titration confirms a 1:1 binding of the ligand with **CS3** (Figure 12b). During the copper(I) titration the peak of the absorbance spectrum shifts from 540 nm to 536 nm. Furthermore, the shape of the absorption spectrum changes slightly becoming sharper compared to the copper(I) unbound form (see Figure 12c).

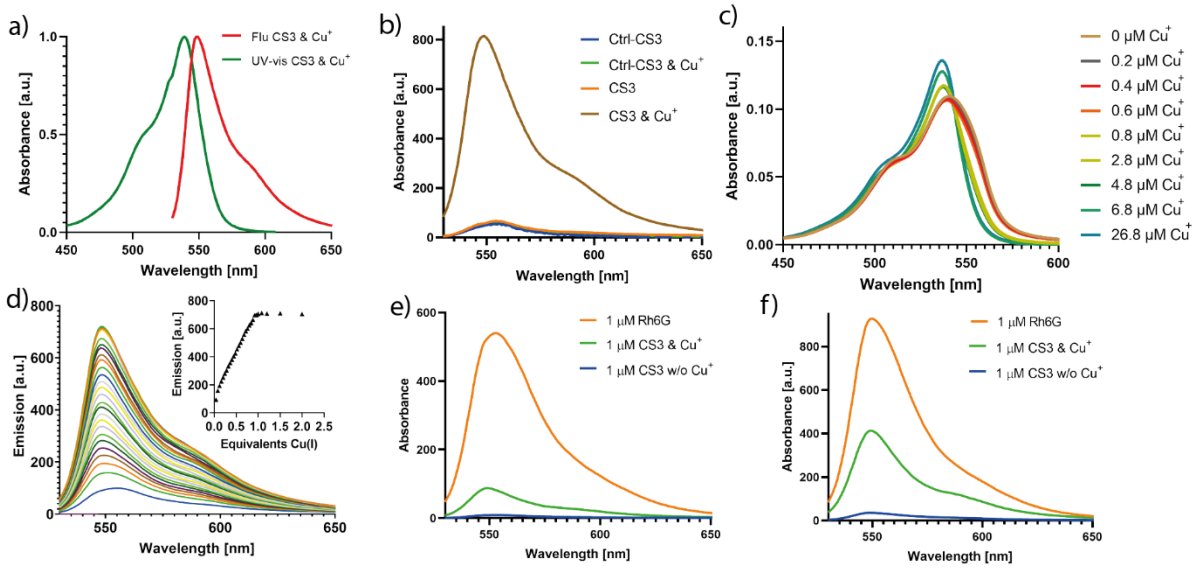

Figure 12: Spectroscopic studies of the interaction of copper(I) with **CS3** and **Ctrl-CS3** in HEPES buffer pH 7.5. a) Normalized absorption and emission spectrum of **CS3** (1 µM) with excess copper(I) showing a 10 nm Stokes shift. b) Emission spectrum comparison of **CS3** and **Ctrl-CS3** (1 µM) upon addition of excess copper(I). c) Absorption spectra for **CS3** copper(I) titration showing a 4 nm blueshift of the main peak. d) Fluorescence emission spectra of copper(I) titration to **CS3** (λ_{ex} = 520 nm); inset showing the binding plot recorded at the fluorescence peak maximum (λ_{em} = 540 nm). Fluorescence emission comparison with Rh6G and **CS3** (1 µM) with and without excess copper(I) in e) HEPES buffer; f) EtOH.

The quantum yield Φ of **CS3** was determined to be 0.4 in comparison to rhodamine 6G with ethanol as solvent. The quantum yield dropped to 0.1 when using HEPES buffer at pH 7.5 (see Figure 12e, f). However, the turn-on response in both solvents was roughly a 10-times increase after copper(I) addition over the unbound form of **CS3**. As expected, **Ctrl-CS3** did not show a fluorescence increase upon copper(I) addition (see Figure 12b).

In a fluorescence spectroscopy experiment in different solvents, it became obvious that the probe is very much dependent on the environment which it was interacting with. **CS3** showed good turn-on responses in PBS buffer and MeOH, in DCM and ACN the signal decreases and in acetone and EA the signal did not change upon addition of copper(I) (see Figure 13a-f). Furthermore, the addition of excess of the competing ligand BETA just showed a reversibility of the signal in MeOH and PBS and caused a surprising increase in ACN as solvent (see Figure 13f). These results indicated that the cellular experimental results that were later carried out for this research needed to be interpreted with caution because the local environment of the probe had a strong effect on its fluorescent properties.

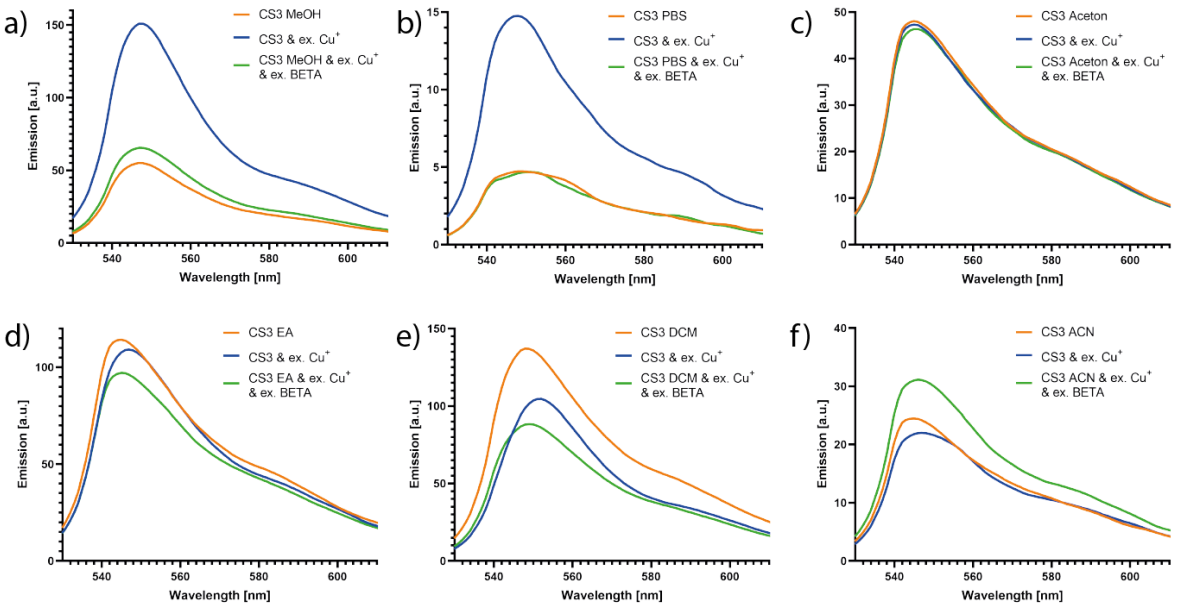

Figure 13: Effect of solvents on **CS3**. **CS3** (1 µM) in a) MeOH; b) PBS; c) Acetone; d) EA; e) DCM; f) ACN with and without excess copper(I).

1.3.1.3. pH effect and CS3 aggregation

In a pH experiment with the **CS3** probe with fluorescence spectroscopy the fluorescence response was stable over all acidic pHs, displaying a consistent fluorescence increase after copper(I) addition. However, under basic conditions starting from pH 8 the fluorescence signal declined over time (see Figure 14a). Furthermore, DLS was used to investigate the possibility of aggregation of the probe in an aqueous environment. This has been already

discussed in the literature for the first generation of this BODIPY based probe (**CS1**).[105] For a concentration of 2 µM of **CS3** in PBS buffer the aggregation behaviour was confirmed displaying an average particle size of 200 nm (see Figure 14b). Interestingly, when adding copper(I) the measured particle size increased slightly to 250 nm (see Figure 14c). When measuring **CS3** in MeOH, the particle size could not be determined because of an inconsistent detection signal of the DLS device resulting in a calculated particle size between 1000 nm and 7000 nm. This could be due to the fact that the probe is actually dissolved in MeOH and that the background signal could have caused these inconsistent results. Interestingly, in both solvents (PBS and MeOH) a fluorescence increase upon copper addition could be observed suggesting that the probe could follow a different signal mechanism for the different solvents. From these preliminary experiments a combination mechanism of PET with de-aggregation of the probe could be one possible explanation. However, this phenomenon was not investigated further for this probe.

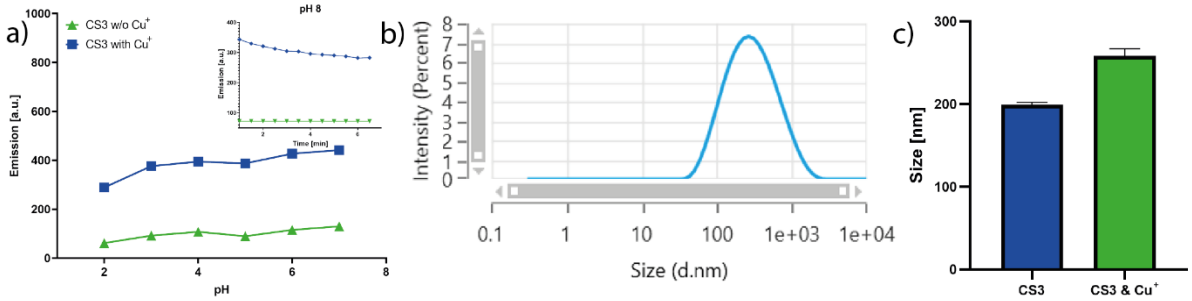

Figure 14: Fluorescence of **CS3** at different pH and **CS3** DLS experiments. a) Fluorescence response of **CS3** (1 µM) in PBS at different pH before and after addition of 3 µM copper(I); inset showing fluorescence signal at pH 8 after addition of 3 µM copper(I) over time. b) DLS results of **CS3** (1 µM) in PBS. c) DLS particle size of **CS3** (1 µM) in PBS before and after addition of excess copper(I).

1.3.1.4. CS3 and fluorescence lifetime

Next, the fluorescence lifetime properties of **CS3** in MeOH using a Time-Correlated Single Photon Counting (TCSPC) system was investigated. The decay traces changed with increasing amounts of copper(I) (see Figure 15a). By fitting the data with a global fit with two components the fluorescence lifetimes were calculated with τ_1 and τ_2 being 0.97±0.02 ns and 6.59±0.04 ns, respectively. The interpretation of τ_1 was associated to the unbound and τ_2 to the copper-bound probe which is consistent with the amplitude contributions during the copper(I) titration where α_1 and α_2 have opposing trends with increasing amounts of copper(I) (see Figure 15b).

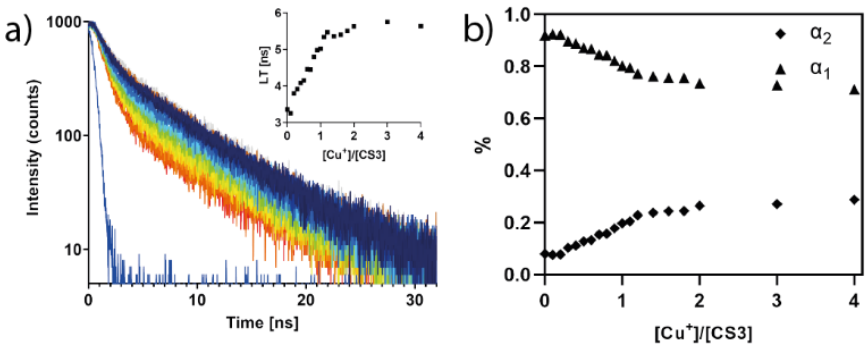

Figure 15: Fluorescence lifetime measurements of **CS3**. a) Time-resolved fluorescence decays of **CS3** (λ_{ex} = 530 nm, λ_{em} = 540±10 nm); Instrument response function (IRF) is shown in blue; inset shows calculated intensity-weighted average lifetime. b) Titration amplitude trends.

The average intensity weighted fluorescence lifetime showed an increase during the copper(I) titration starting at 3.18±0.01 ns without copper(I) and reaching a maximum at 5.27±0.02 ns with an excess of copper(I). Representative examples of the fitted traces with variable and fixed lifetimes can be seen in Figure 16. The fits for the decays show a low χ^2 value which indicated a good fit of the biexponential decay curve. The full set of parameters of the titration data can be found in the Appendix in Table 5.

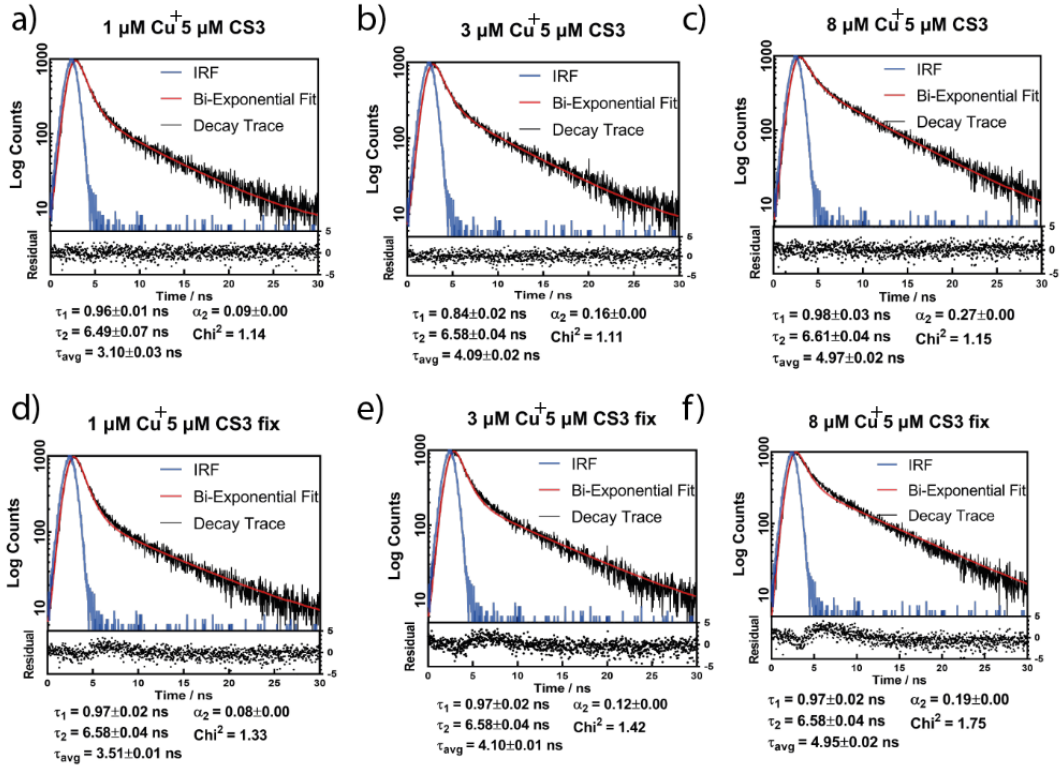

Figure 16: Biexponential lifetime fitting comparison. Fluorescence decay curves of **CS3** (5 µM) in MeOH with copper(I) (1, 3, 8 µM) were measured and traces were fitted with two exponentials keeping τ_1 and τ_2 variable (a, b, c) and fixed τ_1 = 0.97±0.02 ns and τ_2 = 6.58±0.04 ns (d, e, f).

This data suggested that BODIPY probes with a NS_4 binding site for copper(I) had the ability to monitor changes of copper(I) concentrations by fluorescence lifetime measurements.

1.3.1.5. Cellular studies with CS3

After establishing the functionality of **CS3** *in vitro*, the copper(I) probe was tested on different cell lines to investigate its properties and behaviour in a cellular environment and was imaged with point-scanning confocal fluorescence microscopy. Furthermore, some colocalization experiments were carried out with alpha-synuclein (AS) and amyloid-beta (AB) to investigate the potential role of copper(I) in Parkinson's and Alzheimer's disease.

1.3.1.5.1. CS3 and Ctrl-CS3 in cells

First, the copper(I) binding probe **CS3** was compared with the control ligand **Ctrl-CS3** which does not have the functional copper(I) binding site. For this experiment cells from the neuroblastoma cell line SH-SY5Y were incubated for 15 min with **CS3** (2 μM) in PBS. The fluorescence microscopy images confirmed a successful uptake of the probe and showed bright punctate localization of the **CS3** probe indicating that copper(I) was in those cellular compartments (see Figure 17). When treating the same cell line under the same conditions with **Ctrl-CS3** no fluorescence signal was observed in the cell. Under the assumptions that the control ligand has the same polarity as the actual probe and the same subcellular localization and cellular uptake, the probe's signal was believed to correspond to copper(I) and was not caused by any other fluorescent turn-on responses.

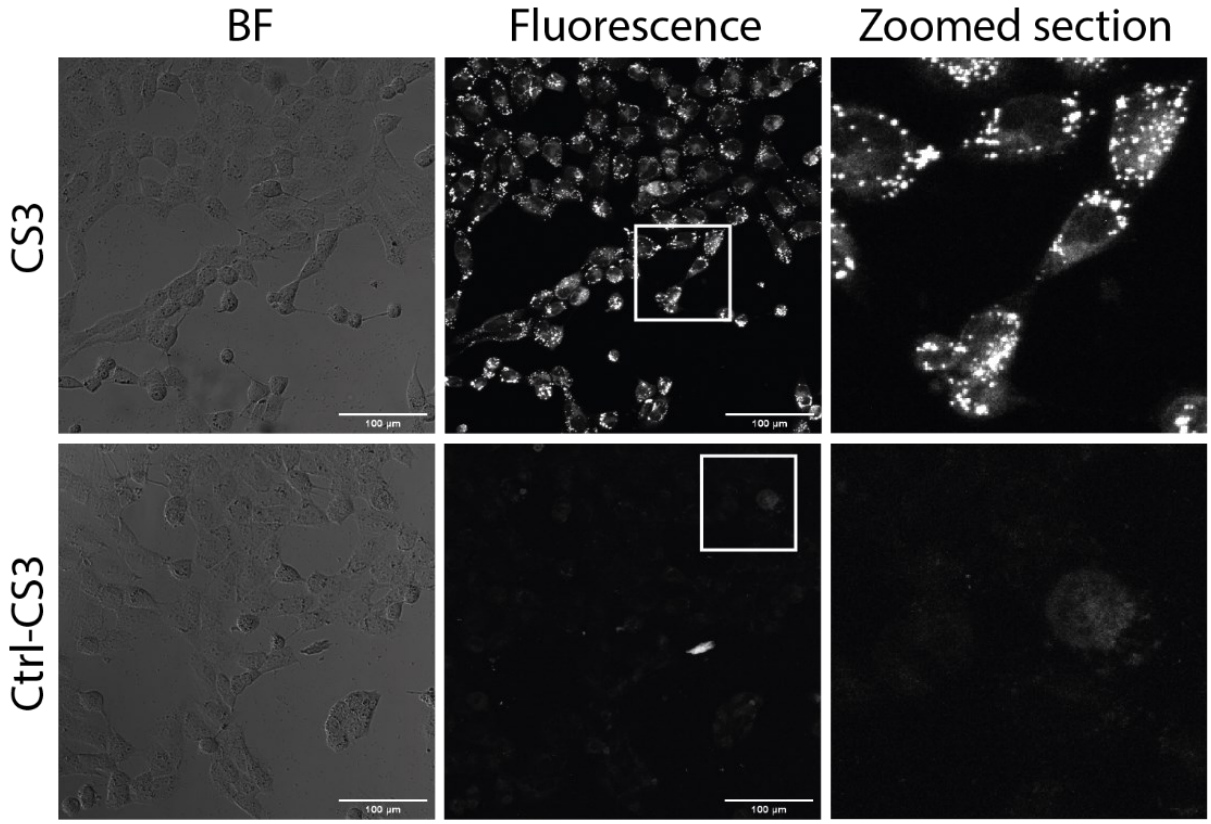

Figure 17: Comparison of **CS3** and **Ctrl-CS3** signals in SH-SY5Y cells. Cells were treated with **CS3** and **Ctrl-CS3** (2 µM) in PBS for 15 min and imaged at 40x magnification (λ_{ex} = 530 nm).

1.3.1.5.2. Colocalization of CS3 with AS and AB

Next, the localization of copper(I) measured with **CS3** was compared with the localization of labelled alpha-synuclein. AS (0.5 µM) which was labelled with the dye Alexa 647 was used to incubate SH-SY5Y cells overnight. Before imaging of the cells, copper(I) was labelled with **CS3** (2 µM) and both dyes were imaged with a confocal microscope. Comparing the fluorescence signal of **CS3** with the signal of labelled AS showed that no colocalization of the copper(I) probe was found with the fluorescently labelled protein (see Figure 18). By closer inspection and comparison of the brightfield channel with the fluorescent puncta from the **CS3** probe, it was found that these fluorescent signals often colocalized with punctate structures in the brightfield channel likely to be lipid droplets (see white arrows in zoomed in sections in Figure 18).

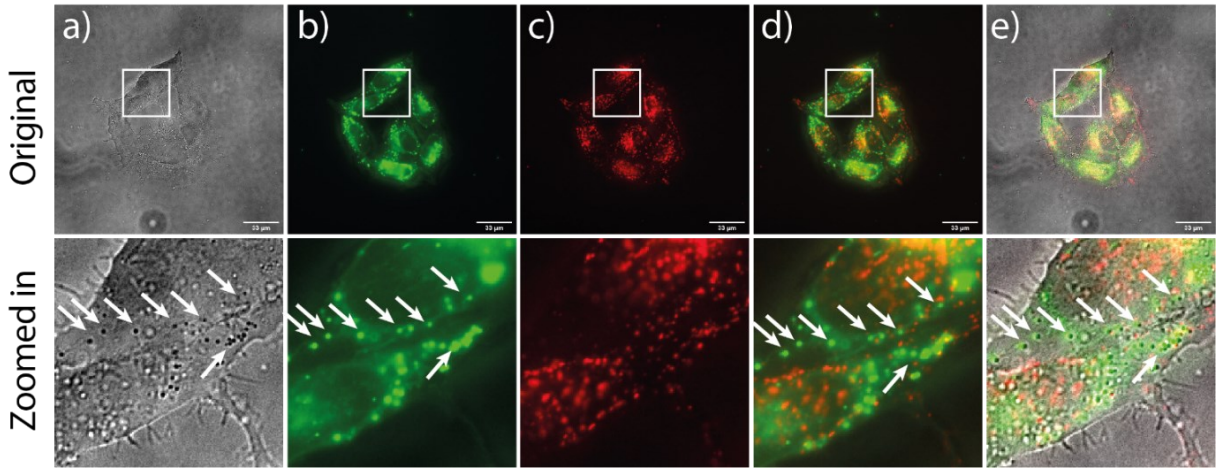

Figure 18: Colocalization of **CS3** and AS. SH-SY5Y cells were stained with **CS3** (2 µM) for 15 min (λ_{ex} = 530 nm) and AS labelled with Alexa 647 (0.5 µM) was incubated overnight (λ_{ex} = 630 nm); zoomed in sections highlight colocalization of **CS3** signals with punctate structures in brightfield image likely to be lipid droplets.

Since AS and **CS3** copper(I) did not show any colocalization the same experiment was performed to compare the localization of Alexa 488 labelled AB and **CS3** in SH-SY5Y cells (see Figure 19). There **CS3** and the labelled AB also did not colocalize in this cell line.

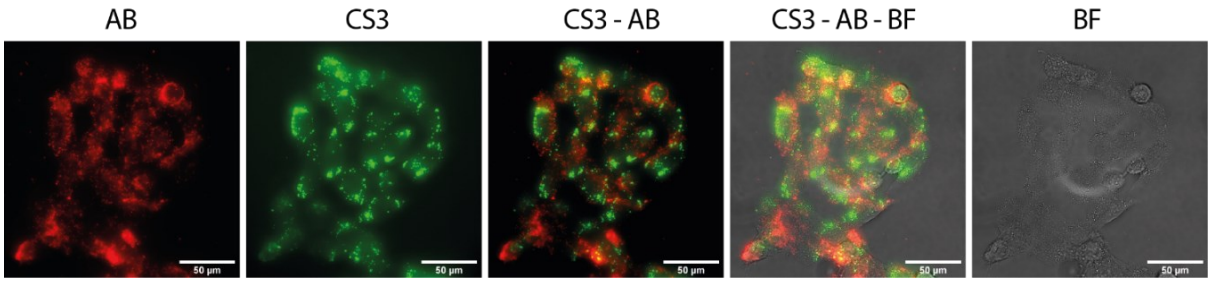

Figure 19: Colocalization of **CS3** and AB. SH-SY5Y cells were stained with **CS3** (2 µM) for 15 min (λ_{ex} = 530 nm) and AB labelled with Alexa 488 (0.5 µM) incubated overnight (λ_{ex} = 450 nm).

Following the suggestions from the literature in Parkinson's and Alzheimer's disease, copper is believed to play a crucial role in the aggregation behaviour of alpha-synuclein and amyloid-beta, respectively.[133] With this experimental setup of investigating copper(I) with the **CS3** probe in combination with fluorescently labelled proteins, an interaction could not be confirmed and no colocalization of those species in cells was measured.

1.3.1.5.3. Colocalization experiments with lipid droplets

To investigate the localization of the **CS3** dye the two human cell lines A2780 and SH-SY5Y were used for this experiment. When these cells were incubated with **CS3** (2 µM) for 10 mins at 37 °C, the dye stained positively for lipid droplets (LDs) (Figure 20a, b). This was further confirmed by counterstaining the cells by BODIPY™, a commonly used marker dye for LD.

Furthermore, LDs were isolated from A2780 cells and incubated with **CS3** dye *in vitro*. The fluorescence of the **CS3** dye increased upon binding to LDs (Figure 20c), this sample when spotted on a coverslip and imaged under confocal microscope also showed **CS3** stained lipid droplets (Figure 20d).

This experiment indicated that **CS3** dye had a polarity affinity that results in a preferable localization of **CS3** in lipid droplets. This must be considered when analysing cellular studies which investigate copper(I) in correlation with other cell organelles or proteins.

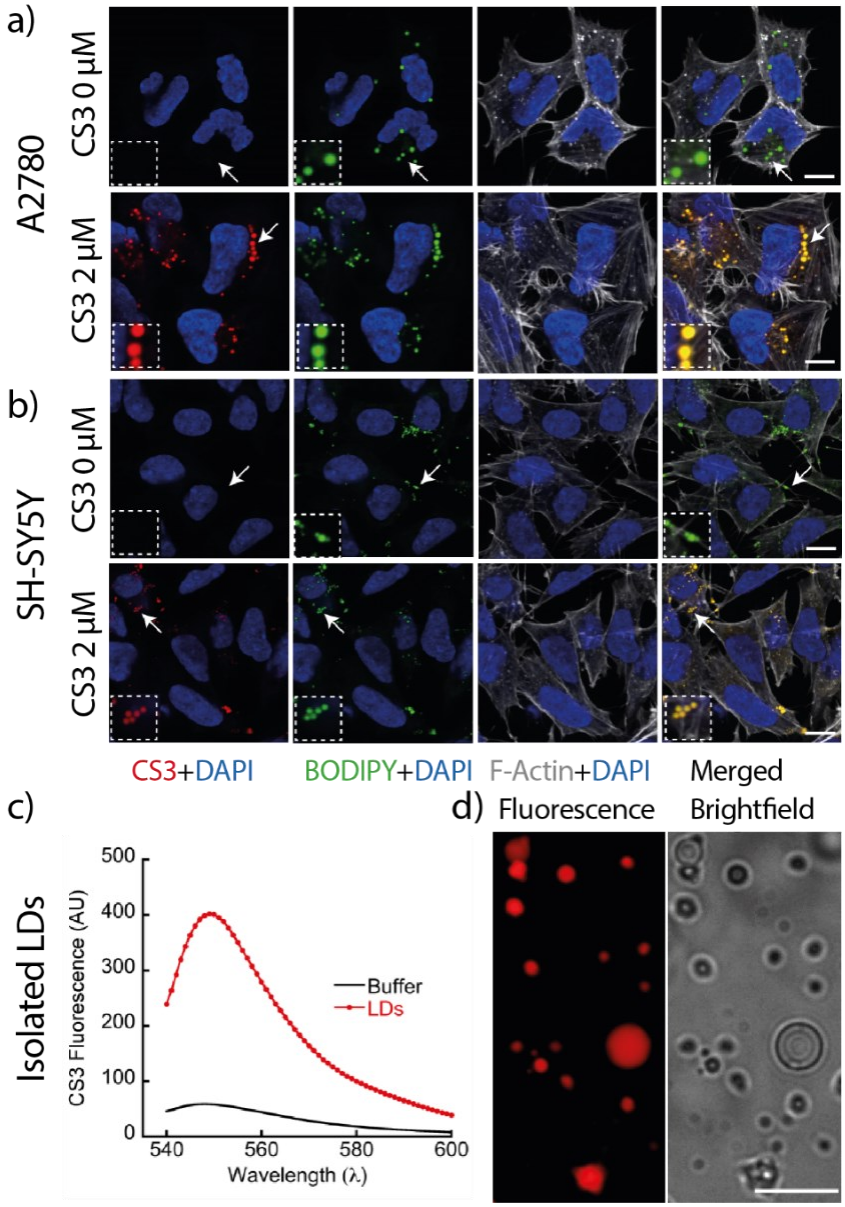

Figure 20: Colocalization study of **CS3** with lipid droplet dye. Colocalization of **CS3** (2 µM) with BODIPY LD dye in a) A2780; b) SH-SY5Y cells with DAPI and F-Actin staining. c) Fluorescence spectrum of extracted LD from A2780 cells, d) image of extracted **CS3** stained LD under fluorescence and brightfield microscope.

1.3.1.5.4. Cell depolarization effects on CS3 signal

To further investigate the behaviour of the copper(I) dye in cellular environment a depolarization experiment was performed with **CS3** in HEK293 cells. This experiment was carried out in the original paper on primary hippocampal neurons showing a shift of fluorescence signal from the soma into the dendrites of the cells.[101] For this experiment the cells were incubated with **CS3** (2 μM) in PBS and then changed back to cell culture media. While recording the cells, 50 mM KCl was added to the well which showed a spike of fluorescence signal (as shown in Figure 21). The selectivity experiment which was carried out in the original paper of this probe has shown that **CS3** is selective for copper(I) and does not show a turn-on response with other metals usually present in the cellular environment.[101] Therefore, these results indicate that the depolarization of the cell changes the concentration of copper(I) in the compartments where **CS3** is located.

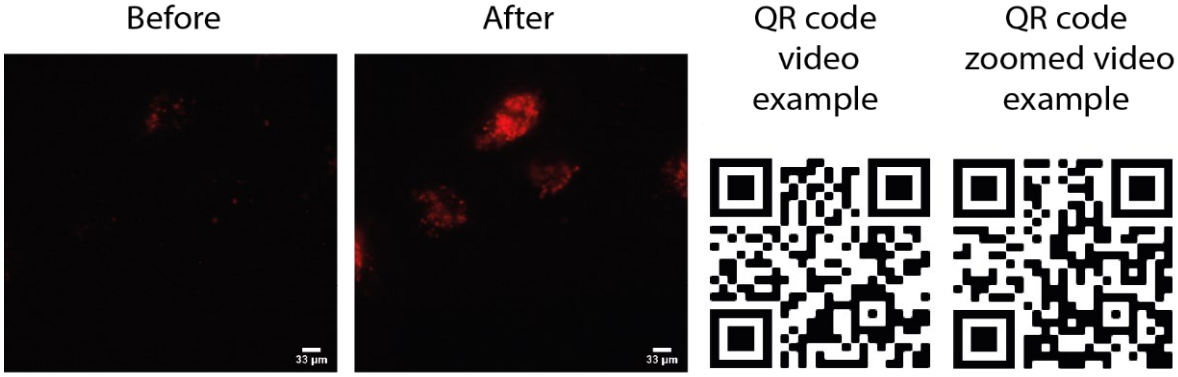

Figure 21: Signal increase of HEK293 cells stained with **CS3** (2 μM) in PBS for 15 min during KCl (50 mM) addition.

However, then performing the same experiment on rat primary hippocampal neurons as it was carried out in the original paper no differences of the copper distribution between the before and after treatment was observed (see Figure 22). In that experiment the neurons were also incubated with AS (0.5 μM) for 24 h with the aim to see, if the AS location would also change after depolarization. Surprisingly, both of the signals, before and after the treatment with KCl did not show any changes except the natural photo bleaching of the fluorescent dyes. Furthermore, there was no colocalization of **CS3** and AS found in primary hippocampal neurons.

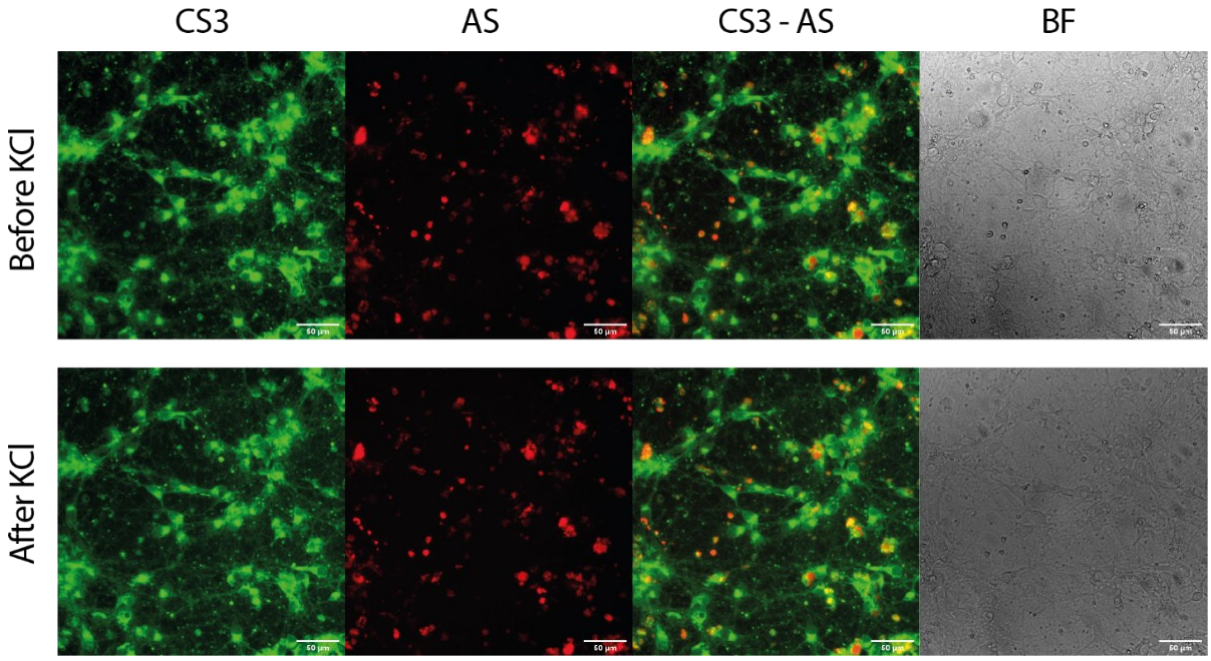

Figure 22: Colocalization study and effect of depolarization of primary hippocampal neurons stained with **CS3** (2 µM) in PBS for 15 min and AS (0.5 µM) incubated overnight before and after treatment of KCl (50 mM).

1.3.1.5.5. Photo bleaching of CS3

Since the previous experiment did not show any indications of fluorescence increase after KCl treatment of the cells but a significant decrease of fluorescence signal most likely caused by photobleaching, an experiment was carried out to investigate this further. Neuroblastoma SH-SY5Y cells were incubated with the **CS3** dye (2 µM) for 15 min and the cells were washed with PBS and changed back to media before imaging. The fluorescence microscope was set to a 5 % laser power (λ_{ex} = 530 nm) and the cells were measured over time. As can be seen in Figure 23, the signal started to decrease significantly straight after the beginning of the imaging process. The intensity drop shows an exponential decay and the intensity of the bright puncta dropped below 50% after 17 recorded images and approached almost 0% after around 60 recorded images.

These results suggest that **CS3** could face difficulties in the application for fluorescence lifetime imaging microscopy (FLIM) because compared to normal fluorescence microscopy where the recording of one image takes usually less than a second, in FLIM the collection process of the photons necessary to reconstruct the decay curve can take several seconds and up to minutes depending on the brightness of the dye. Therefore, a dye with better photostability and stronger fluorescence would be desirable for this specific use case.

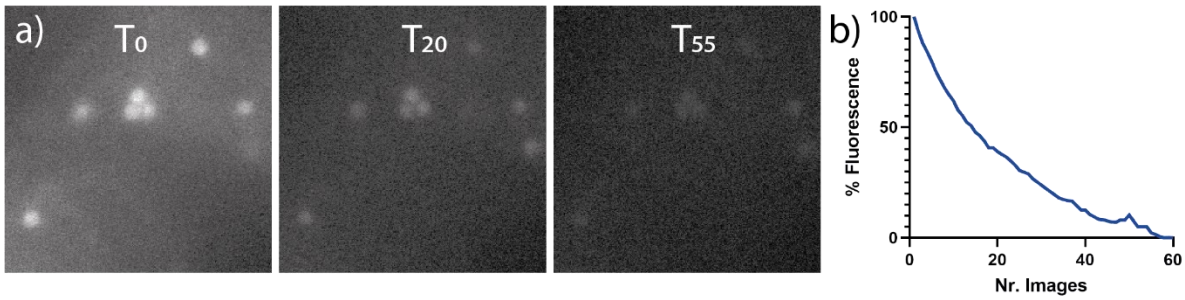

Figure 23: Photobleaching experiment of SH-SY5Y cells stained with **CS3** (2 µM) in PBS measured with fluorescence microscopy (λ_{ex} = 530 nm) with a 5% laser power; a) shows example images at the different recording times and b) shows the signal drop measured on the intensity of the bright puncta inside the cells.

1.3.1.5.6. PFA fixation effect on CS3 staining

Before continuing the investigation of copper(I) measured by **CS3** with internally produced AS, the behaviour of the **CS3** dye with different fixation techniques was investigated. This was necessary to establish a protocol for performing antibody staining of overexpressed AS in SH-SY5Y cells. The two different fixation techniques used for this experiment were the use of 4% PFA in PBS and cooled down MeOH at -18 °C. First SH-SY5Y cells were incubated with **CS3** (2 µM) for 10 min and imaged before fixing the cells. For PFA the cells were incubated with the dissolved PFA in PBS solution for 20 min before measuring the same cells again (see Figure 24a). There, the form of the cell as well as the fluorescence signal of the punctate structures remained the same as measured before fixation. The fixation with cold MeOH however, showed a complete vanishing of the signal after the fixation process (see Figure 24b). Therefore, the fixation protocol with PFA was used for the next experiment to investigate the colocalization of AS with **CS3** measured copper(I) in overexpressed AS in SH-SY5Y cells.

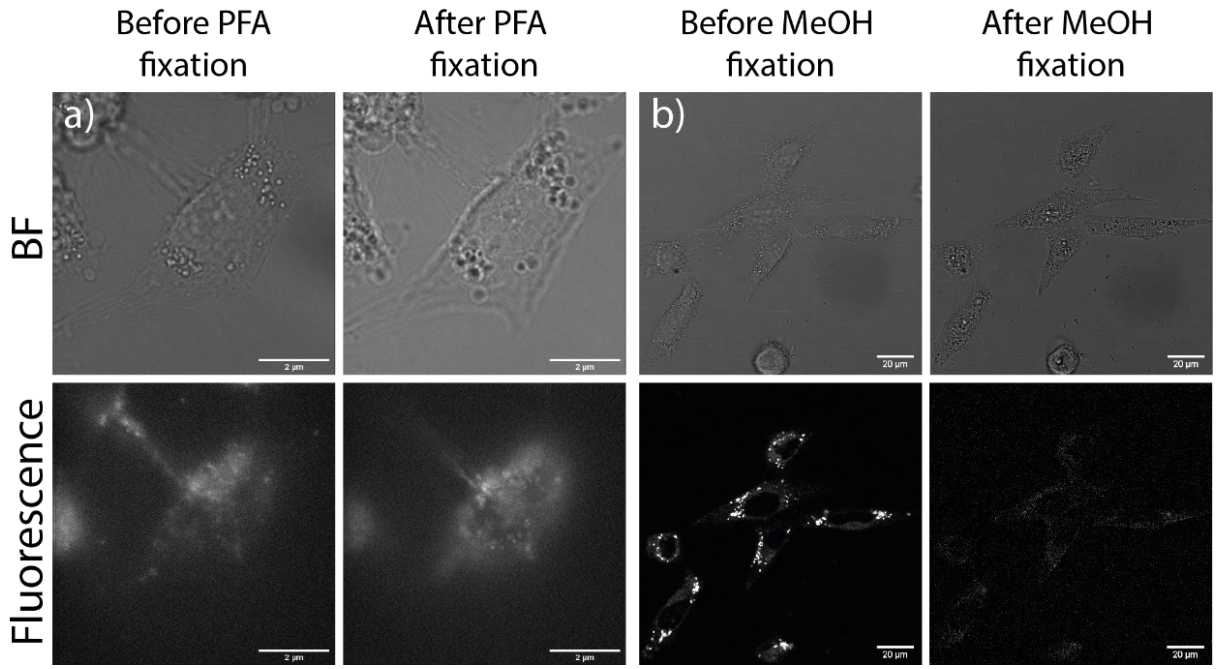

Figure 24: Fluorescence signal comparison of **CS3** on SH-SY5Y cells with PFA fixation (4% in PBS) and MeOH (-18 °C).

1.3.1.5.7. Colocalization of CS3 with overexpressed AS

With the established fixation protocol with 4% PFA in PBS the location of overexpressed AS in SH-SY5Y cells was investigated. The cells were transfected with a plasmid using a Turbofect transfection reagent which caused an overproduction of this protein in the cells. After 24 h the cells were first stained with **CS3** (2 µM) for 10 min, then fixed with 4% PFA in PBS solution for 20 min, followed by blocking with 0.2% Triton X and 1% BSA in PBS. After blocking, the cells were incubated with a primary antibody and then labelled with the AS secondary antibody with an Alexa 647 dye. Furthermore, the nucleus stain DAPI was used after this staining procedure. In the fluorescence images, it could be seen that the overexpressed AS signal was uniformly distributed throughout the cell with an increased signal in the nucleus. The **CS3** copper(I) staining showed the expected punctate structure in the cytosol similar to the previous observations in life cells with little or no overlap in the nucleus (see Figure 25)

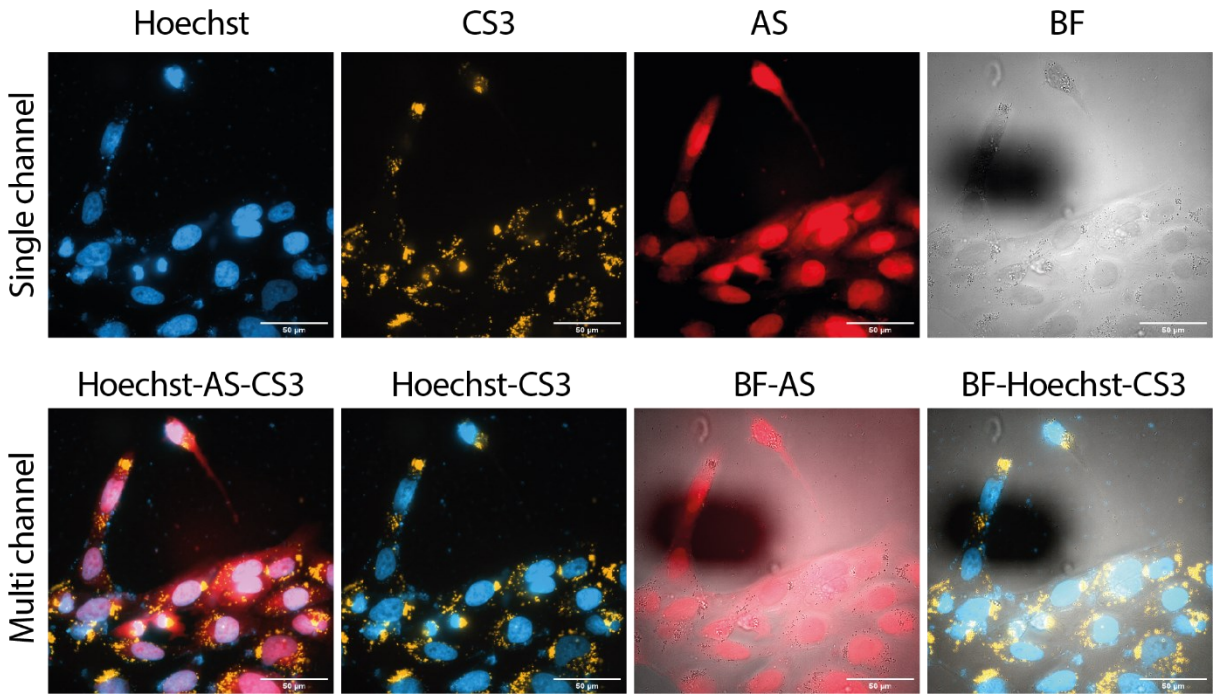

Figure 25: Co-staining experiment of **CS3** with AS and Hoechst 33342 nucleus staining with overlays including brightfield of SH-SY5Y cells.

1.3.1.5.8. CS3 staining of mouse brain slices

Before re-evaluating the capabilities of the synthesized probe **CS3** from the literature and to draw conclusions for the next iteration for developing an improved version of a copper(I) probe the use of **CS3** on mouse brain slices was investigated. Here, fixed mouse brain slices were used and treated with 0.25% Triton X before staining the sample with **CS3** (4 µM) for 10 min. The results show a shaded fluorescence signal without the typical punctate structures that were observed in the *in vivo* cell experiments. However, the staining seemed to uniformly stain the brain tissue and even penetrated the tissue for several micrometres (see Figure 26).

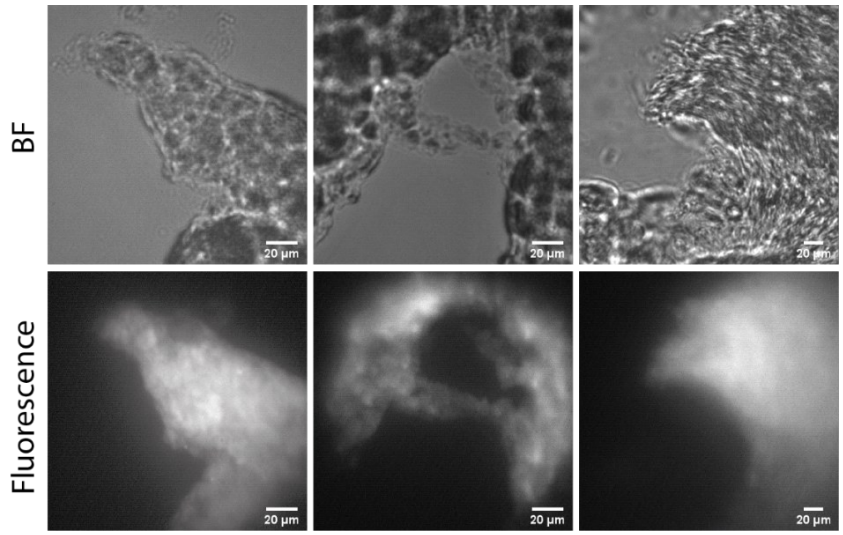

Figure 26: Brightfield and fluorescence signal of **CS3** on fixed mouse brain slices.

1.3.1.5.9. Conclusion of copper(I) probe CS3

CS3 was successfully synthesized, and its characterization was in accordance with the results of the published literature.[101] It was a copper(I) selective turn-on probe showing a 10-fold increase of fluorescence intensity signal when bound to the target metal. Its maximum quantum yield after copper(I) binding was around 0.4 in comparison to Rh 6G in EtOH which droped to 0.1 in aqueous solution. The fluorescence response to copper(I) was strongly dependent on the environment of the probe resulting in a naturally turned-on state in polar aprotic solvents like DCM or EA and turned-off in solvents like acetone and ACN. However, the probe was stable in the acidic pH region and showed a slow decline of signal over time in a basic pH environment. The concerns from the literature that **CS3** formed aggregates in aqueous solution was confirmed with DLS but could not be tested in MeOH where the probe also showed strong fluorescence turn-on response after copper(I) binding. **CS3** changed the average intensity weighted fluorescence lifetime after copper(I) binding by shifting the amplitude contributions of the lifetime component of the unbound form towards the lifetime component of the copper(I) bound species. Therefore, BODIPY based dyes with a NS_4 copper(I) binding moiety showed good potential for sensing copper(I) with fluorescence lifetime. **CS3** was also successfully used in cellular studies showing to be non-toxic and cell permeable as previously reported.[101] In cell experiments **CS3** displayed punctate patterns which were identified to colocalize with lipid droplets. The control ligand **Ctrl-CS3** did not show any signal in cells and colocalization experiments with labelled internalized alpha-synuclein and amyloid-beta did not confirm a colocalization with the two different proteins. Depolarization with KCl of **CS3** in HEK293 cells displayed a fluorescence signal spike which could not be confirmed in primary hippocampal neurons. Also, the previously reported changes of copper(I) location in primary hippocampal neurons could not be confirmed in this research. The **CS3** probe was shown not to be very photostable, limiting the recording of copper(I) over longer time periods in confocal microscope settings. Finally, **CS3** was successfully used to stain fixed brain slices.

The main identified limitation of **CS3** for fluorescence lifetime imaging microscopy was its poor photostability. Furthermore, the aggregation behaviour in aqueous environments and its colocalization in lipid droplets in SH-SY5Y cells was something that needed to be considered when answering biological questions in the context of cellular copper(I).

Based on the gained knowledge from the **CS3** copper(I) probe a new improved fluorescent copper(I) sensor should be designed which should overcome some of the limitations of **CS3**.

1.3.2. Design criteria of FLCS1

In the next phase of the project, a new and improved copper(I) probe was designed, synthesized, and characterized and the photophysical properties of the new probe were compared with **CS3**.

Based on the knowledge gained from the first synthesized selective copper(I) probe **CS3**, some key properties were identified and were considered in the design process of the new probe:

- The probe needs to be selective for copper(I) over other biologically relevant metal ions.
- It needs to show a significant turn-on response upon binding of copper(I).
- It should be possible to use the probe in cell experiments which demands the compound to be non-toxic.
- The molecular design of the new probe should display a high photostability.
- The probe should show changes in fluorescence lifetime when binding to copper(I) ions to target a potential use for measuring changes of copper(I) levels using fluorescence lifetime imaging microscopy (FLIM).

The basic idea for the design of the new fluorescent copper(I) probe which from now on will be named as Fluorescence Lifetime Copper Sensor 1 (**FLCS1**) was the combination of two concepts. The copper-sensing part of the molecule was selected to be the same thioether-rich NS_4 receptor that was already successfully used in many other copper(I) ligands[96,102,104,114,115] and provides a selective and stable binding of soft copper(I) ions. This binding site should be combined with the very good photophysical properties such as good photostability and brightness of BODIPY-based KFL-fluorophore previously successfully developed for calcium(II) sensing by Suzuki *et al.*[76]

Combining a thioether-rich copper(I) binding side on the BODIPY-based fluorophore is expected to invoke a photoinduced electron transfer (PET) from the electron-rich ion chelating moiety to the fluorescent dye moiety.[134] In the absence of copper(I), the fluorescence of the dye is expected to remain quenched due to this PET process, and emission should recover upon binding to copper(I) because of the weakening of the electron-donating ability of the tetrathiaza moiety. The very good photophysical properties of the extended conjugated system of the BODIPY dye molecule was expected to display fluorescence in the red region of the spectrum allowing for good penetration of signal in tissue and its high photostability should allow for the use of this probe for fluorescence lifetime imaging

microscopy. As a control a second version of the ligand without the thioether bridges in the copper(I) binding site should be synthesized. The structure of the designed target molecules **FLCS1** and **Ctrl-FLCS1** are shown in Figure 27.

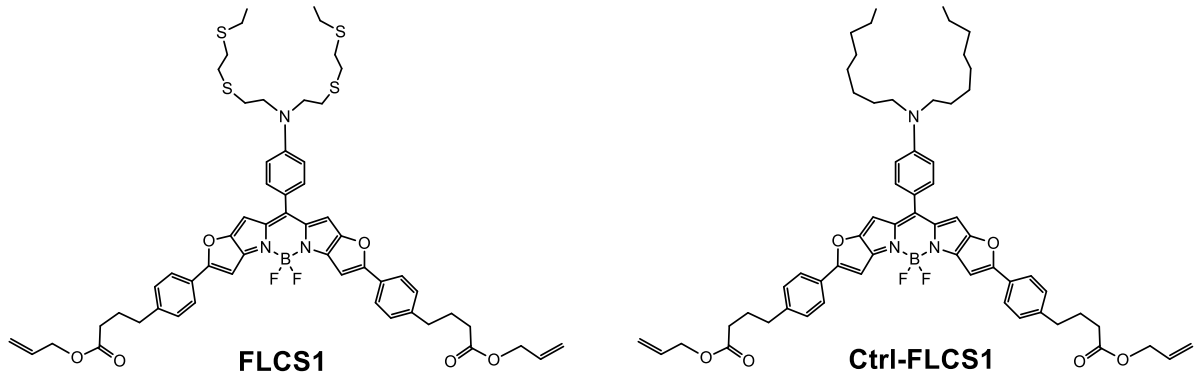

Figure 27: Target molecules: copper(I) ligand **FLCS1** and control ligand **Ctrl-FLCS1**

1.3.2.1. Synthesis of FLCS1

The synthesis of the **FLCS1** probe was carried out following previously reported procedures for the synthesis of the BODIPY dye core and the copper(I) binding moity.[135–137]

FLCS1 was obtained in an 11 step synthesis shown in Scheme 6 and can be broken down into three synthetic parts. Generally, the synthetic route from compound **5** to **7** and **12** to **16** was following previously published literature from a similar BODIPY-based compound[112,137] and the synthesis of compounds **17** to **27** was inspired by the synthetic procedure of a previously published Ca^{2+} probe.[136]

In the first part of the synthesis of **FLCS1** (see Scheme 6a) the tetrathia receptor **15a** was delivered in three steps. Ethyl 2-hydroxyethyl sulfide **5** with thiourea **6** and HBr as solvent generated thiol **7** in 72% yield. This slightly yellow transparent oil was characterised by ^{1}H NMR spectroscopy and used crude for the next reaction step. In parallel *n*-phenyldiethanolamine **12** dissolved in pyridine with toluenesulfonyl chloride **13** reacted to **14**. The product was characterizable by ^{1}H NMR spectroscopy, displaying characteristic peaks for the three aromatic rings and two triplets in the aliphatic region corresponding to the ethyl groups on the amine. In the next reaction step of **14** with **7** and *in situ* generated sodium ethanolate produced 6-phenyl-3,9-dithia-6-azaundecane **15a**. On the aniline derivative **15a** a formylation reaction with phosphorus oxychloride in DMF at low temperatures produced the intermediate product **16a** with a 35% yield after workup and purification. This product displayed the typical aldehyde peak in the ^{1}H NMR spectrum and showed an additional carbon in the ^{13}C NMR spectrum which supported the formation of the product. The same

reaction was carried out with the sulphur free compound **15b** which was commercially purchased. These compounds served later as the connection element of the two arms in the *meso* position of the BODIPY fluorophore.

In the second part of the synthesis (see Scheme 6b) the side arms of the BODIPY platform were synthesized. This started with a Suzuki coupling using 5-formyl-2-furanboronic acid **17** with 4-(4-bromo-phenyl)-butyric acid **18**, with the palladium catalyst **19** and potassium carbonate as a weak base and dimethoxyethane as a solvent.

Next, an esterification step of the crude product was carried out with EDC to activate the carboxy group and DMAP as a catalyst together with allyl alcohol **20** to form the ester bond with the alcohol. This reaction yielded compound **21** with an overall yield of 5% to 12% after workup and purification.

This sequence of reactions was seen as a big limitation due to its very low yields and was therefore attempted to optimize by varying the amounts of catalyst, temperature of the reaction and speed of the acidification step. This led to limited successes and only a minor increase of the reaction yield. Three variables that were identified to increase the yield were the use of degassed solvent in the first part of the reaction while working under strict N_2 atmosphere. Furthermore, the quality of the Pd catalyst was identified as one cause for decreased yields and a slow acidification step was identified as being beneficial to produce a purer product. The ^{1}H NMR spectrum of this product showed sharp aromatic peaks of the benzol and the furan moiety as well as a multiplet around 6 ppm from the allyl-ester attached to the butyl-acid. *tert*-Butyl 2-azidoacetate **23** was synthesised by reacting bromoacetate **22** with sodium azide. The reaction yielded 95% of compound **23** which was used for the fused pyrrole ring formation with **21**. From this reaction step onwards, all reactions were strictly carried out under a N_2 atmosphere. The ring formation was performed in a 2-step reaction. First the azido ester was mixed in THF and compound **21** and potassium *tert*-butoxide dissolved in *t*-butanol were slowly added at low temperatures (-15 °C to -20 °C). After a partial purification by column chromatography on silica gel the product mixture was dissolved in toluene and heated up to 120 °C for 1 h resulting in the ring closure. The product was again purified by column chromatography yielding 38% of product **25**. Then **25** was decarboxylated using TFA and immediately after 0.5 equivalents of the linking compound **16a** was added to the reaction. Thereafter, the reaction completion was monitored by TLC, the solvent was exchanged to THF, the DDQ was added to oxidize the bridging carbon between the two BODIPY arms to generate a fully conjugated system. An aluminium oxide

column removed some of the impurities including the excess DDQ. The product mixture of **27a** was dissolved in 1-2-dichloroethane and reacted with DIEA and $BF_3 \cdot Et_2O$ complex. **FLCS1** was obtained after column chromatography and preparative TLC separation in very low 2-3 % yield and was characterized by ^{1}H and ^{13}C NMR spectroscopy as well as MALDI-TOF MS. All other isolated reaction product steps were characterized by ^{1}H and ^{13}C NMR spectroscopy and were confirmed by comparing them with the literature reported values.

The control ligand **Ctrl-FLCS1** was synthesized following the same procedure but exchanging **15a** for **15b** which was commercially available, and compound **16a** with compound **16b**.

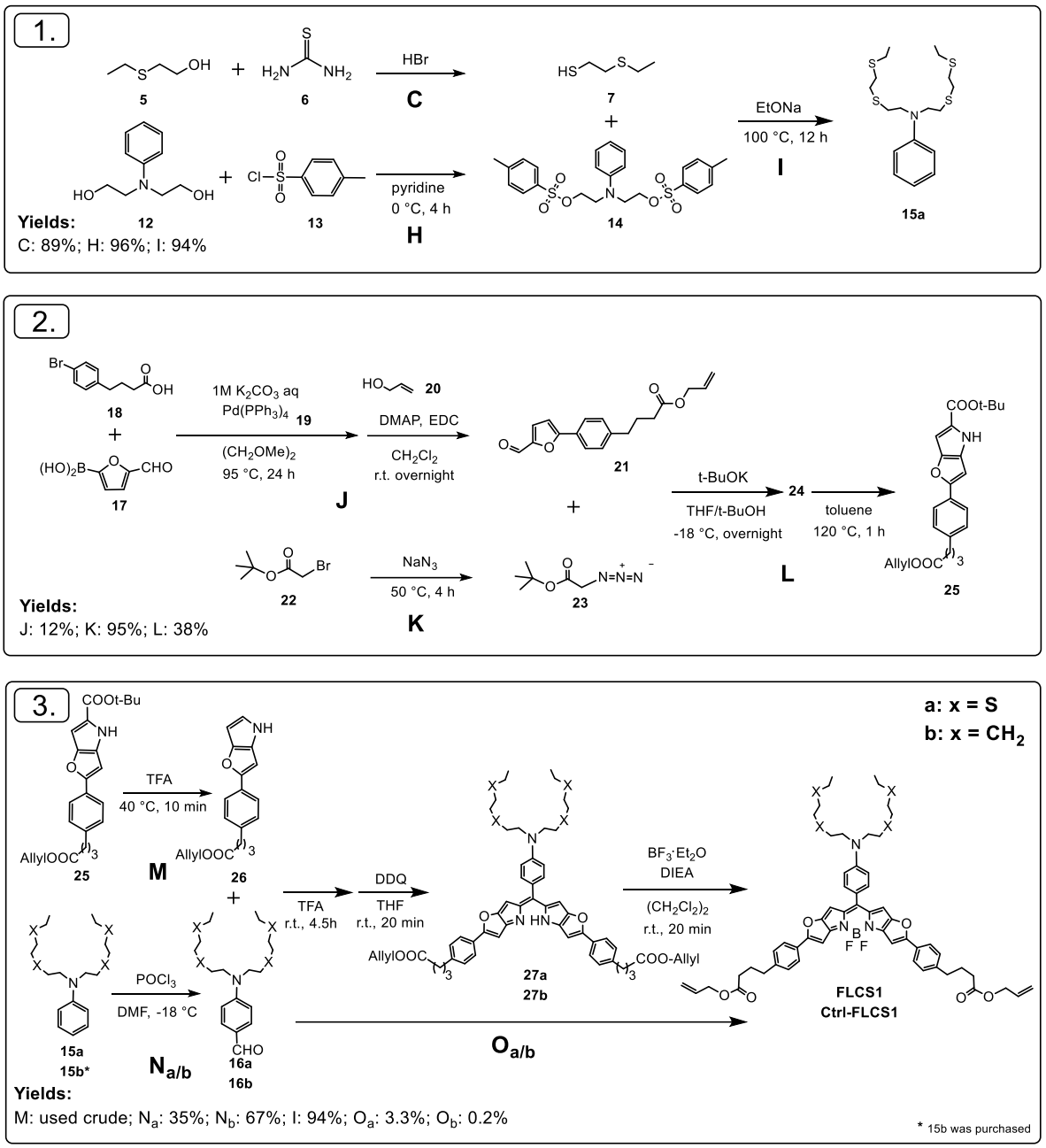

Scheme 6: Synthetic scheme for the preparation of the new BODIPY-based optical copper(I) probe **FLCS1** and control ligand **Ctrl-FLCS1**.

1.3.2.2. Spectroscopic characterization of FLCS1 in MeOH

With this new probe at hand, the photophysical properties were first investigated in MeOH as solvent. The probe displayed characteristic optical features of a BODIPY chromophore. The extended conjugated system of the apo probe exhibits two red-shifted absorption bands with a main peak at 646 nm ($\varepsilon = 2.48 \times 10^5$ M^{-1} cm^{-1}) and a broad shoulder at 594 nm ($\varepsilon = 8.07 \times 10^4$ M^{-1} cm^{-1}) with a slight redshift of 4 nm upon copper(I) addition (Figure 28b, 29b). An effective photoinduced electron transfer quenching (PET) by the azatetrathia receptor, resulted in weak fluorescence in its apo form of **FLCS1** ($\Phi = 0.032$) and after addition of copper(I), the fluorescence intensity increased by ca. 20-fold ($\Phi = 0.66$) with a 1:1 ratio of dye to copper(I) binding and a Stokes shift of 10 nm resulting in an emission peak at 660 nm (see Figure 28a). The corresponding emission maximum of this compound also shifted slightly from 657 nm to 660 nm at an equimolar concentration of copper(I) to dye. Interestingly, after reaching the titration maximum, when adding a big excess (100 eq.) of copper(I) to the already saturated solution another signal increase was observed. This could be due to another probe equilibrium such as dissolving of small aggregates at higher ion concentrations. Even though a 1:1 binding ratio of copper(I) and dye was confirmed by a Job's plot (Figure 28f), the emission intensity kept increasing over time upon addition of excess copper(I) amounts, and an equilibrium was reached after 4 h (see inset Figure 28e). After the equilibrium was reached, further addition of excess copper led to another rapid step increase of the fluorescent signal (inset, Figure 28c).

The K_d of **FLCS1** and copper(I) was determined in a buffered thiourea solution (in methanol) as previously reported (see Figure 28g, h),[101,138] giving a value of 2.6×10^{-9} M. This value however cannot be directly compared to the K_d values previously reported for similar copper(I) probes since different solvents were used. The emission of **FLCS1** was not activated in the presence of 2 mM calcium(II), sodium(I), magnesium(II) and zinc(II), nor did the other biologically abundant transition metal ions 20 µM potassium(I), cobalt(I), iron(II), manganese(II) or nickel(II) showed a turn-on effect with the probe. However, in accordance with previously published literature on probes with the same thioether rich binding side,[101,104] a large excess of copper(II) (20 µM) also showed a minor increase of emission signal (see Figure 28d).

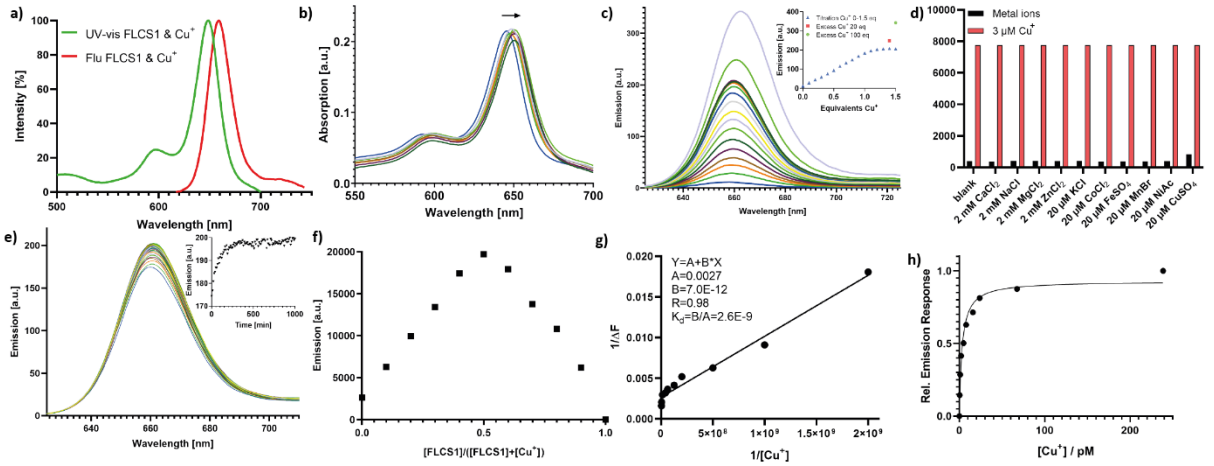

Figure 28: Spectroscopic studies of the interaction of copper(I) with **FLCS1**. a) Normalized absorption and emission spectrum of **FLCS1** (1 µM) with excess copper(I) showing a Stokes shift of 10 nm. b) Absorption spectra for **FLCS1** copper(I) titration with 4 nm redshift of main peak. c) Fluorescence spectra (λ_{ex} = 610 nm); inset shows the binding plot recorded at the fluorescence peak maximum, λ_{em} = 660 nm with two extra titration points for big excess of copper(I) (20 and 100 eq.). d) Response of **FLCS1** (1 µM in MeOH) to the addition of different metal ions with bars representing the integrated fluorescence response of the probe. Black bars represent the response of the addition of excess metal ions (2 mM calcium(II), magnesium(II), zinc(II) and sodium(I); 20 µM cobalt(II), iron(II), manganese(II), nickel(II), potassium(I) and copper(II)); red bars represent the response of the subsequent addition of copper(I) (3 µM) to the corresponding metal ion solutions. e) Fluorescence emission over time is increasing for 4 h before reaching equilibrium. f) Job's plot of **FLCS1** with copper(I) at concentrations of 2.5-0 µM for **FLCS1** and 0-2.5 µM for copper(I). The total combined concentration of **FLCS1** and copper(I) was kept constant at 2.5 µM. The spectra were acquired in MeOH. The maximum fluorescence response at 1.25 µM fraction of **FLCS1** indicates the formation of a 1:1 copper(I):**FLCS1** complex. g) Normalized binding affinity titration for K_d determination. Response of **FLCS1** (1 µM) in MeOH containing thiourea (400 µM) to free copper(I) ions (0, 0.49, 0.99, 1.98, 4.97, 7.95, 15.91, 23.86, 67.61, 238.63 pM). h) Benesi–Hildebrand plot of competition titration (from g)) resulting in a calculated K_d value of 2.6×10^{-9} M (not directly comparable to previously reported values due to usage of organic solvent). Excitation wavelength was 610 nm and collection range 615-700 nm.

The quantum yield for **FLCS1** was determined in comparison to Alexa647 (see Figure 29a). The extinction coefficient for copper(I) unbound and bound **FLCS1** was determined to be 243,064 $M^{-1}cm^{-1}$ and 248,271 $M^{-1}cm^{-1}$, respectively (see Figure 29b). To assess the reversibility of the copper(I) binding process, the **FLCS1**:copper(I) complex was treated with 2 equivalents of PSP-2, which is known to have a very strong binding constant to copper(I).[139] This led to a decrease of the fluorescence intensity down to the basal level, observed for the free probe. Addition of excess copper(I) to this solution led to a complete restoration of the fluorescence intensity, initially observed for the **FLCS1**:copper(I) complex (see Figure 29c). Next the control ligand was investigated. As expected, the **Ctrl-FLCS1** ligand did not display

any increase in the emission spectrum after addition of excess copper(I) (see Figure 29d). To get a better understanding of the nature of the fluorescence properties of the probe, a variable temperature experiment was performed. This unveiled that the emission was slightly temperature dependent resulting in an increased signal in the apo and copper(I) bound form of the probe at low temperatures (see Figure 29e). This could be explained due to the nature of the probe which at higher temperatures is more mobile and flexible and can therefore lose energy by rotation of the NS_4 moiety or the whole ligand attached to the *meso* position of the BODIPY core.[140] Next, the probe was tested in aqueous solution containing DMCP lipids which did not display any fluorescence even when adding excess copper(I). However, when MeOH was added to the solution mixture a slight signal increase was observed (see Figure 29f). This indicated that the solubility of the probe might be limited in water. In the next section, experiments were carried out to investigate the behaviour of **FLCS1** in aqueous solutions in more details.

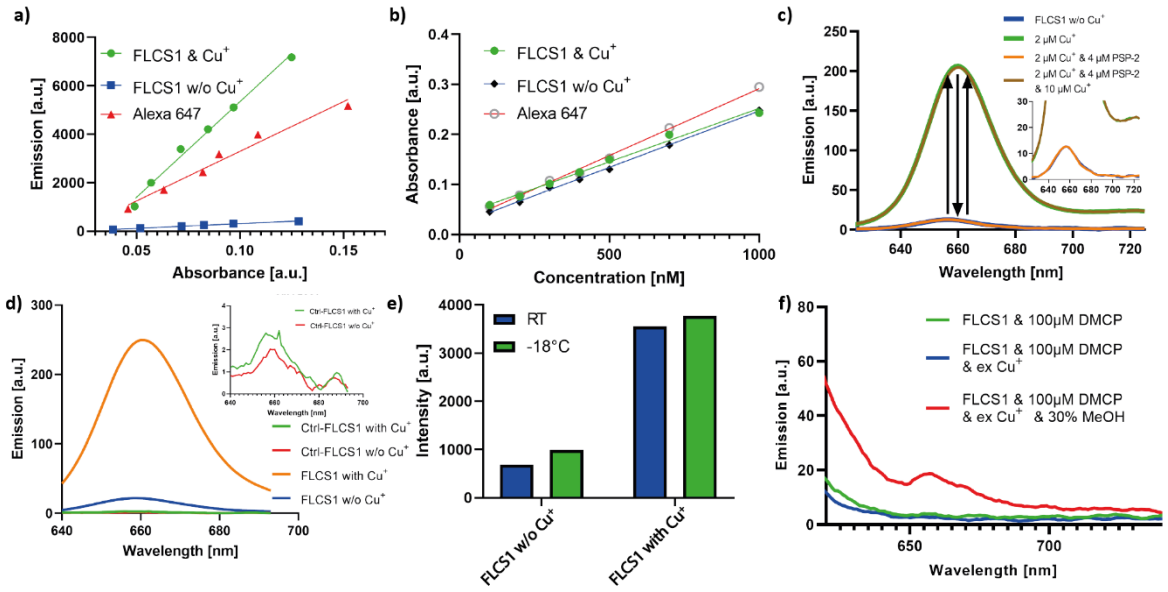

Figure 29: Spectroscopic studies of **FLCS1** and **Ctrl-FLCS1**. a) Quantum yield determination experiment of **FLCS1** with copper(I) in comparison to Alexa 647 (λ_{ex} = 625 nm). b) Absorption comparison of **FLCS1** with and without copper(I) in comparison to Alexa 647 for extinction coefficient determination. c) **FLCS1** (1 µM) in MeOH was repeatedly measured before and after copper(I) (2 µM) addition, followed by addition of PSP-2 (4 µM) and repeated addition of excess copper(I) (10 µM) showing reversibility of the probe's response to copper(I) addition/depletion. d) Fluorescence response comparison of **FLCS1** and **Ctrl-FLCS1** (1 µM) in MeOH to excess copper(I) (λ_{ex} = 625 nm). e) Fluorescence response of **FLCS1** (1 µM) in MeOH at RT and -18 °C. f) Fluorescence spectra of **FLCS1** in PBS with DMCP lipids (100 µM) and addition of MeOH.

1.3.3.1. Spectroscopic characterization of FLCS1 in aqueous solution

As established before in a UV/vis titration with **FLCS1** in MeOH the probe has very good solubility in that solvent. However, increasing concentrations of H_2O led to a steep drop of absorbance (Figure 30a) and already at water concentrations of 14% the absorbance started dropping significantly and the formation of a very broad band in the observed wavelength range indicated nanoparticle formation. This in turn also influenced the emission abilities of the probe reducing the signal at higher concentration of water (Figure 30b). A similar but slightly better solubility trend for the probe was observed in EtOH, showing a decreased fluorescence signal with higher concentrations of H_2O (see Figure 30c**)**. Since it was suspected that this abnormal behaviour might be due to aggregation of the dye in the solvent, as was mentioned to be the case for the **CS1** and **CS3** dye,[105,141] DLS measurements were carried out. The DLS experiment of **FLCS1** in PBS confirmed the formation of small particles with a diameter size of roughly 120 nm which increased in diameter to 150 nm when copper(I) was added (see Figure 30d, e). Similar to **CS3**, the DLS experiments of **FLCS1** in MeOH did not give any meaningful results, potentially due to a high background noise of the measured signal. To evaluate the potential applications of **FLCS1** in different biological environments, the changes in fluorescence intensity under various pH values was evaluated. Based on findings of improved solubility in EtOH a 1:1 ratio (v:v) of EtOH and PBS buffer was used for the pH experiments. The fluorescence signal of **FLCS1** showed consistent fluorescence increase upon copper(I) addition across different acidic to neutral pH values. Interestingly, at pH 8 the signal initially increased when copper(I) was added but displayed a steep decline of the signal over time (see Figure 30f). Since the cellular environment is in the neutral or in the case of lysosomes in the acidic pH range[109] this was not seen as a problem for the use of the probe in cells, however the limited solubility of the probe was seen as a potential challenge for the investigations of cellular copper(I).

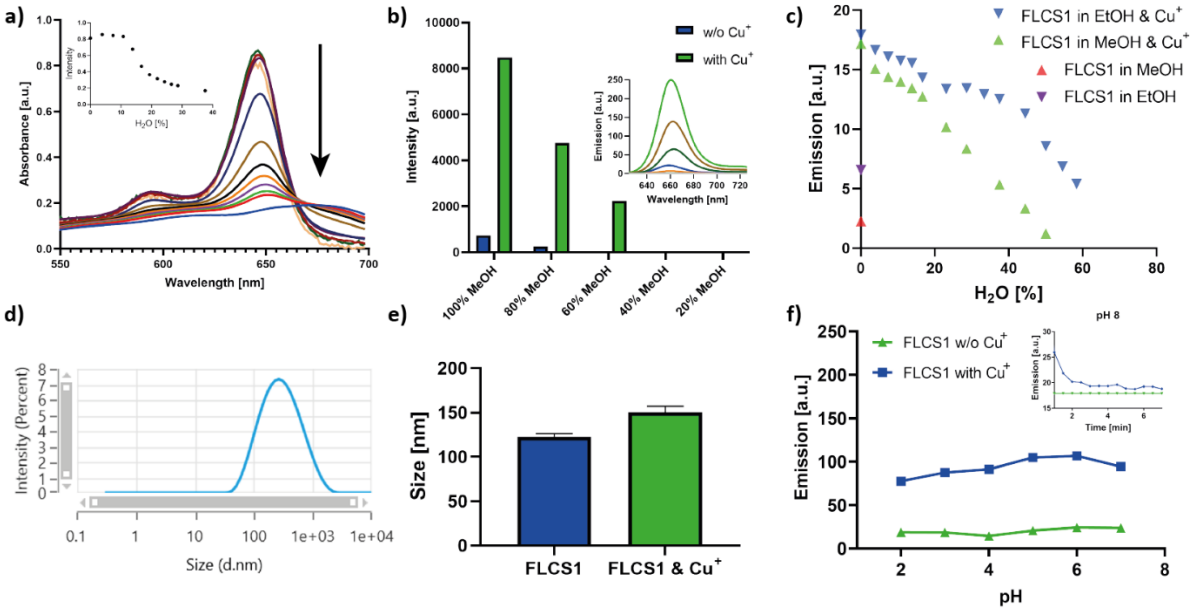

Figure 30: Solubility investigations with **FLCS1**. a) UV/vis spectra from **FLCS1** (1 µM) in MeOH with increasing concentrations of H_2O (0-37%); inset displaying maximum intensity at different H_2O concentrations. b) Integrated fluorescence emission of **FLCS1** (1 µM) with/without excess copper(I) at different H_2O concentrations (MeOH:H_2O; 100:0, 80:20, 60:40, 20:80); inset showing fluorescence spectra. c) Fluorescence turn-on response for **FLCS1** (1 µM) in EtOH and MeOH with increasing concentrations of H_2O. d) DLS results of **FLCS1** (1 µM) in PBS. e) DLS particle size of **FLCS1** (1 µM) in PBS before and after addition of 3 µM copper(I). f) Fluorescence response of **FLCS1** (1 µM) in EtOH:H_2O (1:1) at different pH before and after addition of 3 µM copper(I); inset showing fluorescence signal at pH 8 after addition of 3 µM copper(I) over time.

1.3.2.3. Spectroscopic characterization of FLCS1 in aqueous solution

Next, the fluorescence response of **FLCS1** in different solvents was investigated. There the probe showed the expected fluorescence increase upon copper(I) addition in MeOH (see Figure 31a). In H_2O no fluorescence signal was observed most likely due to aggregation and particle formation of the dye in that solvent (see Figure 31b). Similarly, to **CS3**, also **FLCS1** displayed a strong fluorescence turn-on in DCM as solvent which decreased slightly after copper(I) addition (see Figure 31d). In the solvents acetone, DMSO and ACN just a small signal was observed but no change of fluorescence was measured after copper(I) was added to the solution mixture (see Figure 31d, e, f). These experiments indicated that the dye might be sensitive to the polarity of the environment of the dye. This needed to be considered when drawing conclusions in following cellular experiments.

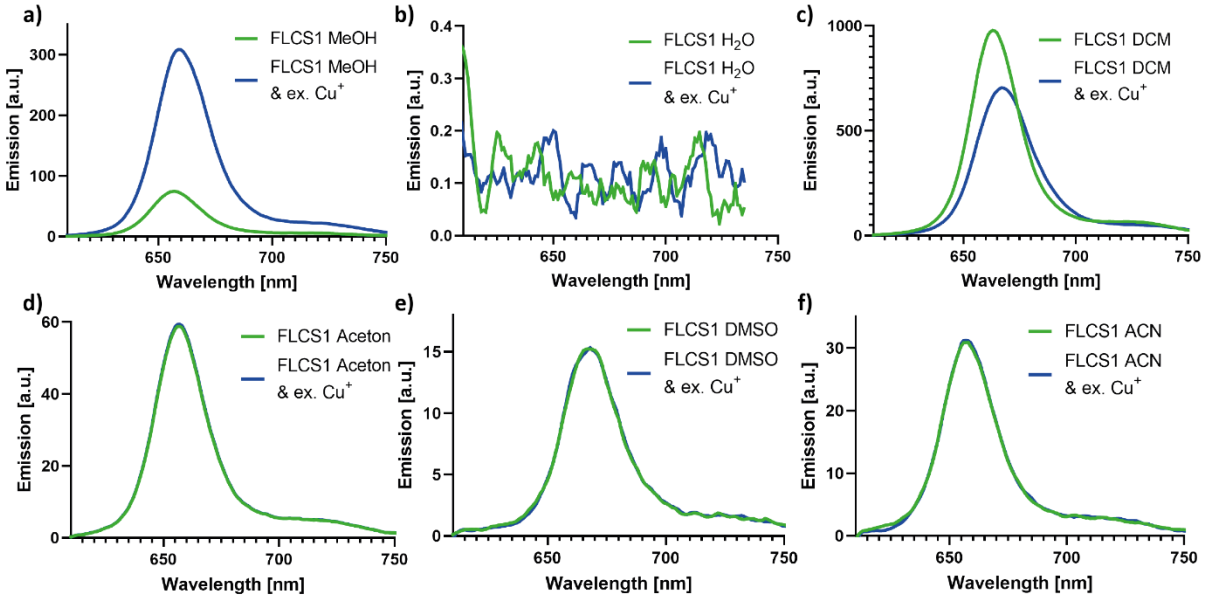

Figure 31: Solvent experiment with **FLCS1** and copper(I). Fluorescence spectrum of **FLCS1** (1 µM) with and without excess copper(I) was tested in a) MeOH; b) H_2O; c) DCM; d) Acetone; e) DMSO; f) ACN solvent.

1.3.2.4. FLCS1 and fluorescence lifetime

After the investigation of the effects of different solvents on the **FLCS1** probe and confirming a higher photostability of **FLCS1** than **CS3** (as it is demonstrated in Section 1.3.2.9.5 in an imaging experiment in Figure 48) the fluorescence lifetime behaviour of the new probe in MeOH was investigated. In a copper(I) titration experiment the time resolved fluorescence traces were best fitted using a biexponential decay function, with the two lifetime components (τ_1 = 0.39±0.00 ns and τ_2 = 3.08±0.01 ns) which were extracted from a global fit of the data. The short lifetime (τ_1 = 0.39 ns) was assigned to the copper-free **FLCS1** and the long lifetime (τ_2 = 3.08 ns) to the copper(I) bound form of **FLCS1**, which was supported by the change in fitted amplitudes of the two components upon copper(I) titration showing an opposing trend during the titration (see Figure 32c). As the copper(I) concentration increased, the lifetime of the probe changed from 0.6 ns (apo probe) to 2.75 ns when more than one equivalent of copper(I) was added – i.e., mostly copper(I) coordinated probe (see inset Figure 32a). When investigating the different τ values at the different concentrations there was a slight systematic change in the τ_2 value, whereas τ_1 was randomly distributed and not changing significantly (see inset Figure 32c, d). Since the changes of the long fluorescence lifetime with increasing copper(I) concentrations were not very big and could not be explained, investigation was continued with the suggested fixed τ values from the global fit.

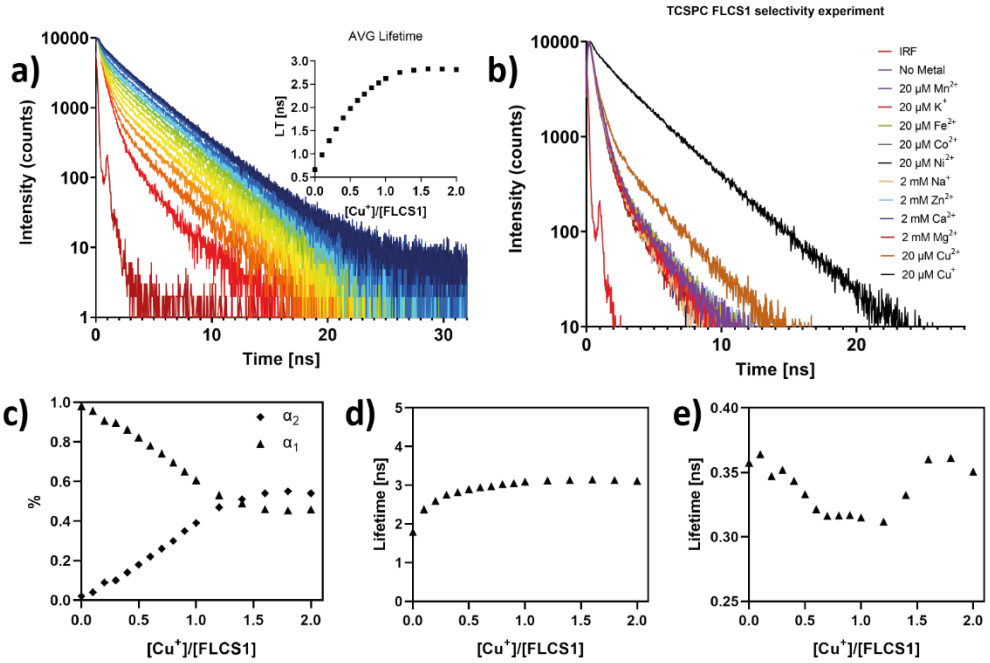

Figure 32: TCSPC copper(I) titration and selectivity of **FLCS1**. a) Time-resolved fluorescence decays of **FLCS1** (λ_{ex} = 630 nm, λ_{em} = 660±10 nm). Instrument response function (IRF) is shown in dark red; inset shows calculated intensity-weighted average lifetime. b) Time-resolved fluorescence decay curves of **FLCS1** with excess of different metal ions (2 mM calcium(II), magnesium(II), zinc(II) and sodium(I); 20 µM cobalt(II), iron(II), manganese(II), nickel(II), and potassium(I)); brown line shows 20 µM copper(II) and black line shows 3 µM copper(I). c) *In vitro* fluorescence lifetime titration results of a methanolic solution of **FLCS1** (1µM) with copper(I) showing amplitude trend at fixed values of τ_1 = 0.39±0.00 ns and τ_2 = 3.08±0.01 ns, obtained from the global fit of the whole dataset. d) τ_2 values and e) τ_1 values for the copper(I) titration at different copper(I):**FLCS1** ratios.

Representative examples of the fits of the traces with variable (a-c) and fixed (d-f) lifetimes are shown in Figure 33. The fits for the decay showed a low χ^2value which indicated a good fit of the biexponential decay curve, however, for the beginning of the decay fitting some systematic deviations from the curve fit could be seen. The full set of parameters of the titration data can be found in the Appendix (Table 6).

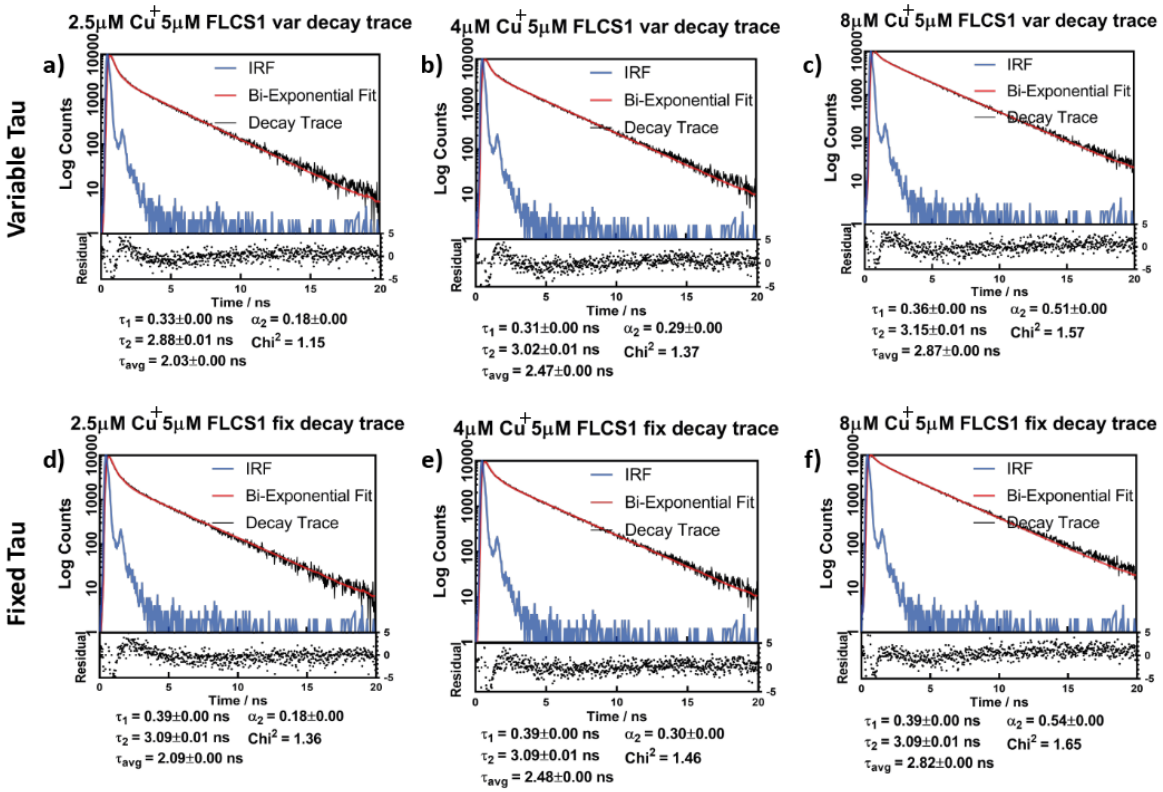

Figure 33: Biexponential lifetime fitting comparison. **FLCS1** (5 µM) in MeOH with copper(I) (2.5, 4, 8 µM) lifetime was measured and traces were fitted with two exponentials with variable τ_1 and τ_2 (top) and fixed at τ_1 = 0.39±0.00 and τ_2 = 3.09±0.01 ns (bottom).

To verify the validity of the biexponential decay fit a triexponential fit was also performed on the data and two representative example fits are shown in Figure 34. Although, the χ^2 value for the triexponential fit improved slightly compared to the biexponential fit, the fitting with the determined fixed lifetime values still displayed the error at the beginning of the trace, which can be seen in the residual plots. Furthermore, the amplitude contributions of the very fast lifetime had the biggest contribution to the overall lifetime which was not physiological explainable. Therefore, the biexponential model was used for evaluating future experiments.

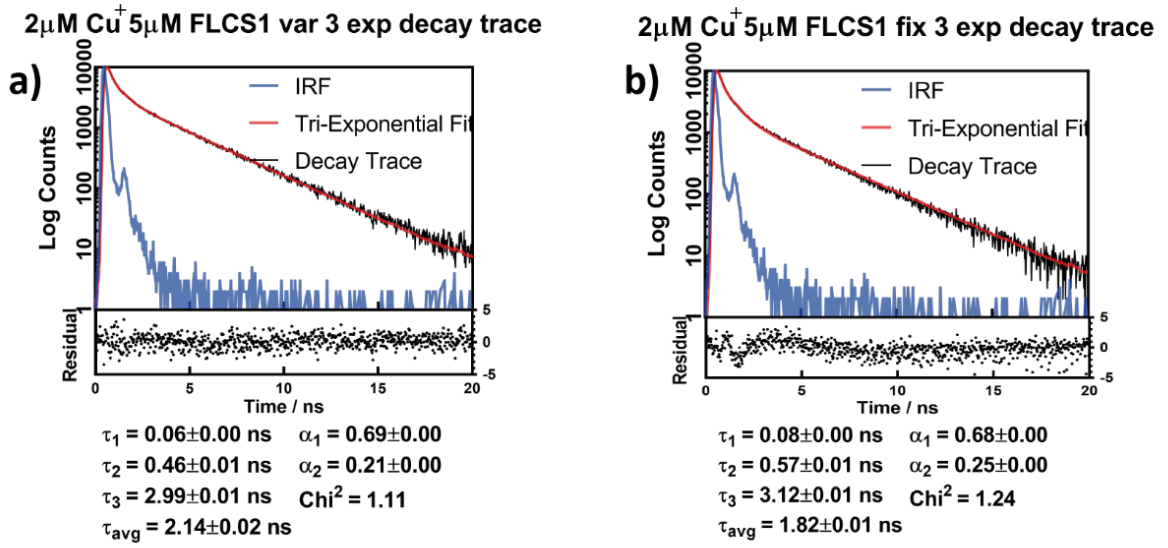

Figure 34: Triexponential lifetime fitting comparison. **FLCS1** (5 µM) in MeOH with copper(I) (2 µM). TCSPC traces were recorded and fitted with three exponentials with variable τ_1, τ_2 and τ_3 (left) and fixed at τ_1 = 0.08±0.00 ns, τ_2 = 0.57±0.01 ns, and τ_3 = 3.12±0.01 ns (right).

Next, the influences of polarity, viscosity and pH on the fluorescence lifetime of **FLCS1** was investigated. To test the effects of polarity on **FLCS1**, increasing amounts of H_2O was used in a methanolic solution of **FLCS1** with an excess of copper(I). A systematic shift towards higher contributions of the shorter lifetimes were observed. The same trend was also seen for increasing viscosity by increasing the amount of glycol in the solution and finally the pH also had a slight effect on the fluorescence lifetime shifting the decay trace towards lower lifetimes. Those effects were important control experiments whose effects would need to be considered when analysing FLIM images. Example traces of each category are shown in Figure 35.

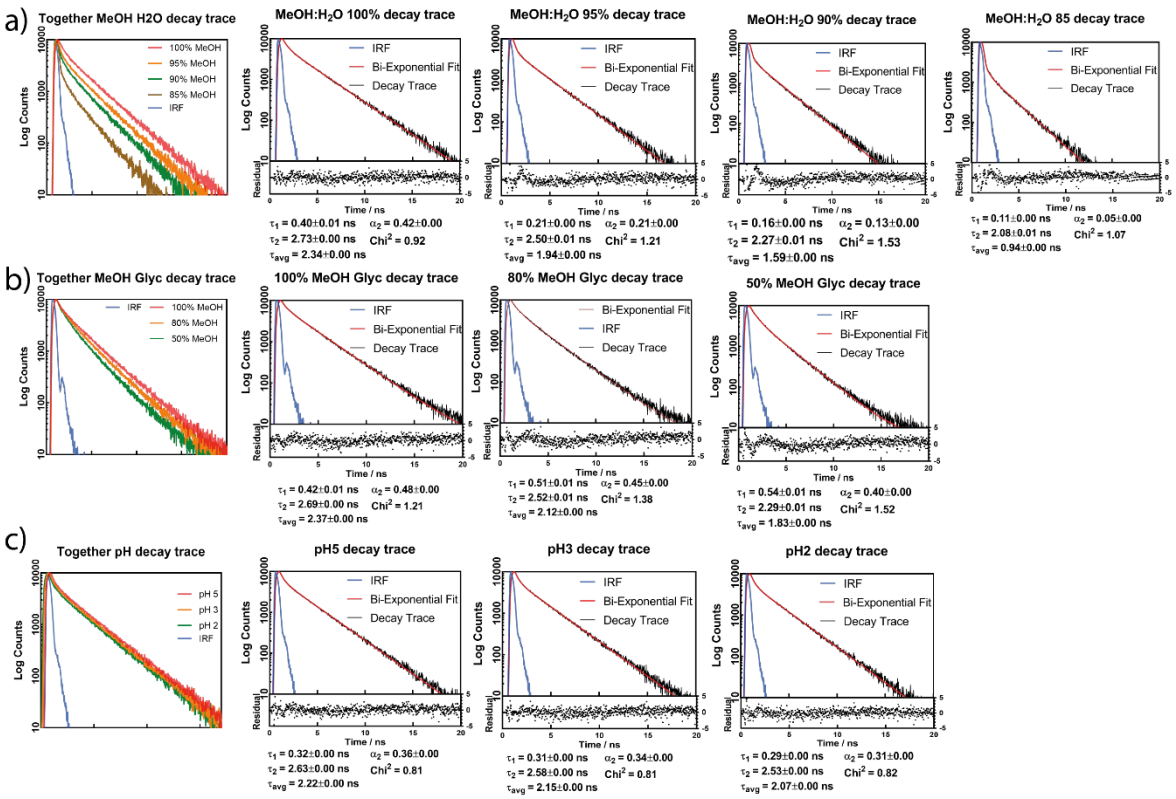

Figure 35: Lifetime dependency of **FLCS1** on H_2O concentration/viscosity/pH. **FLCS1** (1 µM) with copper(I) (3 µM) was measured a) at different H_2O:MeOH ratios (100:0, 95:5, 90:10, 85:15); b) at different glycol:MeOH ratios (100:0, 80:20, 50:50); c) at different pH values. The pH values were calibrated with diluted HCl and NaOH solutions. The average lifetime was evaluated by biexponential fitting with τ_1 and τ_2 kept variable.

1.3.2.5. FLCS1 with cell lysate

To evaluate the ability of **FLCS1** to detect cellular copper(I), an *in vitro* experiment was carried out investigating the effect of cell lysate (from SH-SY5Y cells) on the copper(I) sensing ability of the probe. There, a lysis buffer was used to digest the cell membrane and 10 µL of the lysate (1 mg/mL) was added to a methanolic solution of **FLCS1**. Surprisingly, no fluorescence increase due to the cellular copper(I) was observed and even adding 1 µM of copper(I) externally did not show a fluorescence increase but when adding excess copper(I) then the signal increased (see Figure 36a). Alternatively, when adding lysate to a 1:1 mixture of **FLCS1** and copper(I) the lysate addition resulted in a signal decrease successfully removing copper from the **FLCS1**:copper(I) complex (see Figure 36b). This indicated that the binding affinity of intercellular chaperones, proteins and GSH was higher than the binding affinity of **FLCS1**. This suggests that the probe can just be used to study cellular copper(I) in specific compartments of the cell which is not competing with those strong binding proteins and chaperones in the cytosol of the cell.

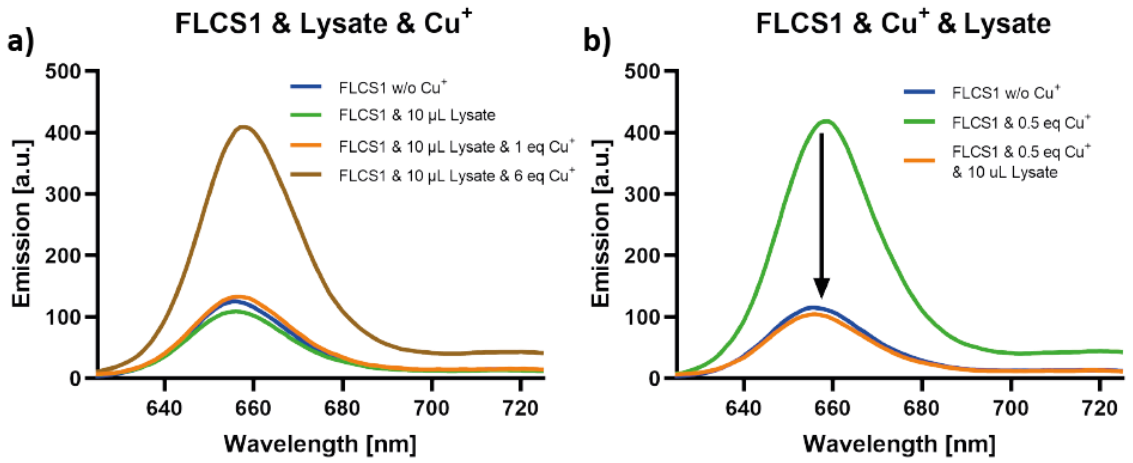

Figure 36: Competition of **FLCS1** and cell lysate. a) Fluorescence spectrum of **FLCS1** (1 µM) in MeOH with 10 µl cell lysate (1 mg/mL) followed by addition of 1 µM copper(I) and 6 µM copper(I). b) Fluorescence spectrum of **FLCS1** (1 µM) in MeOH with 0.5 µM copper(I) followed by addition of 10 µl cell lysate. The proteins and chaperones from the cell lysate bind copper(I) stronger than **FLCS1**.

1.3.2.6. FLCS1 cellular control experiments

Before, investigating the behaviour of **FLCS1** in cells some more control experiments with the **FLCS1** probe in MeOH were carried out with compounds that would be used later in the cellular studies to alter the copper(I) levels in the cell (see cellular experiments in Section 1.3.2.9.6). First, two compounds which were previously used in the literature for depleting copper(I) from cells, i.e. 2,9-dimethyl-4,7-diphenyl-1,10-phenantrolinedisulfonic acid disodium salt (BCS),[46] and bis(2-((2-(ethylthio)ethyl)thio)ethyl)amine (BETA)[114] were tested. The addition of the compounds to the methanolic **FLCS1:**copper(I) complex solution led to a reduction of fluorescence signal (see Figure 37a, b). Clioquinol, a well established zinc and copper(I) ionophore did not remove copper(I) from the **FLCS1**:copper(I) complex (see Figure 37c).[142] Cu-GTSM[143] is a copper(II) ligand which is cell permeable and after a bioreductive process in the cell it releases copper(I) into the cytosol. In the cell free environment however, the complex just contains copper(II) in a bound form and does not form copper(I). Therefore, not surprisingly, in methanolic solution Cu-GTSM did not show a turn-on response after addition to **FLCS1** (see Figure 37e). The compound 2,2'-dipyridyldisulfide (DTDP) is a thioselective reductant and was previously reported in the literature to bind to thiols of proteins in the cells releasing the copper(I) usually bound to those proteins making them available for the other copper(I) binding molecules.[143] This reagent did not alter the fluorescent signal of the **FLCS1**:copper(I) complex (see Figure 37d). Triton X, which is a commonly used blocking agent for tissue staining showed surprising results. After addition of

1 µL of that compound to the **FLCS1** solution a fluorescence increase over time was observed (see Figure 37f).

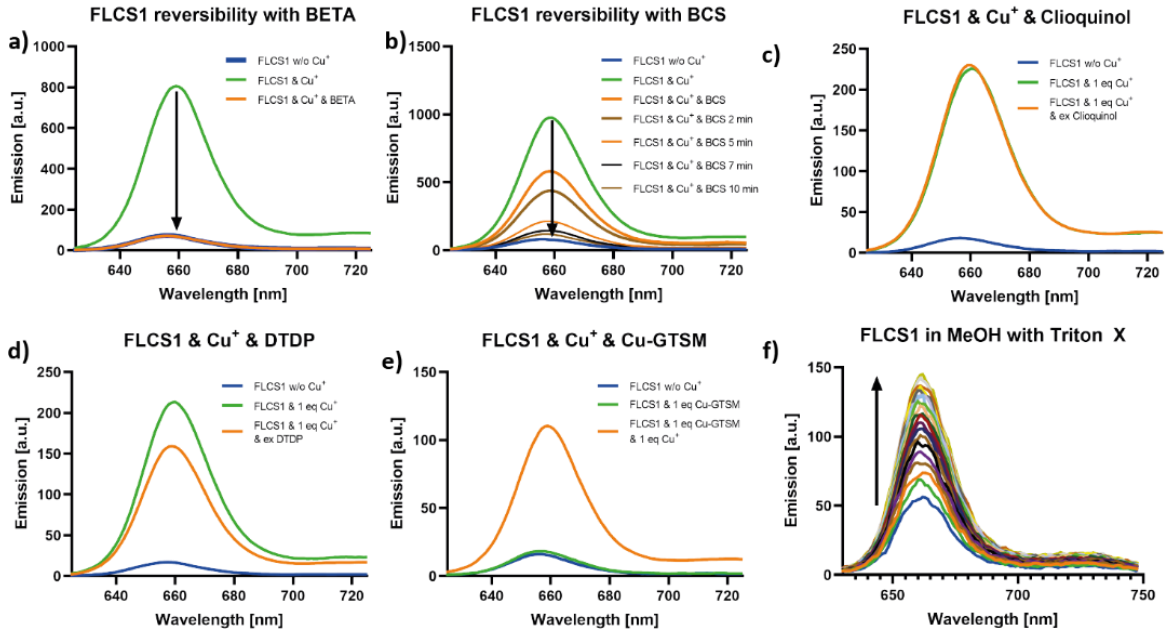

Figure 37: FLCS1 fluorescence control experiments with chemical reagents used in cell studies. Competition of **FLCS1** (1 µM) in MeOH with 3 µM copper(I) with a) 5 µM BETA; b) 10 µM BCS; c) 100 µM clioquinol; d) 500 µM DTDP. Fluorescence turn-on experiment with e) 5 µM Cu-GTSM; f) 0.1% Triton X over time.

1.3.2.7. Effects of surfactants on FLCS1

Since the non-ionic surfactant Triton X displayed a fluorescence increase over time of a methanolic solution of **FLCS1**, this phenomenon was investigated in more detail. Here the two surfactants Triton X and SDS, where SDS in contrast to Triton X is an anionic surfactant, was explored for **FLCS1** in MeOH, H_2O and TRIS buffer for fluorescence and absorption measurements. In MeOH both surfactants displayed a strong fluorescence increase over time where Triton X developed a signal quicker than SDS, where it took a week for the fluorescence to increase. The UV/vis spectra in both experiments over time were not influenced and remained the same (see Figure 38a, d, and Figure 39a, d). In 1 M TRIS buffer **FLCS1** was first insoluble judging from the broad band in the absorbance spectrum, however over time an increasing peak developed in the absorbance which also resulted in an increased fluorescence signal for both surfactants (see Figure 38b, e, and Figure 39b, e). In pure water **FLCS1** was again insoluble and remained insoluble even after 1 week incubation with Triton X but anionic surfactant SDS managed to partially dissolve the aggregates which led to a small fluorescence increase (see Figure 39c, f, and Figure 39c, f). Taken together it seemed that surfactants had a positive turn-on response with the fluorescent dye not only in MeOH

but also in ionic aqueous solutions. Based on these findings an ionic solution of water in combination with surfactants could dissolve the small particles and produce a turn-on effect of the dye even without addition of copper(I).

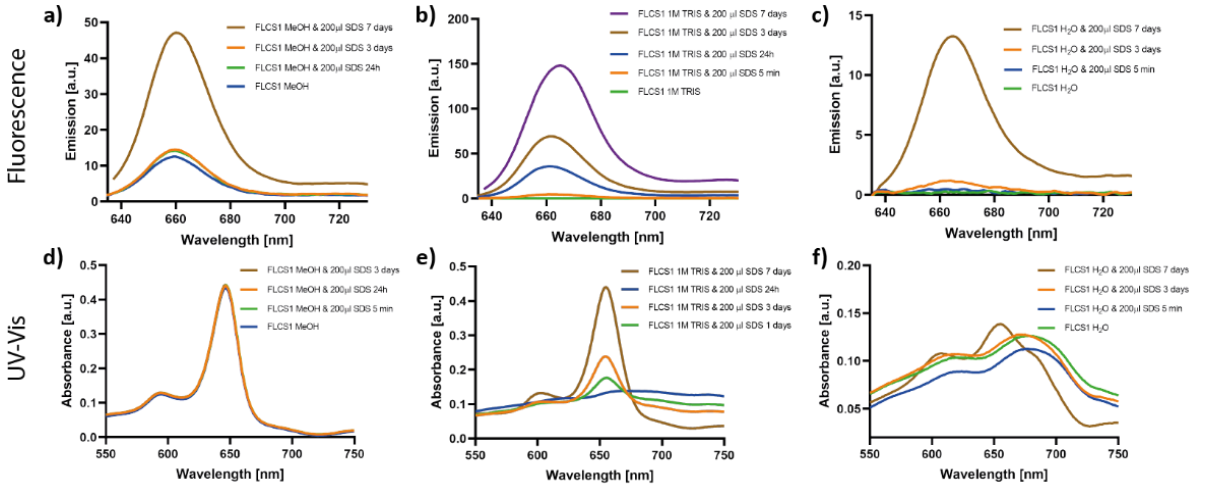

Figure 38: SDS effect on **FLCS1** in different solvents. Fluorescence and absorbance spectra for **FLCS1** (1 µM) in a, d) MeOH; b, e) 1 M TRIS buffer; c, f) H_2O over time.

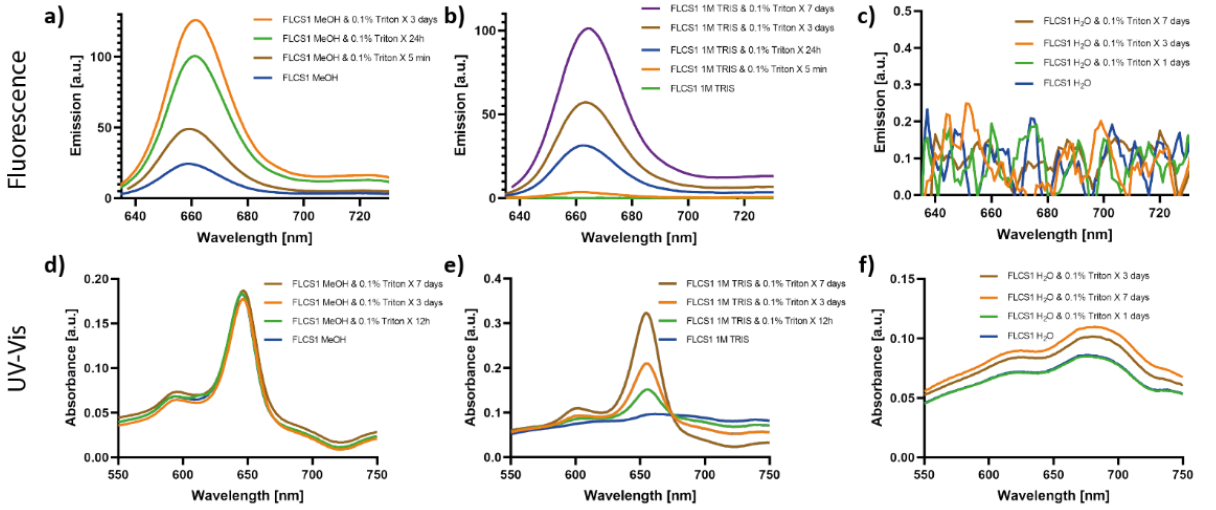

Figure 39: Triton X effect on **FLCS1** in different solvents. Fluorescence and absorbance spectra for **FLCS1** (1 µM) in a, d) MeOH; b, e) 1 M TRIS buffer; c, f) H_2O over time.

1.3.2.8. Cell experiments

1.3.2.8.1. FLCS1 dye delivery with co-solvent

For the first cell experiments a protocol had to be established to overcome the poor solubility of **FLCS1** in water and to search for a method to get the probe into the cells. In a first set of experiments DMSO and EtOH as co-solvents were tried at different concentrations to elaborate whether the dye would successfully at least partially dissolve and enter the cells. Even with a DMSO concentration of 40% in PBS, the probe did not succeed to enter the cells

(see Figure 40a). Low concentrations of EtOH as co-solvent also did not show any successes, however when reaching 25% or more, **FLCS1** managed to enter the cell over time (see Figure 40b) and the more EtOH was used the quicker the signal appeared inside the cell. When comparing the signal of the first copper(I) probe **CS3** with **FLCS1** delivered with a 1:1 H_2O:EtOH mixture both dyes colocalized in the same compartments (see Figure 40c). The same procedure was also carried out on primary hippocampal neurons which also stained nicely with **FLCS1** (see Figure 40d). The obvious disadvantage of this approach was that the cells did not survive the treatment with the dye because of the high concentration of ethanol and thus no cellular processes or other experiments could be carried out with this protocol. Therefore, other protocols and methods for delivering the dye into the cells were investigated.

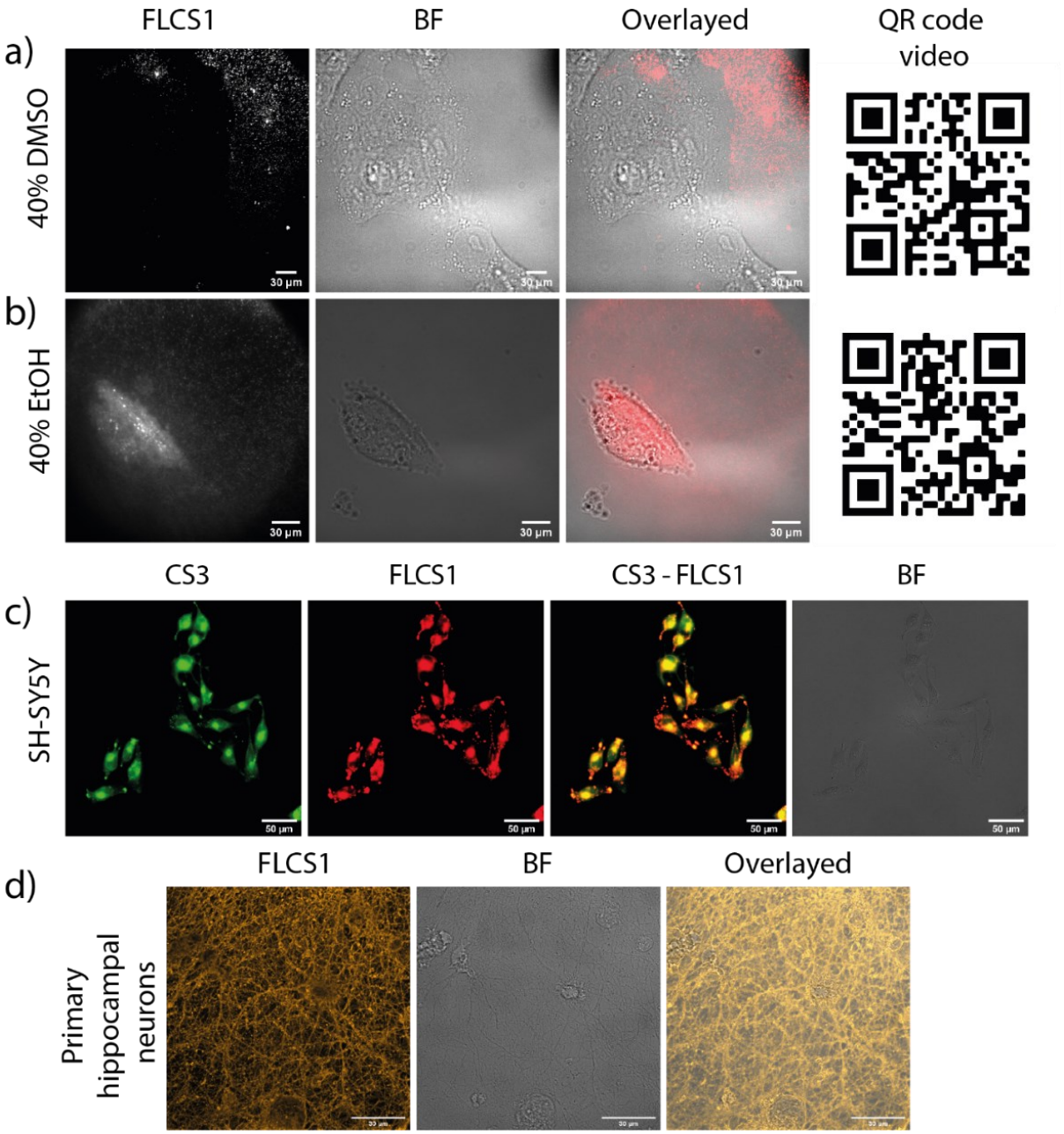

Figure 40: FLCS1 internalization attempts with DMSO/EtOH:PBS (40:60, v:v). SH-SY5Y cells treated with **FLCS1** (1 µM) in a) DMSO:PBS showing no cellular uptake of the dye; b) EtOH:PBS mixture showing successful uptake; QR codes show example videos of the dye in those solvent mixtures. c) Colocalization experiment of **FLCS1** (1 µM) treated with EtOH:PBS mixture followed by treatment with **CS3** (1 µM) in PBS for 20 min showing colocalization of both dyes inside the cells. d) Primary hippocampal neurons treated with **FLCS1** in EtOH:PBS mixture.

1.3.2.8.2. FLCS1 dye delivery with lipofectamine

Lipofectamine 2000 (LF) is a common transfection reagent sold by Thermo Fisher and it consists of a mixture of two different types of lipids that form liposomes in aqueous environments. It is commonly used to internalize big molecules like mRNA or plasmid DNA into *in vitro* cell cultures by lipofection. This reagent was successfully used to deliver 60nM –

100 nM **FLCS1** into the cells with a 24 h incubation time at 37 °C. With this treatment method **FLCS1** was located inside the cell with punctate locations spread out throughout the cell plasma. When comparing the punctate locations with the spots from **CS3** no colocalization of the dye was observed (see Figure 41). After incubation with **FLCS1** cells showed to be fully viable, growing and replicating for over 48 h (see Figure 42).

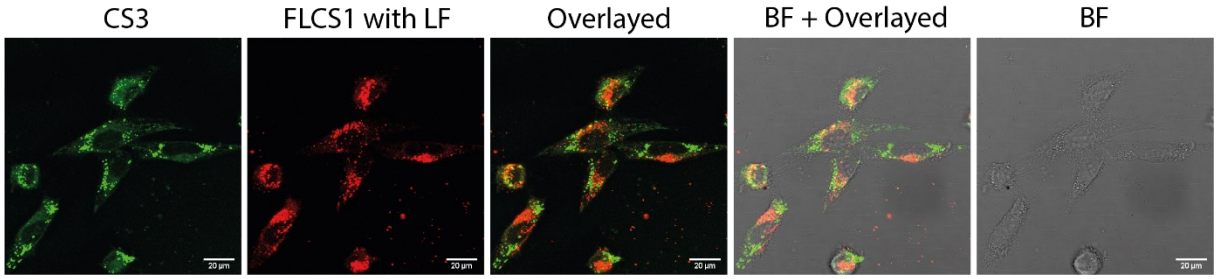

Figure 41: Colocalization experiment of **CS3** and **FLCS1** with lipofectamine protocol. SH-SY5Y cells were treated for 24 h with DMEM containing 60 nM **FLCS1**, 0.2% lipofectamine and 10% FBS, washed twice with PBS and treated with **CS3** (2 µM) in PBS for 20 min. Overlayed images show no colocalization of the two copper(I) probes.

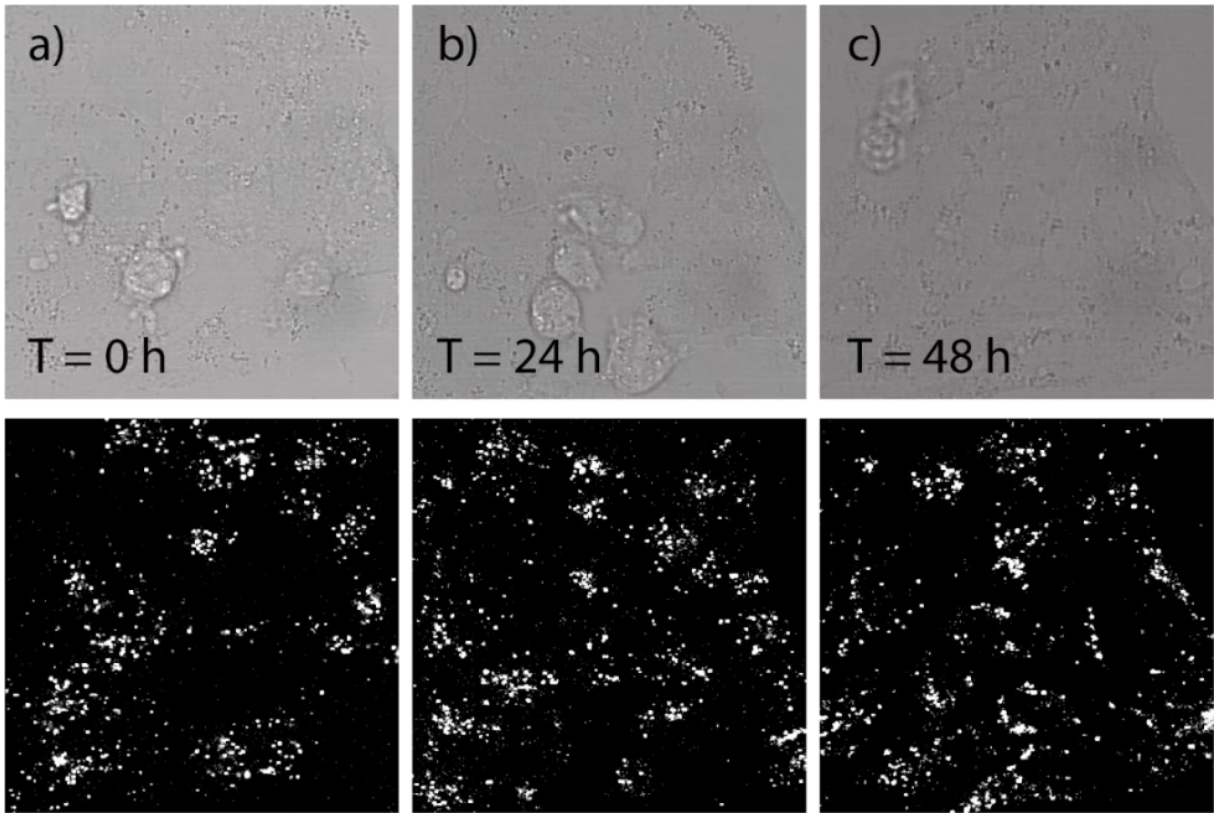

Figure 42: Visual viability inspection. Brightfield (top) fluorescence image (bottom) of SH-SY5Y cells treated for 24 h with DMEM containing 60 nM **FLCS1**, 0.2% lipofectamine and 10% FBS and measured at timepoint a) 0 h b) 24 h and c) 48 h after changing back to unsubstituted media. The cells show normal morphology and cell growth.

In another experiment cells which were first treated with **FLCS1** with 0.2% lipofectamine overnight, were recorded and afterwards treated with the first treatment protocol with the H_2O:EtOH solvent mixture. The overlaying of the images showed that the **FLCS1** location pattern changed after the treatment with the solvent mixture (see Figure 43). This confirmed again that the first treatment protocol mostly likely did not reflect the correct location of copper(I) inside the cells but just shows a turn-on response in lipid droplets which was previously confirmed with the **CS3** copper(I) probe (see Figure 20).

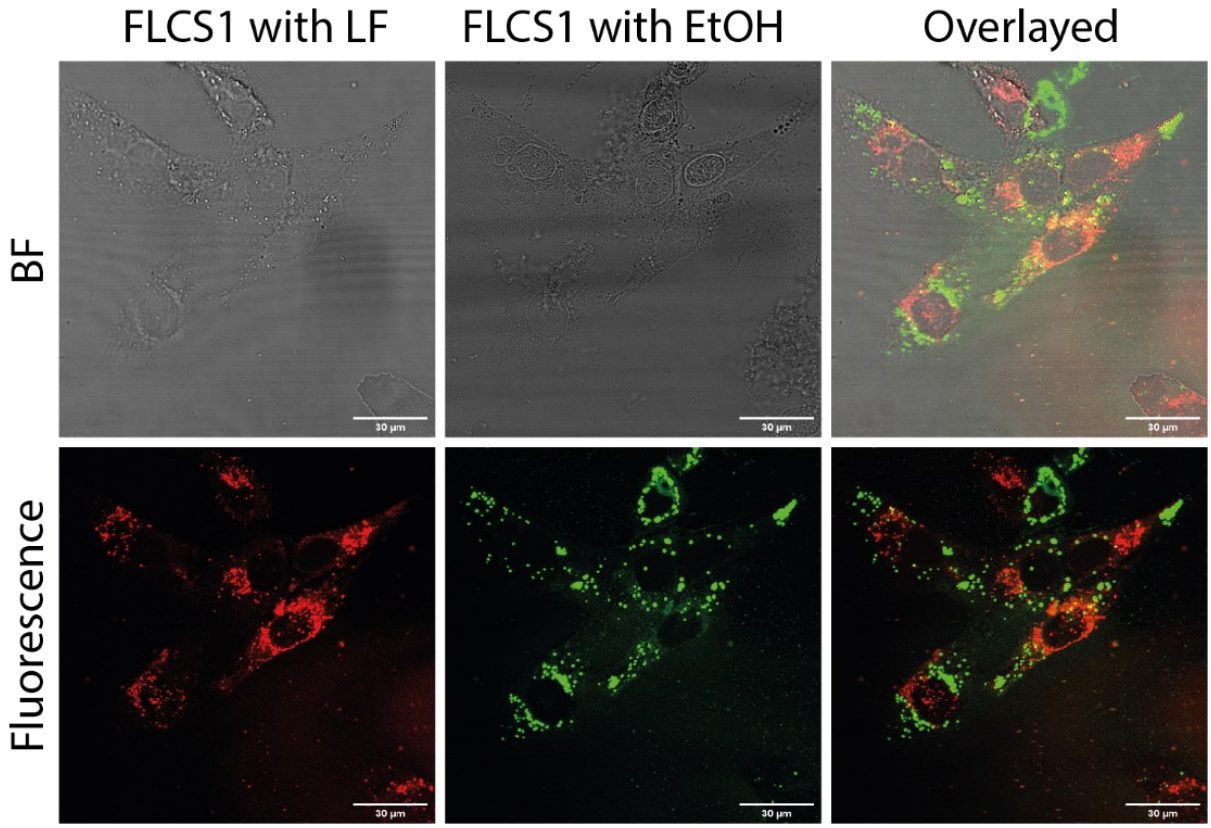

Figure 43: Comparison of **FLCS1** cell internalization protocols. **FLCS1** (60 nM) incubated with 0.2% lipofectamine in DMEM with 10% FBS imaged for 24 h (left) followed by treatment with **FLCS1** (1 µM) in EtOH:H_2O 1:1 mixture for 20 min (middle). Overlayed images showing a change of **FLCS1** location inside the cell after treatment with the ethanolic solvent mixture (right) (λ_{ex} = 620 nm, λ_{em} = 630-700 nm).

1.3.2.8.3. Colocalization FLCS1 and AS and Lysotracker Green

Next, in a colocalization experiment of the copper(I) dye **FLCS1** and externally treated labelled alpha-synuclein was investigated. There the three different cell lines N27, SH-SY5Y and HEK293 were simultaneously incubated with **FLCS1** and Alexa488 labelled AS with 0.2% lipofectamine for 24 h. The results for all three cell lines show strong colocalization patterns with AS and the copper(I) probe (see Figure 44).

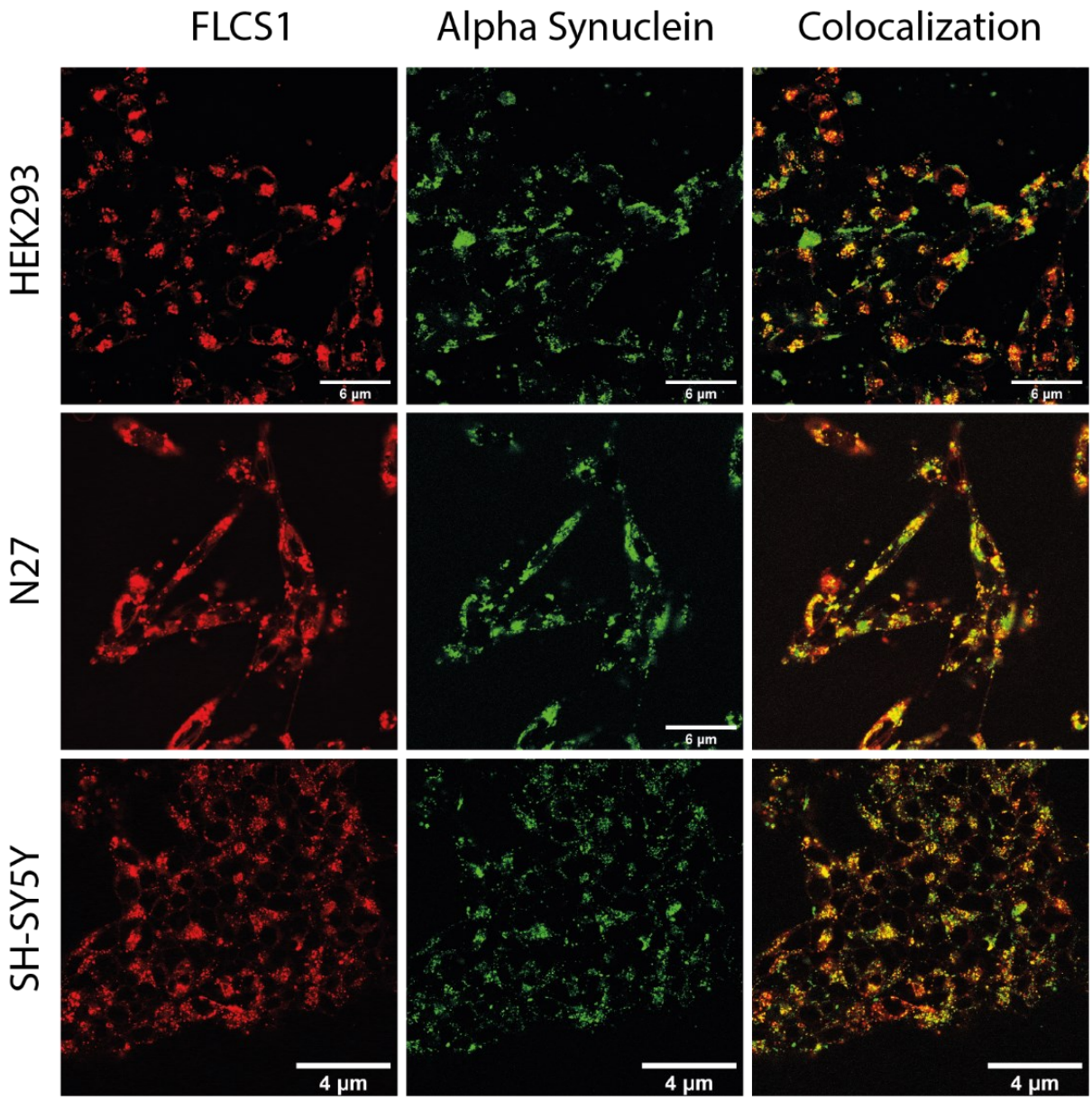

Figure 44: Colocalization of **FLCS1** with AS. HEK293, N27 and SH-SY5Y cells were simultaneously incubated with **FLCS1** (60 nM) with 0.2% lipofectamine for 24 h in DMEM with 10% FBS imaged together with AS (0.5 µM) labelled with Alexa 488 overnight and imaged the day after on confocal microscope at 40x magnification (λ_{ex} = 500 nm, λ_{em} = 510-550 nm for AS and λ_{ex} = 620 nm, λ_{em} = 630-700 nm for **FLCS1**).

Furthermore, the colocalization of **FLCS1** and Lysotracker Green showed strong overlaps in the fluorescence signal for all three cell lines (see Figure 45). The colocalization was also confirmed in primary hippocampal neurons. However, when looking more closely in some examples the fluorescence signals of the **FLCS1** signal did not 100% overlap with the labelling signal of the lysotracker (see Figure 46). These results suggest that the **FLCS1** probe as well as alpha-synuclein are present in lysosomes and copper(I) is potentially interacting with the protein in this cellular compartment. This is in accordance with the literature where

growing body of evidence has indicated that lysosomes, well known for being involved in the degradation and recycling of cellular waste and energy metabolism,[144,145] also play a vital role in the regulation of transition metal homeostasis including copper ions.[41,110]

One question which remained was whether the copper(I) probe was present in lysosomes because of its affinity towards copper(I), because of other turn-on reasons like polarity or because of the method used for delivering the dye to the cells.

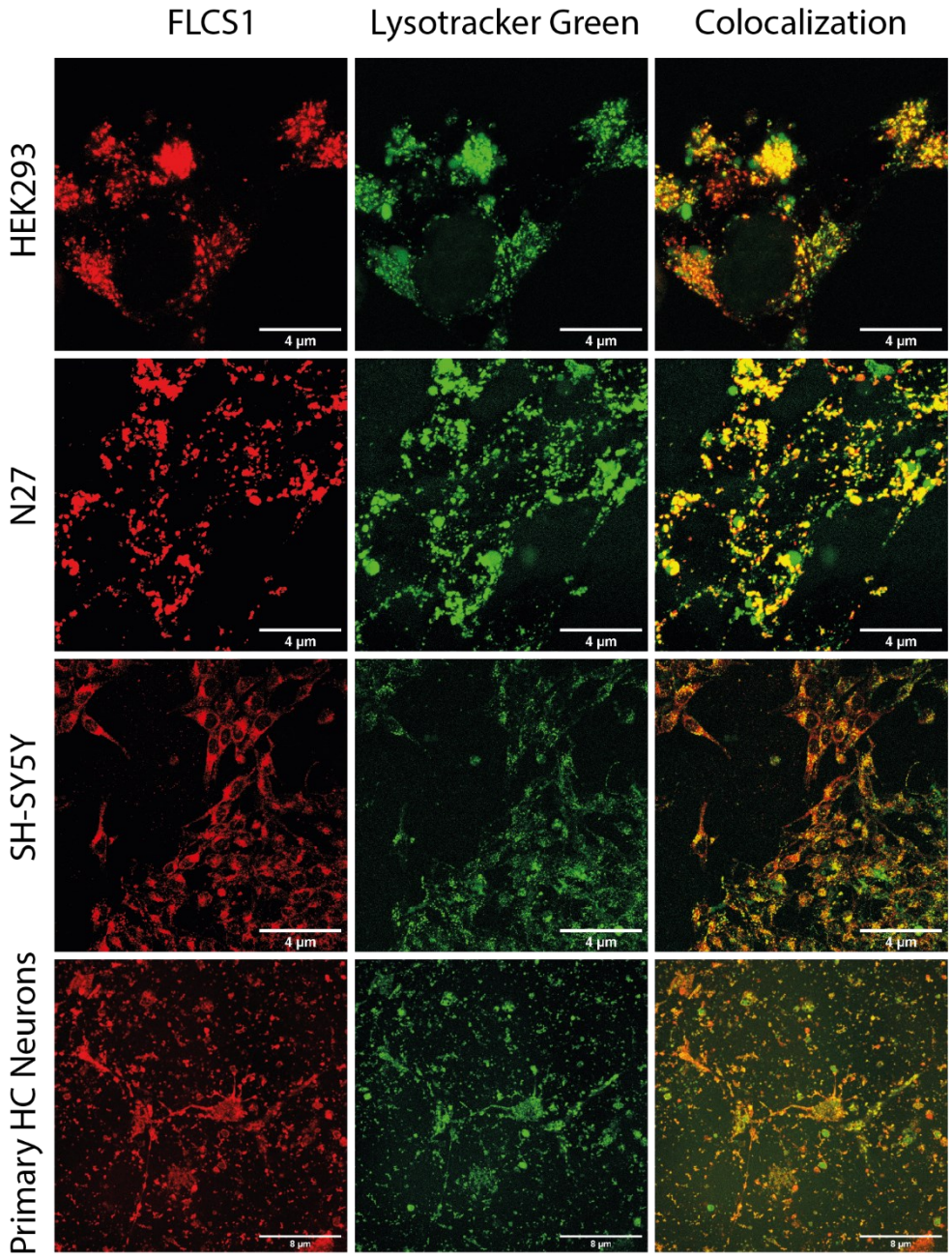

Figure 45: Colocalization of **FLCS1** and Lysotracker Green. HEK293, N27, SH-SY5Y cells and primary hippocampal neurons were incubated with **FLCS1** (60 nM) with 0.2% lipofectamine for 24 h in DMEM with 10% FBS. Before imaging, the cells were treated with Lysotracker Green (LTG) (50 nM) for 20 min in PBS. Images show colocalization of **FLCS1** with LTG in all cell lines (λ_{ex} = 500 nm, λ_{em} = 510-550 nm for LTG and λ_{ex} = 620 nm, λ_{em} = 630-700 nm for **FLCS1**).

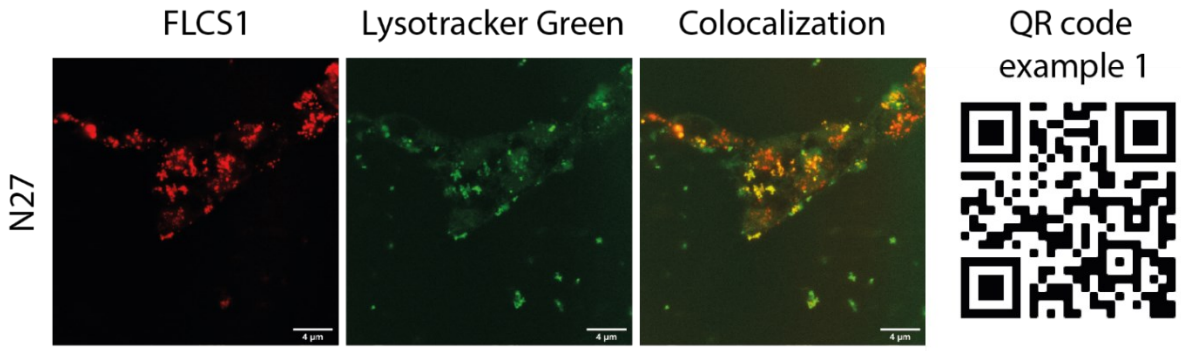

Figure 46: Partial colocalization of **FLCS1** with Lysotracker Green. N27 cells incubated with **FLCS1** (60 nM) with DMEM containing 0.2% lipofectamine and 10% FBS for 24 h and before imaging treated with Lysotracker Green (50 nM) for 20 min in PBS. Cells imaged show only partial colocalization of **FLCS1** and lysosomes. QR code shows video of full z-stack of the displayed cells.

1.3.2.8.4. FLCS1 on organotypic cells cultures

Next, the functionality of **FLCS1** was tested on organotypic cultures. The organotypic cell cultures were treated with the same protocol as for normal cell cultures with 0.2% lipofectamine in Neurobasal-A media with B27 supplement for 24 h. The fluorescence image showed some signal at the cells at the border of the brain slice but most of the organotypic cell tissue remained unlabelled (see Figure 47).

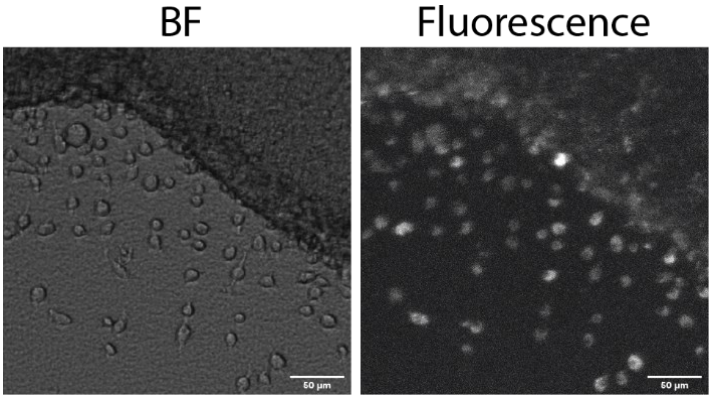

Figure 47: Organotypic cell culture labelling with **FLCS1**. Organotypic cell culture slices were treated with **FLCS1** (60 nM) with 0.2% lipofectamine in neurobasal-A medium with B27 supplement. Dye got internalized just for peripheral regions of the brain slice.

1.3.2.8.5. FLCS1 and CS3 photobleaching experiment

A photobleaching experiment was carried out on SH-SY5Y cells with both copper(I) probes to compare their stability. The cells were incubated with **FLCS1** (60 nM) with 0.2% lipofectamine for 24 h and **CS3** (2 µM) for 20 min before imaging. The signal for both dyes was equally intense at the beginning of the recording process, however the signal of **CS3** dropped significantly faster compared to **FLCS1**. This indicated that **FLCS1** was

significantly more stable and **FLCS1** stained cells could be recorded for much longer compared to **CS3** incubated cells (see Figure 48).

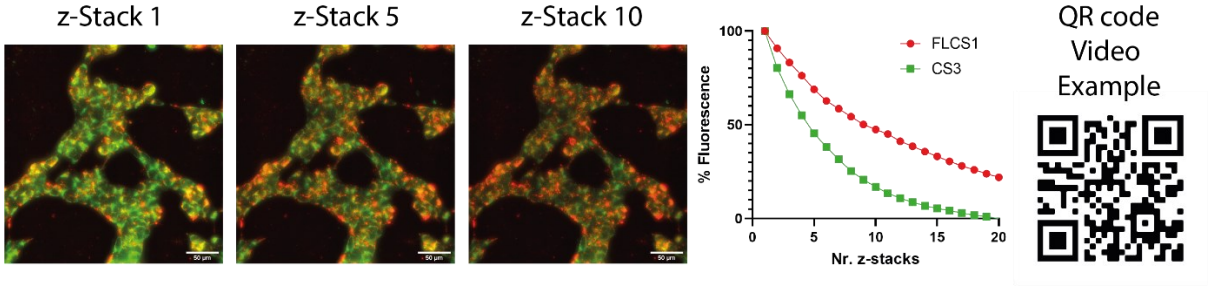

Figure 48: Photobleaching comparison of **FLCS1** and **CS3**. SH-SY5Y cells were stained with **FLCS1** and **CS3** with the usual protocol and imaged over time with confocal microscopy at a 1% laser power for both lasers (λ_{ex} = 520 nm, λ_{em} = 530-580 nm for **CS3** and λ_{ex} = 620 nm, λ_{em} = 630-700 nm for **FLCS1**). QR code shows a video example of the photobleaching experiment.

1.3.2.8.6. Copper(I) alteration experiments with FLCS1

To test whether **FLCS1** can sense copper(I) alterations, several different approaches were carried out to alter the copper(I) levels inside cells. First, the thiol-selective oxidant 2,2'-dithiodipyridine (DTDP) was used, which is known to increase the cellular free copper(I) levels by binding to thiols of proteins releasing copper(I) ions in that process. When SH-SY5Y cells were treated with 100 µM DTDP dissolved in PBS, the cells did not show any changes of their fluorescence signal from **FLCS1** (see Figure 49a). However, when DTDP was added to the cells from the DMSO stock solution a clear turn-on effect was observed which lasted for several seconds before recovering the initial fluorescence intensity. This signal increase could be repeated twice on the same cells (see Figure 49b and QR code videos) indicating that DTDP released copper(I) which was captured back into equilibrium after around 1 min and with a second addition of an increased quantity of DTDP the signal increase could be repeated. Addition of pure DMSO did not show any intensity changes (see Figure 49c) and the laser exposure for the same time period did not significantly change the fluorescence signal of the dye inside the cells (see Figure 49d).

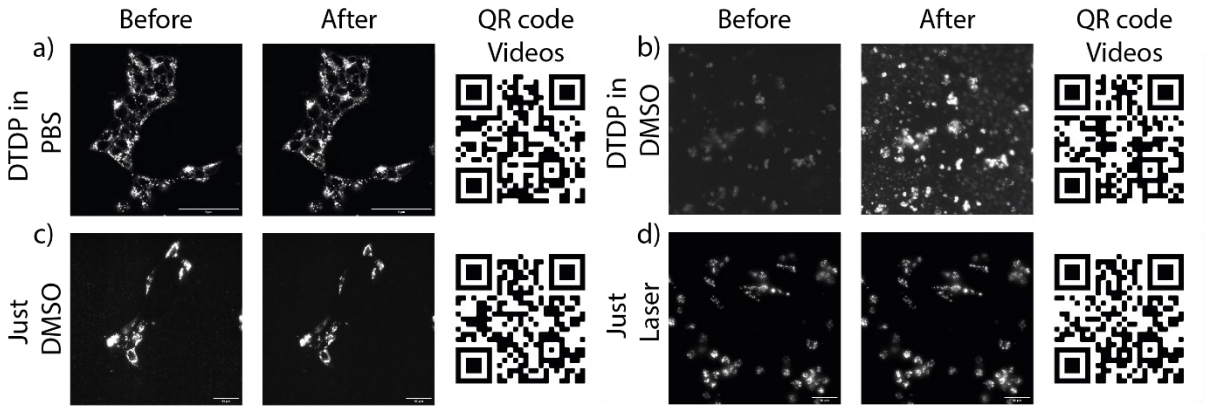

Figure 49: DTDP treatment of **FLCS1** stained SH-SY5Y cells. SH-SY5Y cells were incubated with **FLCS1** (60 nM) with DMEM containing 0.2% lipofectamine and 10% FBS for 24 h and imaged before and after treatment with a) 100 µM DTDP from a PBS stock solution; b) 100 µM DTDP from a DMSO stock solution; c) addition of the same amount of DMSO as for (b); d) repeated laser exposure in the same time intervals as the treated cells. DTDP treatment from DMSO stock showed signal increase in treated cells.

Next, the same cell line was treated with a well-known copper(II) ionophore clioquinol which can reversibly bind to copper(II) in the media and can pass with the ion through the cell membrane increasing cellular copper(I) levels. Addition of a mixture of copper(II) and clioquinol from a PBS stock solution did not show any changes in the fluorescence signal of the dye (see Figure 50a) but when clioquinol was added from a DMSO stock solution onto the cells the signal showed a strong increase (see Figure 50b).

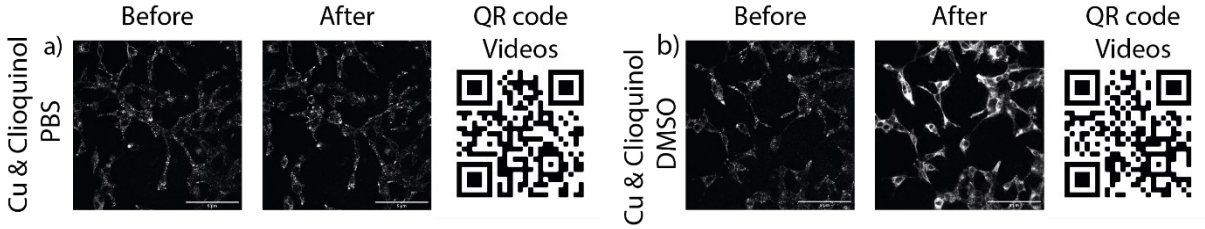

Figure 50: Clioquinol and copper(II) treatment of **FLCS1** stained SH-SY5Y cells. SH-SY5Y cells were incubated with **FLCS1** (60 nM) with DMEM containing 0.2% lipofectamine and 10% FBS for 24 h and imaged before and after treatment with 400 µM copper(II) and 800 µM clioquinol from a) PBS stock; b) DMSO stock.

These first two attempts successfully increased the fluorescence signal inside the cells after treatment with the compounds dissolved in DMSO but with this protocol the cells did not survive the treatment which could be judged from the lack of movement of the cells over time after the addition of the compounds. Furthermore, the fact that DMSO was necessary for observing the effects indicated a poor cell permeability of the compounds used. Because of this, other methods to alter intracellular copper(I) concentrations were tested. For that the ionophoric complex Cu-GTSM was used to increase cellular copper(I) which showed some

signal increase in SH-SY5Y cells over time after treatment (see Figure 51a) and BCS and BETA were used to deplete copper(I) from the cell (see Figure 51b). As a control experiment, cells were repeatedly imaged in the same time intervals as the treated cells to test the effect of repeated laser exposure on the fluorescence signal (see Figure 51c). This did not show a signal decrease to the same extent as the copper(I) depleted cells and a comparison of the signal over time for all four reagents and the control are shown in Figure 51d. These experiments demonstrated that the fluorescence signal was slightly altered by increasing or decreasing the cellular copper(I) concentration.

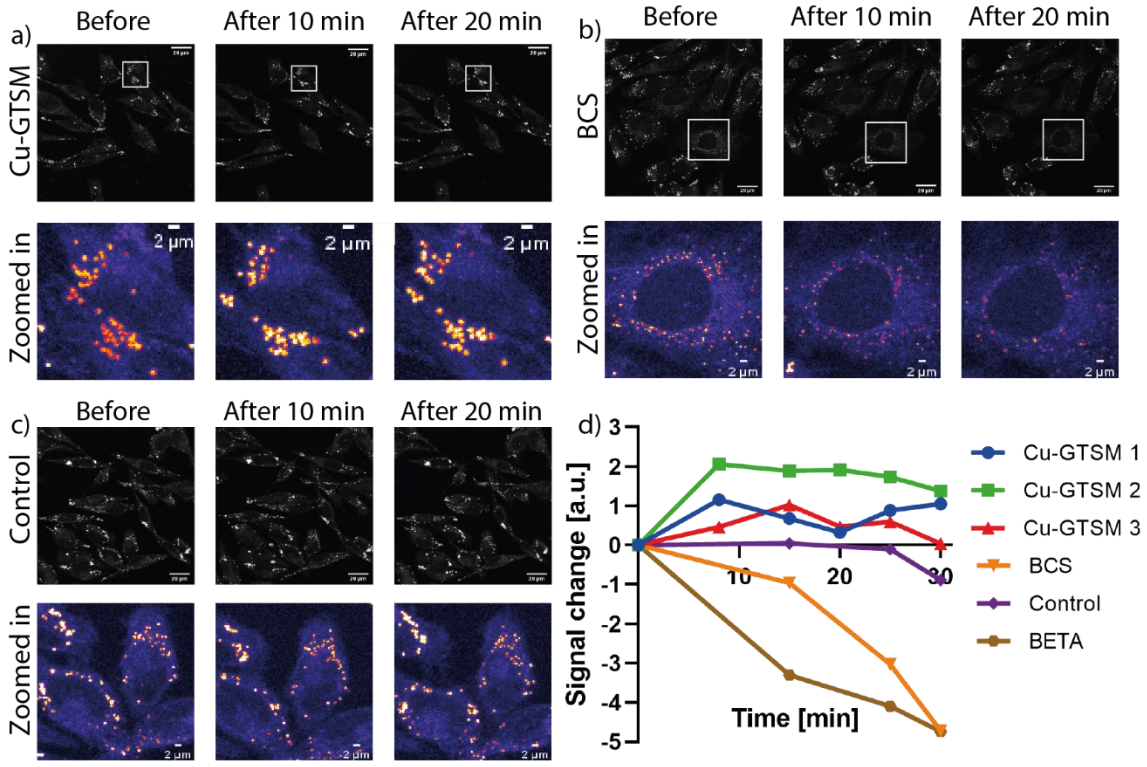

Figure 51: Copper(I) depletion and increase in **FLCS1** labelled SH-SY5Y cells. SH-SY5Y cells were incubated with **FLCS1** (60 nM) with DMEM containing 0.2% lipofectamine and 10% FBS for 24 h and imaged before and after treatment with a) 2.5 µM Cu-GTSM (three repeats); b) 125 µM BCS; c) untreated control cells; d) shows fluorescence signal progression over time for cells treated with different compounds. Cells show slightly increased signal for Cu-GTSM and a decreased signal for copper(I) depleting compounds BETA and BCS.

To confirm that the probe is not influenced by pH changes in lysosomes, cells were treated with bafilomycin A1, which stops lysosomal acidification, thus increasing the pH in the lysosomes. Pleasingly, confocal microscopy showed that this treatment did not alter the fluorescence intensity from **FLCS1** localised in lysosomes suggesting that a pH increase in lysosomes did not affect the intensity signal of the probe (see Figure 52).

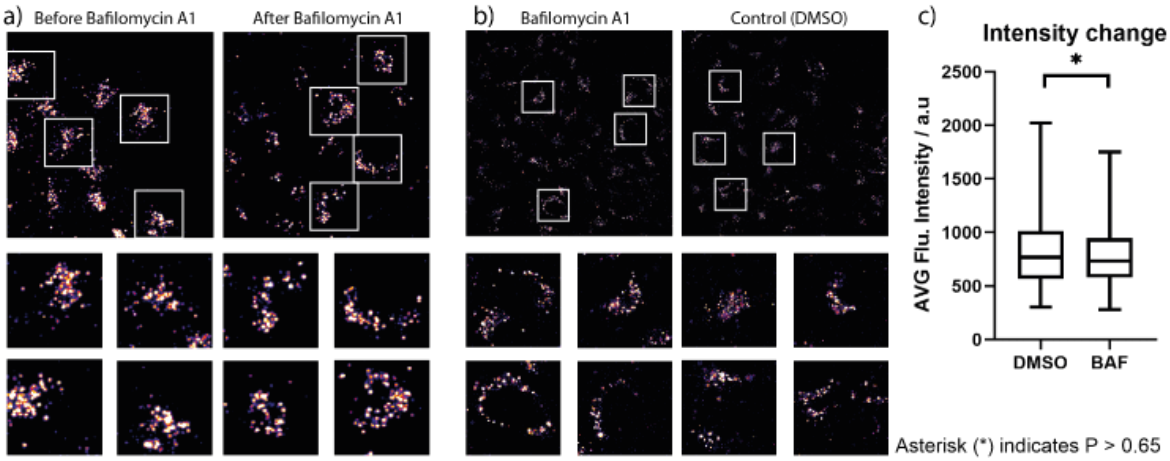

Figure 52: Inhibition of lysosome acidification with bafilomycin A1. SH-SY5Y cells were treated for 24 h with DMEM containing 60 nM **FLCS1** and 0.2% lipofectamine and 10% FBS a) imaged before and after treatment with bafilomycin A1 (30 nM) for 24 h. b) Bafilomycin A1 (30 nM) treated cell compared to equivalent concentrations DMSO (0.01%) treated cells. c) Statistical student t-test of intensity comparing 48 and 41 cells treated with bafilomycin A1 and DMSO, respectively, showing no statistically significant change of lysosomal intensity signals.

1.3.2.8.7. FLCS1 and fluorescence lifetime imaging microscopy (FLIM)

The microscopy studies carried out with **FLCS1** suggested that copper(I) was present in lysosomes and alterations of those copper(I) levels could be measured with the probe which was consistent with existing literature that indicated that there were increased copper(I) levels in those organelles. However, intensity-based probes were generally not concentration-independent and, thus, it was not possible to assess whether the measured fluorescence intensity in the lysosomes was observed, indeed, due to the presence of large pools of copper(I), or simply due to a consequence of high accumulation of the probe in this organelle or due to any other turn-on effect of the probe. As shown before the copper(I) depletion experiments and the experiments for copper(I) increase in cells showed small changes in the intensity profile of the fluorescence on confocal microscopy images. To confirm the functionality of the probe with a different approach, fluorescence lifetime imaging microscopy (FLIM) images of SH-SY5Y live cells incubated with **FLCS1** were recorded. Since the *in vitro* studies of the new copper(I) probe discussed above showed that **FLCS1** displayed significantly longer fluorescence lifetimes when bound to copper(I) as compared to the metal-free probe (see Figure 32a), FLIM should provide an unambiguous confirmation of the presence of copper(I) in lysosomes. A representative example of the FLIM images is presented in Figure 53a. The FLIM signal showed biexponential time-resolved decays (Figure 53g) of **FLCS1** in cells, which was consistent with the cell-free data (see Figure 53a and

Figure 33). When fitting the FLIM images with a biexponential decay function the values of τ_1 and τ_2 in cellular distribution centred around 1.1 ns and 2.6 ns, respectively (see Figure 53g and Figure 53i). These values deviated slightly from the observed *in vitro* values for **FLCS1** which were determined to be 0.39±0.00 ns for τ_1 in a copper(I) free state and 3.08±0.01 ns for τ_2 in the copper(I) bound state. This difference could be due to the complex intracellular environment, as compared to the cell-free assays (e.g. crowding, viscosity, polarity, refractive index) which was established for the *in vitro* experiment with the probe. It was shown that the lifetime was affected by various parameters; for example, adding increasing amounts of water to methanolic solutions of **FLCS1** decreased its fluorescence lifetime; increasing viscosity or decreasing the pH shifted the fluorescence lifetime of the probe to lower values (see Figure 35).

While none of these changes were large, they were sufficient to explain the small discrepancies in the lifetime values between the *in vitro* and *in cellulo* data. The calculated intensity weighted average lifetime (τ_{avg} = 2.06±0.2 ns, τ_1 = 1.1±0.6 ns, τ_2 = 2.6±0.4 ns, α_1= 0.59±0.15, α_2=0.41±0.15, χ^2 = 1.18±0.1) (see Figure 133 and compare to the cell-free data in Table 6 in the Appendix) in lysosomes indicated the probe being partially bound to copper(I).

Next, the cellular concentration of copper(I) was artificially increased using Cu-GTSM as it was done for the fluorescence intensity experiment before. This should confirm the ability of **FLCS1** to image copper(I) *in cellulo.* As indicated above, Cu-GTSM is a well-established reagent that is cell permeable and that undergoes a bio-reduction process releasing copper(I) inside a cell.[146]

For the recorded FLIM images of the SH-SY5Y cells before and after treatment with this compound, the most suitable fitting model remained a biexponential decay. Consistent with the release of additional copper(I) from Cu-GTSM inside the cell, an upwards shift in the average fluorescence lifetime (or, in other words, an upshift in the longer component amplitude, Figure 133a, b in the Appendix) of the **FLCS1** probe was observed upon treating SH-SY5Y cells with Cu-GTSM (5 μM for 20 min) (see Figure 53b, e).

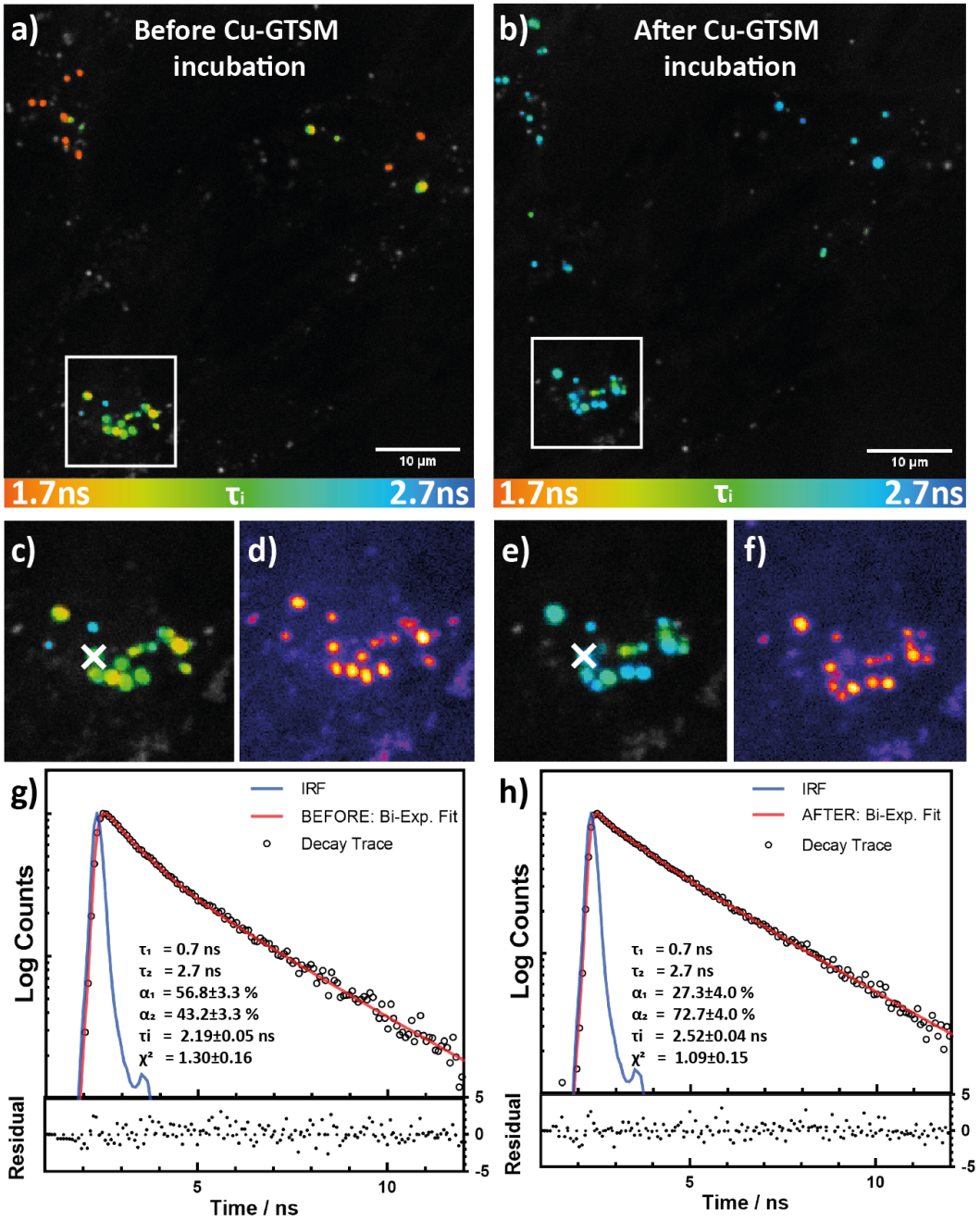

Figure 53: FLIM imaging of SH-SY5Y cells treated with **FLCS1**. a), c), d) FLIM data recorded before and b), e), f) after incubation with 5 µM Cu-GTSM for 20 min; a), b), c), e) show the lifetime maps (τ_{avg}); d) and f) show fluorescence intensity images; c), d), e), f) show the zoomed-in sections highlighted by white squares in a) and b); g) and h) show typical time-resolved fluorescence decay curves from the regions indicated by white crosses in c) and e); fitting parameters (inserts) and residuals (bottom panels) are also shown.

To reduce the uncertainty in the determination of the fitting parameters, the two lifetime components were fixed at τ_1 = 0.7 ns and τ_2 = 2.7 ns for copper(I) treatment analysis. The goodness of fit parameter (χ^2) distribution was not influenced by this adaptation (see Figure 135 in Appendix) but allowed to clearly visualise the changes of the amplitudes of two

lifetimes before and after the treatment (see Figure 54d). These changes were observed without significant altering the distribution of the short and long lifetime components.

The amplitude increase of the longer lifetime component α_2 (see in Figure 134a, b in the Appendix), rather than its lifetime, was consistent with an increase in the fraction of the bound copper(I) seen by FLIM in cells following the treatment. The intensity of the fluorescence signal, as shown before did not undergo significant changes following Cu-GTSM treatment (see Figure 54d, f).

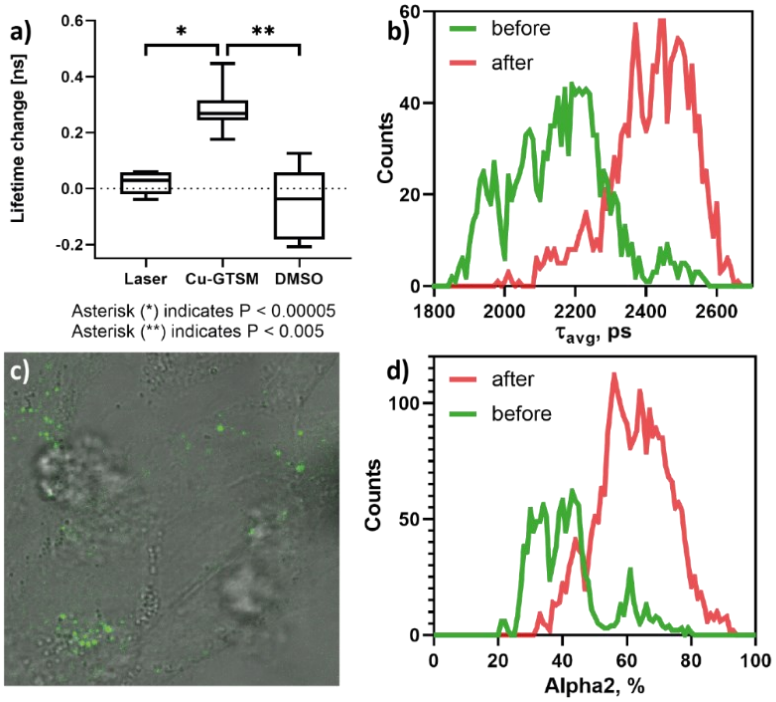

Figure 54: FLIM analysis of **FLCS1** in SH-SY5Y cells. A) Statistics of average lifetime changes before and after treatment with Cu-GTSM in comparison with repeated laser exposure and DMSO treatment of 12 cells, over 3 independent biological repeats. b) Amplitude of the longest lifetime component. d) Average lifetime histograms before and after Cu-GTSM incubation. c) Brightfield image of cells with fluorescence image overlayed.

This confirmed that FLIM is a more sensitive technique compared to intensity-based imaging, allowing to monitor small changes in copper(I) in lysosomal compartments in cells using the newly developed **FLCS1** copper(I) probe. As controls, treatment of cells with DMSO as well as the repeated laser irradiation exposure of the cells with **FLCS1** did not lead to significant changes in fluorescence lifetime compared to cells treated with Cu-GTSM (see Figure 54a and Figure 136 in the Appendix).

1.4. Experimental Procedures

1.4.1. Synthetic Materials and Methods

All chemical reagents and solvents for synthesis were purchased from commercial suppliers and were used without further purification. All moisture or oxygen sensitive reactions were carried out under a nitrogen atmosphere. The composition of solvent mixtures is given by volume ratio (v/v). Analytical and preparative thin layer chromatography was performed using Merck 60 F254 silica gel with 0.25 mm and 2 mm thickness, respectively. Flash chromatography (FC) was performed using Merck Kieselgel 60 at room temperature (RT) under a positive pressure. ^{1}H NMR spectra were collected in $CDCl_3$ or DMSO-d_6 (Cambridge Isotope Laboratories, Cambridge, MA) at 25 °C on a Bruker AV-300 or AV400 spectrometer. Chemical shifts (δ) are given in ppm and coupling constants in Hz. Notation for the ^{1}H NMR spectral splitting patterns include singlet (s), doublet (d), triplet (t), quartet (q), quintet (qui), broad (br) and multiplet/overlapping peaks (m). Matrix-assisted laser desorption/ionization MALDI analyses were carried out with a Thermo Scientific MALDI mass spectrometer and CHCA was used as embedding matrix.

1.4.1.1. Synthetic procedure for CS3 and Ctrl-CS3

Synthesis of 10-(chloromethyl)-2,8-diethyl-5,5-difluoro-1,3,7,9-tetramethyl-5H-4l4,5l4-dipyrrolo[1,2-c:2',1'-f][1,3,2]diazaborinine (3)

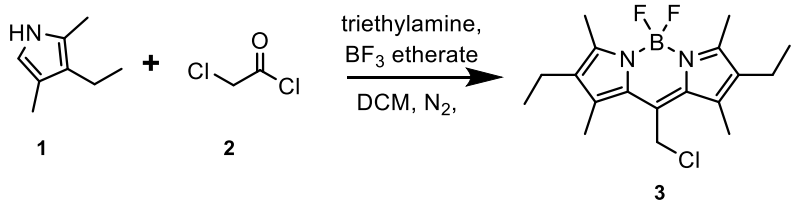

1 2 3

The basic structure of the BODIPY compound was synthesized following an already existing procedure from the literature.[131] In a 50 mL two necked flask chloroacetyl chloride **2** (0.228 g, 2.01 mmol, 1 eq.) and 2.4-dimethyl-3-ethylpyrrole **1** (0.498 g, 4.04 mmol, 2 eq.) were mixed in with nitrogen degassed DCM (25 mL). The deep purple reaction mixture was heated up to 50 °C and was stirred for 2 h under a nitrogen atmosphere. Then the solution was allowed to cool down to room temperature and the solvent was removed on a rotary evaporator under reduced pressure. The residue was dissolved in toluene (50 mL) with a trace of DCM (2.5 mL). The reaction flask was put under nitrogen and after adding triethylamine (1.35 mL, 9.6 mmol, 4.8 eq.) the colour changed from purple to dark green. After stirring for 30 min boron trifluoride diethyl etherate (1.75 mL, 14.18 mmol, 7.1 eq.) was added. With this reagent the

colour changed again back to a dark purple and the reaction was heated up to 50 °C for 2 h. After that, the reaction mixture was cooled down and the solvent was removed on a rotary evaporator under reduced pressure. The residue was again re-dissolved in dichloromethane, washed with water, dried over Na_2SO_4, evaporated to dryness and purified with flash chromatography (silica gel, 3:1 toluene/*n*-hexane; 214 mg, 30% yield).

^{1}H NMR ($CDCl_3$, 400 MHz): δ 4.86 (s, 2H,), 2.54 (s, 6H), 2.49 (s, 6H), 2.44 (q, 4H, J = 7.6), 1.09 (t, 6H, J = 7.6).

^{13}C NMR ($CDCl_3$, 400 MHz): δ 155.2, 136.5, 134.4, 133.8, 131.1, 38.2, 31.2, 17.4, 14.9, 12.9.

Synthesis of 10-(chloromethyl)-2,8-diethyl-5,5-dimethoxy-1,3,7,9-tetramethyl-5H-4l4,5l4-dipyrrolo[1,2-c:2',1'-f][1,3,2]diazaborinine (4)

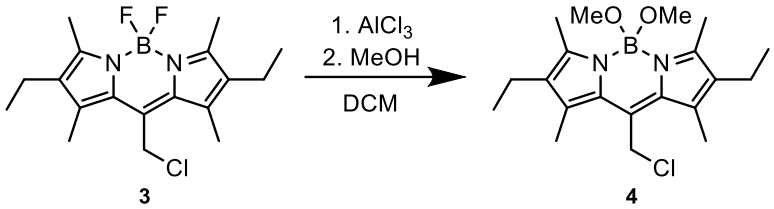

3 **4**

The methoxylated form of BODIPY was synthesized following an already existing procedure from the literature.[101] The BODIPY starting material **3** (71 mg, 0.20 mmol, 1 eq.) was weighted into a 5 mL vial. The solid was dissolved in DCM (2 mL) and $AlCl_3$ (80 mg, 0.60 mmol, 3 eq.) was added to it. After this addition of $AlCl_3$ the purple solution changed to a more bluish colour. Then the mixture was sonicated at room temperature for 6 min and then methanol (1 mL) was added, and the reaction mixture was stirred for an additional 6 min. The reaction was then diluted with EA (10 mL) washed twice with water and once with brine solution, and dried over Na_2SO_4. The pure dark red solid product **4** was obtained after flash chromatography (silica gel, EA; 39.3 mg, 52% yield).

^{1}H NMR ($CDCl_3$, 400 MHz): δ 4.86 (s, 2H), 2.80 (d, 2H, J = 5.1)*, 2.49 (s, 6H), 2.47 (s, 6H), 2.41 (q, 4H, J = 7.6), 1.05 (t, 6H, J = 7.5).

^{13}C NMR ($CDCl_3$, 400 MHz) δ 155.3, 134.2, 134.1, 133.1, 132.4, 60.4, 49.1, 38.5, 17.3, 14.9, 12.7.

* Splitting was not explainable and became a singlet in the next reaction step

Synthesis of 2-(ethylthio)ethane-1-thiol (7)

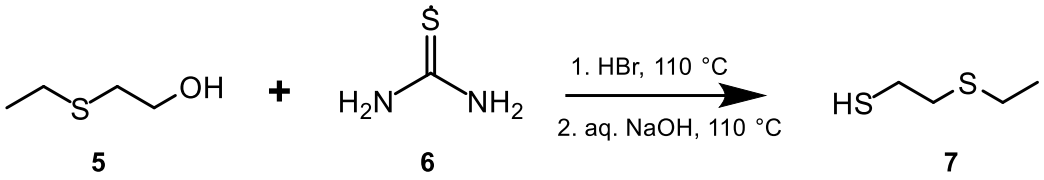

5 **6** **7**

2-(Ethylthio)ethane-1-thiol **7** was synthesized following an already existing procedure from the literature.[100] Ethyl-2-hydroxyethyl sulfide **5** (4.25 g, 40.0 mmol, 1 eq.) and thiourea **6** (3.05 g, 40.0 mmol, 1 eq.) were mixed in 48% hydrobromic acid (8.5 mL, 75.0 mmol, 1.88 eq.) and heated up to 110 °C under nitrogen atmosphere for 20 h. Afterwards the reaction mixture was cooled down to room temperature, concentrated aq. NaOH (3.2 g, 80.0 mmol, 2 eq.) was slowly added to the reaction solution and pH paper was used to verify a final pH of 8-9. Then the reaction was heated up to reflux at 110 °C overnight. Following this, the reaction was cooled to room temperature, neutralized with concentrated HCl. The pH was monitored using pH paper and after reaching pH 7 the solution was extracted using DCM (3×30 ml). The organic phase was washed with water, dried over Na_2SO_4 and the solvent was removed on a rotary evaporator under reduced pressure. The remaining product was a very strong-smelling slightly yellow to orange oil which was used without further purification (4.36 g, 89% yield).

^{1}H NMR ($CDCl_3$, 400 MHz): δ 2.85-2.68 (m, 4H), 2.59 (q, 2H, J = 7.4), 1.76 (t, 1H, J = 7.9), 1.29 (t, 3H, J = 7.4).

Synthesis of 3,6,12,15-tetrathia-9-monoazaheptadecane (9)

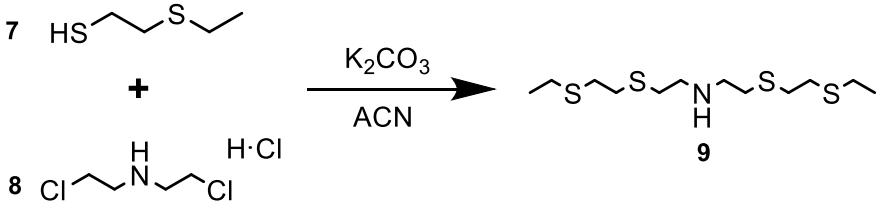

Tetrathia-monoazaheptadecane **9** was synthesized following an already existing procedure from the literature.[100] Sodium (0.194 g, 8.4 mmol, 4 eq.) was added to 2-thiapentan-1-thiol **7** (0.615 g, 5.0 mmol, 2.4 eq.) dissolved in absolute EtOH (9 mL) kept under nitrogen. The resulting solution was then heated up to reflux and a solution of bis(2-chloroethyl)amine hydrochloride **8** (0.30 g, 2.1 mmol, 1 eq.) dissolved in absolute ethanol (5 mL) was added

dropwise via dropping funnel to the thiolate solution. After that the reaction mixture was refluxed for 4 h. The solvent was removed on the rotary evaporator under reduced pressure and the product **9** was purified using flash chromatography (silica gel, 10% MeOH/DCM) resulting in a light brown oil as product (0.38 g, 72% yield).

^{1}H NMR ($CDCl_3$, 400 MHz): δ 2.86 (t, 4H, J = 6.5), 2.72-2.81 (m, 12H), 2.60 (q, 4H, J = 7.5), 1.87 (br, 1H), 1.29 (t, 6H, J = 7.4).

Synthesis of *N*-((2,8-diethyl-5,5-dimethoxy-1,3,7,9-tetramethyl-5H-4l4,5l4-dipyrrolo[1,2-c:2',1'-f][1,3,2]diazaborinin-10-yl)methyl)-2-((2-(ethylthio)ethyl)thio)-*N*-(2-((2-(ethylthio)ethyl)thio)ethyl)ethan-1-amine (CS3)

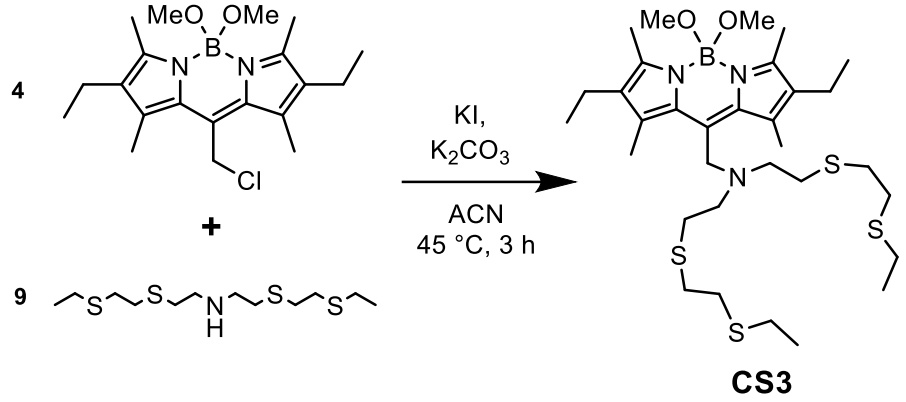

The final BODIPY copper(I) ligand **CS3** was synthesized following an already existing procedure from the literature.[101] The methoxylated BODIPY compound **4** (35 mg, 0.093 mmol, 1 eq.), the copper(I) binding ligand **9** (38 mg, 0.121 mmol, 1.3 eq.), KI (16 mg, 0.096 mmol, 1 eq.) and K_2CO_3 (26 mg, 0.190 mmol, 2.1 eq.) was weighted into a 25 mL Schlenk tube. Then ACN (1 mL) was added via syringe and the solution was stirred at 45 °C for 3 h under nitrogen atmosphere. The reaction mixture was then concentrated using the vacuum from the Schlenk line and the residue was re-dissolved in DCM (50 mL) and washed with water twice. The organic phase was dried over Na_2SO_4, concentrated to dryness and purified by column chromatography (silica gel, 100% EA). The product **CS3** was a dark red oil. (29 mg, 48% yield)

^{1}H NMR ($CDCl_3$, 400 MHz): δ 4.07 (s, 2H), 2.91 (t, 4H, J = 7.8), 2.82 (s, 6H), 2.69–2.54 (m, 16H), 2.52 (s, 6H), 2.48–2.39 (m, 10H), 1.26 (t, 6H, J = 7.4), 1.06 (t, 6H, J = 7.6).

ESI-MS: *m/z* calcd. for $C_{32}H_{56}BN_3O_2S_4$: 653.87; found: 654.3062 [M+H].

Synthesis of *N*-((2,8-diethyl-5,5-difluoro-1,3,7,9-tetramethyl-5H-4l4,5l4-dipyrrolo[1,2-c:2',1'-f][1,3,2]diazaborinin-10-yl)methyl)-*N*-octyloctan-1-amine (11)

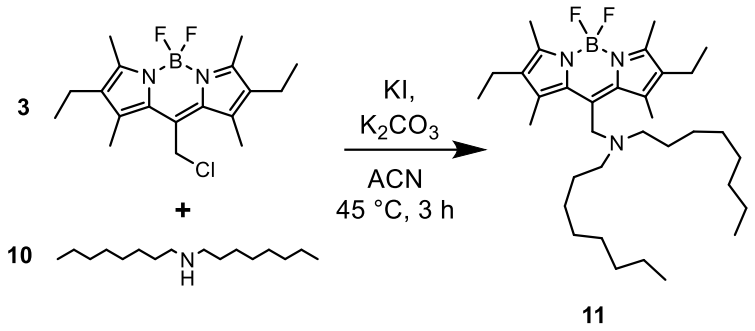

The control BODIPY ligand **Ctrl-CS3** was synthesized following the same procedure as for the **CS3** ligand.[101] The BODIPY starting material compound **3** (90 mg, 0.255 mmol, 1 eq.), dioctylamine **10** (155 mg, 0.642 mmol, 2.5 eq.), KI (84 mg, 0.506 mmol, 2 eq.) and K_2CO_3 (71 mg, 0.513 mmol, 2 eq.) was weighted into a 25 mL Schlenk tube. Then ACN (1 mL) was added via syringe and the solution was stirred at 45 °C for 3 h under nitrogen atmosphere. The reaction mixture was then concentrated using the vacuum from the Schlenk line and the residue was re-dissolved in DCM (50 mL) and washed with water twice. The organic phase was dried over Na_2SO_4, concentrated to dryness, and purified by column chromatography (silica gel, 100% EA). The product **11** was a dark red oil. (25 mg, 18% yield)

^{1}H NMR ($CDCl_3$, 400 MHz): δ 3.85 (s, 2H), 2.49 (t, 4H, J = 7.3), 2.43 (s, 6H), 2.34 (s, 6H), 2.32 (q, 4H, J = 7.50), 1.37-1.26 (m, 4H), 1.23-1.03 (m, 20H), 0.97 (t, 6H, J = 7.50), 0.80 (t, 6H, J = 7.0).

Synthesis of *N*-((2,8-diethyl-5,5-dimethoxy-1,3,7,9-tetramethyl-5H-4l4,5l4-dipyrrolo[1,2-c:2',1'-f][1,3,2]diazaborinin-10-yl)methyl)-*N*-octyloctan-1-amine (Ctrl-CS3)

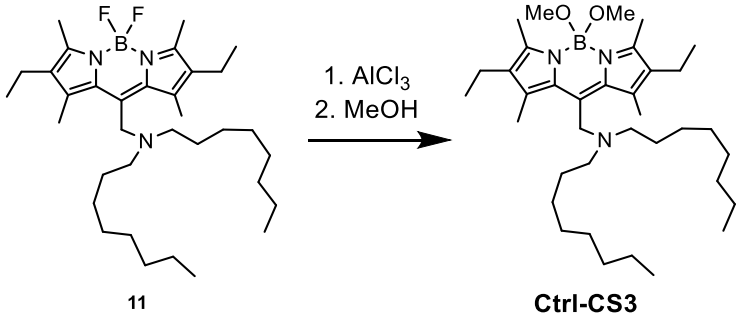

The methoxylated form of **Ctrl-CS3** ligand was synthesized following the same procedure as previously mentioned.[101] Compound **11** (71 mg, 0.122 mmol, 1 eq.) was weighted into 5 mL vial. The solid was dissolved in DCM (2 mL) and $AlCl_3$ (80 mg, 0.608 mmol, 5 eq.) was

added to it. After the addition of $AlCl_3$ the purple solution changed to a more bluish colour. Then the mixture was sonicated at room temperature for 6 min and then MeOH (1 mL) was added, and the reaction mixture was stirred for an additional 6 min. The reaction was then diluted with EA (10 mL) washed twice with water and once with brine solution, dried over Na_2SO_4. The pure dark red oily product **Ctrl-CS3** was obtained after flash chromatography (silica gel, 100% EA; 39.3 mg, 55% yield).

^{1}H NMR ($CDCl_3$, 400 MHz): δ 3.97 (s, 2H), 2.81 (s, 6H), 2.60 (t, 4H, J = 7.36), 2.51 (s, 6H), 2.45 (s, 6H), 2,42 (q, 4H, J = 7.6), 1.53-1.45 (m, 4H), 1.34–1.16 (m, 20H), 1.06 (t, 6H, J = 7.5), 0.89 (t, 6H, J = 6.8).

ESI-MS: *m/z* calcd. for $C_{36}H_{64}BN_3O_2$: 581.51; found: 580.50 [M-H].

Synthesis of 1,5-bis(*p*-tolylsulfonyloxy)-3-phenyl-3-azapentane (14)

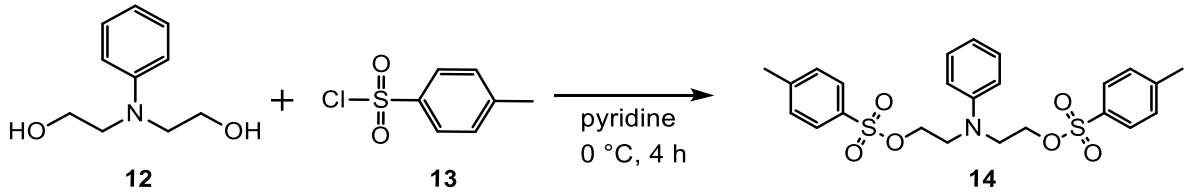

Compound **14** was synthesized following an already existing procedure from the literature.[112] *N*-Phenyldiethanolamine **12** (2 g, 11.04 mmol, 1 eq.) was ground to a rough powder with a mortar and pestle and added to 20 mL pyridine. After the compound was completely dissolved the solution mixture was cooled down to 0 °C and 4-toluenesulfonyl chloride **13** (6.4 g, 33.57 mmol, 3 eq.) was added. Then the reaction was put under a nitrogen atmosphere and stirred at 0 °C for 5 h. Following that, water was added to the reaction mixture and an extraction was carried out with DCM. The organic layer was dried over Na_2SO_4 and the DCM and partially pyridine was removed on a rotary evaporator under reduced pressure. The crude product was purified by a recrystallization step using petroleum ether (60-80 °C). The clean product crystals formed after putting the mixture for 24 h at -18 °C. The crystals **14** were collected by filtration, washed with petroleum ether and dried on air (5.1 g, 94% yield).

^{1}H NMR ($CDCl_3$, 400 MHz): δ 7.74 (d, 4H, J = 8.3), 7.30 (d, 4H, J = 8.3), 7.16 (dd, 2H, *J* = 8.9, 7.3), 6.73 (tt, 1H, J=7.3, 1.0), 6.46 (d, 2H, J = 8.0), 4.11 (t, 4H, J = 6.1), 3.58 (t, 4H, J = 6.1), 2.45 (s, 6H).

^{13}C NMR ($CDCl_3$, 400 MHz): 145.7, 145.0, 132.6, 129.9, 129.5, 127.9, 117.7, 112.1, 66.6, 50.2, 21.7.

Synthesis of 6-phenyl-3,9-dithia-6-azaundecane (15a)

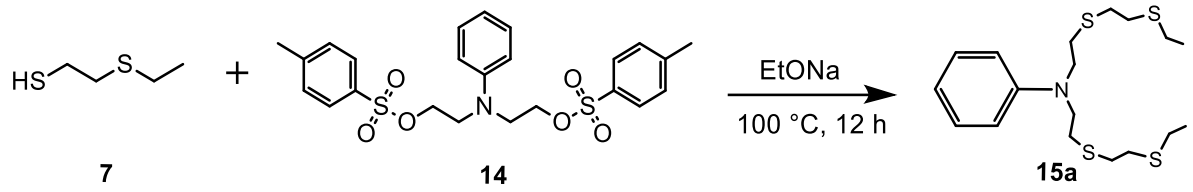

7 14 15a

Compound **15a** was synthesized following an already existing procedure from the literature.[112] Sodium (0.21 g, 9.13 mmol, 2.2 eq.) was dissolved in dry EtOH (50 ml) under a nitrogen atmosphere. Then ethanethiol **7** (1.0 g, 8.18 mmol, 2 eq.) was added to the solution mixture and stirred at room temperature for 1 h. After that the reaction was heated up to reflux and 1,5-bis(*p*-tolylsulfonyloxy)-3-phenyl-3-azapentane **14** (2.0 g, 4.08 mmol, 1 eq.) was added to the hot solution and the solution was kept stirring overnight. After that, the solution colour changed from yellow to red. The reaction solvent was evaporated on a rotary evaporator under reduced pressure and then an extraction was carried out with water (40 ml) and $CHCl_3$ (3×40 ml). The organic phase was dried over Na_2SO_4 and after removing the solvent the product was obtained as an orange-coloured oil **15a**. (1.5 g, 94% yield)

^{1}H NMR ($CDCl_3$, 400 MHz): δ 7.26 (t, 2H, J = 7.2), 6.75 (tt, 1H, J = 7.2, 1.1), 6.69 (d, 2H, J = 7.9), 3.58 (t, 4H, J = 7.5), 2.83-2.73 (m, 12H), 2.59 (q, 4H, J = 7.4), 1.29 (t, 6H, J = 7.4).

^{13}C NMR ($CDCl_3$, 400 MHz): δ 146.6, 129.6, 116.9, 111.9, 51.7, 32.5, 31.9, 29.4, 26.1, 14.9.

Synthesis of 4-(bis(2-((2-(ethylthio)ethyl)thio)ethyl)amino)benzaldehyde (16a)

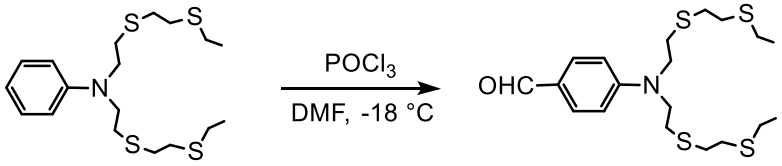

15a 16a

Compound **16a** was synthesized following an already existing procedure from the literature.[112] Dimethylformamide (4 mL) was cooled down under nitrogen atmosphere to -20 °C using acetone and dry ice. Then phosphorus oxychloride (1.96 mL, 3.08 g, 22.4 mmol, 7.5 eq.) was slowly added to the solvent. After 20 min stirring at this low temperature the solution turned white because of the formation small crystals of the frozen salt. 6-Phenyl-3,9-dithia-6-azaundecane **15a** (1.18 g, 3.0 mmol, 1 eq.) was dissolved in DMF (2 mL) and added very slowly over the course of 1 h with an automated syringe system to the reaction solution

while maintaining the temperature below -20 °C. When the addition of the compound was finished, the reaction solution has changed from white to a dark greenish colour. The reaction solution was heated to 70-80 °C for 3 h and the progression of the reaction was monitored by taking small samples and performing TLCs (*n*-hexane:EA = 2:1). When the reaction was completed the mixture was poured on ice, neutralized to pH 7-8 using K_2CO_3 and extracted with DCM (3×10 ml). The organic solvent was dried over Na_2SO_4 and the solvent was removed on a rotary evaporator under reduced pressure. Then a silica column purification was carried out using an eluting gradient from 0-20% EA in *n*-hexane. (0.44 g, 35% yield)

^{1}H NMR ($CDCl_3$, 400 MHz): δ 9.78 (s, 1H) 7.78 (d, 2H, J = 8.9), 6.73 (d, 2H, J = 8.9), 3.68 (t, 4H, J = 7.7), 2.86-2.74 (m, 12H), 2.60 (q, 4H, J = 7.4), 1.29 (t, 6H, J = 7.4).

^{13}C NMR ($CDCl_3$, 400 MHz): δ 189.4, 146.2, 129.5, 116.8, 111.0, 52.1, 32.6, 31.9, 29.1, 26.2, 14.8.

Synthesis of 4-(dioctylamino)benzaldehyde (16b)

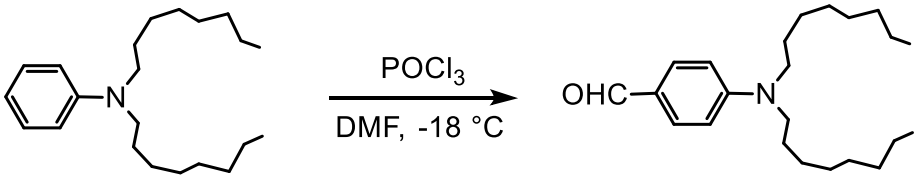

15b **16b**

Compound **16b** was synthesized following an already existing procedure from the literature.[112,137] The synthesis of compound **16b** was following the exact same procedure as for compound **16a** with the only difference of using *N,N*-dioctylaniline **15b** (1.17 g, 3.7 mmol, 1 eq.) as starting material obtaining product **16b** (0.7 g, 55% yield).

^{1}H NMR ($CDCl_3$, 400 MHz): δ 9.74 (s, 1H), 7.74 (d, 2H, J = 9.1), 6.74 (d, 2H, J = 9.1), 3.36 (t, 4H, J = 7.8), 1.68-1.60 (br, 4H), 1.38-1.27 (br, 20H), 0.91 (t, 6H, J = 7.0),

^{13}C NMR ($CDCl_3$, 400 MHz): δ 190.0, 152.1, 132.2, 124.3, 111.5, 51.5, 31.8, 29.4, 29.3, 27.2, 27.0, 22.7, 14.1.

Synthesis of *tert*-butyl 2-azidoacetate (22)

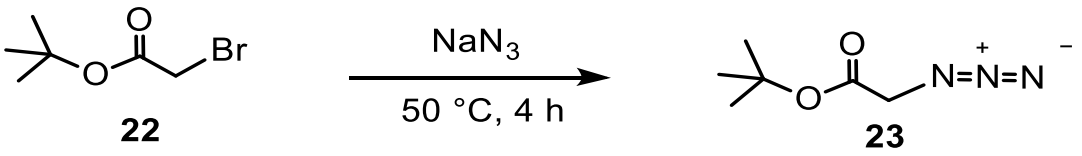

Compound **23** was synthesized following an already existing procedure from the literature.[135] *tert*-Butyl 2-bromoacetate **22** (0.28 mL, 0.37 g, 1.9 mmol, 1 eq.) and sodium azide (0.2 g, 3.1 mmol, 1.6 eq.) was mixed in acetone (1.2 mL) and water (0.8 mL). Then the reaction mixture was refluxed at 50 °C overnight. The mixture was cooled to room temperature and the remaining acetone was removed by gently blowing compressed air into the flask. The product with the remaining water was then extracted with diethyl ether. The organic phase was washed with brine solution and water and then it was dried over Na_2SO_4. The diethyl ether was again removed by blowing compressed air and the product was used without further purification. (0.29 g, 97% yield)

^{1}H NMR ($CDCl_3$, 400 MHz): δ 3.77 (s, 2H), 1.50 (s, 9H).

^{13}C NMR ($CDCl_3$, 400 MHz): δ 167.3, 82.9, 31.0, 27.7.

IR: Azide band (2105 cm^{-1}), CO band (1740 cm^{-1})

Synthesis of allyl 4-(4-(5-formylfuran-2-yl)- butyric acid allyl ester (21)

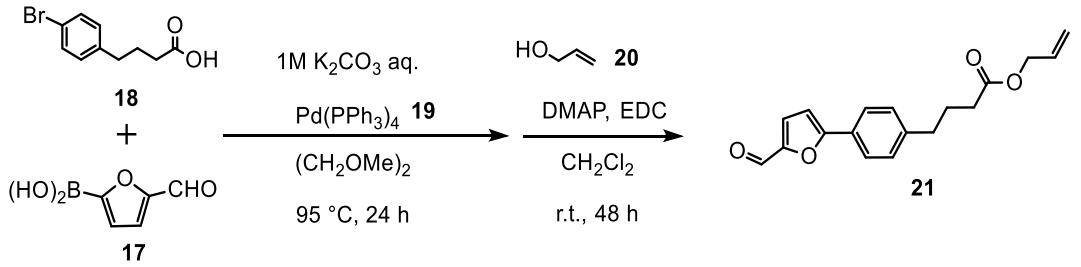

Compound **21** was synthesized following an already existing procedure from the literature.[135] Potassium carbonate (11.04 g, 79.9 mmol, 2.35 eq.) was dissolved in water (80 mL) and was degassed by purging it with nitrogen for 2 h. 4-(4-Bromo-phenyl)-butyric acid **18** (8.72 g, 35.9 mmol, 1.06 eq.) and 5-formyl-2-furanboronic acid **17** (4.79 g, 34.2 mmol, 1 eq.) were dissolved in 1,2-dimethoxyethane (150 mL). The reaction solution was kept under nitrogen and was degassed by repeatedly freezing the solution with liquid nitrogen and slowly thawing it under high vacuum. After that, the aqueous degassed potassium carbonate solution was added to the mixture via dropping funnel. The solution was heated up to 95 °C and the tetrakis(triphenylphosphine)palladium(0) catalyst **19** (200 mg, 0.173 mmol) was added. The

reaction was stopped after 24 h by letting the reaction cool down to room temperature and filtering it through a celite pad. Most of the filtered solution was evaporated and then aqueous HCl solution (1 M) was slowly added to the remaining solution at 0 °C to acidify the mixture to pH 2. During this process, a solid sticky slurry was formed which was filtered washed with water and dried on the freeze dryer by repeatedly freezing it with liquid nitrogen. The resulting crude compound (4-[4-(5-formyl-furan-2-yl)-phenyl]-butyric acid) was dissolved in DCM, cooled down to 0 °C, and allyl alcohol **20** (2.35 mL, 2.01 g, 34.6 mmol, 1 eq.), DMAP (0.55 g, 4.5 mmol, 0.13 eq.) and EDC (5.81 g, 37.4 mmol, 1.1 eq.) was added to the mixture. Then the reaction was stirred for 2 days at room temperature. Thereafter, water was added to the reaction mixture to stop the reaction, followed by an extraction with DCM. The organic phase was washed with brine solution and water, was dried over Na_2SO_4, and evaporated with a rotary evaporator under reduced pressure. The residue was purified using silica flash chromatography (*n*-hexane and 0-20% EA). (1.65 g, 16% yield)

^{1}H NMR ($CDCl_3$, 400 MHz): δ 9.65 (s, 1H), 7.77 (d, 2H, J = 8.3), 7.34 (d, 1H, J = 3.7), 7.28 (d, 2H, J = 8.3), 6.83 (d, 1H, J = 3.7), 5.99-5.89 (tdd, 1H, J = 5.8, 10.4, 17.2), 5.34 (d, 1H, J= 17.2), 5.26 (d, 1H, J = 10.4), 4.60 (d, 2H, J = 5.8), 2.72 (t, 2H, J = 7.4), 2.40 (t, 2H, J = 7.4), 2.01 (tt, 2H, J = 7.2, 7.5).

^{13}C NMR ($CDCl_3$, 400 MHz): δ 177.2, 173.0, 159.7, 151.9, 143.4, 132.2, 129.1, 127.0, 125.5, 118.3, 107.3, 65.1, 34.9, 33.5, 31.0, 26.3.

HR-MS: *m/z* calcd. for $C_{18}H_{18}O_4$: 299.1283, found: 299.1283 $[M+H]^+$.

Synthesis of *tert*-butyl 2-(4-(4-(allyloxy)-4-oxobutyl)phenyl)-4H-furo[3,2-b]pyrrole-5-carboxylate (25)

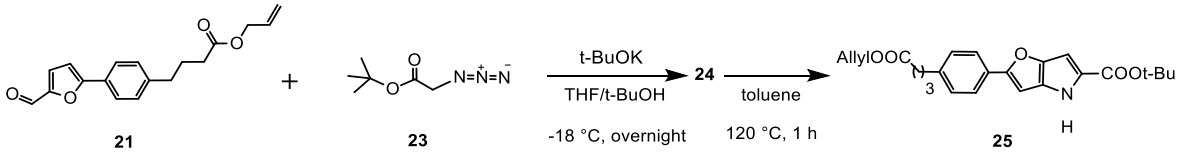

Compound **25** was synthesized following an already existing procedure from the literature.[135] *tert*-Butanol (8.7 mL) was used to dissolve potassium *tert*-butoxide (1.1 g, 9.8 mmol, 2 eq.) and the solution was added dropwise into the mixture and 4-[4-(5-formyl-furan-2-yl)-phenyl]-butyric acid allyl ester **21** (1.45 g, 4.9 mmol, 1 eq.) and azido acetic acid *tert*-butyl ester **23** (2.5 g, 15.9 mmol, 3.2 eq.) were dissolved in THF (100 mL) and was stirred and cooled down to -18 °C. With an automated syringe the *tert*-butanol potassium *tert*-butoxide solution was slowly added to the THF reaction mixture. The reaction mixture was

slowly warmed up to room temperature and was stirred for 14 h. An excess of saturated aqueous NH_4Cl solution (50 ml) was added to the reaction and THF was removed by evaporation on a rotary evaporator under reduced pressure. The remaining aqueous solution was extracted with ethyl acetate, washed with brine, and water and the organic phase was dried over Na_2SO_4. The residue was further purified by flash chromatography on silica gel (eluent: *n*-hexane/EA = 100/0 to 80/20) which resulted in a still crude mixture of products. This mixture was then dissolved in toluene (60 mL) and heated up to 120 °C for 1 h. The reaction colour changed from yellow to dark orange. After the ring-closing reaction of the fused pyrrole ring was confirmed by TLC the reaction was stopped by letting it cool down. Then the solvent was evaporated under vacuum (~10-20 mbar) with a water temperature of 30 °C. The residue was again purified with silica flash chromatography (eluent: *n*-hexane/EA = 90/10 to 80/20) which resulted in the clean final product 2-[4-(3-allyloxycarbonyl-propyl)-phenyl]-4H-furo[3,2-b]-pyrrole-5-carboxylic acid *tert*-butyl ester **25** (0.76 g, 38% yield)

^{1}H NMR ($CDCl_3$, 400 MHz): δ 8.75 (s, 1H), 7.68 (d, 2H, J = 8.1), 7.24 (d, 2H, J = 8.1), 6.76 (s, 1H), 6.69 (s, 1H), 5.99-5.90 (tdd, 1H, J = 5.7, 10.5, 17.1), 5.34 (d, 1H, J = 17.1), 5.26 (d, 1H, J = 10.5), 4.61 (d, 2H, J = 5.7), 2.71 (t, 2H, J = 7.5), 2.40 (t, 2H, J = 7.5), 2.01 (qui, 2H, J = 7.5), 1.62 (s, 9H).

^{13}C NMR ($CDCl_3$, 400 MHz): δ 173.1, 161.4, 159.7, 147.7, 141.4, 132.2, 129.8, 129.2, 128.9, 125.3, 124.1, 118.3, 96.5, 93.1, 81.0, 65.1, 34.9, 33.5, 28.5, 26.4.

Synthesis of divinyl 4,4'-((11-(4-(bis(2-((2-(ethylthio)ethyl)thio)ethyl)amino)phenyl)-5,5-difluoro-5H-4l4,5l4-furo[2',3':4,5]pyrrolo[1,2-c]furo[2',3':4,5]pyrrolo[2,1-f][1,3,2]diazaborinine-2,8-diyl)bis(4,1-phenylene))dibutyrate (FLCS1)

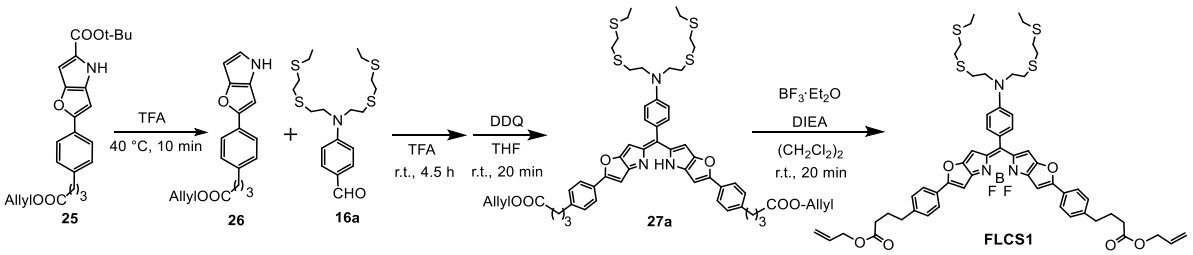

Compound **25** (500 mg, 1.22 mmol, 2 eq.) was dissolved in acetone (5 ml) and transferred into a Schlenk flask. The solvent was carefully evaporated on the vacuum of a Schlenk line. After that, **25** was redissolved in trifluoroacetic acid (5 mL) and the mixture was heated up under nitrogen atmosphere to 40 °C. After 10 min when the starting material was consumed, the mixture containing compound **26** was cooled down to room temperature and compound

16a (0.254 g, 0.61 mmol, 1 eq.) was added to the reaction mixture. After 15 min the solvent was evaporated on the Schlenk line, and the residue was redissolved in THF (8 mL). DDQ (276 mg, 1,22 mmol, 2 eq.) was separately dissolved in THF (1 mL) and slowly added with a syringe through a septum into the Schlenk flask. The reaction was stopped after 20 min by adding water and the crude products was extracted with DCM. The organic layer was washed with brine and water, dried over Na_2SO_4, and evaporated. The mixture was partially purified via flash column chromatography (eluent: *n*-hexane/$CHCl_3$ = 40/60; solid phase: alumina) to remove the remaining DDQ from the reaction mixture. The remaining product mixture containing crude compound **27a** was dissolved in 1,2-dichloroethane under nitrogen, DIEA (0.83 mL, 0.62 g, 4.8 mmol, 7.8 eq.) was added and the reaction mixture was heated-up to 60 °C. Then $BF_3{\cdot}Et_2O$ (0.83 mL, 0.95 g, 6.7 mmol, 11 eq.) was added which led to an instant colour change from green to very dark blue. After 25 min toluene was added to the reaction mixture and an extraction was carried out. The organic phase was again washed with brine and water and the solvent was evaporated on a rotary evaporator under reduced pressure. The final purification steps was by flash chromatography on silica gel (eluent: *n*-hexane/EA = 100/00 to 80/20) followed by a preparative thin layer chromatography (eluent: *n*-hexane/EA = 66/33) for which both of the silica used was first neutralized with 0.1% TEA in *n*-hexane. The crude product was dissolved in acetone and deposited on a preparative TLC plate with a pipette. The product band was scratched off from the TLC and extracted with MeOH. The solvent was then removed under reduced pressure to yield the pure **FLCS1** product, which is a dark blue compound (21.7 mg, 3.3 % yield). A sample of the compound was used to prepare a 10 mM stock solution in DMSO and stored at -18 °C. For all further spectroscopic measurements, this sample was diluted to 1 mM and 20 µM which served as a stock solution for the optical experiments and for the cell experiments respectively.

^{1}H NMR ($CDCl_3$, 400 MHz): δ 7.77 (d, 4H, J = 8.3), 7.53 (d, 2H, J = 8.8), 7.30 (d, 4H, J = 8.2), 6.99 (s, 2H), 6.79 (d, 2H, J = 8.9), 6.46 (s, 2H), 5.98-5.91 (tdd, 2H, J = 5.8, 10.5, 17.1), 5.35 (d, 2H, J = 16.9), 5.27 (d, 2H, J = 10.4), 4.61 (d, 4H, J = 5.7), 3.70 (t, 4H, J = 7.5), 2.91-2.78 (m, 12H), 2.74 (t, 4H, J = 7.6), 2.63 (q, 4H, 5.7), 2.41 (t, 4H, J = 7.4), 2.03 (qui, 4H, J = 7.4), 1.31 (t, 6H, J = 7.4).

^{13}C NMR ($CDCl_3$, 400 MHz): δ 172.3, 167.1, 153.5, 148.6, 148.2, 143.8, 139.2, 132.8, 132.2, 129.2, 127.9, 125.5, 122.8, 118.4, 111.2, 103.5, 95.2, 65.1, 51.6, 35.1, 33.5, 32.6, 31.9, 29.5, 29.3, 26.3. 26.2, 14.9.

MALDI: *m/z* calcd. for $C_{57}H_{64}BF_2N_3O_6S_4$: 1064.20 found: 1064.40 [M].

Synthesis of divinyl 4,4'-((11-(4-(dioctylamino)phenyl)-5,5-difluoro-5H-4l4,5l4-furo[2',3':4,5]pyrrolo[1,2-c]furo[2',3':4,5]pyrrolo[2,1-f][1,3,2]diazaborinine-2,8-diyl)bis(4,1-phenylene))dibutyrate (Ctrl-FLCS1)

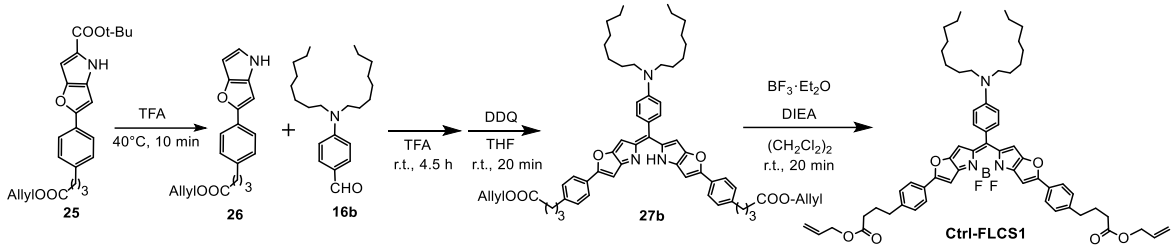

Ctrl-FLCS1 was synthesized following the same procedure as **FLCS1** by just exchanging the bridging ligand **16a** for **16b** (0.21g, 0.61 mmol, 1 eq.) yielding the final compound after column chromatography and preparative TLC purification (4.8 mg, 0.8% yield).

^{1}H NMR ($CDCl_3$, 400 MHz): δ 7.76 (d, 4H, J = 8.2), 7.51 (d, 2H, J = 8.7), 7.29 (d, 4H, J = 8.6), 6.99 (s, 2H), 6.74 (d, 2H, J = 8.7), 6.52 (s, 2H), 6.01-5.88 (m, 2H), 5.34 (d, 2H, J = 17.0), 5.27 (d, 2H, J = 10.4), 4.61 (d, 4H, J = 5.7), 3.39 (t, 4H, J = 7.9), 2.73 (t, 4H, J = 7.6), 2.41 (t, 4H, J = 7.4), 2.03 (qui, 4H, J = 7.5), 1.43-1.25 (br, 24H), 0.90 (t, 6H, J = 7.2).

^{13}C NMR ($CDCl_3$, 400 MHz): δ 173.4, 167.1, 153.8, 150.1, 148.4, 143.9, 139.4, 133.2, 132.6, 129.6, 125.8, 121.5, 118.7, 111.3, 104.1, 95.6, 65.5, 51.5, 35.5, 33.9, 32.2, 31.3, 30.1, 29.9, 29.7, 27.7, 27.6, 26.6, 23.1, 14.5.

MALDI: *m/z* calcd. For $C_{61}H_{72}BF_2N_3O_6$: 992.07 found: 992 [M].

1.4.2. General protocols and instrumentation

UV/vis spectra were recorded in a Perkin-Elmer spectrometer. Emission spectra were obtained on Varian Cary-Eclipse or Perkin-Elmer fluorescence spectrometers. The raw data was smoothed with a factor 15, the slit width was set to 5 nm and the PEM was 600 volts. Data were recorded on-line and analysed by Excel and Prism software. Time-resolved fluorescence decay traces were obtained using a TCSPC DeltaFlex Lifetime System using the 635-nm NanoLED-02B R excitation source (HORIBA Scientific Ltd, FWHM <200 ps). The detection system consisted of a PPD Series Picosecond Photon Detection Modules (HORIBA Scientific Ltd). A long-pass filter (645 nm long pass) was used in the detection channel to avoid light scattering for fluorescence decays. Signal intensity was at least 10,000 counts in the peak maximum. A neutral density filter was used for the instrument response function (IRF) measurements using a Ludox solution, detecting emission at the excitation wavelength. The TCSPC, absorption and emission measurements were performed in 1 cm × 1 cm quartz cuvettes with septum (3.5 mL volume, Starna, Atascadero, CA) or 0.35 cm × 1 cm quartz

cuvettes (Cole-Parmer). The titration experiments were all performed under N_2 atmosphere by supplying positive nitrogen pressure to the cuvette with a nitrogen balloon. Because of the delayed fluorescence increase of the probe, the sample was stirred with a small stirrer bar in the dark before measuring each titration point by TCSPC and fluorescence spectrometer. Fluorescence quantum yield for **FLCS1** was determined by reference to Alexa 647 in water as a standard (Φ_f = 0.33) and to rhodamine 6G in ethanol (Φ = 0.95) for **CS3**.

Preparation of metal ion solutions for spectroscopic experiments

For the spectroscopic fluorescence and absorbance experiments the MeOH was degassed by purging with N_2 for 2 h before the experiment to avoid oxidation of the copper(I) salt. During the experiment the solution was kept under N_2 atmosphere using a nitrogen balloon. 10 mM **FLCS1** stock solution was further diluted to 1 mM in DMSO. 37.3 mg of the copper(I) metal tetrakis(acetonitrile)copper(I) hexafluorophosphate $[Cu(MeCN)_4][PF_6]$ was dissolved in 5 mL degassed MeOH resulting in a 20 mM copper(I) stock solution. This stock was then further diluted to 1 mM and 0.1 mM for the titration experiments. For the selectivity experiments with the different competing metals, 100 mM stock solutions of $CaCl_2$, NaCl, $MgCl_2$, $ZnCl_2$ and 10 mM stock solutions of KCl, $CoCl_2$, $FeSO_4$, $MnBr_2$, $Ni(OAc)_2$, and $CuSO_4$ in H_2O were prepared and 20 µl of each was added to a 1 mL methanolic solution of **FLCS1** (1 µM).

Time-correlated single photon counting

Traces from the TCSPC were fitted by iterative reconvolution to the equation $I(t) = I_0(\alpha_1 e^{-\frac{t}{\tau_1}} + \alpha_2 e^{-\frac{t}{\tau_2}})$ where α_1 and α_2 are variables (in %), with α_1+α_2 normalized to unity. The fractional contribution to the steady-state emission is calculated from the equation $f_i = \alpha_i \tau_i / \sum_j \alpha_j \tau_j$. The τ_1 and τ_2 were fixed to 0.39 ns and 3.08 ns based on the global fit over the whole titration data. To account for the differences in the emission wavelength between the IRF and decay, a prompt shift was included in the fitting. The goodness of fit was judged via a weighted residuals plot by consideration of the deviations from the model.

Preparation and staining of cell cultures

SH-SY5Y, N27 and HEK297 cells were cultured in Dulbecco's Modified Eagle Medium (DMEM, Invitrogen, Carlsbad, CA) supplemented with 10% Fetal Bovine Serum (FBS, Invitrogen), glutamine (2 mM), and penicillin/streptomycin (50 µg/mL, Invitrogen). All cells were grown in a 5% CO_2 incubator at 37 °C. The cells were plated and grown on 8-well

chamber slides (LabTekII Chamber Coverglass) in 250 µL of culture media at a plating density of 25,000 cells per well and allowed to grow for 24 h. Next the media was changed to media containing lipofectamine 2000 (2 µL/mL) and **FLCS1** (60 nM). The cells were incubated with the dye for 24 h. Prior to imaging the cell media was changed back to DMEM with 10% FBS (250 µL/well). The lysosome stain Lysotracker Green (λ_{ex} = 500 nm; λ_{em} = 510-550 nm; Invitrogen, ThermoFisher) was incubated with cells at 50 nM for 5 min prior to 3 washing cycles in DMEM and subsequent image acquisition on a confocal microscope (Leica SP5) with 40x or/and 63x magnification 1.4 NA oil objective. For FLIM imaging the coverslide was mounted in a microscope chamber heated by a circulating thermostat (Lauda GmbH, E200) with feedback control of temperature and 0.2 C precision. Cells were measured by FLIM, as described below, in the 'before' and 'after' treatment states.

Fluorescence microscopy imaging

For the cell experiments several different microscope setups were used. For the colocalization studies a widefield microscope (Axio Observer 7, Carl Zeiss) with a Colibri 7 LED illumination (Carl Zeiss) and a 63x or 40x NA 1.4 was used with a Plan-Apochromat objective. The **CS3** probe was excited at 530 nm and fluorescence was collected at 560-600 nm. The Alexa 647 dye and **FLCS1** was excited at 630 nm and fluorescence was collected at 650-700 nm. Lysotracker Green was excited at 480 nm and fluorescence was collected at 500-520 nm. The single channel images were performed on two TE2000U inverted optical fluorescent microscope (Nikon). One is equipped with a Coolview 1000 EMCCD camera (Photonic Sciences) and a 532 nm DPSS laser. The other is equipped with an ORCA FLASH 4.0 sCMOS camera (Hamamatsu) and a 633 nm He-Ne laser (Thorlabs). The intensity studies were imaged on a Leica SP5 II confocal microscope with an APD detector unit.

Alpha-synuclein, Lysotracker Green, CS3 and FLCS1 colocalization experiment

HEK293, N27, SH-SY5Y cell lines and primary hippocampal neurons were treated with a 500 nM labelled alpha-synuclein for 24 h in DMEM. The **CS3** stock solution (2 mM in DMSO) and the probe was loaded just before the measurement (2 µM, 10 min in PBS). Lysotracker green (50 nM) was incubated for 20 min before measuring. For both dyes the DMEM was removed, and the cells were washed with PBS twice to remove the excess dye and labelled AS. The cells were acquired using z-stacks with a 0.3 µm slice thickness. **FLCS1**

(1 μM) was either delivered in a 1:1 ration EtOH:PBS just before measuring or by incubating the cells with 0.2% lipofectamine at a dye concentration of 60 nM for 24 h.

Photobleaching experiment with CS3 and FLCS1

SH-SY5Y cells were incubated with **FLCS1** (60 nM) and 0.2% lipofectamine in DMEM with 10% FBS at 37 °C for 24 h. After washing the cells twice with PBS the cells were treated with **CS3** (2 μM) in PBS for 15 min and washed again before imaging the cells with the confocal microscope. z-stacks of the cells were recorded over time at 40x magnification and 1% laser power for both excitation wavelength (**CS3** λ_{ex} = 520 nm and **FLCS1** λ_{ex} = 620 nm). The emission was collected for at λ_{em} = 530-600 nm for **CS3** and λ_{em} = 630-700 nm for **FLCS1**.

pH/viscosity/H_2O-effect experiments with TCSPC

The TCSPC pH measurements were carried out in a methanolic solution of **FLCS1** (1 μM). The pH was calibrated using diluted HCl and NaOH solutions. For the viscosity experiment the probe was dissolved in different ratios of MeOH and glycerine and for the water-effect on the lifetime the solvent ratios were altered between water and MeOH. All the measurements were carried out with excess copper(I) (3 μM).

AS transfection and staining of SH-SY5Y

The plasmid for the transfection of SH-SY5Y cells was provided by Prof. Magdalena Sastre from Imperial College London.

The cells were plated with a seeding density of 25,000 cells per well and the 4 μg of the DNA plasmid for AS overexpression was mixed with 8 μL Turbofectamin in 400 μL Opti-MEM starvation media. After 20 min incubation period in an Eppendorf tube 50 μL of this mixture was added with 500 μL Opti-MEM starvation media in the well. After 24 h incubation the media was changed back to DMEM with 10 % FBS and the cells were continued to grow for another day. After this treatment the cells were fixed with 4% PFA in PBS for 20 min, treated with 0.2% Triton X and 1% BSA in PBS for 30 min and then a primary antibody (ratio 1:1000) in PBS was used on the cells for another 60 min, followed by labelling with the alpha-synuclein selective secondary antibody (ratio 1:500) with Alexa 647 labelling for 60 min. After these steps the cells were washed with PBS and the other stains (**CS3** and Hoechst33342) were employed with the usual staining procedure.

Lysate experiment

The cell lysate was provided by postdoc student Maria Maneiro Rey from the group of Prof. Tate from Imperial College London.

Confluent SH-SY5Y cells were detached from the flask using trypsin transferred into a falcon tube with media and centrifuged to collect a cell pellet. After removing the cell media these cells were treated with a RIPA lysis buffer containing protein inhibitor and benzonase. The cell content concentration was determined with UV/vis measurements.

Lipid droplets staining

This experiment was carried out by Reeba Jacob a postdoc student in the group of Prof. Philipp Selenko from the Weizmann Institute of Science in Israel.

A2780 and SH-SY5Y cells were incubated with **CS3** (2 μM) dye for 10 min at 37 °C, followed by incubation of BODIPY^{TM} (1 μM) again for 10 min which is a dye for selective lipid droplet staining. Then, LDs were isolated from A2780 cells and incubated with **CS3** (1 μM) dye *in vitro* and the fluorescence was measured with a fluorometer. This sample was then spotted on a coverslip and imaged under confocal microscope which showed **CS3** stained lipid droplets.

Determination of dissociation constant K_d

For the determination the dissociation constant (K_d) a methanolic solution of **FLCS1** (1 μM) containing thiourea (400 μM) as competitive ligand was used to provide a buffered copper(I) after copper(I) addition. To calculate the available copper(I) the stability constants for thiourea binding was used taken from the literature: $\beta_{12} = 2.0 \times 10^{12}$, $\beta_{13} = 2.0 \times 10^{14}$, $\beta_{14} = 3.4 \times 10^{15}$.[147] For this titration the copper(I) stock solution was further diluted to 1 μM to provide the necessary low copper(I) amounts. Excitation was provided at λ_{ex} = 610 nm and collected emission was integrated from λ_{em} = 620 to 750 nm. The binding affinity was calculated following the literature references[101,138] using the Benesi–Hildebrand plot (see Figure 28) with the equation: $(F_{max} - F_{min}) = \Delta F = [copper(I)](F_{max} - F_{min})/(K_d + [copper(I)])$ where F is the observed fluorescence F_{max} is the fluorescence for the **FLCS1**/copper(I) complex, and F_{min} is the fluorescence for the copper(I) free probe. When plotting the 1/△F against 1/[copper(I)] the linear relation equation (Y= A + BX) was used to calculate K_d from B/A.

Bafilomycin A1 treatment experiment

SH-SY5Y cells were grown in DMEM with 10% FBS with added penicillin and streptomycin at 37 °C. The healthy cells were plated on LabTek II coverslides at a seeding density of 20,000 cells per well and let grow for 48 h in an incubator. Then the media was changed to media containing 0.2% lipofectamine and 60 nM **FLCS1** and the cells were incubated for another 24 h. After that the media was changed back to grow media and the after a calming period of 1 h the cells were imaged in their "before treatment" state on a Leica SP7 confocal microscope at 630 nm excitation and a laser power of 0.1%. The location of the cells was precisely recorded by measuring the coordinate distances of a set reference point of a cover glass impurity at the well corner. Then the cells were treated with bafilomycins A1 (30 nM) in DMEM and was incubated for 24 h. For the second time point the same cells were searched based on the recorded coordinates and measured with the same microscopy settings as before. For the control comparisons the cells were treated with DMSO (0.01%) and also incubated for 24 h. After the incubation time images were taken with the same settings as for the bafilomycin A1 treated cells.

Primary Hippocampal Neurons

The primary hippocampal neurons were provided by doctorate student Nicola Davis from the group of Magdalena Sastre and postdoc student Darya Kiryushko from Imperial College London.

Organotypic cell cultures

The organotypic cell cultures were provided by doctorate student Nicola Davis from the group of Magdalena Sastre from Imperial College London.

H_2O titration with FLCS1

In a small cuvette 0.5 mL of 1 µM **FLCS1** was prepared. For the titration several aliquots of 20 µL H_2O were added to the cuvette and were thoroughly mixed before measuring. The resulting concentration of H_2O was calculated considering the increased volume of each titration step and the concentration of the dye was volume and dilution corrected.

Copper alteration experiments

SH-SY5Y cells were incubated with **FLCS1** (60 nM) in DMEM with 0.2% lipofectamine and 10% FBS for 24 h. For the test of the cells with DTDP (100 µM) and clioquinol with

copper(II) (800 µM/ 400 µM), images were recorded before and during the addition process of DTDP from a PBS stock and a DMSO stock solution over time. The experiments with Cu-GTSM (2.5 µM), BCS (125 µM) and BETA (5 µM), cells were recorded before the treatment and in certain time steps after addition up to 1 h.

pH experiments with fluorescence spectroscopy

For the fluorescence pH measurements **FLCS1** (1 µM) and **CS3** (1 µM) was prepared in EtOH:buffer (60:40, v:v, 20 mM TRIS and 100 mM NaCl, pH 7.4). The pH was calibrated prior mixing using diluted HCl and NaOH. Excitation for spectroscopic emission measurements were provided at λ_{ex} = 610 nm for **FLCS1** and collected emission was integrated from λ_{em} = 615 nm to 750 nm for **FLCS1** and excited at λ_{ex} 520 nm and emission was collected from λ_{em} = 520 nm to 650 nm for **CS3**. For the TCSPC pH experiment a methanolic solution of **FLCS1** or **CS3** (1 µM) without buffer was used to avoid the effects of water on the lifetime of the probe. The pH was calibrated using a diluted HCl solution.

Fixed mouse brain slice imaging

The fixed mouse brain slice was provided from doctorate student Tiffany Chan from James Choi group from Imperial College London.

C57BL/6J mice were transcardially perfused with ice-cold phosphate buffered saline (pH 7.4; 137 mM NaCl, 2.7 mM KCl, 8 mM Na_2HPO_4 and 2 mM KH_2PO_4) with added heparin (10 units/mL), and then fixed with 20 mL ice-cold 10% formalin solution. Brains were extracted and submerged in 10 mL 10% formalin solution at 4 °C, and then cryoprotected by immersing in 15% sucrose for 6 h followed by 30% sucrose overnight. Samples were cryosectioned into 20 µm sections and allowed to air-dry prior to staining.

Alpha-synuclein labelling

The fluorescently labelled alpha-synuclein probe mutated at D122C was produced and labelled in collaborator with Giuliana Fusco (postdoc student in Prof. Dobson's Group at Cambridge University).

After purification by column (Sephadex G25; Amersham Biosciences) a protein labelling was performed with amino-reactive fluorescent dye Alexa Fluor-647-O-succinimidylester.

To achieve this 500 mL PBS was prepared and stirred for 20 min. Then 10 mL Sephadex G25 resin was swelled up with 40 mL of water, the slurry was transferred into a column and the column was rinsed with 50 mL water followed by 50 mL of degassed PBS. The concentrated

AS protein was mixed with 10 mM dithiothreitol (DTT) which ensured that the proteins were in the monomeric form. The protein was loaded onto the column and flushed with PBS and the protein was collected in several Eppendorf tubes. The concentration of the individual Eppendorf tubes was determined via UV/vis spectrometry (ε = 5600 $M^{-1}cm^{-1}$ at 275 nm). 1 mg of Alexa 647 dye was dissolved in 100 µL DMSO. The protein in the Eppendorf tubes was mixed with an excess (4 eq.) of the dye and incubated on a roller in a cold room overnight. The following day a new PBS buffer solution was prepared and degassed. Several new columns were prepared using the same procedure as the day before (10 mL Sephadex G25 and 40 mL water). The Eppendorf tubes with the proteins were centrifuged for 1 min and a maximum of 2 mL protein was loaded onto each column. PBS was flushed through the column separating the labelled protein (first coloured band) from the free dye (second coloured band). The combined labelled protein fractions were concentrated using a falcon filter (vivaspin 6, 5,000 MW) on a centrifuge (8 min, 4,000 rpm, 4 °C) and the concentration of the protein was determined by UV/vis (Alexa 647, ε = 265,000 M^{-1} cm^{-1}) resulting in 11.6 µM labelled AS solution (10 mL).

Cu-GTSM preparation

The Cu-GTSM was prepared fresh before every use by mixing stock solution of 10 mM GTSM dissolved in DMSO with the same volume of 10 mM $CuCl_2$ dissolved in H_2O. The compound formed instantly after thorough mixing by pipetting the two solutions which could be observed by a colour-change from transparent to dark orange. The compound was then used within a few hours. The 250 µL of DMEM containing the treatment agent (10 µM Cu-GTSM) resulting in a chamber concentration of 5 µM, was added to chambers for 20 min following FLIM measurements of the “after treatment” state.

FLIM imaging experiments

FLIM imaging of **FLCS1** was performed on an inverted confocal laser scanning microscope (Leica, SP5 II) with a 63x (NA 1.4) oil objective and a pulsed diode laser (Becker & Hickl GmbH, λ_{ex} = 630 nm, 20 MHz) as an excitation source. The emission (λ_{em} = 640–750 nm) was collected using a cooled Becker&Hickl HPM100-40 hybrid detector, and TCSPC was performed by a SPC-150 Becker&Hickl module. FLIM images of 512 × 512 pixels were obtained, and the images were analysed in the SPCImage software (Becker&Hickl, Germany) using a biexponential decay model with τ_1 and τ_2 fixed at 0.7 ns and 2.7 ns respectively. The

regions of interests (ROIs) for analysis were manually selected, to coincide with bright fluorescence of the dye. The scatter parameter was kept variable and the shift was fixed to the overall average shift of all ROIs. Appropriate bin sizes were chosen (3 × 3 or 4 × 4 circular bin) to ensure a peak count of at least 100 for accurate fitting of biexponential traces and a sum count threshold of 4,000 was used to exclude dye traces in the cytosol or other not relevant regions. A pseudo-colour scale was assigned to each fluorescence lifetime, amplitude and the goodness of fit χ^2 values (red for small values and blue for large values) to visualise the corresponding maps. The IRF was obtained by measuring the reflection of urea crystals on a glass coverslide. Cellular images were acquired using the same settings, and the acquisition times was ca. 15 s - 30 s (live cells) depending on the brightness of the dye. The decays in the region corresponding to the lysosomes of different cells were selected and analysed by hand (ca. 15 different cells in 7-8 images, to accumulate good statistics). The fitting of the FLIM images was performed in SPCImage software (Becker-Hickl) using the weighted least squares method and reconvolution algorithm for finding the best fit. Goodness of fit was judged by the χ^2 value and randomness of in the residuals plot. Based on the TCSPC experiments the decay models of the fluorescence dye were judged to be a biexponential and were calculated using the following equation: $I(t) = \sum_{i=1}^{n} \alpha_i e^{-t/\tau_i}$ where I is the fluorescence intensity, t is the time, α_i is the amplitude, and τ_i is the fluorescence lifetime of the biexponentially decaying components. The calculation of the mean intensity-weighted fluorescence lifetime was according to the equation: $\tau_{avg} = \frac{\sum \alpha_i \tau_i^2}{\sum \alpha_i \tau_i}$.

CHAPTER II

2.1. Introduction

Biologists have a strong interest and research focus for investigating the complex interactions between different cellular organelles. Central to these investigations are non-invasive techniques which are capable of visualizing dynamic processes with a high spatiotemporal resolution. Microscopy technologies which meet these demands have revealed that intracellular organelles distribute in a highly non-homogeneous dynamic fashion over time and space, and their organization is responding to biochemical and mechanical inputs which are essential in many biological processes. These dynamic processes include nuclear organization and signalling in cell division, differentiation, cell adhesion and migration.[148] Getting a better understanding in the mobility of the dynamic processes and organization of the individual cellular compartments is therefore crucial for understanding living organisms and can help to get a more profound understanding in health and disease at a microscopic level. There have been significant progresses in the development of novel imaging hardware platforms and fluorescent probes which allowed for visualization of biological processes at the level of whole organisms, single cells, and subcellular organelles. Equally important have been the development of software analysis tools that allow the extraction of quantitative data of the dynamic processes examined by microscopy. Specifically, the development of particle tracking software enabled objects to be followed computationally in time-lapse movies and to quantify their dynamics became an essential toolbox for life-cell imaging.[149] The task of

detecting and following individual particles in a time series of 2D or 3D images is referred to as 'single-particle tracking' (SPT).[150]

The technology that fulfils the need for high spatiotemporal resolution in 3D which allows organelle tracking to be performed are point-scanning microscopy technologies such as laser scanning confocal microscopes or electron microscopes. These point-scanning microscopy techniques suffer from an effect called the “eternal triangle of compromise” which states that at a given signal-to-noise ratio (SNR) improving any of the three, i.e. resolution, system sensitivity or imaging speed, comes at the cost of the other two. Therefore, the speed, sample preservation, and SNR of point-scanning systems are difficult to optimize simultaneously. To draw conclusions from multi-dimensional microscopy images the timescale is of great importance to correctly understand cellular processes and movement patterns. Improving the SNR or increasing the dimensionality of the data recording (e.g. 4D (3D+t) acquisitions) on the one hand provides more information of the imaged details, but on the other hand slows down the recording speed making it more difficult to understand those dynamic processes. The image acquisition in z-dimension for 3D tracking over time increases the acquisition time from one time point to the next proportional to the number of layers in the z-dimension. When increasing the image resolution of point-scanning systems, a higher number of acquired pixels is necessary to ensure the correct sampling which in turn increases the image acquisition time and the sample damage proportional to the size of pixel sampling. To analyse dynamic processes in cells all these limiting parameters should be as high as possible. Therefore, finding and developing tools to improve the limitations of point-scanning systems could be transformative and is of great importance. More recently deep learning started being applied for postprocessing of microscopy images which improved some of limitation corners of the “Eternal Triangle of Compromise”.

This chapter focuses on the topic of image enhancement for microscopy which is used to improve the limitation corners of the “Eternal Triangle of Compromise” in relation to monitoring the copper trafficking of lysosomes in SH-SY5Y cells. To put this research in context, a detailed background section is provided which covers some technical background of key technologies that made microscopy of subcellular organelles possible, and it points out the limitations and how new inventions such as deep learning are pushing the boundaries of these limitations. Furthermore, it provides an introduction into deep learning, its terminology, explains the importance of assessment metrics for evaluating image enhancement algorithms

and finally describes the neural networks that are implemented and used in this research project.

2.2. Theoretical Background

2.2.1. Confocal Microscopy

In 1961 the American computer scientist Marvin Minsky developed a microscopy technique which solved some of the challenges of widefield microscopes. By introducing a pinhole system in the detection and excitation path it became possible to just illuminate a small section of the whole specimen by aligning the excitation volume, the detection volume, and the detector. His new approach made it possible to remove the out of focus contributions to the image. This confocality of excitation and detection path gave the new microscopy technique the name “Confocal Microscope”.[151]

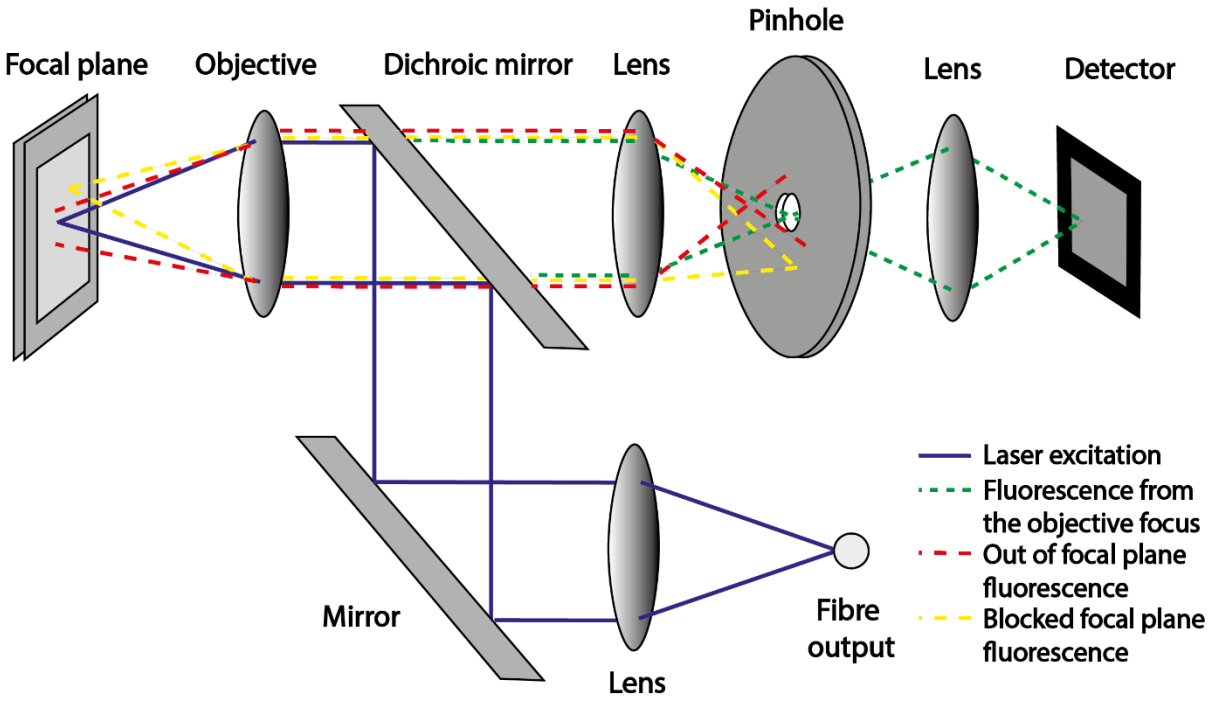

Figure 55: Schematic illustration of a confocal microscope: A laser illuminates the specimen by passing through a dichroic mirror. It is controlled by a single mode fibre which acts as confocal excitation pinhole (blue). The fluorescent emitted light passes through the dichroic mirror and the pinhole (green). The out of focus light and light from the side of the focal plane (red and yellow) is blocked by the pinhole. A system of lenses focusses the laser beam of interest to align the focal plane with the pinhole.

The basic setup of a confocal microscope is shown in Figure 55. First the laser beam is guided through a single mode fibre, which creates a Gaussian shaped laser signal. The small diameter of the output fibre of a few µm diameter acts as the first confocal pinhole for the excitation

path. Then the excitation light is redirected over a dichroic mirror which also has the function of a long-pass filter that only allows fluorescence response signal to pass through. The laser then reaches a focal plane of the specimen, and the resulting fluorescence is collected by the objective and directed through a set of lenses through the dichroic mirror to the pinhole. Fluorescence signals away from the focal plane as well as signals from the lateral offset of the excitation region are blocked by the pinhole. After another set of lenses, the light is registered by a detector which often includes a photomultiplier tube (PMT) to detect and amplify the signal. The variations of the laser beam on the specimen can either be created by using a piezo controlled stage or through controlled steering of the laser-beam by piezo or galvano controlled mirrors.[152] The actual pinhole in the optical path of a confocal microscope has only a small effect on the spatial resolution but improves the optical sectioning capabilities of the system. The axial and spatial resolution enhancement is dependent on the pinhole diameter measured in Airy units (AU). The Airy unit describes the diameter of the central maximum peak of Airy pattern of the focussed beam to the first minima of the Airy disk pattern[153] multiplied by the magnification of the microscope (see Figure 56).

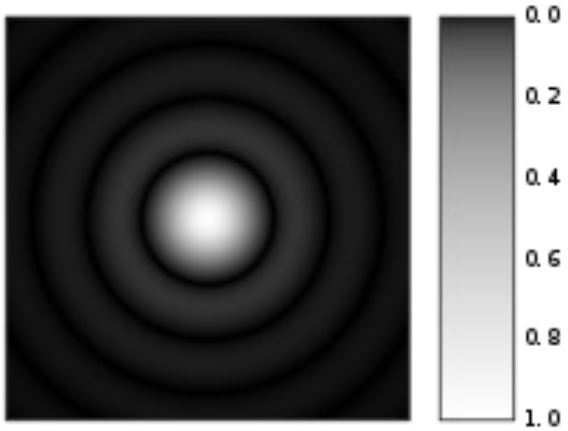

Figure 56: A grayscale intensity image of a computer-generated an Airy disk. Figure take from the following reference.[154]

If the pinhole diameter is larger than 1 Airy unit, the resolution in spatial and axial directions can be calculated with the following equations:

$$\Delta xy = \frac{0.51\lambda}{NA} \qquad \text{Equation (12)}$$

and

$$\Delta z = \frac{0.88\lambda}{n - \sqrt{n^2 - NA^2}} \qquad \text{Equation (13)}$$

Where λ is the wavelength, n the refraction index of objective immersing medium and NA is the numerical aperture of the objective. For pinhole diameters smaller than 1 AU, the equation changes to

$$\Delta x = \frac{0.37\lambda}{NA} \quad \text{Equation (14)}$$

and

$$\Delta z = \frac{0.64\lambda}{n-\sqrt{n^2-NA^2}} \quad \text{Equation (15)}$$

Therefore, the introduced pinhole in the light path of the image plane led to an improvement of the optical sectioning capabilities of the scanning microscope by rejecting out of focus light. However, the pursuit of even better spatial resolution comes at a price of reduced image signal.

2.2.1.1. Limitations of confocal microscopy

The standard pinhole size of a conventional confocal microscope is 1 Airy unit which already improves the resolution compared to wide-field microscopy images by a factor of 1.06. A reduced pinhole size improves the spatial resolution even further but comes at the price of a big reduction of detectable emission light. The maximum potential for resolution enhancement of a confocal microscope is by a factor of 2 which can only be achieved if the pinhole is closed to its minimum value. However, the image quality of all point-scanning confocal microscopy techniques is directly proportional to the ratio of detected signal (photons) and the amount of noise in the image (SNR) which is usually already low in confocal microscopy imaging because of the small labelling density and the optical sectioning of the pinhole. When the pinhole is closed too much the resulting statistical number of detected background photons called “shot noise” or “photon noise” become the dominant factor of the image and therefore reduces the image contrast and quality. Since the shot noise follows Poisson statistics, it is directly proportional to the square root of the signal or the square root of the number of photons (N):

$$SNR \sim \sqrt{N} \quad \text{Equation (16)}$$

Background fluorescence is another statistical noise that can also occur in confocal microscopy and originates from out-of-focus signals or autofluorescence of the investigated specimen. This background can be defined as an offset in signal intensity that is omnipresent in the whole image such as stray light that enters the detector.[155] This also limits the contrast of the signal in comparison to the background signal and overall reduces the image quality. This signal-to-background ratio (SBR) increases with a closing of the pinhole and would

reach its maximum when being completely closed which would also exclude all the actual signal from reaching the detector. Therefore, the pinhole aperture opening needs to be chosen such that the SNR is maximum while keeping the SBR level at acceptable levels to yield a good contrast in the image. A typically recommended pinhole size is between 1.0 and 0.85 AU to achieving a good compromise between resolution enhancement and detection yield.

Some other limitations of point-scanning microscopy technologies are an unwanted stretch of the point spread function (PSF) by a factor of ~2x in the z-axis compared to the spatial dimensions. This leads to a reduced axial resolution and errors in 4D object tracking.[156] Furthermore, the photonic interaction of the laser with biological samples can produce unwanted scattering, thus producing out of focus fluorescence.[157–159] A refractive index mismatch between thick specimens, glass, and immersion media could lead to further spherical aberration which increases errors in z-localization.[160] Several of the mentioned limitations are interconnected and improving one of them leads to a reduced quality in the aspect of another criteria. This phenomenon was termed “Eternal Triangle of Compromise” by Shotton (Figure 57).[161]

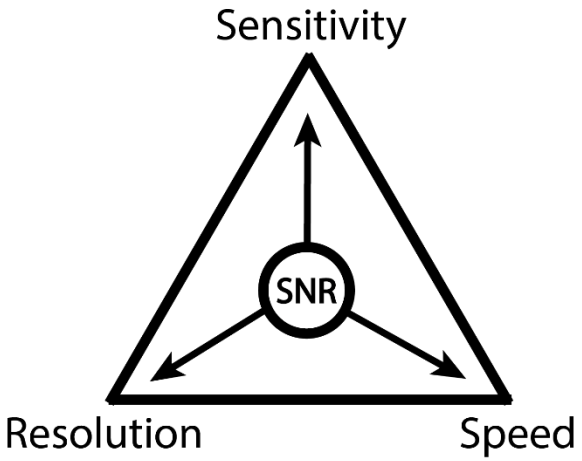

Figure 57: Eternal triangle of compromise stating that at a given SNR the sensitivity, spatial resolution (pixel sampling) and imaging speed of a point-scanning microscopy system cannot be optimized simultaneously.

Imaging with point-scanning microscopy systems such as confocal microscopes is always a trade-off between several different factors. At a given signal-to-noise ratio of a recorded image sequence, the imaging speed (sampling frequency), the sensitivity (sample frequency and pinhole size) and the spatial resolution (pinhole size) are influencing each other and are difficult to optimize simultaneously.

For example, to improve the imaging speeds the image acquisition rate needs to be increased. This is just possible by reducing the sampling pixel dwell time resulting in a lower photon

count and a drop of sensitivity. On the other hand, to enhance the spatial resolution of the image the pinhole size needs to be lowered which again results in a reduced sensitivity. Alternatively, to increase the sensitivity, the pinhole size must be increased which leads to a loss of resolution. The only physical way of simultaneously improving all parameters without compromising any one of them is by increasing the number of detected photons (SNR).

There are two physical ways of achieving this, one is by improving the efficiency of the collecting photon detector, and the second one is by increasing the illumination laser power on the specimen.

The first approach increases the SNR of an image by increasing the detection quantum efficiency of the PMT used in the confocal systems.

The second approach of improving the SNR by increasing the laser power has some significant limitations in fluorescence microscopy imaging. Especially when increasing the dimensionality, moving from 2D to 3D and further to time-lapse 3D+t (4D) images, those disadvantages and limitations get even more pronounced. The two problems most significant for 4D imaging in the context of laser power are a limited imaging frame rate and an increased phototoxicity.

2.2.1.2. Frame rate limitations

A big challenge in 4D microscopy is the limited imaging acquisition speed. The development of point-scanning microscopy techniques such as confocal laser scanning microscopy (CLSM) or two-photon microscopy (2PM) have led to major breakthroughs in the field of structural cell biology by enabling precise 3D imaging of cells, tissues, and whole animals. This is achieved by a pinhole that rejects out of focus fluorescence and selective excitation of a small optical section of the probe.[162] In spite of their advantages, scanning microscopy techniques like the ones described are poor at 4D imaging due to their limited acquisition speed. Both techniques rely on a laser exciting the whole image with one voxel position at a time for all 3 dimensions (XYZ) of the sample. The additional the z-dimension of the image collection leads to a significant increase of acquisition time for each time point. Therefore, the higher the resolution images the higher is the number of sequentially acquired pixels. Furthermore, the image time as well as the damage to the sample are in direct proportion to the pixel resolution. This highlights the trade-off between time resolution, image volume and z-resolution. For the detection of dynamic cellular processes such as rapid organelle movements, microtubule dynamics or organelle interactions this becomes increasingly problematic because for

capturing those processes it requires both high temporal and spatial resolution in 4D (3D + time) for motion tracking analysis.

Although CLSM just illuminates the in-focus image volume, the entire z-axis of the specimen is exposed to excitation throughout scanning. Because of a limited quantum efficiency of the PMT detectors the laser excitation intensity in CLSM needs to be quite high at ~1 mW/μm^2. The quantum efficiency of a fluorophore and its photo-stability determines how many photons the dye can emit and for how long this can be done at a given laser power. If the excited laser power gets too high the fluorophore can be pushed into a saturated excited state which limits the photon flux. Furthermore, depending on the stability of the fluorescent dye, a high laser power might lead to undesirable decomposition which leads to photobleaching and in turn to phototoxicity when investigating live samples.

2.2.1.3. Photobleaching and phototoxicity

In 4D microscopy imaging the sample specimen gets exposed to the laser-beam much more often due to the inherent need to collect several z-planes for each time-point. This leads to increased problems with photobleaching of fluorophores and therefore causes stronger phototoxicity compared to the 2D time-lapse recording. The reason for phototoxicity in fluorescence microscopy is because of a generation of reactive oxygen species (ROS).[163] These highly reactive compounds get created when high energy electrons in excited fluorophores are not emitting energy in the form of fluorescence but instead react with dissolved oxygen. This leads to a bleaching of the fluorophore and the production of highly reactive substances that cause the phototoxic effect.[164–166] The use of simple antioxidants that scavenge the ROS species such as L-ascorbic acid[167] can reduce the effects of phototoxicity. However, this is unfavourable when investigating delicate cellular processes in which exposure of additional foreign substances could lead to unforeseen effects in the biological system. Phototoxicity and photobleaching are cumulative effects which means that they are directly proportional to the total photon load which correlates with the time of laser light exposure and light intensity.[168] This highlights the need for strategies to minimize the exposure of high intensity laser light to the sample.

2.2.2. Technological developments in microscopy

To improve the limitations of point-scanning systems there have been several advances on the hardware as well as on the software side. Several different microscopy techniques have been

introduced that each improved at least one of the limitation factors and the recent advances in machine learning and especially deep learning in the field of microscopy show promising improvements to tackle these limitations. In the context of the thesis only the software based data post acquisition processing aspects will be covered in this section and more information on improved hardware for microscopy can be found in the following review paper.[164]

2.2.2.1. Video microscopy and computational methods

The last century saw steep developments in the field of quantitative analysis for microscopy images which provided important insights into many disciplines such as physics and biology. From the first tracking experiment carried out by manually drawing the trajectories on paper by Perrin in 1910 to the break throughs with the start of the digital age of microscopy in the 1950s the recording speed of microscopes improved significantly. With the start of the age of digital microscopy in the 1950s with the developments of analogue electronics, the acquisition and analysis speed of microscopes increased even further. In the early 1960s, the first digital computers found their way into microscopy imaging and analysis adding speed and functionalities to the field that was previously not possible to achieve. The first use cases for this technology were in biomedical applications such as the achievements from Prewitt and Mendelson in 1965 who managed to distinguish cells in a blood smear by using computers to analyse images obtained with a flying spot microscope.[169] In the 1970s, the use of digital microscopy expanded from the research laboratories to clinical settings with the development of computerized tomography scanner in 1972[170] and the automated flow cytometer in 1974.[171]

In the last decade machine learning has started to be employed for image analysis obtained from digital microscopy. Together with the "gold rush" of the deep learning revolution[172] it has seen massive improvements in the field of computer vision in tasks such as image recognition,[173] semantic segmentation,[174] and image generation,[175] which are now easily automatized. Some of these achievements have now also demonstrated its potential to apply deep learning to microscopy.

One milestone achievement in microscopy was the implementation of a special kind of neural network (U-Net) by Ronneberger *et al.,* in 2015 which is now widely used as a backbone structure for many applications such as for the segmentation of biomedical images cell segmentation and classification,[176] images object counting,[176] depth-of-field extension,[177] and

image enhancement.[178–180] In the context of tracking, deep learning has also been successfully used in the task of multiple particle tracking surpassing standard mathematical models.[181]
These are just some of the early successes that demonstrate the potential of deep learning to analyse or/and improve microscopy data. It also highlights one of the key limitation factors for the deployment of deep learning to microscopy which is the need for experimentally acquired and often manually annotated data. In biomedical applications this is often time consuming, expensive and potentially a biased process.[182]
In the next few sections, the definition and the concepts of deep learning are elaborated, and examples are given of how it found its way into post processing and image enhancement for microscopy images. Furthermore, the networks used for this thesis are broken down and are conceptually explained.

2.2.3. Deep Learning in microscopy

2.2.3.1. Machine learning

Machine learning is a branch of artificial intelligence that uses computational algorithms capable of learning from data without being specifically programmed to do so. This technology is considered the work horse in the new era of the so called “Big Data” and the different techniques have been applied in many different fields such as pattern recognition, computer vision, finance, computational biology and biomedical applications amongst others.[183]
Conventional computer algorithms required a user to define explicit rules to process the data. Machine learning algorithms, however, provide the benefit to be able to learn patterns and rules to perform specific tasks directly from a series of data mostly in a supervised way. This means that the machine learning algorithm learns from sets of input data and the corresponding desired outputs (the ground truth) by adjusting their behaviour accordingly. The input-output data pairs are usually collected by experiments or through simulations and are called the training dataset.
Despite the advances with conventional machine learning approaches they still require a good amount of engineering skills and domain expertise. So called feature extractors, which reduce the dimensionality of the dataset and transform raw data into a good feature vector must be carefully engineered and designed. These features are then fed into learning system such as classifiers that could identify patterns from a given input.[172] More recently, representation

learning has been developed which feeds in raw data and automatically discovers the representations needed to perform the detection or classification. Deep learning is one very common representation-learning method.

2.2.3.2. Deep learning

Deep learning is a subfield of the broader family of machine learning and is inspired by the information processing of biological systems such as the human brain. The aim of this algorithmic technology is to try to emulate the brain's ability to learn which is achieved by using artificial neural networks (ANN) to perform representation learning.[172] One major difference of ANNs is that, neural networks have static architectures while the biological brains are dynamic (plastic).[184–186] Neural networks consist of interconnected simple computing units called artificial neurons which are often just capable of calculating a non-linear function from a given input. The organization of these neurons into layers allow different architectures to be designed of the neural networks with different connectivity. The most popular architecture is simply connecting each neuron of one layer with all the neurons in the following layer. This layer computes some transformation into a representation at a higher slightly more abstract level and feeds the result again into the next layer by connecting each neuron with each other. Especially for computer vision tasks this process is repeated for several layers (often more than ten) which describes the "depth" of the ANN and therefore implies the name "deep learning". The different layers of representation focus on different aspects of the input. With several of those abstraction transformations, very complex functions can be learned which can be used for classification tasks but also for more difficult image reconstruction tasks.[172] In an image for example, which is fed into the network in the form of an array of pixel values, the first layer typically represents the absence or presence of edges at particular orientations and locations in the image[172] whereas the second layer could detect particular arrangements of those edges without taking the precise position of those arrangements into consideration. Then the third layer may assemble certain motifs into larger combinations of familiar objects and subsequent layers then further transform the information until it reaches the last layer which provides a presented output again. The main aspect of deep learning is that these levels of abstraction created by the different features are not designed by humans, but they are learned by the network using a learning procedure.[172] In that way, the ANNs can be designed to perform many different tasks such as classification, forecasting and recreation tasks amongst others. In that way several different variations of

deep neural networks have been designed such as convolutional neural networks (CNN), deep belief networks (DBN) or recurrent neural networks (RNN) which have produced results that are comparable and in some cases surpassed human expert performance.[173,187–189]

2.2.3.3. The learning-phase

In machine learning, including deep learning, learning can be performed supervised, semi-supervised or unsupervised of which the most common one is supervised learning.[172,190,191] In supervised learning the algorithm or network is presented with examples of input-output pairs. Each example pair consists of an input which is presented typically in the form of a vector and an output which is called a supervisory signal. The final aim of the learning algorithm is to learn to generalize from the training data in a "reasonable" way to be able to later map new unseen examples correctly. In the supervised learning task, the network produces an inferred function based on the analysed labelled training data by modifying the internal adjustable parameters to reduce the error. These parameters are called "weights" and a typical deep learning system can have billions of them.

The training phase can be broken down into four steps. In the first step, the first layer of an ANN receives an input which propagates through the network and produces an output based on the given weights. The second step takes the predicted output signal and compares it to the true desired output provided from the training data pair (ground truth) and it calculates the gradient vector of the error using a loss function. In the third step, in order to decrease the error of future inputs, the ANN propagates the error backwards through the network and recalculates each weight to determine whether it should increase or decrease it in order to reduce the error. In the final/fourth step the weights are updated with an optimizer function that calculated how much the weight values should be altered before restarting with the next training example.

The most common objective function for optimizing the predicted results used in deep learning is called stochastic gradient descent (SGD). The algorithm is presented with sets of examples, of which it computes the outputs and errors. Then the average gradient is computed, and the weights are adjusted for many cycles until the objective function stops decreasing. The name stochastic derives from the fact that each set of examples provides a noisy estimate of the average gradient of all examples. When the training is finished the network is usually tested on unseen data called "test set" to evaluate the generalization ability of the network. The inferred function produced by the algorithm after training could be seen as a hilly

landscape in a multi-dimensional space of weight values and the negative gradient vector shows the steepest decent which brings the algorithm to an output where the error is low.

2.2.4. Deep Learning terminology

Before explaining some of the commonly used network architectures for deep learning in the field of computer vision, some specific terminologies about the different building blocks of neural networks are explained in this section.

2.2.4.1. Convolution layers

The convolutional layer is the core building block of any CNN and is usually used as the first layer of such a network. It is sometimes called feature extractor layer and the parameters of this layer consist of filters (so-called kernels) which offers a certain receptive field of the image dimension volume (height × width × channels). When passing the information to the next layer, the input area of the same dimension as the filter is convoluted by using the dot product of the filter entity and the input region which produces a feature map of the filter (see Figure 58). This convolution step converts all the pixels in the receptive field into a single pixel value on the output feature map. Depending on the size of the filter kernels the size of the image is reduced. Sometimes, in order to not reduce the image size during this process an image manipulation called zero-padding is performed before the convolution step. This adds a circle of zeros around each image dimension which increases the input image dimension size by the number it will be reduced in the convolution step.

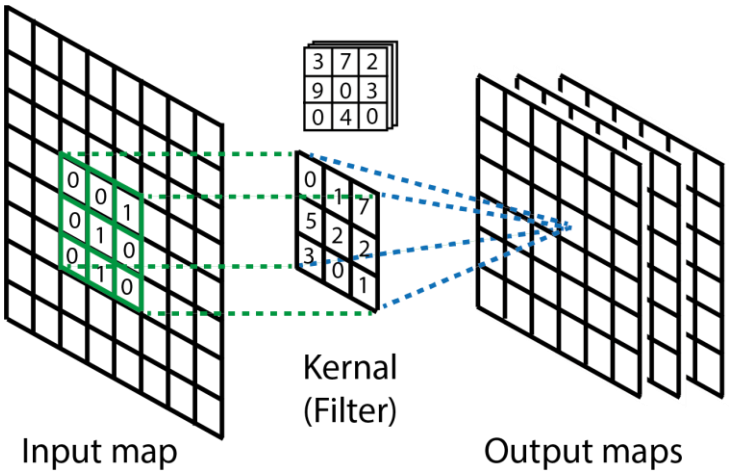

Figure 58: Schematic representation of a convolution layer with a series of filter kernels producing different output maps.

The activation maps of all the filters are stacked along the depth dimension and form the full output of the convolution layer. Every single feature map can therefore be interpreted as the

receptive field of one single neuron which looks at a small region of the full image and all the neurons in this layer share the same parameters in the activation map. The shared parameters allow this network to extract a different sets of features within an image by using the same parameters on each receptive field of the image which make CNNs more efficient compared to fully connected networks because of the reduced dimensionality of the data. Furthermore, the division of images into small blocks help in extracting feature motifs.[192]

2.2.4.2. Pooling layer

The pooling layer is a form of non-linear down-sampling of the data. There are several down-sampling functions that can perform the pooling of which the max-pooling is the most popular one. This function splits the image into a set of rectangles for which it outputs the maximum value of the observed sub-regions. These values form the new image with the two dimensions of the number of the subregions. The main idea of a pooling layer is that the exact location of a feature is less important than the relative location of the feature to other features. The main function of the pooling layer is to reduce the number of parameters by reducing the size of the representation. This also reduces the computational effort for the network and reduces the risks of overfitting. This down-sampling step is usually done after a convolution layer and is often followed by an activation function such as a ReLU layer. A very common filter size for a max pooling layer is 2x2 with a stride of 2 (see Figure 59). This leads to a down-sampling of the input along the width and height and results in a 75% reduction of activations. Other options for pooling layers are average pooling and L2-norm pooling.

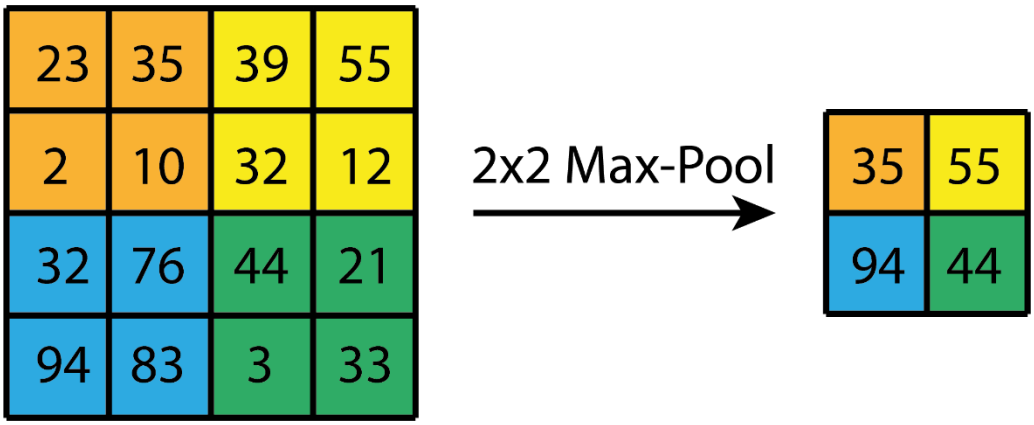

Figure 59: Example of 2x2 max pooling. Down-sampling the image by taking the highest number of a 2x2 matrix.

2.2.4.3. ReLU - Rectified Linear Unit

The Rectified Linear Unit layer is usually applied immediately after a convolution layer. It applies a non-linear activation function to each element of the computed convoluted layer.

The reason for this mathematical operation is to introduce non-linearity to a system. In the early days of neural networks, the functions used for this layer were usually a tanh or sigmoid function but more recently it was found that a ReLU operations work better because of an increased training speed without compromising on the accuracy (see Figure 60).

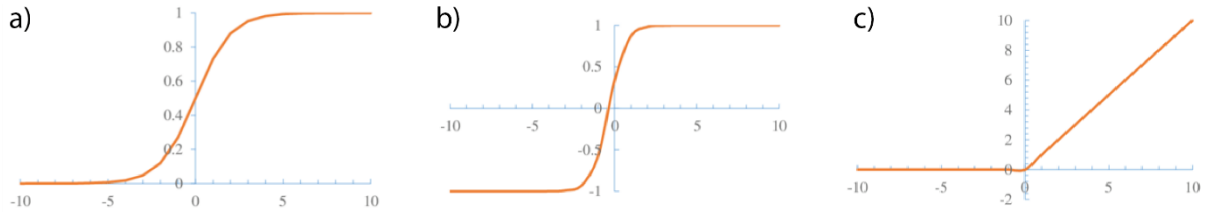

Figure 60: Activation functions. a) Sigmoid function; b) tanh function; c) ReLu function.

Furthermore, it also helps to avoid the so-called vanishing gradient problem. This problem describes the phenomenon that the early layers of a neural network train slower because of an exponential decrease of the gradient for the backpropagation through the layers of the network. The ReLU function applies the function $f(x) = max(0, x)$ to all the values of the previous layer which basically removes all negative values from the activation map by correcting them to the value zero. It does not influence the receptive field of the convolution layers but introduces non-linear properties to the decision function.

2.2.4.4. Fully connected layer

Fully connected layers are connecting each artificial neuron of one layer with every neuron in the next layer. It is usually used as part of a deep learning model where the last few layers are fully connected which compiles the data extracted and processed in the previous layers to form a final output.

2.2.4.5. Stride and padding

The stride is the value that denotes how many pixels the attention field of a convolution is moving in each step. By default, it would be one, but to reduce the size of the output even further the stride can be as big as the dimension of the receptive field. To maintain the dimension size of the output compared to the input, padding can be used. Padding is the systematic addition of zeros around the input matrix of the actual image to increase the investigated area. For example, by increasing the matrix dimension by one pixel around the image allows to perform a convolution 3x3 convolution with a stride of 1 without reduction of the dimension of the input image (see Figure 61).

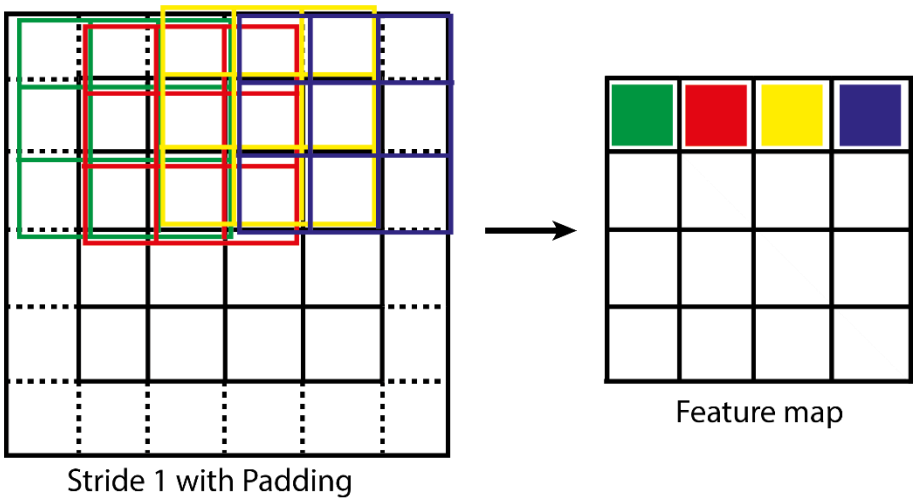

Figure 61: Example convolution of 4x4 input with stride of 1 and padding of 1 resulting in a feature map of dimensions 4x4.

2.2.4.6. Dropout layer

In many neural networks which are trained on relatively small datasets for a long time the network tends to overfit. This means that the weights of the network are specifically tuned to the training examples they are given but the network does not perform well when given new examples. One way of overcoming this problem is the use of dropout layers. This layer randomly sets a certain percentage of the activations to zero which forces the network to generalize for the correct output even when some activations are dropped out. The removed neurons are reinserted after each training example into the network with their original weights. This layer is just used during the training phase but not in the test phase. By avoiding training all neurons on all the training data, the dropout layer decreases the likelihood of overfitting.

2.2.4.7. Transfer learning

Transfer learning in the context of machine learning (ML) is defined as the storage of knowledge gained while solving one problem and applying it to a different but related problem.[193] In deep learning, transfer learning is used by applying a neural network that has been previously trained on a big dataset to solve a certain problem and use this pretrained model as starting weights for fine-tuning the same neural network for a different task using a new or smaller dataset. Often a pretrained network is integrated into a bigger network structure where for example, the input and output layers are specifically adapted for the task, but the centre of the network is used from the already trained network. The idea is that the pretrained network acts as a feature extractor. When training such a network it is common practice to freeze the layers of the pretrained network to make sure that the fine-tuning does

not alter this part of the network. The benefit of such a workstream is that a network does not need to be trained from scratch which would take a very long time on a big dataset. By using the pretrained network the fine-tuning of the network is taking just a fraction of the time that it would have taken to train the full network architecture.

2.2.4.8. Data augmentation techniques

Data augmentation techniques are very useful to increase the amount of training data for training a neural network. The general principle works that an algorithm alters the available training data while keeping the label the same. This step artificially expands the dataset and can easily double or triple the number of training examples. The most popular augmentation methods are horizontal and vertical flips, rotation, random cropping, introduction of random noise and colour alterations amongst others. The reason why this works is because those transformations change the values of the image input which might appear as little changes for a human observer but for a neural network those changes can be significant as the classification or label of the image does not change, while the array values do change a lot.
In the following section the most common neural network architectures used for deep learning applications in microscopy are explained and discussed in more detail.

1.3.4. Deep learning architectures

In the field of microscopy, the most common artificial neural networks architectures are dense neural networks, convolutional neural networks, convolutional encoder-decoders, U-Nets, recursive neural networks, and generative adversarial networks.[178–180]

2.2.4.9. Dense Neural Network

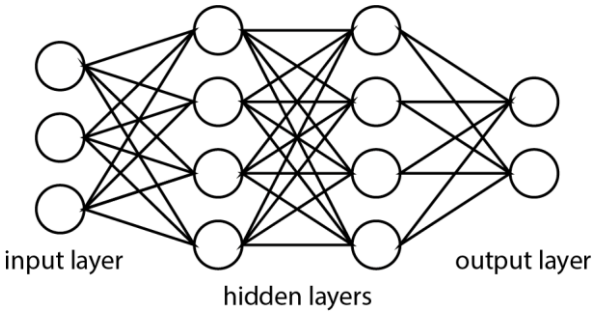

Figure 62: Schematic representation of a dense neural network

The most popular ANN is the dense neural network (DNN) the architecture which consists of several fully connected layers. This fact is at the same time its strength and weakness. A sufficiently large DNN has the potential to calculate any function, however, the computational

costs for running these calculations increase with the increasing number of layers and quickly reach their limits if for example large inputs are provided. This is the reason why they are usually employed as just one part of a network which is most often for the last few layers of the network architecture.

2.2.4.10. Convolutional Neural Networks

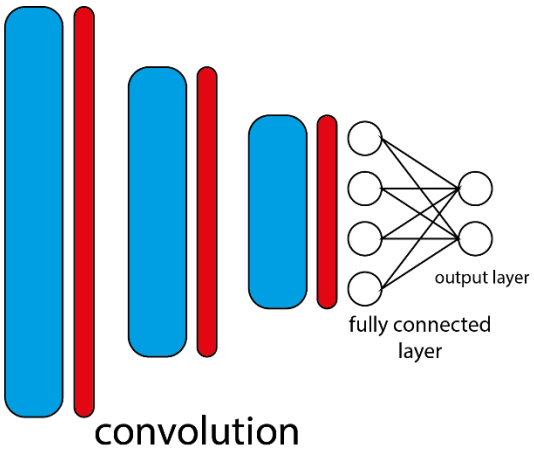

Figure 63: Schematic representation of a convolutional neural network (CNN); blue bars represent convolution layers of neurons; red bars represent pooling layers. The higher the bar the more neurons are in that layer. Last layer is usually a fully connected layer to the output neurons.

On the other hand, convolutional neural networks (CNNs) are widely used for analysing and handling of image input data. As the name implies, they are built upon convolutional layers where in each convolutional layer a set of 2D filters with varying dimensions are used to produce feature maps as output of the layer. The filter size of the convolutional layer determines the dimensions of the features that can be detected by the specific network layer. A trick that is widely used to also enable to detect bigger features in high dimensional images is that the feature maps are down-sampled after each convolutional layer and are fed with the new dimensions into the next processing layer of the network. In current applications it is often that a small DNN is integrated at the end of the network architecture to integrate the information contained in the output feature maps.

1.3.4.1. Convolutional Encoder-Decoder Network

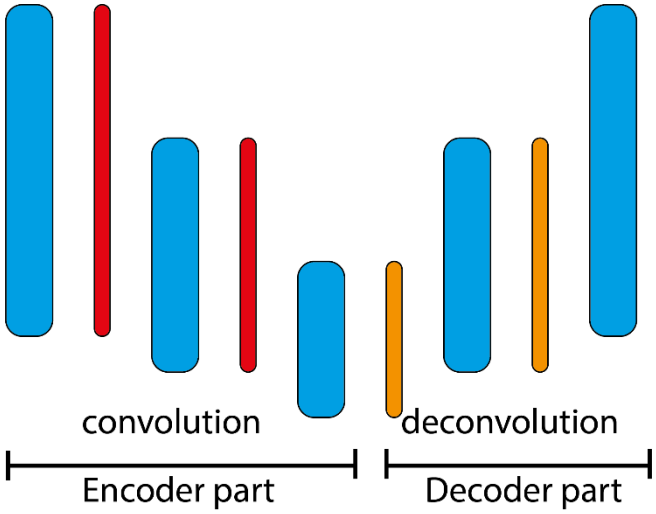

Figure 64: Schematic representation of a convolutional encoder-decoder network; blue bars represent convolution layer of neurons; red bars represent pooling layers; orange bars represent deconvolution layers. The higher the bar the more neurons are in that layer.

Convolutional encoder-decoders are similar to CNN in a way that they are constructed by using two parts (see Figure 64). The first part which is called the encoder part, reduces the dimensionality of the input through down-sampling or convolutional layers. This step encodes the information of the original input image. The second part called decoder part, uses the information provided at the end of the encoder and can either reconstruct the original image or perform some transformations on the output of the image (e.g. used in style transfer or segmentation tasks). In a trained version of the network the output of the encoder part can serve as a compressed version of the input image.

1.3.4.2. U-Nets

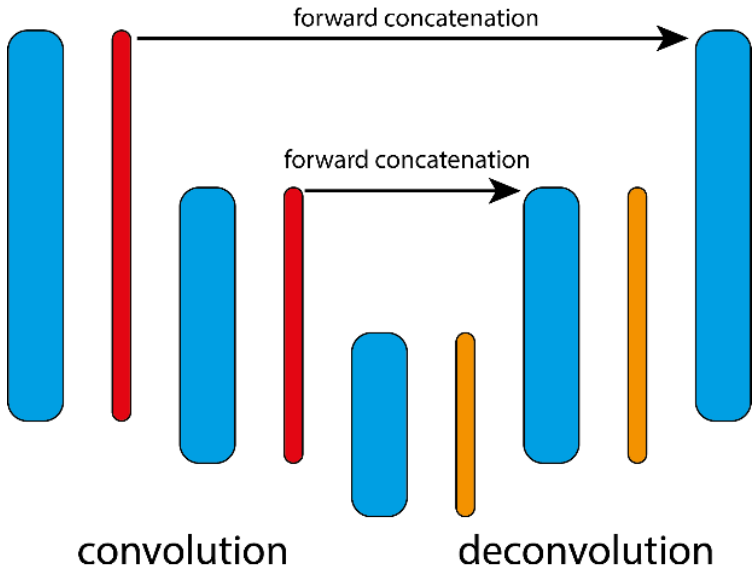

Figure 65: Schematic representation of U-Net architecture; blue bars represent convolution layer of neurons; red bars represent pooling layers; orange bars represent deconvolution layers. The higher the bar the more neurons are in that layer. The arrows indicate some direct connections between the indicated layers.

The architecture of so-called U-Nets have been found to be especially useful for many microscopy-related tasks. Their architecture is seen as an evolution of the convolutional encoder decoder networks. The difference lies in a feature forward concatenation step which is introduced in the corresponding levels of the encoder and decoder path. This allows for preservation of more detailed information which otherwise would have gone lost when reducing the image resolution in the encoding path. They have been particularly useful in segmenting and analysing biomedical image data[194–196] and were also used for spatial image upscaling.[180]

2.2.4.11. Generative Adversarial Networks

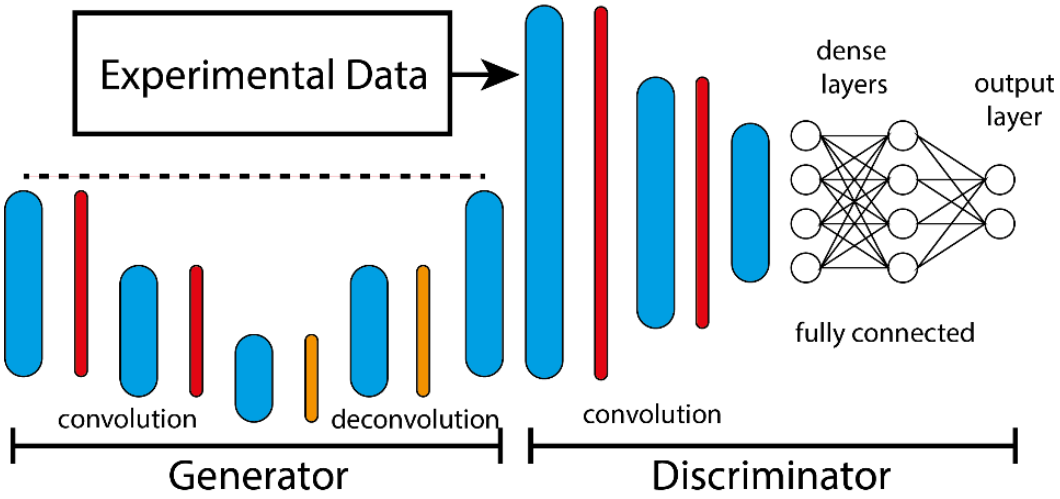

Figure 66: Schematic representation of a generative adversarial network (GAN); blue bars represent convolution layer of neurons; red bars represent pooling layers; orange bars represent deconvolution layers. The last part of the network represents a fully connected dense layer.

A very different concept provides the generative adversarial network (GAN). This architecture describes the combination of two different network structures regardless of their specific designs.[188] The first one is a generator and the second one is the discriminator (see Figure 66). The generator creates new data from a set of input data and the discriminator is classifying the inputs from the generator as either being real data or synthetic data artificially created. The name *adversarial* comes from the fact that both networks compete against each other, where the generator tries to fool the discriminator and the discriminator tries to uncover the synthetic input presented by the generator. The generator structure can be either a convolutional encoder-decoder network or the architecture of a U-Net. It is trained to generate new images through this subnetwork and mixes it with the real images as input for the discriminator which is often a convolutional neural network. The obvious advantages of GANs are that they can generate additional training data given some examples, but they are difficult to train and often very sensitive to hyperparameter tuning. Furthermore, small architecture changes sometimes lead to lack of convergence, vanishing gradients, and loss of image quality.[189]

1.3.4.3. Recurrent Neural Network

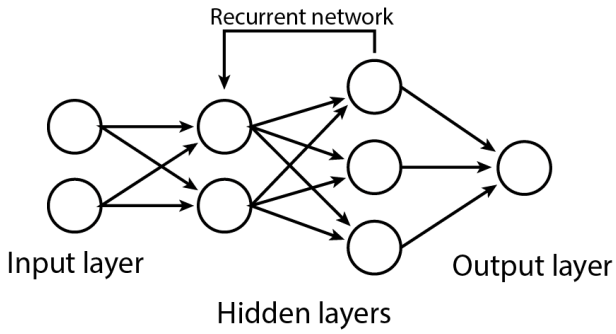

Figure 67: Schematic representation of a recurrent neural network (RNN).

Recurrent neural networks (RNN) are another class of ANNs where the connections of the artificial neurons form a graph system along a time sequence. This means that they can take input of time series data and allow outputs of one layer to be fed into previous layers creating a "memory effect" of the information flow. In traditional feed forward neural networks inputs and outputs are independent of each other and can be seen as a directed acyclic graph that can be unrolled in one direction. In contrast to that RNNs can be seen as directed cyclic graphs that cannot be unrolled. The output of RNNs depend strongly on the element of the sequence and allow a temporal dynamic behaviour because they can learn from past inputs. This makes them a useful tool for especially natural language processing (NLP) related tasks.

2.2.4.12. ConvLSTM

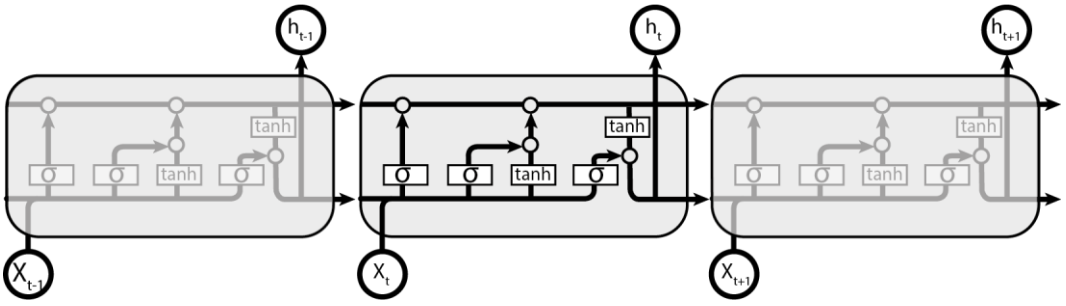

Figure 68: Schematic representation of a ConvLSTM which includes several gates controlled with sigmoid or tanh functions for controlling the flow of information.

A special type of a RNN architecture is a long short-term memory (LSTM) network. This network has the characteristics of a normal RNN providing feedback loops within the network. Additionally, it provides special gates that can store information states which is under direct control of the network. These gates can also incorporate time delays or further feedback loops which are then called LSTMs. LSTMs usually consist of three building blocks within a cell which are an input gate, an output gate and a forget gate. This cell can remember time

sequence data and the three gates define how the information in the cell is remembered replaced or forgotten. In a ConvLSTM which is a special type of recurrent neural network which combines the convolutional layer structure of with the idea of a gated cell structure of LSTMs is used for spatio-temporal prediction. It can determine the future state of a certain cell in a grid by the inputs and past states of its local neighbours. In context of image processing tasks ConvLSTM with a larger transitional kernel is able to capture faster motions while ones with a smaller kernel can capture slower motions.

2.2.5. Microscopy image enhancement neural networks

In context of this research four different neural network types were implemented to improve the image quality of a recorded 4D or 3D image sequence. The first attempt was to try to perform artificial labelling of copper of brightfield images. Then three image special resolution enhancement algorithms were implemented and benchmarked against classical mathematical models. Additionally, one network for improving the signal-to-noise ratio of the recorded images was used and finally two networks were implemented that are capable of interpolating images between images of two time points of a sequence, increasing the image frequency which is shown to be specifically beneficial for improving the performance of tracking algorithms.

2.2.5.1. Artificial labelling

Fluorescence microscopy uses a high laser power to excite fluorophores in cells which produces significant amount of phototoxicity perturbing the sample and creating a trade-off between data-quality and the time scale of life cell imaging. Additionally, the number of simultaneous recordings of different fluorescence channels further puts constraints on the cell health and limits the time resolution of life cell imaging. On the other hand, transmitted-light microscopy (TLM) (such as bright-field microscopy) is relatively cheap and is a label free technology which has negligible phototoxicity in comparison to fluorescence microscopy. Even though TL microscopy provides valuable information on the cell organization, it lacks the contrast of fluorescence microscopy for clearly identifying the cell organelles of interest. In 2018, Johnson *et al*., developed a deep neural network that allows for cross-modality analysis between fluorescence and TLM microscopy images.[199] It allows to perform artificial labelling of cell organelles by training a neural network with brightfield and fluorescence labelled organelle image pairs. This label-free prediction neural network recognizes the

relationship between 3D TLM and fluorescence live cell images and can label several different subcellular structures. The deep learning tool is based on a CNN U-Net architecture shown in Figure 69.

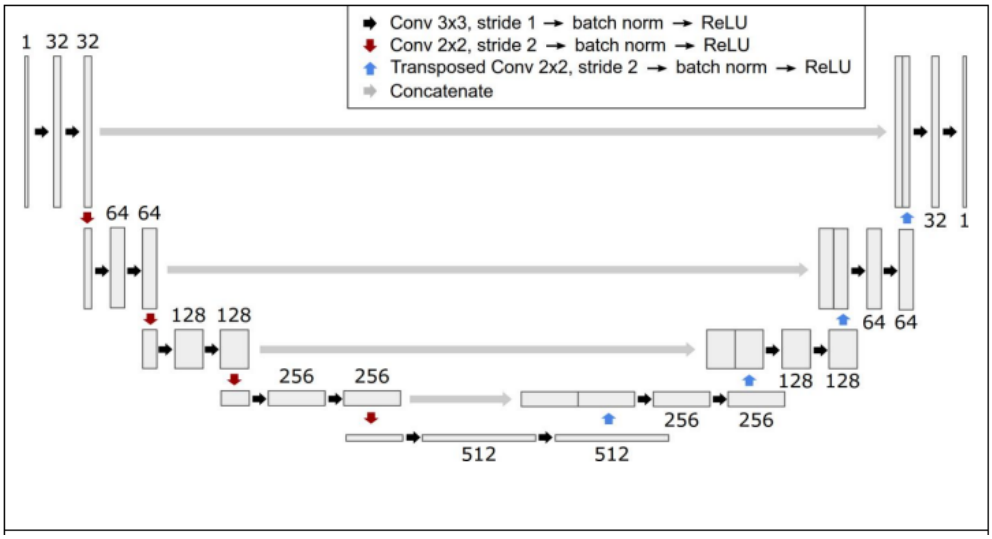

Figure 69: Schematic representation of the neural network architecture of the fNET network. It shows the different dimensions throughout the network with the different dimensionality reductions in the convolution layers (black and red arrows), the transposed convolution layers (blue arrows) and the concatenation between data from different layers within the network. The figure was taken with permission of the publisher from the following reference.[199]

It consists of three convolution layers with different pixel and stride dimensions followed by a batch normalization and ReLU operation. In the paper it allowed corresponding fluorescence images to be predicted directly from three-dimensional (3D) TLM live cell images. Even though the authors of the paper mentioned some challenges regarding the dependency of the results on the cell line of interest and dependence on the contrast of the organelle of interest in the TLM, the network was used in this research to try to predict the cellular copper(I) distribution based on the fluorescence labelling signal results of the newly developed fluorescence copper(I) sensor.

2.2.5.2. Signal-to-noise enhancement

The image restoration task of improving the signal-to-noise levels of an image, is a reconstructing problem where the corrupted image should be recovered from the information that is available. A poor SNR in microscopy can be the result of a too weak laser power used to excite the fluorescent dye, a low dye concentration present in the cell, or also a too low quantum yield of the fluorescent molecule. All three mentioned reasons result in a poorer SNR.

The neural network implemented in the content-aware image restoration (CARE) network can improve the SNR of poor-quality images given that it was trained on pairs of images with high and low SNR. It is a classical U-Net architecture consisting of a convolutional neural network in combination with an encoder-decoder structure. The encoder part of the network reduces the spatial resolution with pooling layers which typically takes the maximum value of the local neighbourhood. The decoder part performs the up sampling by enlarging the image to its original input size. However, the up sampling of the image can lead to blurred CNN outputs. To overcome this problem, skip connections in the high-resolution feature layers in the decoder part were integrated that concatenate the feature layers of the encoder part with the decoder part of the network.[176,200] The network is set up to not learn the output of interest directly (such as the restored image) but the *residual* $\hat{g}$ of the input of the network i.e. $g(x) = x + \hat{g}(x)$. Furthermore, instead of calculating a single output value per pixel, the CARE network calculates a distribution of probabilities, by predicting the location and scale of a Laplace probability density function.

The training of the network is carried out by providing it with high and low SNR input pairs which are used to calculate a loss function by minimizing stochastic gradient descent (Adam optimizer[201]). In contrast to conventional CNN image restoration networks the loss function is calculated by averaging the per pixel negative log-likelihood of the Laplace distributions.

2.2.5.3. Interpolation-based image spatial pixel resolution up sampling

In mathematical terms interpolation is the problem of approximating the value of a function for a non-given point in some space when given the value of that function in positions around that point. Image interpolation, which is also called image scaling, is the process of digitally resizing images. It is still widely used in many image-related applications and the most famous traditional methods are nearest-neighbour, bilinear and bicubic interpolation (see Figure 70). All these algorithms can be performed along each dimension of a multi-dimensional image series and since these methods are easy to implement they are still widely used in some CNN-based SR models.[182]

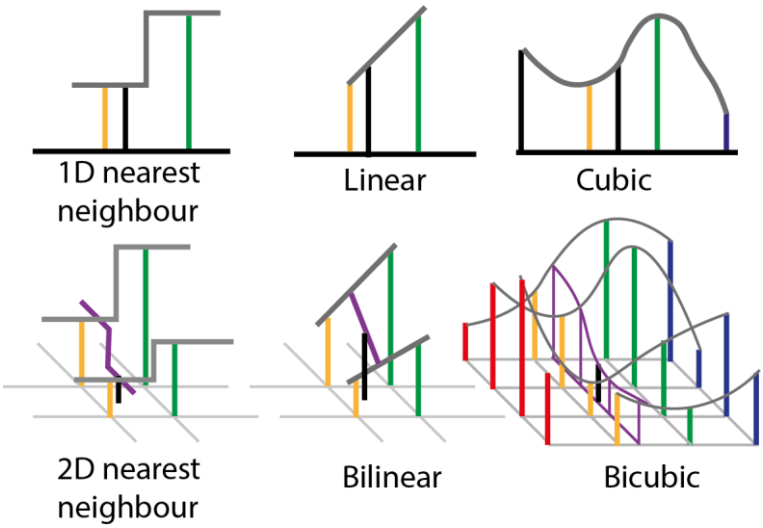

Figure 70: Graphical representation of nearest neighbour, linear and cubic interpolation in 1 or 2 dimensions.

2.2.5.3.1. Nearest-neighbour interpolation

The nearest-neighbour interpolation simply takes the same value of the nearest pixel next to the newly interpolated one. This increases the spatial resolution of the image and is a very fast process but as a downside it produces blocky patterns with low quality resulting images.

2.2.5.3.2. Bilinear interpolation

In bilinear interpolation (BIL) a receptive field of 2 × 2 is linearly interpolated along one axis first and then along the second axis. Since this is a quadratic interpolation taking 4 pixels into account this algorithm performs better than the nearest neighbour interpolation while remaining a relatively fast and computational inexpensive method.

2.2.5.3.3. Bicubic interpolation

The bicubic interpolation (BIC) takes 4 × 4 pixels for their interpolation into consideration performing the interpolation along each axis sequentially. This algorithm results in smoother results with fewer artefacts but it compromises on calculation speed.

All mathematical interpolation-based up-sampling methods just use the existing image signals to increase the spatial resolution of the image without bringing any more information into the image, but they introduce some side effects, such as noise amplification and blurring results. The current trend is to replace mathematical interpolation-based methods with learnable layers. Neural network based up-sampling methods have shown to provide the advantage that they can recognize patterns from the training data and therefore, can introduce new information into the reconstructed images.

2.2.5.3.4. Deep learning based single-image-super-resolution

Single image super-resolution (SISR) is a research field which aims to reconstruct a high-resolution (HR) image from a low-resolution (LR) observation. Especially deep learning approaches have drawn significant attention to this topic and brought strong improvements for this reconstruction task over the past decade. The general principle how a neural network learns to reconstruct a high-resolution image is by providing it with training pairs of high-resolution and down-sampled low-resolution counterparts (usually down-sampled by bicubic interpolation) and let it learn to reconstruct high level features that are lost in the low-resolution images. In most existing DL based image SR networks, the information often flows in a feedforward direction, which leads to many high-level features and details getting lost in this network architecture. In recent years there have been several SISR methods proposed which include example-based,[202] reconstruction based,[203,204] and deep learning-based approaches. Especially the deep learning approaches have taken the super-resolution performance on synthetic low-resolution images to a new level. Two examples of such a state-of-the art deep learning-based image super resolution network, implemented for this research project were published in 2019 by Qilei Li *et al*., with the name "Gated Multiple Feedback Network for Image Super-Resolution" (in short: GMFN)[205] and in 2019 by Zhen Li *et al*., with the name "Feedback Network for Image Super-Resolution" (in short: SRFBN-S).[206] Both networks follow a similar principle and structure, allowing a spatial resolution upscaling of up to 4-times and both have been tested competitively on several real-life photographic datasets. In traditional linear feedforward networks, the information flows solely from the shallower layers directly to the reconstruction layer of the SR image. This brings the disadvantage that the narrower receptive fields in the shallower layers cannot take the valuable contextual information into account which hinders the reconstruction ability. The GMFN network overcomes this problem by integrating several gated multiple feedback loops in the architecture of the network. Those gated feedback modules efficiently select high-level information from several provided feedback connections and uses this information to enhance the high-level information to refine the details of the low-resolution image in the super-resolved output. Following this logic, the GMFN network is designed as a convolution recurrent neural network which unrolls along t time steps. At each time step the sub-network can be regarded as an independent CNN which aims to reconstruct the SR image from the original LR image. This is achieved by cascading multiple residual dense blocks (RDBs) and recurrently unfolding them across time by processing the same low-resolution image in

several timepoints. Each sub-network consists of four parts which are an initial low-level feature extractor, multiple residual dense blocks (RDBs), multiple gated feedback modules (GFMs), and a reconstruction block (RB). Multiple gated-feedback connections allow the subnetwork to communicate with the different sub-networks across time. Those feedback connections across different time points support to refine the low-level features using high-level information. The only difference between SRFBN-S and GMFN is that SRFBN-S has just a single gated feedback module whereas GMFN has several which explains the slightly better performance of GMFN based on the benchmark studies performed in the original papers.

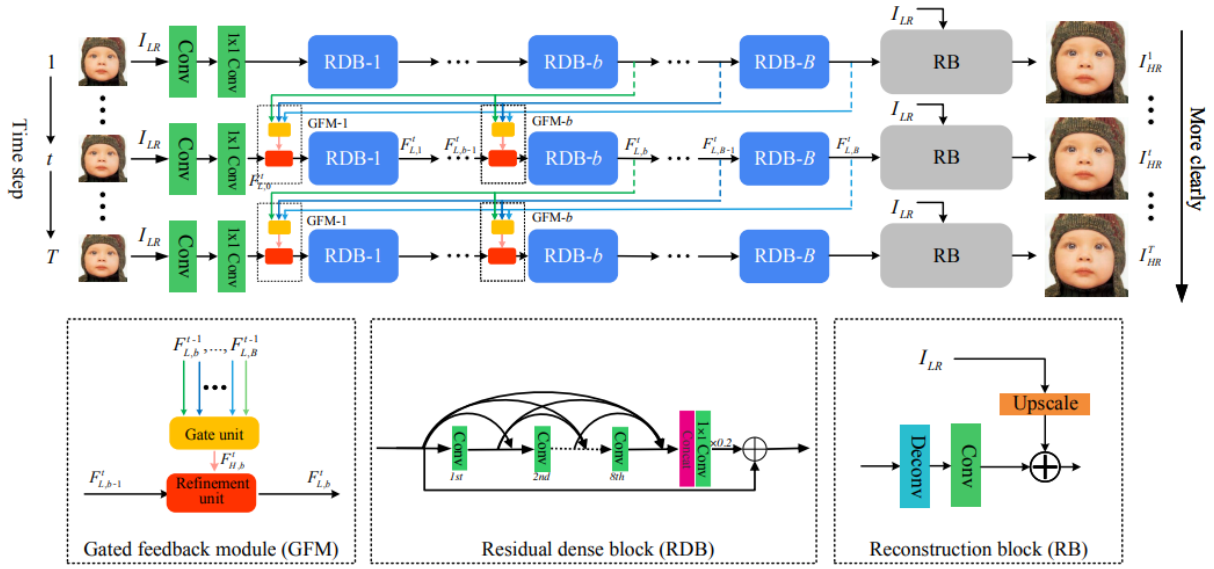

Figure 71: Schematic representation of the GMFN network showing the information flow from the convolutional RNN rolled out along t time steps where the same low resolution input image is fed into the network providing increasing amounts of information to the GFM modules which improves the HR image reconstruction. Image taken with permission from the publisher from the following reference.[205]

The results of this image super-resolution upscaling are evaluated with PSNR, SSIM and RMSE and compared with classical mathematical interpolation-based upscaling methods.

2.2.5.4. Video frame interpolation

Video frame interpolation is an important research area in the field of computer vision. It was found useful in the areas of video post-processing, surveillance, and in video restoration tasks. In general, it aims to increase the frame rate of a video sequence by calculating intermitted frames between consecutive input frames. This field has seen big improvements over the last decade in the film and video related industries but has not been employed to the field of microscopy imaging yet.

For high-quality video frame interpolation, precise motion estimation techniques are used (such as mathematical or deep learning models) which allow the correlation between consecutive frames to be predicted to preserve a continuity of flow vectors and retain the colour constancy of the objects in the intermediate frames. There are several approaches that are being used to perform the interpolation task. The most common video interpolation approaches are using convolutional neural networks and can be subdivided into two categories: i) based on interpolation convolution kernel estimation and ii) based on optical flow estimation.[207] The first process uses a combination of motion estimation and pixel synthesis in one process producing a convolution kernel of each pixel. This allows the motion information of two consecutive image frames to be captured. The second approach of flow-based methods estimates the flow of motion of each pixel in a sequence of frames where the information flows bi-directional across consecutive images and it captures dense pixel correspondences. The estimated flow vectors guide the blending of the two input images to the interpolated frame. In the process often energy minimization processes are used to determine the flow vectors. One disadvantage of these CNN based approaches is that kernel-based methods[207] are computationally expensive, and for flow-based methods the accuracy of the calculations (optical flow or convolution kernel estimations) directly affect the quality of the generated frame, and they will produce unrealistic and blurry results if the intermediate process fails.[208] An alternative approach uses generative adversarial networks (GANs) which have achieved great successes in the field of image and video generation.[208,209] In the context of image interpolation GANs consist of a generator network (G) and a discriminator network (D). They are trained simultaneously where D tries to distinguish real inputs from artificially created ones from G. The aim of G is to create realistic video frames that can fool D. An often arising problem with GANs is that the image interpolation task offers a vast search space of possible intermediate frames if no other information is provided for the network resulting in a poor quality of the interpolation.

There are also hybrid approaches which combine two or more different methods to perform the image interpolation. The DAIN network used for this research is one of those hybrid networks.

2.2.5.4.1. DAIN architecture

The implemented network for performing the image interpolation on microscopy images is called Depth-Aware Video Frame Interpolation in short DAIN and was published by Wenbo

et al., in 2019.[209] As the name already implies the network is trained to detect occlusion by exploring depth information and based on this information it performs the frame interpolation. Generally, DAIN can be seen as a hybrid frame interpolation method that uses different information and tools to perform the frame interpolation task. It attempts to combine the two approaches of both convolution kernels and flow vectors that are estimated by using sub-CNNs.

In more detail the network learns hierarchical features by gathering contextual information from neighbouring pixels. The interpolated frame is synthesized by combining the information in an adaptive wrapping layer by integrating the two input frames, depth maps and contextual features based on optical flow and a local interpolation kernel. The depth maps functionality from the input frames is performed by an hourglass network (a special type of convolutional encoder-decoder network) trained on the MegaDepth dataset.[210] Furthermore, the flow estimation is performed by a pretrained PWC-Net[211] and the contextual information is obtained by using a pretrained ResNet[212] architecture. A U-Net network is then used for the kernel estimation and an adaptive wrapping layer combines all the information flows from each sub-network. In order to ensure that the network predicts residuals between the ground truth frame and the blended frame, the two warped frames are linearly blended. The pretrained network used for transfer learning was trained on the Vimeo90K dataset (82GB) which is a large-scale, high-quality video dataset consisting of 89,800 video clips downloaded from the VIMEO streaming platform. A more detailed explanation about the architecture of the network can be found in the original paper.[209]

2.2.5.4.2. Zooming SlowMo interpolation

An alternative second interpolation algorithm was the Zooming SlowMo network. It is based on a paper published in 2021 by Xiaoyu Xiang *et al.*[213] This network aims to perform video frame interpolation (VFI), but in contrast to DAIN, this network offers at the same time the option to perform a simultaneous video super-resolution (VSR) in the same processing step.

Usually, this task can be achieved in a two-stage process by combining a video frame interpolation method such as DAIN with a single-image super resolution method like GMFN in a two-stage manner. However, since those two tasks are intra-related a two-stage method cannot fully take advantage of this natural property. Furthermore, to predict high-quality video frames, both state-of-the-art VFI and VSR networks would need many parameters to

perform a big frame reconstruction which makes a two-stage STVSR model very computationally expensive.

The Zooming SlowMo network allows for a one-stage process of directly reconstructing high-spatial resolution and high frame rate image sequences. The network uses a deformable feature interpolation network to get feature-level temporal information and combines it with a deformable ConvLSTM to aggregate the temporal information. This allows for handling of motions and effectively leveraging global contexts with simultaneous temporal alignment and aggregation. ConvLSTMs are a type of recurrent neural network that are often used for spatio-temporal prediction. They have convolutional structures between their state transitions. Those networks are specifically good in determining the future state of a certain cell in the grid providing the inputs and past states of its local neighbours. The network achieves state-of-the-art interpolation and spatial resolution upscaling results in one calculation step.

One main difference between Zooming SlowMo and the single-image super resolution approach for resolution upscaling (such as GMFN) is that Zooming SlowMo uses the recurrent neural networks (ConvLSTM) as a sequence-to-sequence (S2S) input information compared to single separated images as inputs for GMFN. Therefore, Zooming SlowMo can leverage also temporal information for the resolution upscaling task which is not available for GMFN. The Zooming SlowMo network consists of four main parts which are a *feature extractor, frame feature temporal interpolation module, deformable ConvLSTM*, and an *HR frame reconstructor*. The feature extractor with a convolution layer first produces feature maps which are then used to synthesize LR intermediate frames in the frame feature interpolation module. Then the ConvLSTM performs a simultaneous alignment and aggregation for the consecutive feature maps. In the last step the HR sequence is constructed from the aggregated feature maps.

Schematic representations of both networks (DAIN and Zooming SlowMo) are shown in Figure 72.

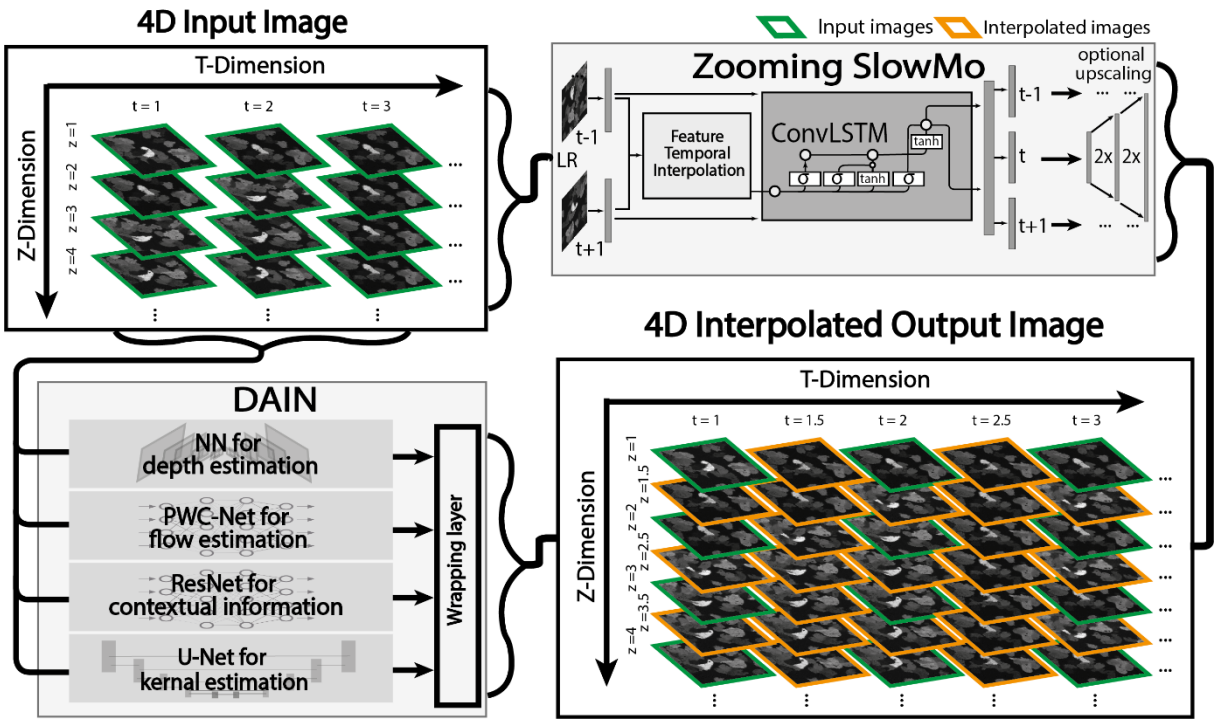

Figure 72: Schematic representation of image interpolation for Zooming SlowMo and DAIN on 4-dimensional input dataset. Low t- and z-dimensional image dataset (top left) used on Zooming SlowMo, interpolating images using a ConvLSTM with an optional convolutional resolution upscaling (top right), compared to DAIN network (bottom left) consisting of 4 different network modules (hourglass network, PWC-Net, ResNet, U-Net) combined with a wrapping layer producing interpolated images in t- and z-dimension (bottom right). Green framed images indicate input images and orange frames indicate interpolated images.

2.2.6. Reliability metrics for image enhancement and image restoration

One of the most fundamental ideas in science is to be able to trust observations from acquired data. If this reliability for the data is not given, the conclusions drawn from the data is prone to error. As the "Eternal Triangle of Compromise" demonstrated in thesis Chapter II, the image quality of modern microscopy image recordings often must be intentionally compromised to improve a certain quality of the recorded images (speed, resolution, or SNR) to be able to capture biological processes. Therefore, restoring or enhancing the quality of an image is important to stretch the boundaries of what is possible to observe. Since some of the image enhancement algorithms can produce unwanted artefacts, it would be desirable to provide the user a measure of uncertainty of the synthesized and enhanced images.

Especially in very powerful data-adaptive deep learning methods where the neural network learns very effectively to adapt to the training data, it makes very strong assumptions about the restored images. This has the advantage that it improves the restoration quality of the

image but also poses the risk of creating artefacts that look very realistic and cannot be detected by human specialists.

The current computer vision research is mostly driven by standardized benchmark datasets, which are used to compare the results of different algorithms on an agreed-upon problem. The used evaluation protocols for these benchmark datasets do not take the prediction uncertainty into account which also does not incentivise other researchers to do so.

There are two main types of uncertainty in the context of modelling, i) *aleatoric* uncertainty and ii) *epistemic* uncertainty.

Aleatoric uncertainty describes an intrinsic uncertainty which is not avoidable. Even in a perfect situation of capturing the same image under the microscope twice, the camera of the microscope will never be able to capture the image situation exactly twice because of the randomness of excitation and collection of photons. Furthermore, there is an inherent uncertainty for the noise observations for any given acquisition. Therefore, there is not a single value capturing this kind of uncertainty but rather a distribution that captures the probability of a given uncertainty.

On the other hand, *epistemic* uncertainty can be improved and reduced if more data and information about the observation is available. If a model got trained on a small dataset the model uncertainty for reconstructing a correct representation of the image is high. This uncertainty can be reduced by collecting additional data and training the network on this bigger dataset. To assess whether neural network created images are close to real observations it is important to perform evaluations which can determine the quality of the reconstructed images.

2.2.6.1. Assessment metrics for image enhancement

To assess the quality of an image enhancement algorithm two evaluation methods can be performed: i) human perception-based subjective evaluation and ii) quality metric-based evaluation. The first evaluation method (subjective evaluation) by human perception is a more direct way but suffers from the limitations of personal preference and bias, and that the evaluation process is very time consuming and cannot be automated. In contrast, the objective evaluation by using certain mathematical evaluation metrics often lacks consistency between each other. The most common mathematical evaluation metrics also used in this research are *peak-signal-to-noise ratio (*PSNR), *structural similarity index measure (*SSIM*)* and *root-mean-square error* (RMSE). All three-assessment metrics can be used if a ground truth image

of the newly synthesized image is available. In that case, the two images can be compared on a pixel-by-pixel basis to calculate a numerical value that can easily be compared between different methods which can perform the same tasks.

2.2.6.1.1. Peak signal-to-noise ratio

The peak signal-to-noise ratio (PSNR) is the most widely used full-reference objective quality assessment metric for image restoration (e.g. SR, denoising, and deblurring). PSNR is defined by the ratio of maximum power signal to the power of noise signal. It describes the difference between the ground truth and prediction in decibels by using the mean-square-error between the images. This metric is more concerned with the proximity between pixels which sometimes can lead to lower consistency with perceptual quality. The higher the score the better the agreement with the compared ground truth image. In the case of a colour image with RGB values for each pixel, the PSNR can be calculated with the mean-square error (sum over all squared value differences divided by the total number of pixels and channels). If a ground truth image is described as X and $\bar{X}$ is the from the network synthesized image, where $\mathrm{H} \times \mathrm{W} \times \mathrm{C}$ denotes the height, width, and channels of the two images, the calculation of PSNR follows the following formula:

$$PSNR = 10 * log_{10}\left(\frac{L^2}{MSE}\right) \quad \text{Equation (17)}$$

where MSE is the mean-square-error between X and $\bar{X}$ and L represents the maximum pixel value (i.e. 255 for an 8-bit image) of each pixel dimension and MSE is defined as follows.[214]

$$MSE = \frac{1}{\mathrm{H}\times\mathrm{W}\times\mathrm{C}}\sum_{i=1}^{\mathrm{H}\times\mathrm{W}\times\mathrm{C}}(X(i) - \bar{X}(i))^2 \quad \text{Equation (18)}$$

2.2.6.1.2. Structural similarity index measure

The structural similarity index measure (SSIM) is an objective quality assessment metric and is used to measure the image quality by evaluating the perceptual difference of two compared images.[214] SSIM is a normalized metric where values closer to 1 correspond to better similarity. In contrast to PSNR, SSIM maps do not compare on a pixel-per-pixel basis but are considering the surrounding structural similarity in aspects of luminance, contrast, and structure in the neighbourhood of the pixel of interest. SSIM is therefore defined as follows:

$$SSIM = [l(X,\hat{X})]^{\alpha}\,[c(X,\hat{X})^{\beta}\,[s(X,\hat{X})]^{\gamma} \quad \text{Equation (19)}$$

where

$l\,(X,\hat{X}) = \frac{2\mu X\mu\,\hat{X} + C_1}{\mu X^2 + \mu\hat{X}^2 + C_1}$, $c(X,\hat{X}) = \frac{2\sigma X\sigma\,\hat{X} + C_2}{\sigma X^2 + \sigma\hat{X}^2 + C_2}$, $s(X,\hat{X}) = \frac{\sigma X\hat{X} + C_3}{\sigma X + \sigma\hat{X} + C_3}$ Equations (20-23)

α, β, and γ are weighting parameters. μX and σX denote the mean and standard deviation of X, respectively. Similarly, $\mu\hat{X}$ and $\sigma\hat{X}$ denote the mean and standard deviation of $\hat{X}$, respectively. $\sigma X\hat{X}$ is the covariance between $\hat{X}$ and X. C_1, C_2, and C_3 are constants. Further, the previous equation can be simplified when α = β = γ = 1 and C3 = C_2/2 as

$$SSIM = \frac{(2\mu X\mu\hat{X} + C_1)(2\sigma X\hat{X} + C_2)}{(\mu X^2 + \mu\hat{X}^2 + C_1)(\sigma X^2 + \sigma\hat{X}^2 + C_2)} \qquad \text{Equation (24)}$$

SSIM captures in comparison to PSNR visual qualities better and the notation mSSIM is usually used to as an average value of SSIM calculated across the entire window of both images.[214]

2.2.6.1.3. Root-Mean-Squared-Error

The root-mean-square-error (RMSE) map is a metric that displays the root square difference between the normalized synthesized image and the target ground truth image. The smaller the values for the RMSE are the better is the accordance with the ground truth image. However, this value cannot be used to compare different type of data since the measured number is dependent on the scale of the numbers used. Therefore, RMSE is a measure of accuracy that can be used to compare the performance of different models for a particular dataset and not between datasets, as it is scale-dependent.[215] The RSE map with perfect agreement would result in a dark image. The RMSE is the average difference of all pixels in the image with the ground truth. RMSE is sensitive to outliers because single large errors have disproportional large effect on the RMSE due to the squaring of the value.[216,217]

2.3. Aims and Objectives

The second part of this PhD research project was to implement existing deep learning algorithms that improve the limitations of the "Eternal Triangle of Compromise" in regard of signal-to-noise ratio, imaging frequency, and spatial image resolution which should allow imaging of **FLCS1**-labelled lysosomes (see previous thesis Chapter I) over long time periods. This was achieved by: i) using two already implemented AI tools fNET and CARE neural network; ii) implementing three image resolution upscaling networks, i.e., GMFN, SRFBN-S and Zooming SlowMo; iii) implementing two image interpolation neural networks DAIN and

Zooming SlowMo. The improvement of these enhancement algorithms was tested for improvements on tracking results on simulated and real-life data.

- The fNET network was used to test the possibility to train it to recognize the lysosomal compartments by artificially labelling brightfield images after training with collected brightfield and fluorescence image pairs. This would allow lysosomal compartments to be monitored without using fluorescence microscopy.
- The CARE neural network was used for de-noising low SNR images after training it on collected high and low SNR image pairs enabling longer recordings of the lysosomal compartments with low laser power.
- Three image resolution upscaling neural networks (GMFN, SRFBN-S and Zooming SlowMo) were implemented and tested to perform image resolution upscaling on different benchmark datasets and the results were compared with classical BIL and BIC spatial resolution upscaling methods. This allowed us to record image sequences in lower special resolution therefore reducing the laser exposure to the specimen and enabling faster imaging speeds or/and longer recording times.
- Two frame interpolation neural networks (DAIN and Zooming SlowMo) were implemented and tested on their performance on multi-dimensional time series datasets and the results were compared with classical mathematical BIL and BIC frame interpolation techniques. This allowed to increase the image density in t- and z-dimension of 4D (3D + t) datasets therefore, enabling a more reliable tracking of fluorescently labelled lysosomes while reducing the recording speed which lowers the laser exposure and phototoxicity on the sample.
- After implementation and benchmarking of those four image enhancement tools a combination of de-noising, resolution upscaling and image interpolation was used to improve long recordings of lysosomes with point-scanning confocal microscopy.

2.4. Results and Discussion

2.4.1. Artificial lysosome labelling with fNet

The fNET neural network is based on a publication from Johnson *et al.*,[199] where they implemented a U-net architecture that is capable of labelling different cell organelles such as nucleus, mitochondria or cell membrane by providing it with fluorescence and brightfield microscopy pairs for training. For this research, the code was slightly modified, and training

data was collected from SH-SHY5Y cells labelled with **FLCS1** after incubation for 24 h with 0.2% lipofectamine to detect the copper containing lysosomes (see previous thesis Chapter I for experimental details). After labelling, the cells were imaged in z-stack mode on a Leica SP7 confocal microscope at different resolutions (1024 px, 512 px and 256 px) to collect image pairs of brightfield and fluorescence images. The network was then trained with roughly 5 GB of data to teach the neural network to potentially recognize copper containing lysosomes just on the basis of brightfield images. After a 24 h training phase the network was tested on unseen data examples. One representative example is shown in Figure 73.

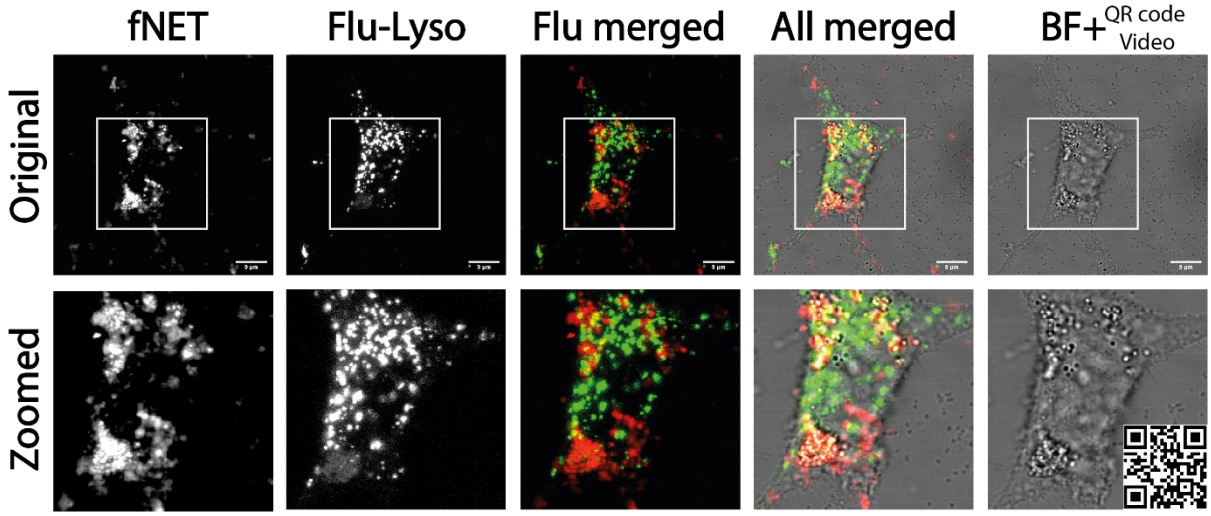

Figure 73: Representative example of artificial labelling of fNET neural network compared to real images of copper(I) containing lysosomes fluorescently labelled with **FLCS1**. Zoomed in sections show no colocalization of the artificial and the real label of lysosomes.

Here the results show that the network confidently learned to recognize certain punctate structures in the brightfield images but when overlaying the images of the real ground truth label of the fluorescence image, the artificial labelling of the fNET neural network labelled lipid droplets instead of lysosomes. When investigating the zoomed-in sections of the image example the lipid droplets can be clearly recognized on the brightfield image whereas the lysosomes are located in parts of the cells where no contrast change is seen in the input image. Therefore, the results demonstrate that fNET is not capable of labelling lysosomes based on brightfield input images.

2.4.2. Denoising with content-aware image restoration (CARE)

To improve the signal-to-noise ratio of fluorescence images the content-aware image restoration (CARE) neural network was used which is based on a publication from Weigert *et al.*[218] It uses a U-Net architecture consisting of a convolutional neural network in combination

with an encoder-decoder structure and is trained on high and low SNR image pairs. The network allows for a reduction of laser power resulting in fewer photons interacting with the sample therefore reducing the phototoxicity and increasing the time that a fluorescent dye can be recorded before bleaching. There the functionality was tested on a synthetic dataset and then the algorithm was used on real-life data of lysosomal movement recorded over time.

2.4.2.1. CARE on simulated dataset

First, the network was tested on simulated synthetic datasets which were created using the ICY plugin from the 2014 ISBI particle tracking challenge.[150] The synthetic dataset produced white particles ("switching uniform") with Brownian motion in a 4D (3D + t) image series in front of a black background. The detailed parameters for the particle simulation with the ICY plugin are provided in Table 7. 1 GB of these simulated moving particle datasets were created and noise was added to it using the ImageJ noise generator (noise level 50) which served as a training dataset for the CARE network. After training the network for 10 h the fine-tuned network was tested on a new sample of noisy data. A representative example of a z-projection of the image input and output of the network can be seen in Figure 74.

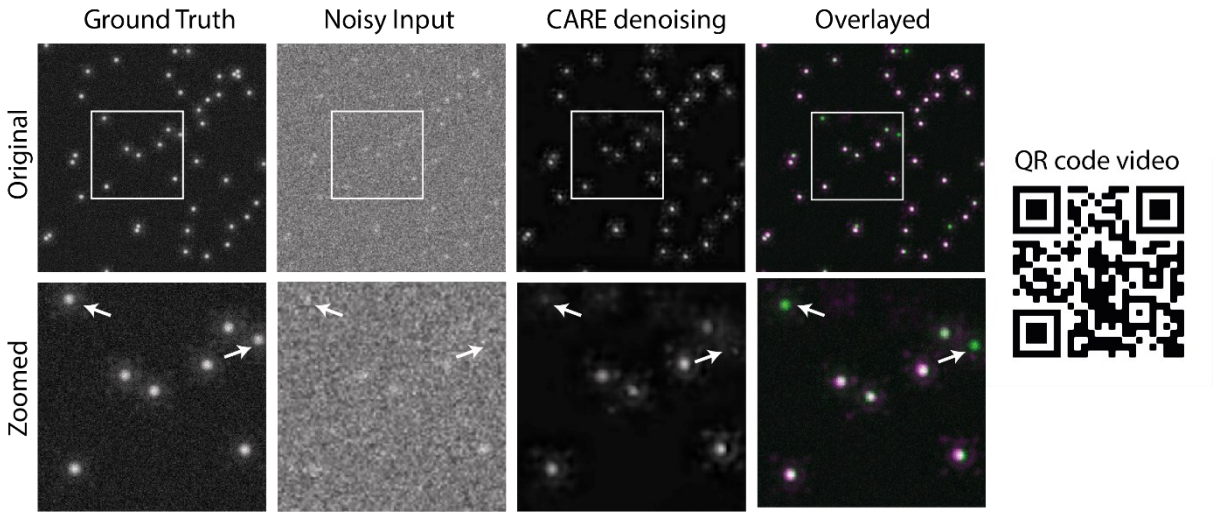

Figure 74: CARE denoising results on simulated noisy dataset. White boxes mark zoomed in sections shown in panel below with white arrows highlighting not recognized particles in the noisy image.

By visual inspection it can be seen that the CARE network is performing reasonably well considering the strong noise level. However, it does make some mistakes which are highlighted with white arrows in the zoomed in section of Figure 74. Furthermore, in the video example it can be observed that the intensity of the denoised particle signals of the CARE network is fluctuating which is not the case in the ground truth image. This fluctuation can be explained by faulty intensity assignments of the CARE network of the dots in the

different z-stack depth levels. In summary, this experiment demonstrates a proof of concept for improving images with very poor SNR levels using the CARE network with the example dataset of white moving particles in front of a black background. Therefore, this same algorithm was then used and fine-tuned on the experimental lysosomal movement dataset.

1.3.4.4. CARE on lysosomal movement dataset

For collecting the high and low SNR image pairs SH-SY5Y cells were labelled with the **FLCS1** dye incubated for 24 h with 0.2% lipofectamine 2000 in the culture media. After washing the cells with PBS and switching back to DMEM with 10% FBS, the training data images were collected on a Leica SP7 confocal microscope using switching laser powers (0.05% and 1%). For every scanned line two images were simultaneously collected with different signal-to-noise ratios for z-stacks at 63x or 40x magnification or 2D+t recordings over several minutes. The collected data were augmented by rotation, horizontal and vertical flipping of the collected images which increased the available dataset for training. The network was trained on roughly 3 GB of high and low SNR image pairs and was tested on an unseen low SNR sample.

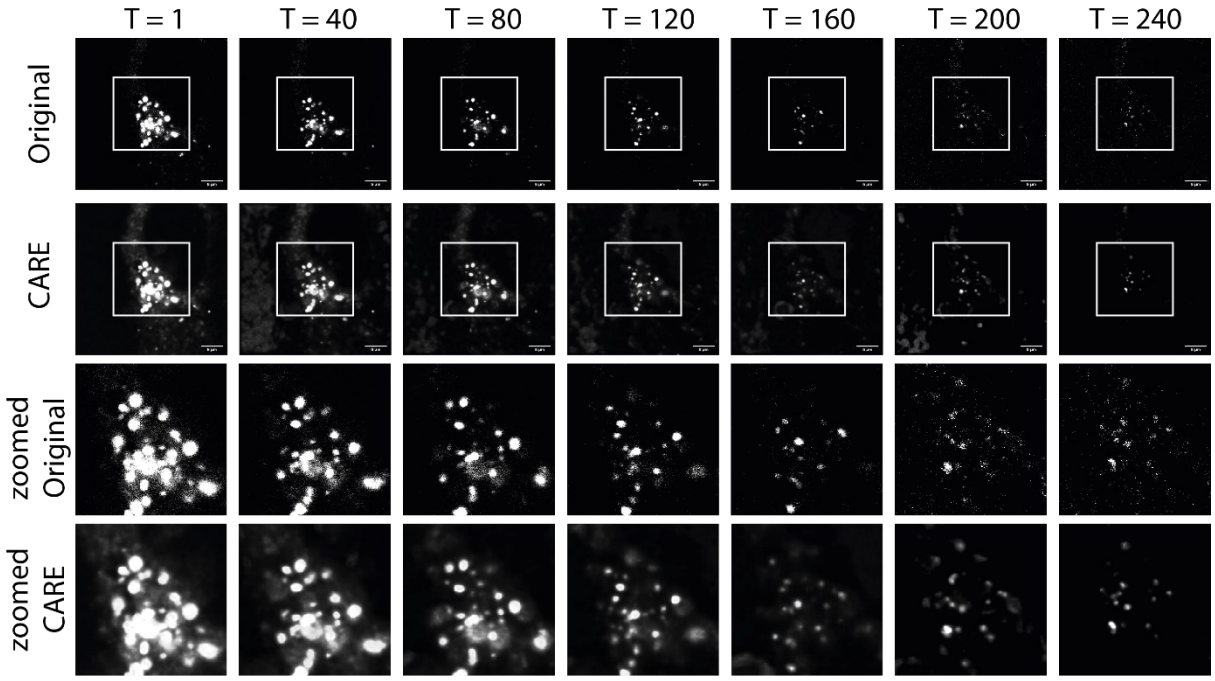

Figure 75: CARE denoising results on real life dataset at different timepoints.

First it was tested whether CARE can recover already bleached areas of the image to a level that is similar to the quality of the non-bleached examples. For this test, images of the labelled cells were recorded for 10 min with high (1%) laser power. After using the CARE denoising

neural network on this dataset the visual inspection shows that there is no quality improvement for later image slices of the already bleached image areas (see Figure 75).
Next, image z-stacks were recorded over time with high (1%) and low (0.05%) laser power and it was tested whether CARE could improve the image quality of initially low SNR from the low laser power images. As it can be seen in Figure 76, the high laser power shows a strong decline of fluorescence signal from the lysosomes over time, whereas the signal of the low laser power remained weak but constant. After processing the low SNR images with the CARE network, it recovers the lysosomal signals nicely from the background and the signal remains stable of the whole imaging period (see Figure 76b).

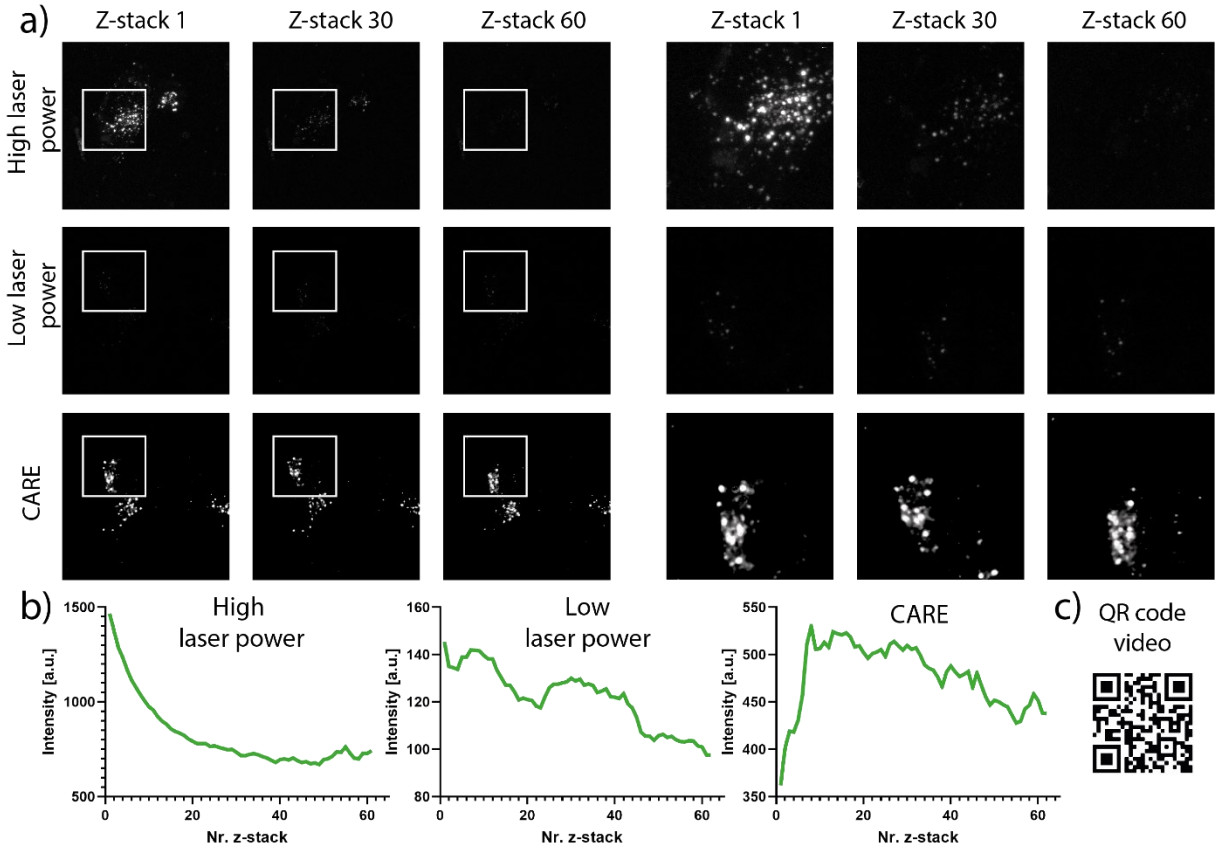

Figure 76: a) Fluorescence signal comparison of lysosomes in SH-SY5Y cells labelled with **FLCS1** for 24 h with 0.2% lipofectamine recorded with 1% (high, first row) and 0.05% (low, middle row) laser power. CARE network was used on the low laser power image sequence resulting in improved signals (third row). Zoomed in sections shown on the right. b) fluorescence intensity profile of high (left), low (middle) laser power and CARE improved (right) images. c) QR code for video demonstration.

In summary CARE was successfully trained and used on a synthetic and experimental dataset showing promising signal improvements for low SNR images but was unable to recover already bleached signal.

2.4.3. Spatial resolution upscaling with GMFN, SRFBN-S and Zooming SlowMo

To improve the spatial image resolution without compromising on imaging speed the three networks GMFN, SRFBN-S and Zooming SlowMo (ZS) based on published literature[205,206,213] were implemented for this research in form of Google Colab notebooks. In those notebooks the user can perform the training/fine-tuning of the network and the upscaling using the free GPU provided from Google. Since the GMFN and the SRFBN-S have the same backbone structure it was implemented within the same notebook. A screenshot of the basic structure of the two notebooks is shown in Figure 77.

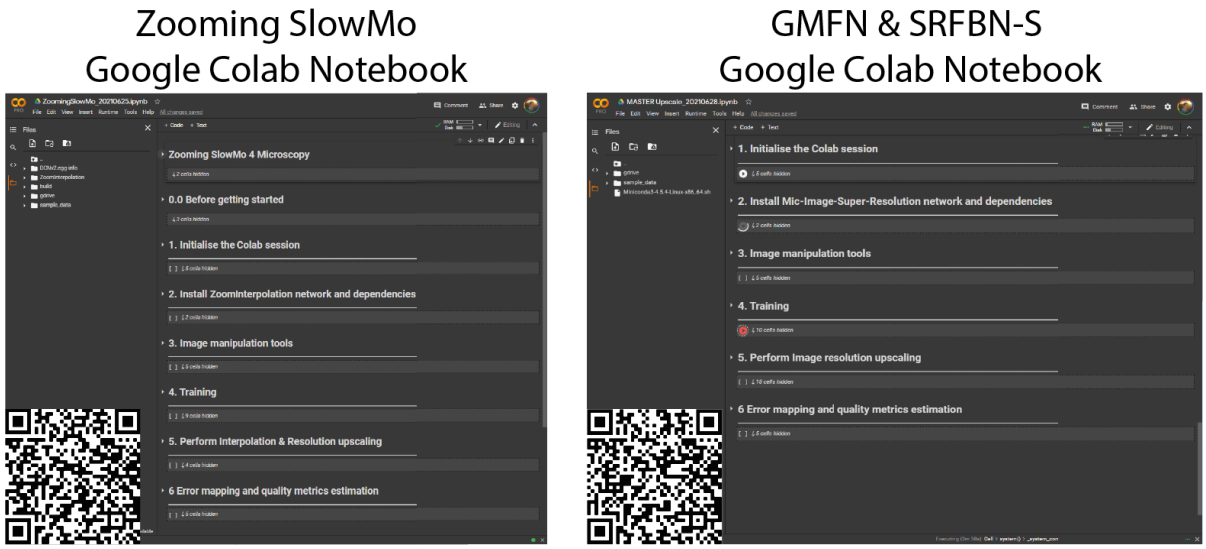

Figure 77: Implemented Google Colab notebooks for Zooming SlowMo and GMFN and SRFBN-S network (combined) with QR-code linked to the website.

The data for training of upscaling can be provided via Google Drive or for bigger quantities via Google Cloud Storage. Furthermore, for the training data preparation a python script was created which allows to process the data off-cloud.

All three networks were tested on three different datasets (BF = brightfield, SDC = spinning disk confocal, Lyso CF = lysosomes with confocal microscope) with two upscaling option (2x and 4x) and were benchmarked against mathematical bilinear (BIL) and bicubic (BIC) upscaling methods. Each neural network was fine-tuned on a subset of the data (2-5 GB for 12-24 h). For every dataset, the ground truth image was first downscaled by a factor of 2x or 4x and then re-upscaled with the different techniques. The quality evaluation was performed within the notebooks comparing the ground truth images with the re-upscaled images of the different upscaling methods. A summary of the quality evaluation together with the file dimensions is presented in Table 1 for 2x resolution upscaling and in Table 2 for 4x resolution

upscaling. In all provided examples all three neural network outperformed their mathematical counterparts and the GMFN network performed slightly better than ZS for most cases. Visual differences between the neural networks were relatively small but more obvious compared to the classical methods. The visual comparisons are presented in Figure 78 to Figure 85.

Table 1: 2x spatial resolution upscaling results of quality metrics comparison of the different datasets with the different upscaling methods.

2x							
		LR	HR	slice	SSIM mean	RMSE mean	PSNR mean
BF	GMFN	256	512	11	0.964	0.092	38.348
	ZS	256	512	11	**0.966**	**0.091**	**38.493**
	SRFBN-S	256	512	11	0.963	0.092	38.135
	BIC	256	512	11	0.956	0.102	35.605
	BIL	256	512	11	0.925	0.120	32.631
SDC	GMFN	256	512	13	**0.730**	**0.157**	**29.994**
	ZS	256	512	13	0.728	0.157	29.978
	SRFBN-S	256	512	13	0.726	0.157	29.932
	BIC	256	512	13	0.705	0.158	29.780
	BIL	256	512	13	0.678	0.161	29.481
Lyso CF	GMFN	256	512	11	**0.774**	**0.141**	**26.306**
	ZS	256	512	11	0.771	0.143	26.270
	SRFBN-S	256	512	11	0.763	0.143	26.259
	BIC	256	512	11	0.713	0.150	25.492
	BIL	256	512	11	0.689	0.154	25.023

Table 2: 4x spatial resolution upscaling results of quality metrics comparison of the different datasets with the different upscaling methods.

4x							
		LR	HR	slice	SSIM mean	RMSE mean	PSNR mean
BF	GMFN	256	1024	11	0.846	0.121	33.914
	ZS	256	1024	11	**0.847**	**0.121**	**33.943**
	SRFBN-S	256	1024	11	0.842	0.122	33.725
	BIC	256	1024	11	0.825	0.128	32.491
	BIL	256	1024	11	0.786	0.139	30.737
SDC	GMFN	128	512	13	**0.620**	**0.168**	**28.746**
	ZS	128	512	13	0.619	0.168	28.736
	SRFBN-S	128	512	13	0.619	0.168	28.720
	BIC	128	512	13	0.601	0.170	28.407
	BIL	128	512	13	0.576	0.173	28.018
Lyso CF	GMFN	128	512	11	**0.638**	**0.161**	24.102
	ZS	128	512	11	0.637	0.161	**24.109**
	SRFBN-S	128	512	11	0.638	0.161	24.102
	BIC	128	512	11	0.623	0.166	23.455
	BIL	128	512	11	0.611	0.169	23.069
PSSR	ZS	125	500	42	**0.408**	**0.241**	**22.659**
	PSSR	125	500	42	**0.408**	**0.241**	**22.648**
	BIC	125	500	42	0.380	0.260	21.371
	BIL	125	500	42	0.398	0.253	21.861

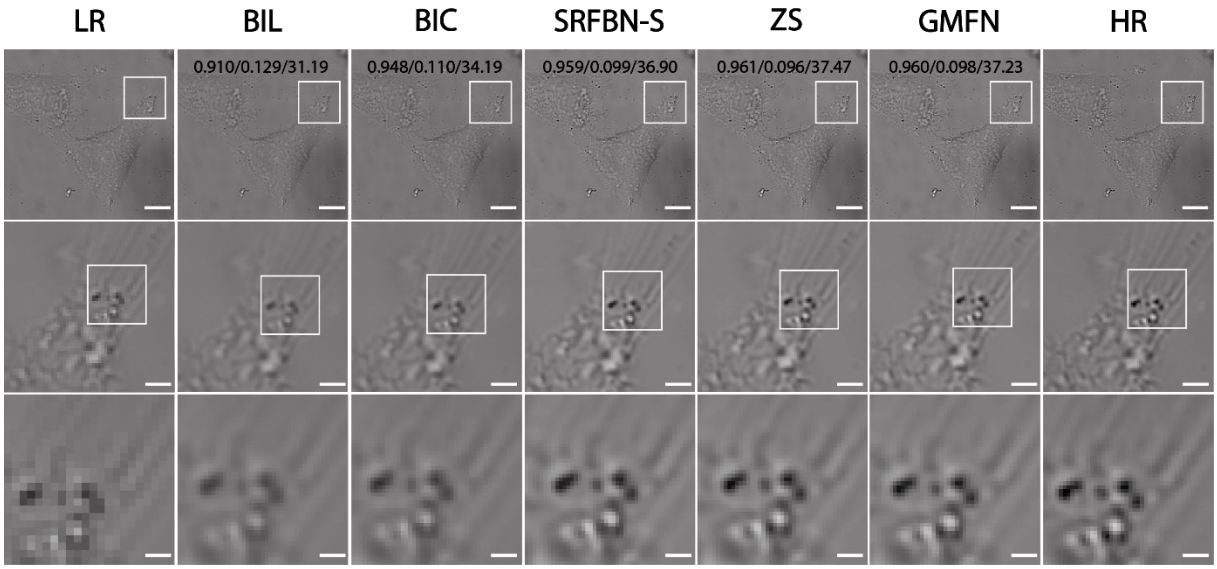

Figure 78: 2x spatial resolution upscaling (256 px – 512 px) of SH-SY5Y cells recorded with brightfield microscope. Scale bars correspond to 10/2.5/0.85 µm for the different zoomed sections, respectively.

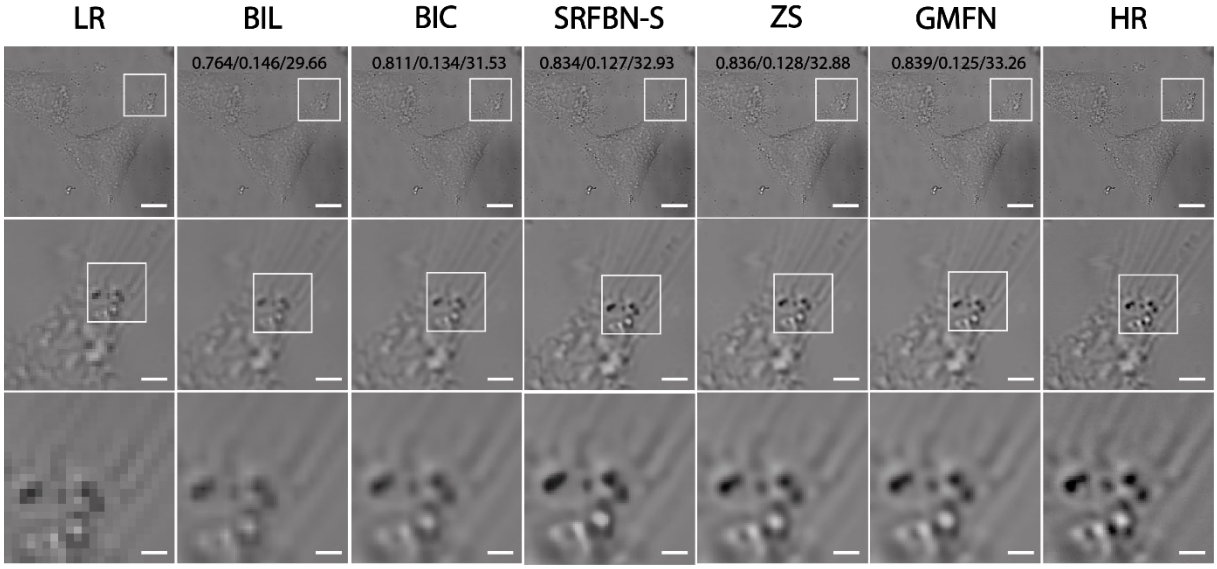

Figure 79: 4x spatial resolution upscaling (256 px – 1024 px) of SH-SY5Y cells recorded with brightfield microscope. Scale bars correspond to 10/2.5/0.85 µm for the different zoomed sections, respectively.

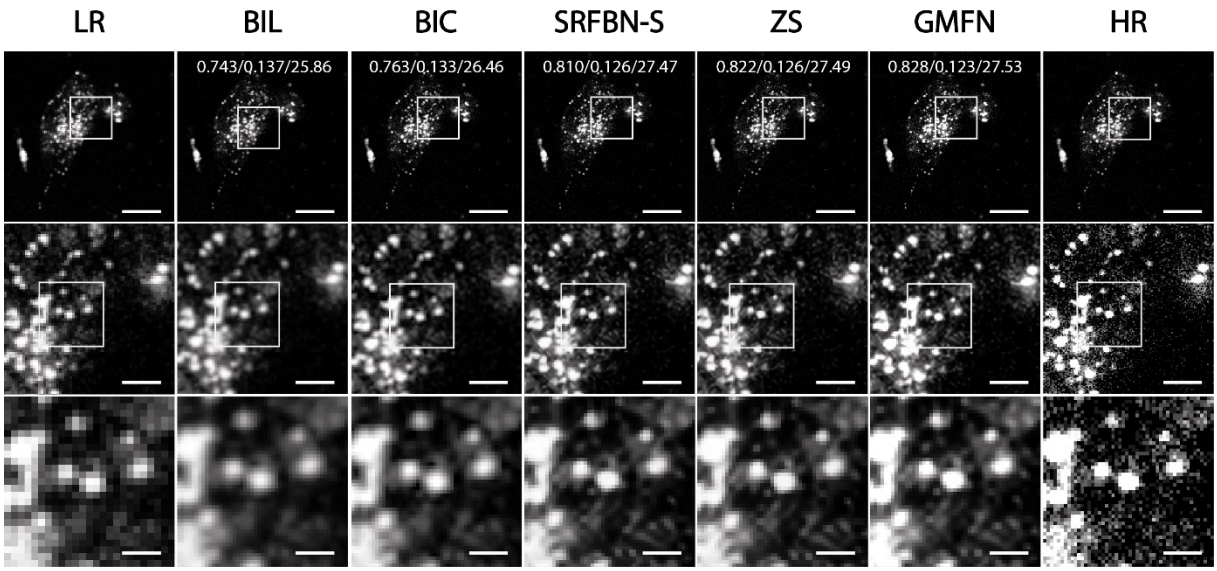

Figure 80: 2x spatial resolution upscaling (256 px – 512 px) of lysosome labelled with **FLCS1** in SH-SY5Y cells recorded with confocal microscope. Scale bars correspond to 20/5/2 µm for the different zoomed sections, respectively.

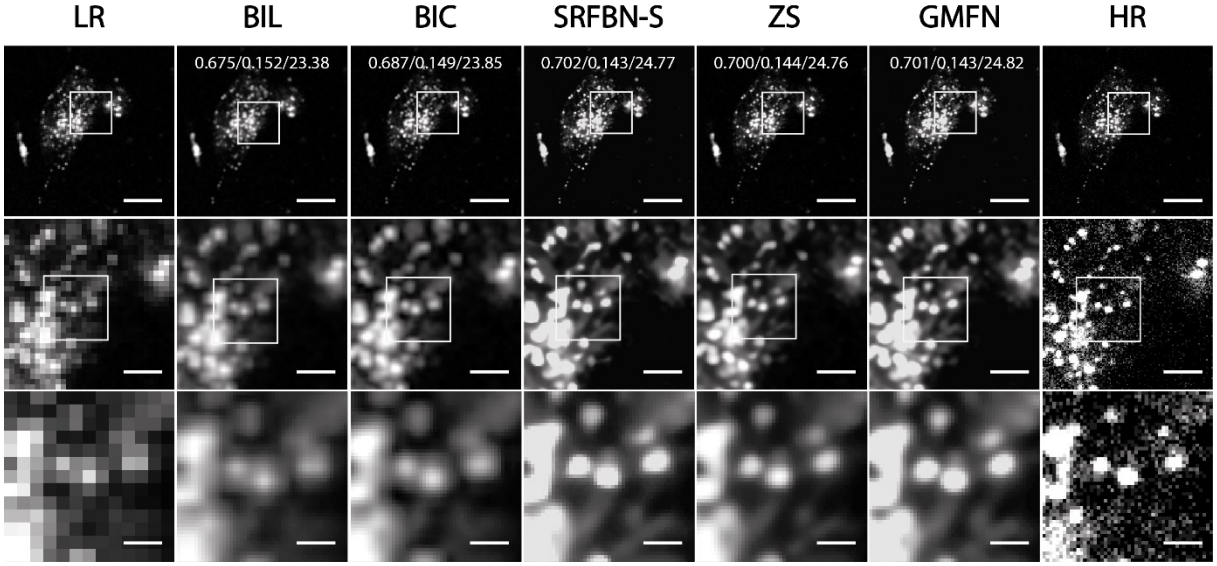

Figure 81: 4x spatial resolution upscaling (256 px – 1024 px) of lysosome labelled with **FLCS1** in SH-SY5Y cells recorded with confocal microscope. Scale bars correspond to 20/5/2 µm for the different zoomed sections, respectively.

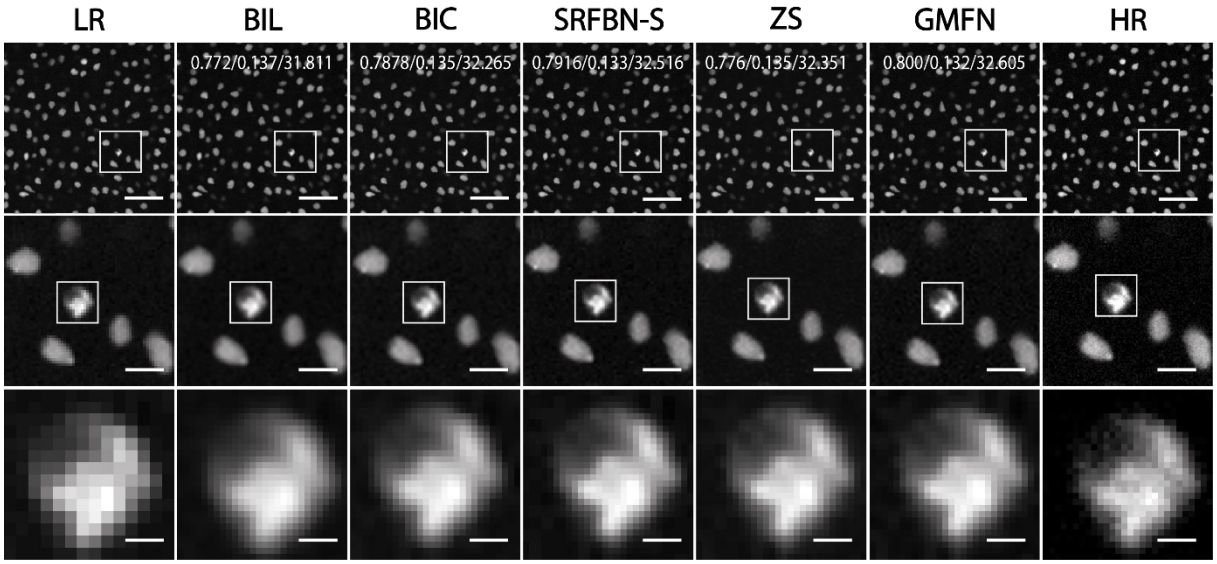

Figure 82: 2x spatial resolution upscaling (256 px – 512 px) of Hoechst 33342 labelled nuclei in Dictyostelium discoideum cells recorded with spinning disk confocal microscope. Scale bars correspond to 20/5/1.25 µm for the different zoomed sections, respectively.

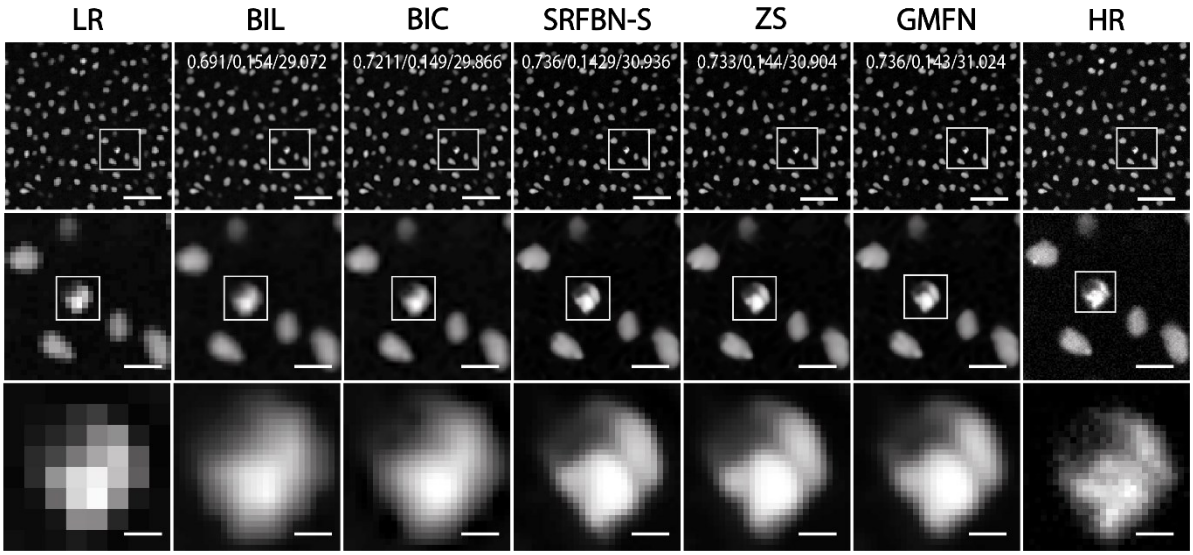

Figure 83: 4x spatial resolution upscaling (256 px – 1024 px) of Hoechst 33342 labelled nuclei in Dictyostelium discoideum cells recorded with spinning disk confocal microscope. Scale bars correspond to 20/5/1.25 µm for the different zoomed sections, respectively.

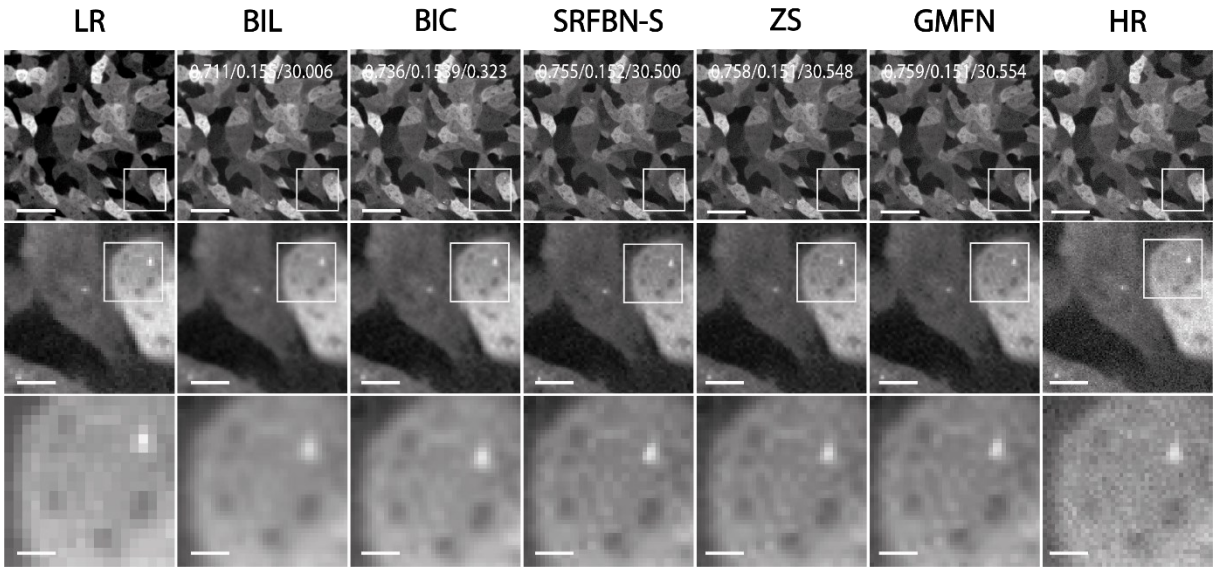

Figure 84: 2x spatial resolution upscaling (256 px – 512 px) of labelled Dictyostelium discoideum cells recorded with spinning disk confocal microscope. Scale bars correspond to 20/5/1.5 µm for the different zoomed sections, respectively.

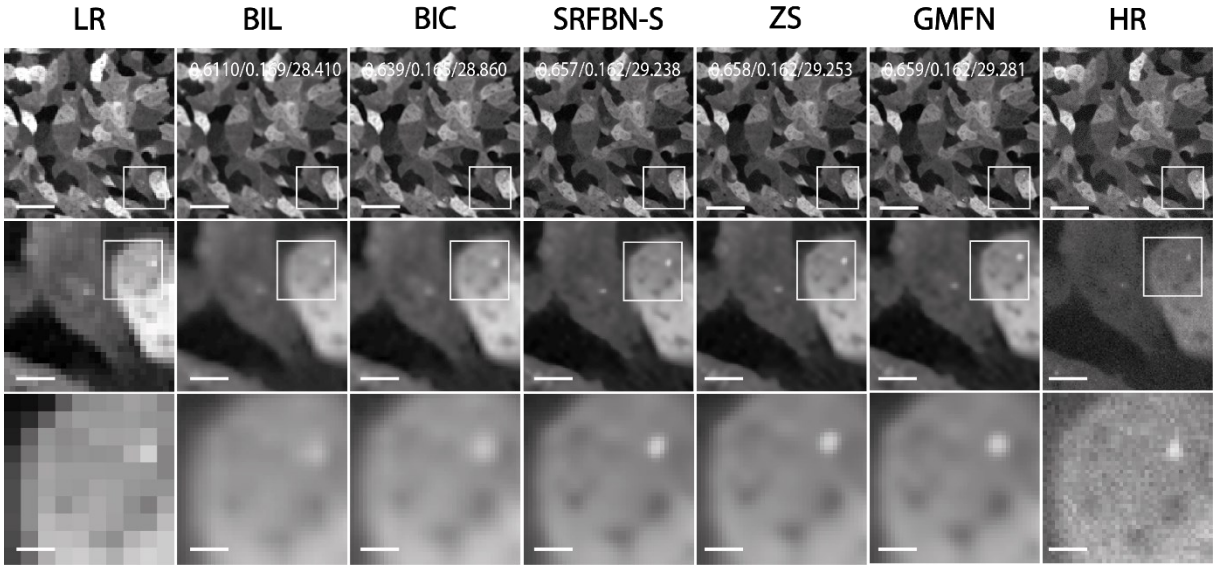

Figure 85: 4x spatial resolution upscaling (256 px – 1024 px) of labelled Dictyostelium discoideum cells recorded with spinning disk confocal microscope. Scale bars correspond to 20/5/1.5 µm for the different zoomed sections, respectively.

In the 4x upscaling option one more dataset was tested with the ZS upscaling functionality as described in the literature[180] where the authors used noisy electron microscopy data and trained their neural network (PSSR) to perform a 4x spatial resolution upscaling based on training of the network with downscaled images where gaussian noise was artificially introduced to the training data. With this dataset the ZS network was also trained and

compared with the results of the PSSR network reported in that paper. Based on the evaluation metrics the results indicate that ZS has equal and sometimes slightly better-quality results. The GMFN and SRFBN-S network were not able to cope with this dataset since it contained a lot of noises which resulted in very strong visual artefacts for those two networks. Representative examples of this dataset are presented in Figure 86 and the quality metrics differences between ZS and PSSR are shown in Figure 87.

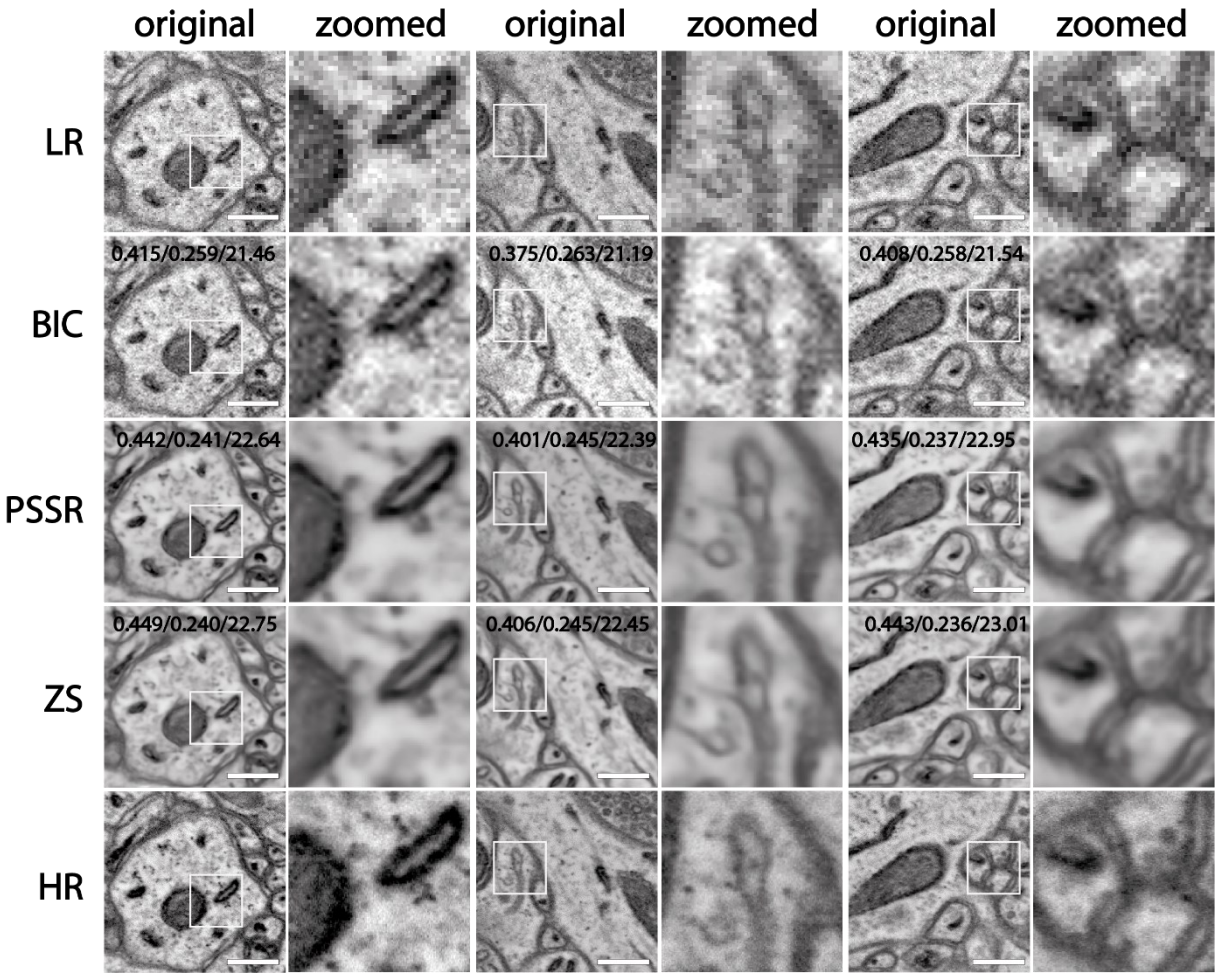

Figure 86: 4x spatial resolution upscaling comparison of electron microscopy dataset including the PSSR network result. PSSR upscaling results was taken with permission of the publisher from the following reference.[180] Scale bars size is 1.5 µm.

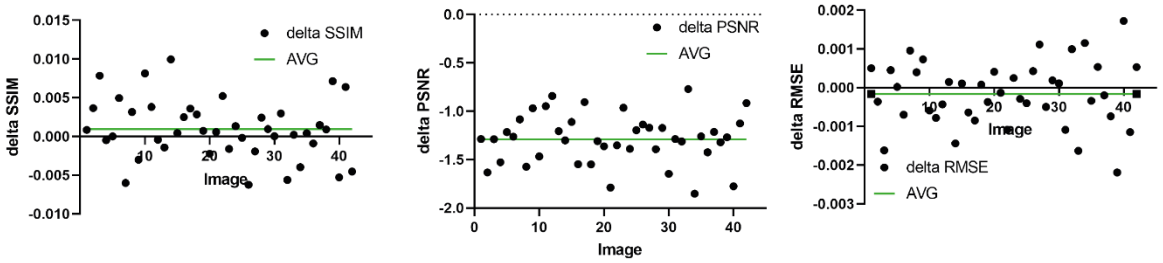

Figure 87: Quality metric comparison of Zooming SloMo with PSSR showing the value difference of all provided images for comparison.

Based on these results, all three neural networks perform significantly better than classical mathematical interpolation techniques such as BIL or BIC. In most cases the GMFN network performed slightly better than ZS which was again better than SRFBN-S. However, in certain cases such as for noisy datasets, ZS performs significantly better than GMFN or SRFBN-S and ZS was equally as good as the PSSR network.[180]

2.4.4. Content-aware-frame-interpolation with Zooming SlowMo (ZS) and DAIN

Next, the possibility of improving the frame rate of multi-dimensional microscopy datasets with frame interpolation tools was explored. This would allow to reduce the frame acquisitions in t- and z-dimension which lowers the laser illumination dose on the specimen. The resulting reduced phototoxicity and photobleaching would enable longer recordings without compromising on cell health and image stack quality. It would also achieve a higher image density which could be beneficial for tracking of fast cellular processes. If point-scanning systems (like confocal microscopy or EM) require higher image resolutions, the reduced imaging speed could be compensated with the interpolation algorithm which maintains a high imaging frequency while achieving a higher resolution. These three examples clearly demonstrate the potential benefits of frame interpolation tools for increasing the frame density of any microscopy modality. Classical mathematical interpolation techniques such as frame duplication, or bilinear (BIL) or bicubic (BIC) frame interpolation or simple frame duplication (NONE) techniques can increase the frame frequency but do not consider moving objects. Therefore, developing computational tools that artificially increase the frame rate while considering moving objects have the potential to be transformative and can push the limits of any frame rate limiting microscopy modality.

In the rapidly advancing computer vision sub-field of video frame interpolation (VFI), several deep learning frameworks have been implemented for increasing the frame rate of videos to produce slow motion movies.[219] Although critical benchmark studies have been carried out to evaluate which network has the best performance and the least visual artefacts, none of the well performing networks has yet been implemented for performing their tasks on microscopy image sequences.

Using deep learning image prediction to artificially increase the frame rates of multi-dimensional microscopy datasets has the potential to be beneficial for any microscopy modality in need for higher image frequencies. However, the interpolation task is not trivial and frame interpolation neural networks are known to sometimes produce visual artefacts[209,220] that could mislead researchers to draw faulty conclusions on biological processes.

To test the capabilities of such frame interpolating networks, two state-of-the-art content-aware-frame-interpolation networks (Zooming SloMo (ZS)[213,221] and Depth-Aware Video Frame Interpolation (DAIN)[209]) were implemented and their ability to increase the image frequency of time-lapse 3D (4D) microscopy datasets was studied. Both networks have shown competitive performance in various benchmark studies against other VFI networks without producing significant visual artefacts.[213,221,209,222] Furthermore, the ZS network also allows for 2x or 4x pixel resolution upscaling of the image sequence within the same interpolation step as it has been demonstrated in the previous section. Since the original source of ZS was implemented and trained just with the 4-times resolution upscaling, the network was modified to let it perform the interpolation step without and with 2x upscaling and trained it on the Vimeo-septuplet (86GB) dataset as it was done for 4x pixel resolution upscaling in the original paper.[213] The two implemented frame interpolation prediction networks were used on six different datasets, tracking performance comparisons on simulated and real-life data was carried out, and the interpolation results of the networks were evaluated by comparing their strengths and weaknesses on 4 different imaging modalities (confocal, brightfield, spinning disk confocal and electron microscopy).

These are the first neural network implementations used to increase the image frequency by artificially interpolating images in the t- and z-dimension of 4D microscopy datasets. The neural networks were made publicly available on the ZeroCost4DLMic platform[223] which makes it easily available to the wider scientific community and allows to fine-tune the network and post-process the microscopy images on the free GPU provided by Google Colab.

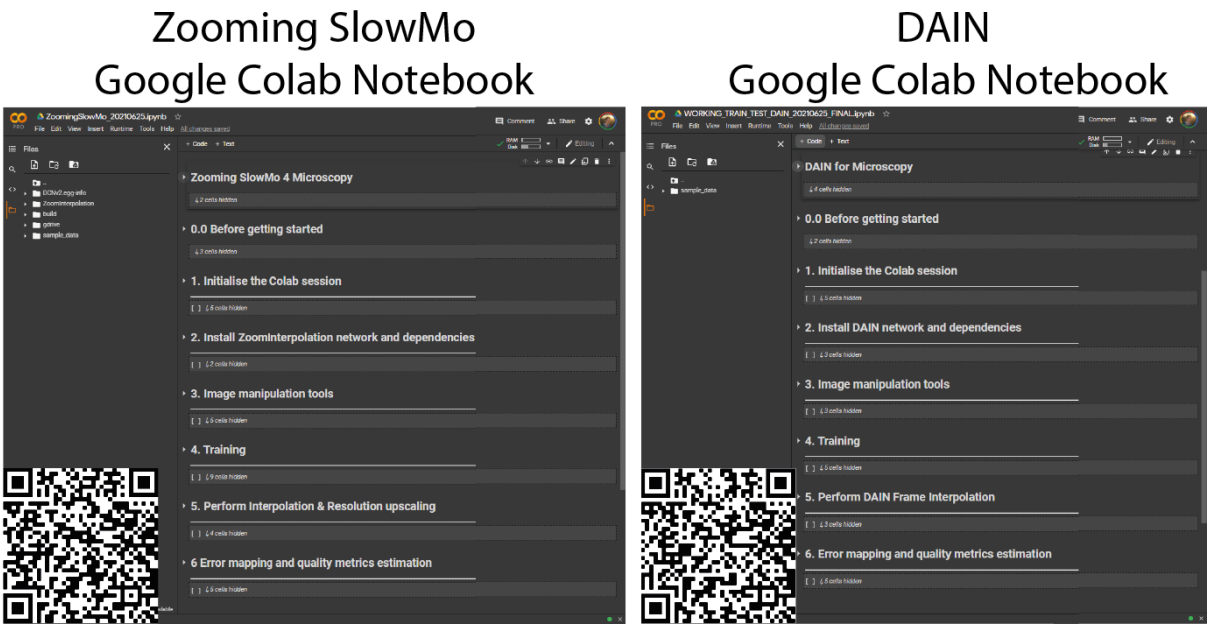

Figure 88: Implemented Google Colab notebooks for Zooming SlowMo and DAIN with QR-code linked to the websites.

2.4.4.1. Zooming SlowMo (ZS) and DAIN on mitochondria movement dataset

Initially the neural network tools were tested on a mitochondrial movement dataset and their performance was compared with classical interpolation techniques such as bicubic (BIC), bilinear (BIL) interpolation and frame duplication (NONE). The quality of the interpolated images was evaluated by visual inspection, and with objective metrics such as Structural Similarity (SSIM), Root-Mean-Square-Error (RMSE) and Peak-Signal-to-Noise Ratio (PSNR). First ZS and DAIN were used with the provided pretrained models trained on a large amount of video data. Already without any fine-tuning both networks performed significantly better than the classical techniques (see Figure 89 for representative examples). After short fine-tuning of Zooming SlowMo (FT ZS) and DAIN (FT DAIN) (2 GB for 2h) the performance improved even further (see quality metrics in Figure 89g). ZS captured movement patterns on the mitochondria branches most accurately and could interpolate movement patterns with great precision (see Figure 89a-f). A video demonstration of 2x and 4x frame interpolation are presented in QR-code link in Figure 89h.

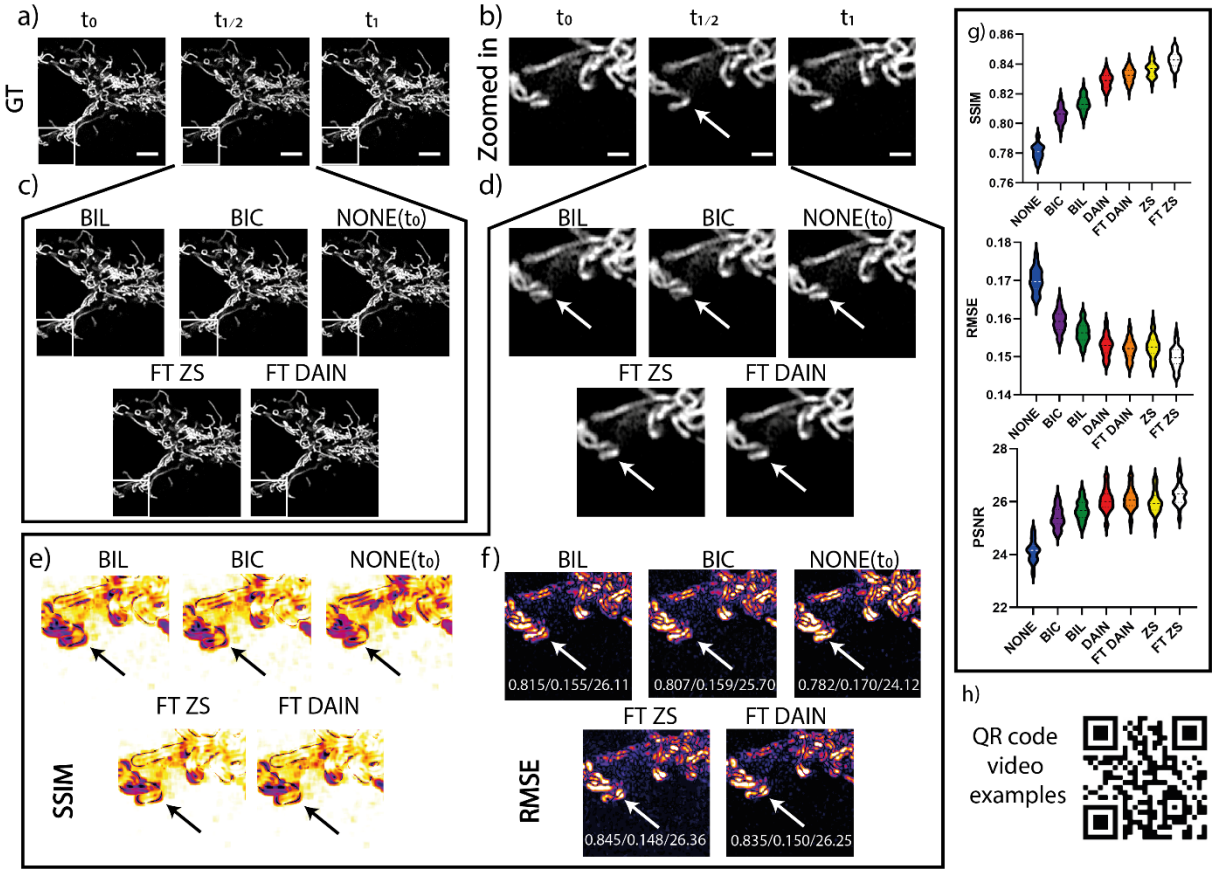

Figure 89: Mitochondrial movement example with 2x frame interpolation using classical NONE, BIC, BIL and neural network FT ZS and FT DAIN interpolation. a) GT image sequence example with b) zoomed in sections; red arrows highlight movement regions (scale bare 5 and 1 µm); c) and d) showing results of different interpolation techniques in original size and zoomed in, respectively; e) showing SSIM and f) RMSR maps of the different interpolation results. ZS produces better-quality results than DAIN and both significantly better results than the classical interpolation techniques. g) PSSR, SSIM and RMSE of 49 interpolated images of mitochondria image sequences compared with each method including best performing fine-tuned Zooming SlowMo (FT ZS). h) QR-code for video example.

2.4.4.2. Predicting simulated particle motion with ZS and DAIN

To investigate the performance of the networks further and to objectively compare the predicted interpolation results, different interpolation techniques were tested on a synthetic dataset of simulated white particles moving in front of a dark background. The synthetic dataset provided the opportunity to control all the parameters such as particle speed, SNR, Brownian motion, sequence dimensions and frame density in z- and t-dimension. Furthermore, it provided the ground truth of the particle locations allowing for easy comparison of the tracking results after frame rate enhancement. The neural network predictions were compared to the results with the bilinear frame averaging (BIL) interpolation method which was the best performing classical technique from the previous experiment. First, the ability of the networks

to cope with increasing particle movement speeds ("switching uniform" with 0.3 Brownian motion) in the t-dimension was evaluated. From a high image frequency synthetic dataset, an increasing number of images between each time point was removed, resulting in increased particle movement speeds and the removed images were kept as ground truth for quality evaluation. The ZS and DAIN networks were fine-tuned on 500 MB of the synthetic dataset produced with the same parameters as the test data. The visual quality metrics showed that the neural network interpolated images clearly outperform the BIL interpolation and ZS performs better than DAIN. With increasing particle speeds ZS declines faster than DAIN reaching a similar performance for both networks at fast movement speeds (see Figure 90a).

As expected, the quality of the image prediction decreased with higher particle speeds. The interpolated results show that at slow particle speeds both networks are almost indistinguishable from the ground truth images. The visual inspection results of overlaying the time series data (see Figure 90b) show that both networks perform very well on particles with slow to medium speeds but at high movement speeds DAIN's interpolation results start performing better than the ones from ZS. For both networks, when the particle speeds reaches a critical limit, or the particles get closer together while having opposing directions the networks start making mistakes. For DAIN in situations of close proximity to other particles with opposing movement directions it sometimes creates visual artefacts of interpolating the signal in multiple different directions (see Figure 90c middle). ZS however, does not create the particles if the travelled distance from one frame to the next becomes too large (see Figure 90c left) and both networks performed significantly better than the BIL interpolation (see Figure 90c right). This is the reason why ZS shows a steeper drop of image quality at higher movement speeds compared to DAIN.

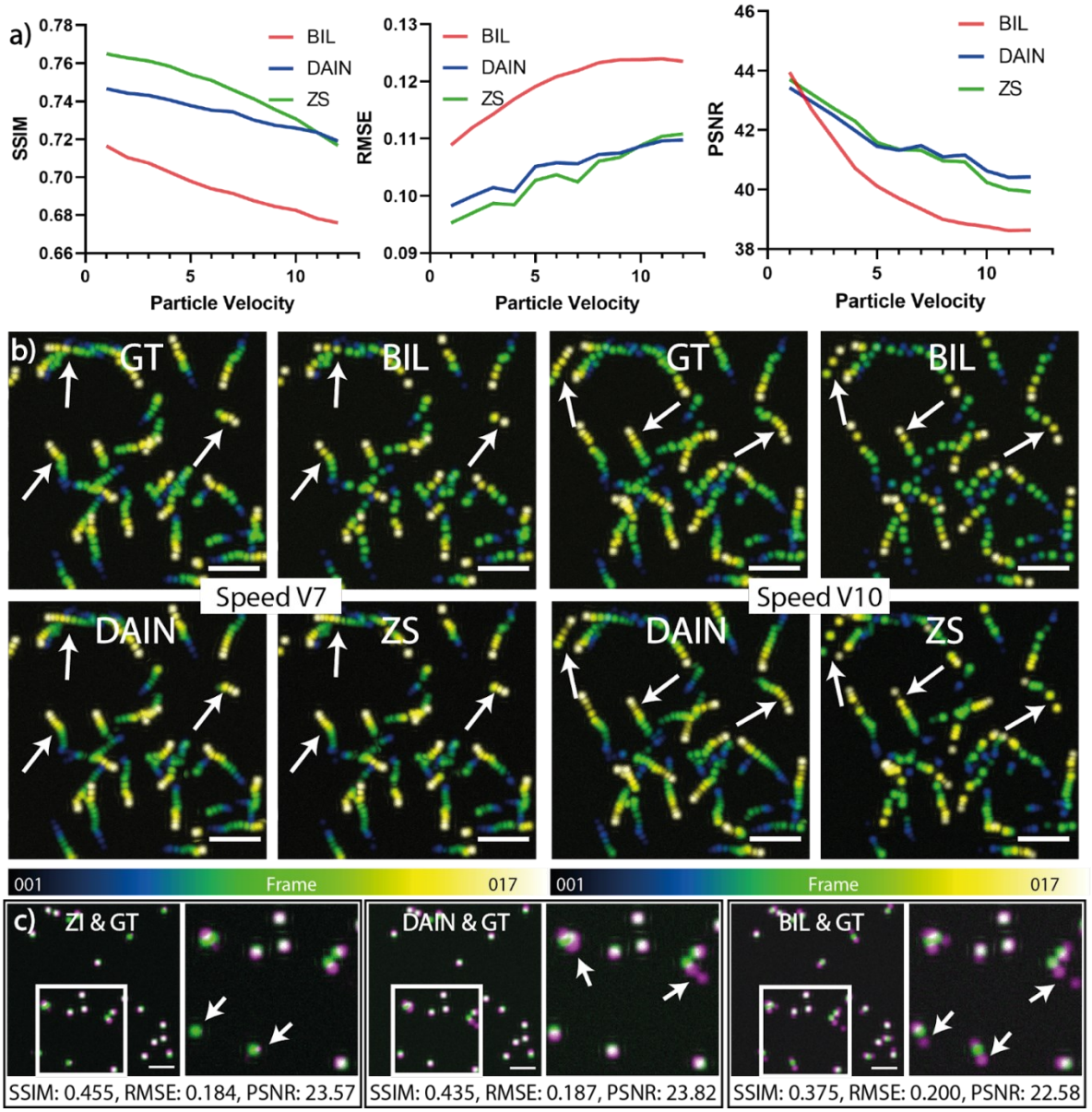

Figure 90: Interpolation in t-dimension: a) Image quality metrics comparison (SSIM, RMSE, PSNR) of simulated dataset interpolation with BIL, DAIN and ZS for increasing particle speeds in the t-dimension. b) Temporal colour coded overlaid projection of image sequences of the different interpolation methods for the particle speeds V7 (left) and V10 (right); white arrows highlighting regions of interest for comparing differences between results, with scale bar size of 100 px. c) Visual artifact comparison of DAIN (left), ZS (middle) and BIL (right) (in magenta) overlaid with GT (in green) of the simulated dataset at particle speed V7 with white boxes indicating zoomed sections displayed next to it; white arrows highlighting regions of interest where different techniques make mistakes. SSIM/RMSE/PSNR values of the presented frame shown below the images. Scale bar size is 50 px for the full image.

Next, the interpolation capabilities of ZS and DAIN in the z-dimension of synthetic z-stack datasets with increased slice distances was investigated.

For this experiment 9 different image z-stacks containing 17 frames with increased slice spacings (50-450 nm) were generated where each z-stack image sequence had the same number of particles within, and the particle height was 900 nm. The “Directed Mix” particle type was chosen here to test the z-interpolation without PSF scattering which would have been present for the particle type used for the previous experiment.

Here, ZS performs marginally better than DAIN on the three quality metrics and both networks were better than the BIL interpolation (see Figure 91a). At low slice spacing ZS performed best, and all three approaches produced good results with little artefacts (see Figure 91b for 200 nm spacing example) but started making mistakes when spacing was increased (see Figure 91c for 400 nm spacing example). After falling below a particle height to slice spacing ratio of 3 (900 nm particle height / 300 nm slice spacing = 3) the quality dropped rapidly for each interpolation method due to an insufficient nyquist sampling of the particle which needs at least 3 slices per particle to be able to do a valid interpolation prediction.

More detailed visual comparisons of these experiments can be found in the Appendix (Figure 139 to Figure 144).

In summary, ZS performs generally better for datasets with moderate movement in both t- and z-dimension. However, ZS makes more mistakes for fast object speeds creating blurry artefacts or letting the object disappear. This is where DAIN’s performance is more stable and should therefore be used for more challenging faster moving objects.

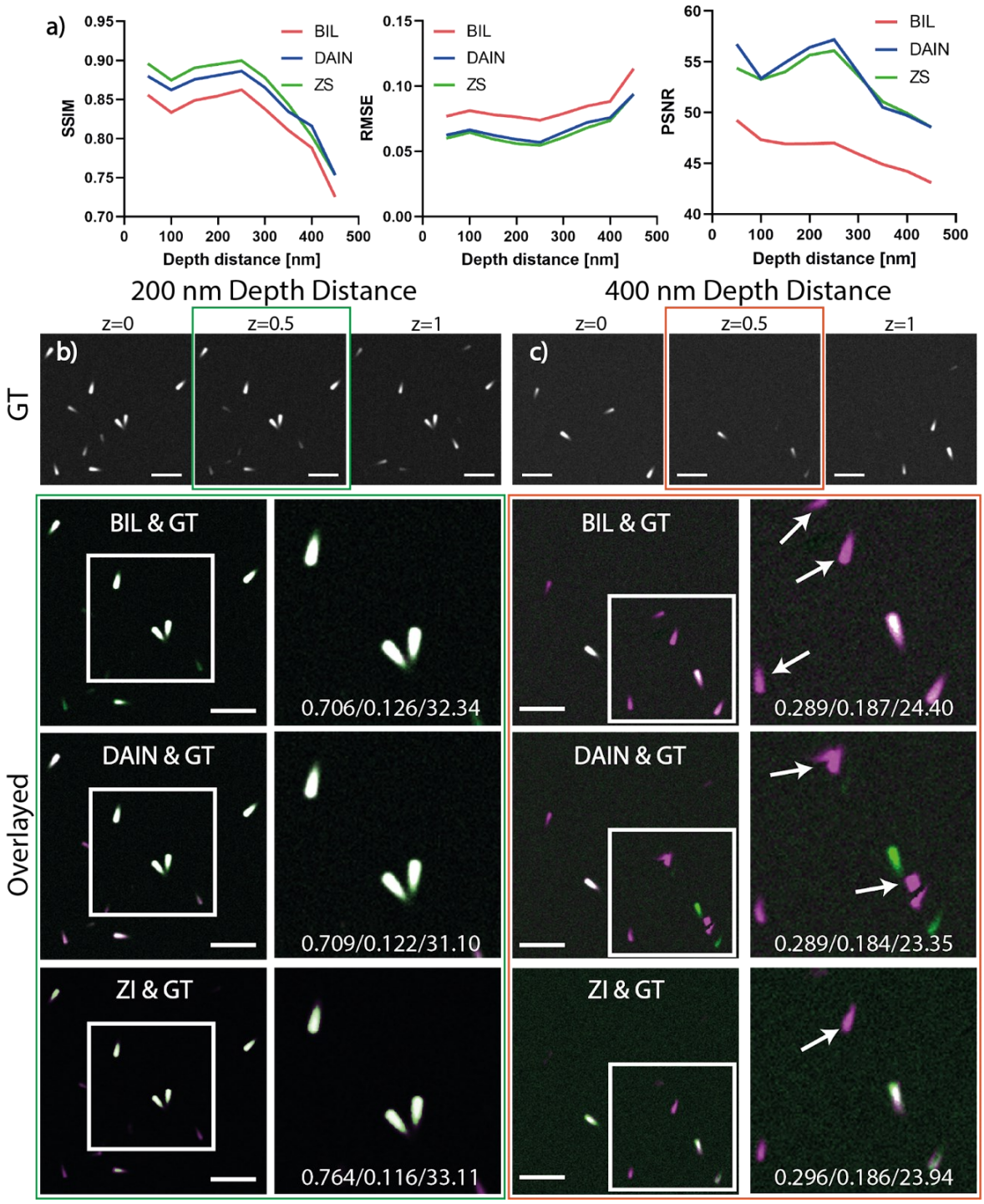

Figure 91: Interpolation in z-dimension: a) Image quality metrics comparison (SSIM, RMSE, PSNR) for z-stack dataset interpolations of BIL, DAIN and ZS with increasing slice distance (50 - 450 nm). b) 200 nm and c) 400 nm z-stack slice GT sequence (top) and visual artifact comparison of interpolated image of BIL, DAIN and ZS (in magenta) overlaid with GT (in green) with white boxes highlighting zoomed areas shown next to original image; white arrows highlighting regions of interest for error comparison. SSIM/RMSE/PSNR values from the image slices are presented in the zoomed in sections.

In summary, ZS and DAIN both performed better than BIL interpolation for temporal and axial interpolation on the simulated particle datasets both for the interpolation in t- and z-

dimension. ZS had slightly better performance for slow to moderately moving particles, however ZS made more mistakes for faster object speeds creating blurry artefacts or letting the object disappear. This is where DAIN's performance is more stable, and it should therefore be used for more challenging faster moving datasets. For interpolation in the axial dimension ZS also performed slightly better than DAIN and both networks showed a steep quality decline when the ratio of particle height to slice spacing distance reached a critical value of 3 (e.g. 900 nm particle height / 300 nm slice distance).

2.4.4.3. ZS and DAIN allow for multi-step 16x temporal resolution improvement

To test the ability of both networks to perform on an extreme case for multi-step interpolation, the densely framed synthetic dataset was down-sampled removing every second image in 4 iterative steps (2x - 4x - 8x - 16x down-sampled) while keeping the removed images as ground truth for comparison. Thereafter, the removed images were re-interpolated (2x - 4x - 8x - 16x interpolation). Both networks were fine-tuned on examples of the same dataset type. After an initial drop in image quality in the first interpolation step for both networks, which is the most demanding one because of the big travel-distance of the particles, the quality for DAIN and ZS just decreases slowly in the following interpolation steps thereafter. Based on the quality metrics both networks show very similar performance in the multi-step interpolation (Figure 92a). When looking into the quality of each interpolated image the quality drop for the centre image between two input images shows the strongest drop for the first interpolation step recovering slightly in the steps thereafter (Figure 92b). The visual inspection shows that for this demanding task of fast-moving particles in the first interpolation step DAIN performs slightly better compared to ZS which lets some particles disappear (see Figure 92c). Furthermore, the simulated Brownian motion of the synthetic particles get lost in those interpolated images for both networks. However, the general direction of the particles can be captured very well with these interpolation techniques (see arrows in Figure 92c).

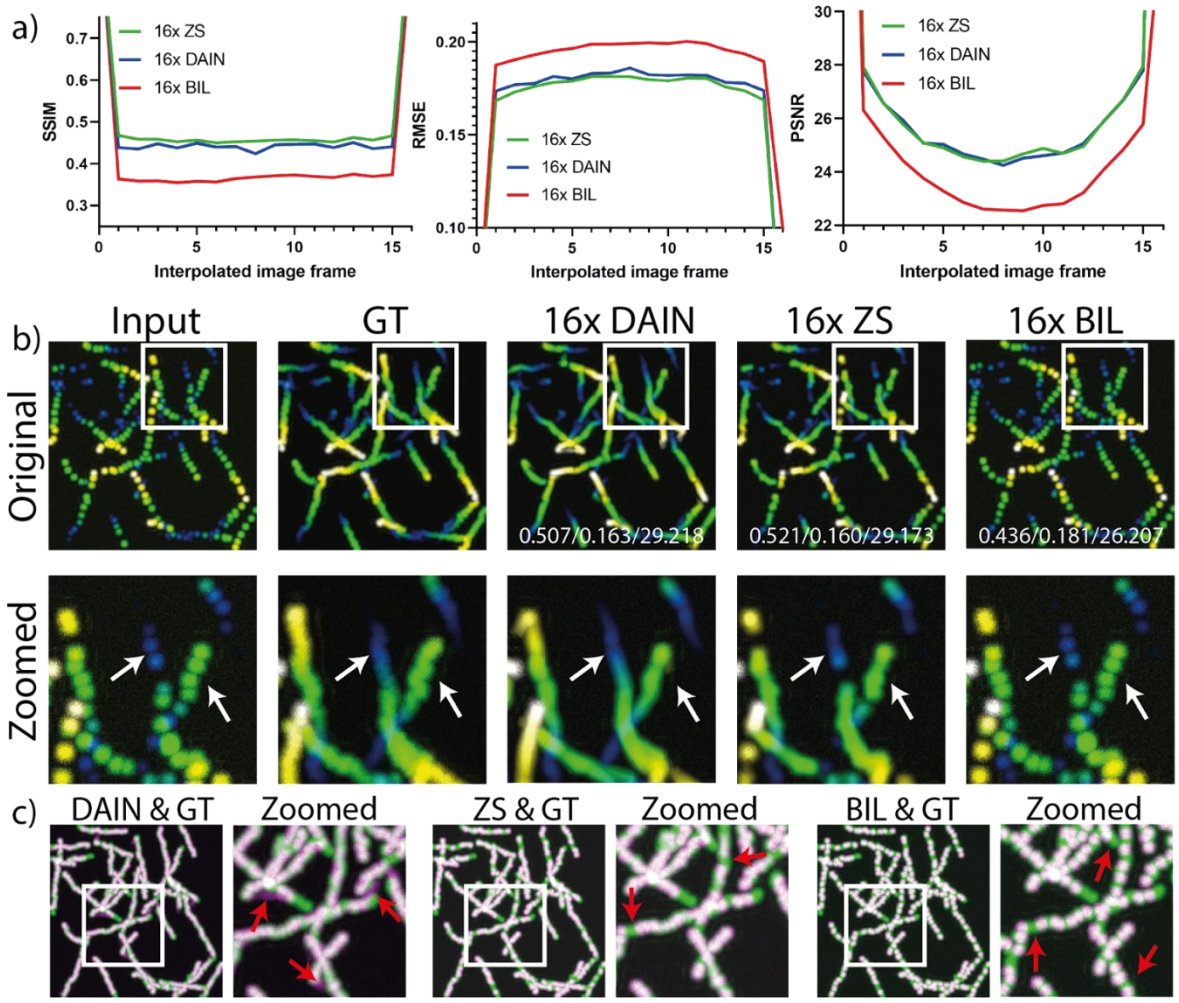

Figure 92: a) Image quality metrics comparison (SSIM, PSNR, RMSE) of BIL, DAIN and ZS on bootstrapped multi-step image interpolation for every image frame between two ground truth input images. b) Temporal colour-coded overlaid projection for visual comparison of 16x interpolated image sequences of ZS, DAIN, BIL and ground truth (GT); SSIM/RMSE/PSNR of image sequence shown in original overlaid images of each interpolation technique. c) Overlaid projections showing the errors between GT (green) and the interpolated results of BIL, ZS and DAIN (magenta) with matching overlaid parts (white); white boxes indicating zoomed in section and red arrows highlighting regions of interest for error comparison.

2.4.4.4. Predicting motion of live-cell dynamics and synthetic data

To quantify the improvements of the interpolated datasets, tracking experiments were carried out using the Fiji[224] TrackMate[149] plugin. Here the ground truth tracks of the image sequences generated by the synthetic dataset generator were compared with the detected tracks from TrackMate of the interpolated image sequences. The five performance criteria from the ISBI particle tracking challenge[150] were used for quality evaluation of the tracks.

At very slow particle movement speeds, all interpolation methods achieved similar results and ZS performed slightly better than DAIN. With increasing particle speeds the tracking results

of both networks were outperforming those of the bilinear frame averaging interpolation by a big margin especially for intermediate movements speeds (see Figure 93a). Representative tracking results of the TrackMate particle tracks at speed 7 are shown in Figure 93b. The visual comparison of the tracks confirms the superiority of neural network interpolation techniques over the BIL method and the down-sampled results.

After applying the different neural network approaches to synthetic data, real experimental data was investigated. A lysosomal tracking experiment on a 4D (3D+t) confocal image series of labelled lysosomes of SH-SY5Y cells was analysed. All z-slices were projected on one image with maximum intensity projection generating a 2D+t dataset where every second image in the temporal dimension was removed and kept for ground truth track comparison. For evaluation, the tracks of the interpolated image sequence were compared with the tracking results of the original dataset which was used as ground truth for comparison. On this experimentally obtained dataset both ZS and DAIN performed significantly better in all tracking evaluation metrics than the down-sampled tracking results and both networks showed very similar quality improvements. The five evaluation metrics (see Figure 93e) and the visual comparison of the tracks showed clear improvements of ZS and DAIN over the down-sampled tracking results (see Figure 93d). Except for the “Pairing distance” metrics where lower values are better, higher values correspond to better results. For a detailed explanation of the performance criteria see the following paper.[150]

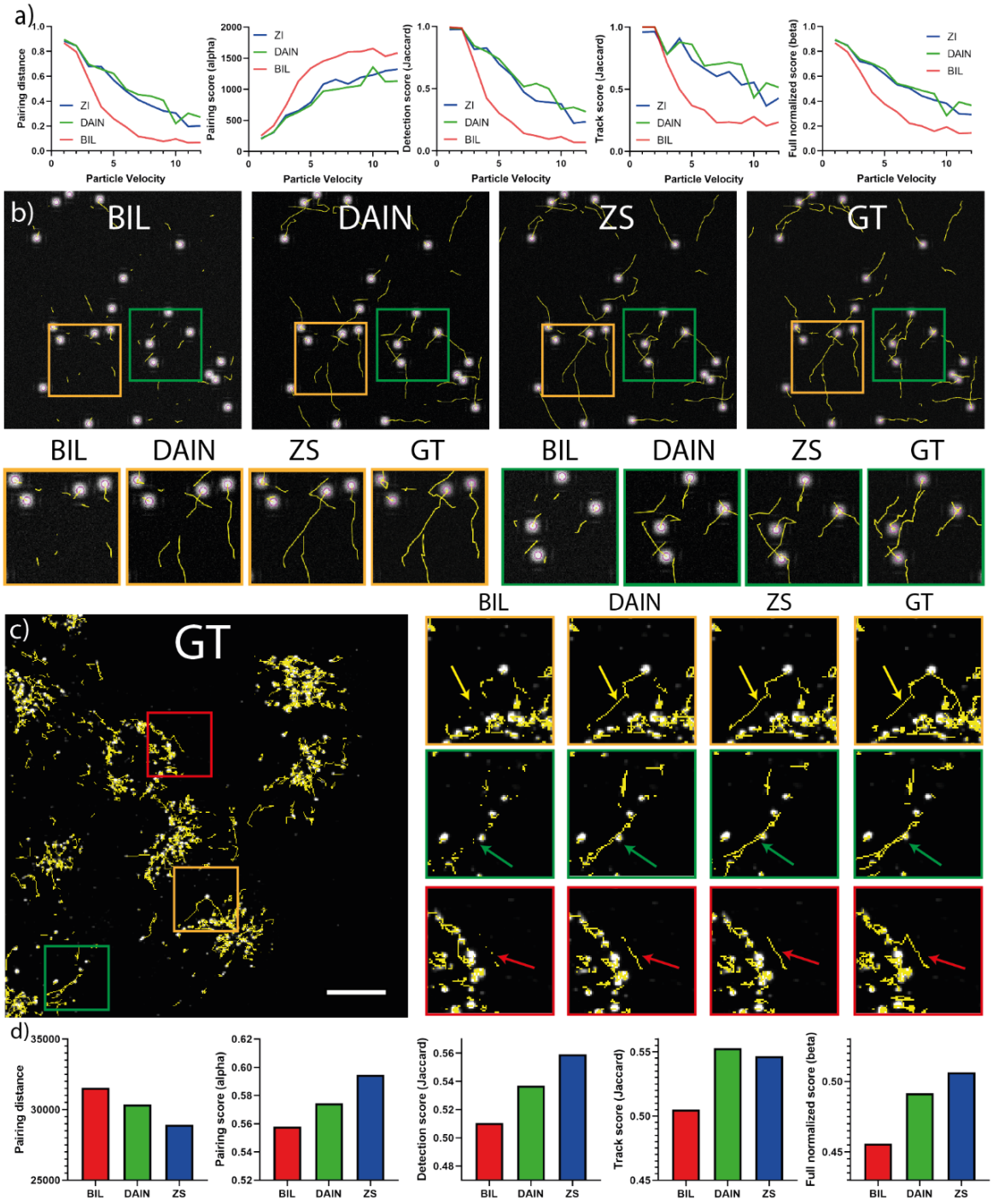

Figure 93: a) Five tracking evaluation metrics results of simulated datasets at different particle speeds with ZS, DAIN, and BIL interpolation. b) TrackMate visual track comparison of ZS, DAIN and BIL interpolation compared to GT dataset at particle speed velocity V7. c) Visual comparison of lysosomal tracking performance on interpolated datasets with zoomed in sections; arrows highlighting region of interest of tracking differences (scale bar: 20 µm). d) Lysosomal tracking performance metrics comparison; ZS and DAIN perform significantly better than tracks of BIL interpolated sequence.

2.4.4.5. Superior performance of ZS and DAIN on different microscopy modalities

After investigating the capabilities of DAIN and ZS to improve tracking results of synthetic and real-life datasets, their interpolation image quality was tested on six more experimental datasets of four different microscopy modalities (fluorescence microscopy, electron microscopy, spinning disk confocal and brightfield microscopy).

For these datasets 2x and 4x interpolation was performed on the previously down-sampled datasets. For 2x interpolation every second frame and for 4x interpolation the three centre frames out of five images were removed and were kept for ground truth comparison and quality evaluation. Next to the bilinear interpolation DAIN's functionality to interpolate multiple images in a single step was compared. Furthermore, ZS and DAIN were tested with the provided pretrained network as well as after fine-tuning on image examples of the same modality (DAIN (FT), ZS (FT)). The results of the quality evaluation metrics data of all compared datasets are presented in Table 3 and Table 4. Based on the evaluation metrics of PSNR, SSIM and RMSE, the provided pretrained network of ZS already outperforms DAIN for all tested datasets in the single image interpolation results (2x) as well as for most 4x frame interpolation results. When fine-tuning the ZS network the performance improves even further, ranking first also for all 4x interpolation tasks. The visual inspection shows that DAIN sometimes displays artefacts by blending the different input images together. On the other hand, ZS creates washed out and smoothened results where the interpolation details cannot be reconstructed with great confidence (see representative examples in Figure 94a-d). A full demonstration of the different neural network interpolated scenarios is presented in a demonstration video and further visual comparisons can be found in the Appendix (see Figure 139 to Figure 144).

Table 3: Quality evaluation of ZS and DAIN, BIL, BIC, and NONE interpolation on 8 different datasets for 2x interpolation. The numbers in red and blue indicate the best and second-best performance.

2x interpolation																								
			2x-NONE			2x-BIC			2x-BIL			2x-DAIN			2x-DAIN (FT)			2x-ZS			2x-ZS (FT)		
	Dim	Images nr.	SSIM	RMSE	PSNR	SSIM	RMSE	PSNR	SSIM	RMSE	PSNR	SSIM	RMSE	PSNR	SSIM	RMSE	PSNR	SSIM	RMSE	PSNR	SSIM	RMSE	PSNR
Lightsheet Data	T	51	0.744	0.160	26.750	0.816	0.121	37.107	0.815	0.124	35.815	0.856	0.096	42.981	0.856	0.096	43.007	0.866	0.095	42.517	**0.867**	0.094	42.917
BF Data	T	63	0.778	0.089	78.786	0.800	0.107	40.953	0.803	0.114	37.792	0.828	0.101	42.051	0.829	0.101	42.057	0.832	0.100	41.429	**0.835**	0.099	42.113
Synthetic Data	T	113	0.748	0.104	41.014	0.762	0.112	35.975	0.766	0.114	36.499	0.808	0.095	42.598	0.810	0.095	42.619	0.818	0.094	42.651	**0.820**	0.093	42.555
CF Lyso Data	T	57	0.922	0.049	80.319	0.926	0.061	41.127	0.924	0.060	40.900	0.935	0.046	81.321	0.940	0.045	81.237	0.941	0.047	53.423	**0.942**	0.046	54.979
CF Mito Data	T	97	0.891	0.101	40.834	0.899	0.107	35.580	0.902	0.107	35.827	0.914	0.094	41.203	0.916	0.094	41.230	0.918	0.094	41.150	**0.921**	0.093	41.310
Fibronectin	T	13	0.663	0.108	78.749	0.680	0.128	42.939	0.682	0.130	42.188	0.732	0.104	46.883	0.733	0.104	46.896	0.732	0.103	46.617	**0.734**	0.104	45.067
Fibronectin	Z	13	0.679	0.123	40.273	0.714	0.128	36.798	0.715	0.128	36.422	0.732	0.112	41.386	0.733	0.111	41.409	0.701	0.114	41.025	**0.752**	0.108	41.653
Actin	Z	33	0.769	0.127	35.265	0.813	0.126	33.219	0.807	0.130	32.395	0.810	0.105	40.077	0.812	0.105	40.105	0.812	0.103	40.180	**0.870**	0.093	41.984
EM Data	Z	97	0.748	0.134	39.966	0.775	0.146	34.249	0.780	0.148	33.565	0.801	0.121	41.449	0.802	0.120	41.483	0.806	0.119	41.587	**0.811**	0.118	41.698

Table 4: Quality evaluation of ZS and DAIN, BIL, BIC, and NONE interpolation on 8 different datasets for 4x interpolation. The numbers in red and blue indicate the best and second-best performance.

4x interpolation																						
			4x-NONE			4x-BIC			4x-BIL			2*2x-DAIN			2*2x-DAIN (FT)			2*2x-ZS			2*2x-ZS (FT)		
	Dim	images nr.	SSIM	RMSE	PSNR	SSIM	RMSE	PSNR	SSIM	RMSE	PSNR	SSIM	RMSE	PSNR	SSIM	RMSE	PSNR	SSIM	RMSE	PSNR	SSIM	RMSE	PSNR
Lightsheet Data	T	49	0.681	0.166	48.492	0.662	0.180	29.551	0.661	0.181	29.094	0.715	0.155	32.806	0.717	0.154	32.901	0.736	0.150	32.248	**0.738**	0.150	32.825
BF Data	T	125	0.689	0.130	52.959	0.701	0.143	32.514	0.705	0.144	31.989	0.750	0.129	35.093	0.751	0.129	35.104	0.754	0.129	34.742	**0.760**	0.128	34.790
Synthetic Data	T	113	0.600	0.148	31.806	0.603	0.155	28.591	0.607	0.156	28.297	0.684	0.132	34.315	0.685	0.131	34.328	0.631	0.138	33.708	**0.689**	0.130	34.051
Flu Lyso Data	T	113	0.881	0.073	54.639	0.884	0.081	33.874	0.885	0.079	33.981	0.899	0.070	55.988	0.910	0.068	55.883	0.910	0.070	40.473	**0.913**	0.069	41.245
Flu Mito Data	T	97	0.825	0.141	32.096	0.827	0.146	28.437	0.830	0.146	28.111	0.856	0.130	32.904	0.859	0.129	32.949	0.861	0.130	32.810	**0.867**	0.128	33.036
EM Data	Z	97	0.585	0.191	31.148	0.612	0.199	27.328	0.615	0.199	27.190	0.676	0.169	33.074	0.677	0.169	33.113	0.670	0.168	33.124	**0.691**	0.164	33.451
Actin	Z	33	0.353	0.221	20.748	0.569	0.178	26.476	0.572	0.178	26.218	0.633	0.157	30.938	**0.635**	0.156	30.965	0.627	0.157	30.967	0.573	0.187	22.899

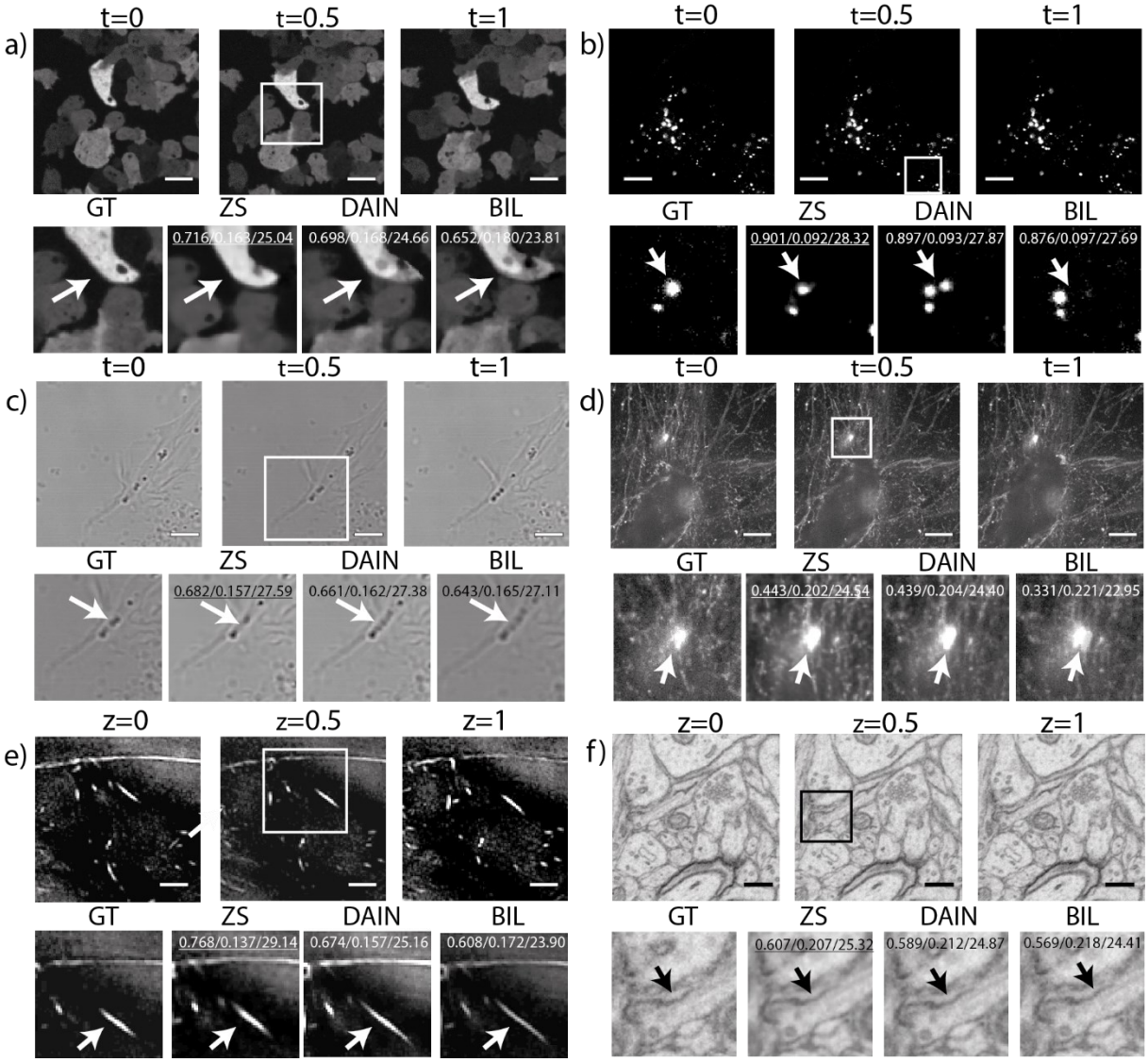

Figure 94: Visual comparison of ZS, DAIN and BIL interpolation results. t-Dimension interpolation datasets from a) spinning disk confocal microscope (scale bar 50 µm); b, d) confocal microscope (scale bars 10 and 50 µm); c) brightfield microscope (scale bar 75 µm); and z-dimension interpolation datasets from e) confocal microscope (scale bar 10 µm), f) electron microscopy (scale bar 1.5 µm), with quality metrics (SSIM/RMSE/PSNR) displayed in zoomed in images. Arrows highlight regions of interest of visible differences between the interpolation techniques.

In conclusion, in this part of the thesis the first two content-aware frame interpolation neural networks (Zooming SlowMo and DAIN) were implemented which are capable of increasing the frame rate of microscopy images by predicting intermediate frames between two provided images along t- and z-dimension. Both neural networks showed significant improvements for computational tracking results on synthetic and experimentally obtained datasets. The networks were tested on 6 different datasets of four different microscopy modalities (spinning disk confocal, fluorescence confocal, brightfield and electron microscopy) for 2x and 4x interpolation and for each dataset ZS before DAIN was outcompeting traditional interpolation techniques such as bilinear and bicubic interpolation. Furthermore, their strength and weaknesses in the context of artifact creation were demonstrated and critically reflected. These universal image prediction tools show great potential for any kind of microscopy modality that is in the need for higher frame rates or higher image density to investigate fast cellular processes. All the tools used in this thesis were implemented in Google Colab notebooks and are made available to the scientific community on the ZeroCostDL4Mic platform.

2.4.5. Combining denoising, spatial pixel resolution upscaling and image frame interpolation

Now that each corner of the "Eternal Triangle of Compromise" was improved with different deep learning neural networks individually, a combination of these tools was studied to improve examples of very poor-quality images (low resolution, low SNR and low recording frequency) by sequentially improving each limitation corner. For the following experiment, the neural networks were just fine tuned for their individual task but were used in sequence. Since a low SNR was seen as the biggest limitation factor, the denoising algorithm CARE was used first, then the spatial resolution upscaling algorithms followed by the frame interpolation algorithms. Since ZS had both functionalities included (resolution upscaling and frame interpolation) this network was used for both tasks and the best performing spatial resolution upscaling network GMFN was combined with the frame interpolation algorithm DAIN.

2.4.5.1. CARE & ZS/GMFN & ZS/DAIN on synthetic dataset

The first dataset on which the neural networks were tested was a synthetic dataset of white points moving in front of a black background. A high-quality image example (XYT) was

artificially degraded in a step-by-step process (see Figure 95a) where first the image frequency was reduced followed by downscaling and addition of noise. This low spatial resolution, low frequency and low SNR image was then first provided to the CARE network which removed the noise from the low SNR image. Then a spatial pixel resolution upscaling (2x) was performed with BIC, ZS and GMFN and finally BIL, ZS and DAIN were used to perform the image interpolation, respectively. In the overlayed imaged in Figure 95b and Figure 95c CARE performed very well for removing the noise from the degraded images. However, the video demonstration shows that the few artefacts created by CARE resulted in increased errors in the following steps of spatial resolution upscaling and especially in the frame interpolation step. This also explains the small differences in quality improvements from the different spatial resolution upscaling and frame interpolation techniques. Regardless of the artefacts, all image enhancement combinations were found performing significantly better than the image where no denoising was carried out before. Therefore, it can be concluded that for very poor SNR CARE is an essential step for improving the image quality.

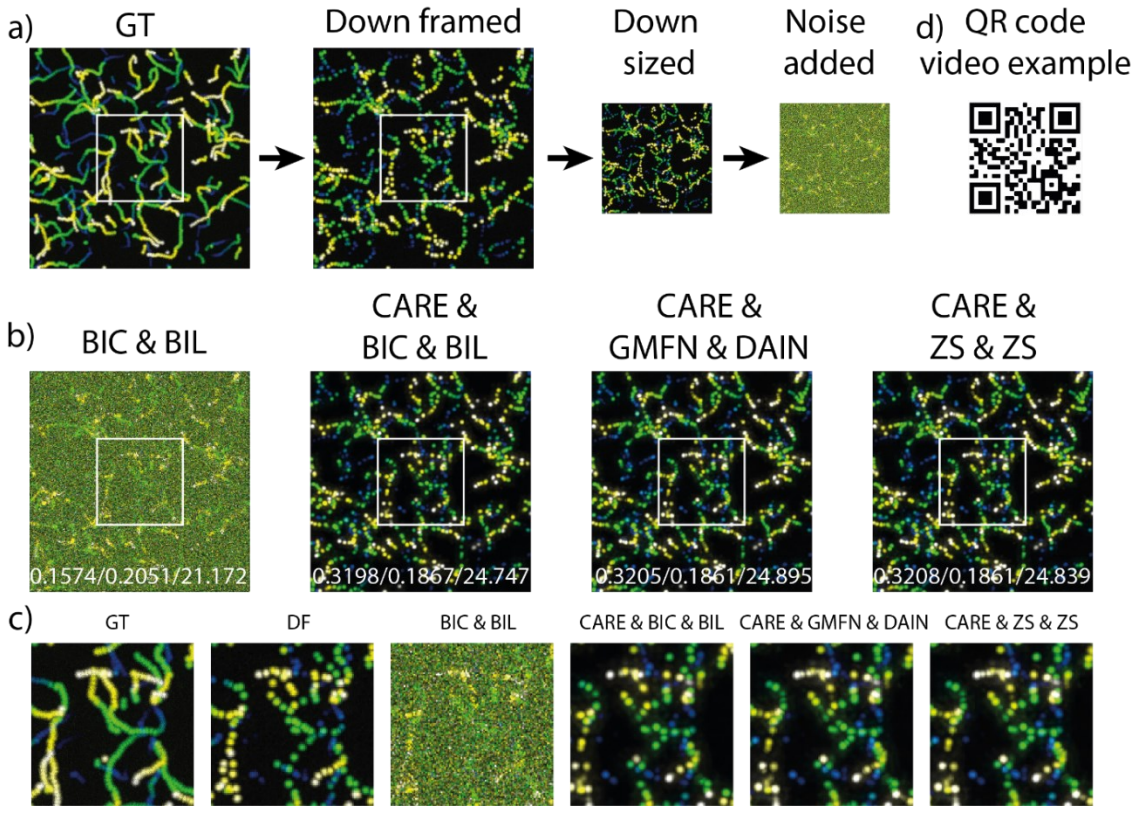

Figure 95: a) Image degradation workflow from high spatial resolution, high frequency, high SNR to low spatial resolution, low frequency, and low SNR image. b) Image enhancement results of different combinations of enhancement algorithms where CARE in combination with ZS for image spatial pixel resolution upscaling and image frame interpolation performs best of all tested combinations. c) Zoomed in section with the different image enhancement techniques compared to GT and down framed (DF) results.

2.4.5.2. CARE & ZS/GMFN & ZS/DAIN on real-life lysosomal movement dataset

Next, the two best performing algorithm combinations (CARE + ZS (resolution) + ZS (frame) and CARE + GMFN (resolution) + DAIN (frame)) were used on an experimental dataset of moving lysosomes labelled with **FLCS1** in SH-SY5Y cells. Images of the cells were recorded at low spatial resolution (256 px) and low laser powers (0.05%) as it was established in the previous section, by recording z-stacks over time (3D + T). For comparison, some examples with high laser power (1%) with the same low spatial resolution was used and the fluorescence intensity profile over time was plotted along the number of z-stacks (see Figure 96a). When looking at the intensity profile comparing low and high laser powers over time low spatial resolution combined with low laser powers show very little photobleaching at those settings whereas high laser powers with low spatial resolution still caused a strong reduction of signal already after a few z-stack recordings. Since the low-resolution - low laser-power settings already showed a relatively stable fluorescence signal, the spatial pixel resolution upscaling network combined with image frame interpolation was also used directly on the low SNR images without performing the CARE denoising step before. To test the improvement quality of the low laser power images, the 4D image sequence was down-sampled once in the z-dimension and twice in the t-dimension before using them on the enhancement algorithms. This down-sampled low laser power image sequence was then enhanced in the same way as it was performed on the synthetic dataset using first the denoising algorithms followed by the spatial pixel resolution upscaling and the image frame interpolation network. The visual comparison of the overlayed image sequence (see Figure 96c) showed that the enhanced results with all three neural networks show quality improvements in terms of signal intensity of the lysosomes, however, CARE introduced artefacts where the lysosome size was significantly increased compared to the ground truth image (see Figure 96e). Furthermore, some of the lysosomes from the ground truth fused together to one big lysosome signal in the denoised image result which also contributed to bigger and less precise reconstruction of the ground truth images (see white arrow in zoomed in sections in Figure 96e for a representative example). As a comparison, the same dataset was enhanced just by the spatial pixel resolution and the image frame rate without using CARE for denoising. Those results were much more similar to the ground truth image sequence than to the enhancement sequences with CARE denoising. The lysosomes were easily recognized by the two networks (GMFN&DAIN or ZS&ZS) and the results of this enhancement combination did not show significant artefacts in comparison to the three-

network enhancement workstream (CARE&GMFN&DAIN or CARE&ZS&ZS). The intensity profile over time also provided additional reasons to not use the denoising CARE network in combination with the other two networks because CARE caused strong intensity fluctuations in the recording over time which was not the case for the spatial resolution and frame rate enhancement algorithms (see Figure 96d). Video examples for the laser intensity comparison and the different enhancement results are presented in the QR code links in Figure 96b. These results demonstrated that combining all three enhancement networks on one input image caused significant errors due to artefacts created in the first enhancement step in the denoising network CARE. However, at low laser powers and low spatial resolutions the fluorescence signal was stable and strong enough to use these input images just on the spatial pixel resolution upscaling and image frame interpolation networks which showed promising improvements over the ground truth input images.

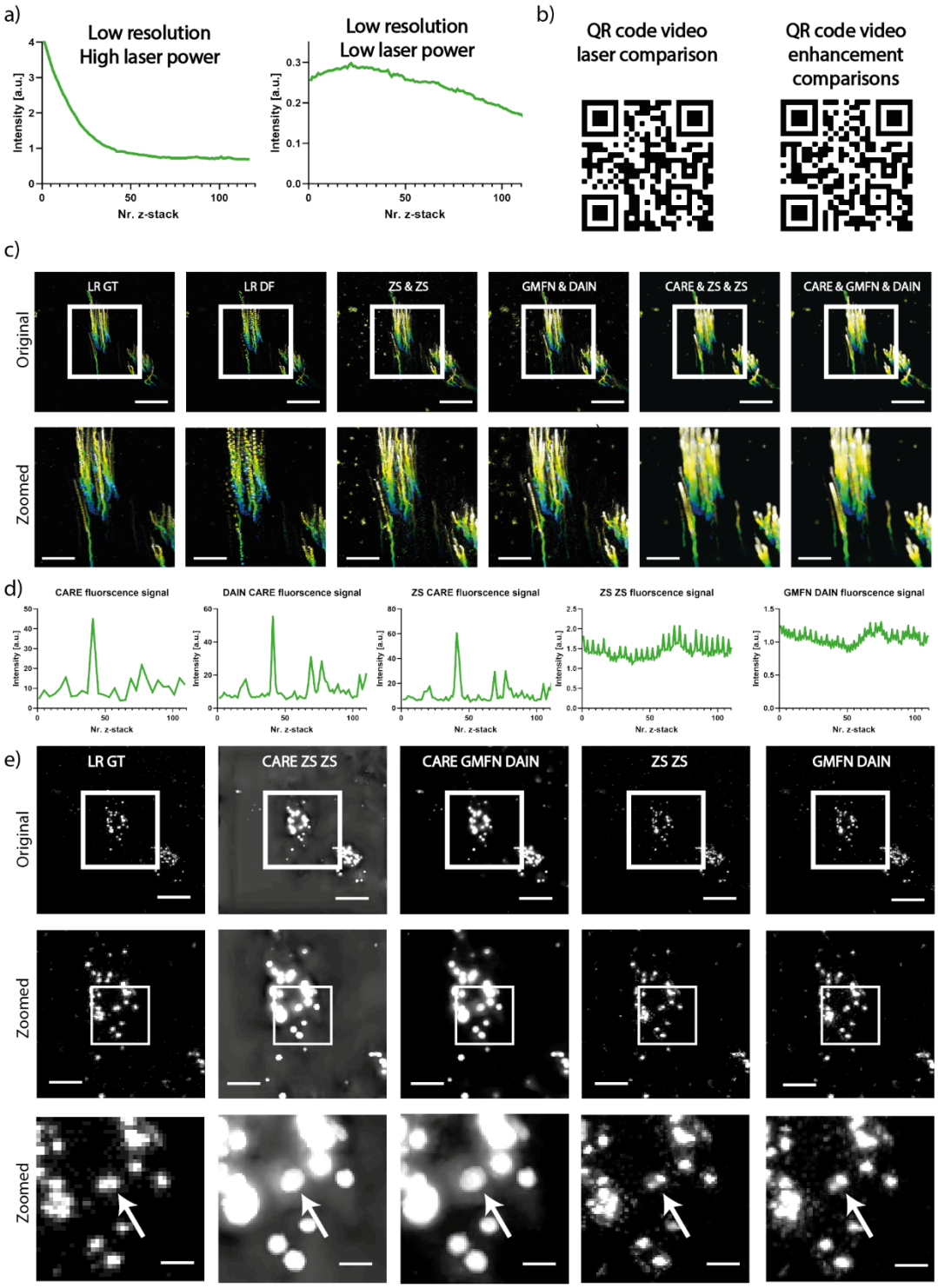

Figure 96: a) Intensity signal of recorded fluorescence over time with high (1%) and low (0.05%) laser powers. b) QR code of example videos showing fluorescence bleaching of over time for high and low laser powers (left), and image enhancement comparison of different neural network combinations (right). c) Overlayed images over time as comparison of neural network combination results (top) with zoomed in sections (below). Scale bars 50/20 µm. d) Intensity profile over time for neural network enhanced image sequence, showing strong spikes for the CARE network combinations. e) Selected images comparing ground truth with the different neural network combinations highlighting reconstruction error from CARE network (see white arrows in zoomed in sections). Scale bars 50/20/5 µm.

2.5. Conclusion

In conclusion, in this part of the thesis neural network solutions for enhancing the microscopy image quality has been explored and it has been found that some are applicable for investigating biological applications such as lysosomal mobility. The fNET network which was implemented with the aim of labelling lysosomes just based on provided brightfield data did not manage to recognize those cellular organelles correctly but falsely labelled them as lipid droplets. Therefore, this network cannot be used for investigating lysosomal movements.
The image enhancement algorithms for SNR enhancement, spatial pixel resolution upscaling and image frame interpolation have kept their promise and have proven to be useful for microscopy applications when applying them individually which improves each one corner of the "Eternal Triangle of Compromise". All implemented neural network enhancement algorithms performed significantly better than classical mathematical methods for the spatial pixel resolution upscaling and image frame interpolation. The denoising algorithm CARE also performs very well when trained on the same type of dataset. However, in some cases this denoising network creates some artefacts which are especially relevant in 4D datasets where it assigns the depths of the particle wrongly or the intensity of the particle is assigned incorrectly.
When combining the denoising algorithms with spatial resolution and frame upscaling methods the results also improve significantly compared to their low-quality input images. However, especially the CARE network introduces some artefacts at the first image enhancement step. Those artefacts caused amplifications of the errors in the final results. Although, a combination of different neural networks led to big improvements in the quality results of very poor-quality image examples, the artefacts that have been introduced by the CARE network propagated and worsened in the following neural networks which in a practical scenario could lead to false biological conclusions. For the application on biological images, it seems advisable to just record the image at a medium to low intensity laser power at lower spatial resolutions. This significantly lowers the laser dose on the sample and the combination of spatial pixel resolution upscaling and image frame interpolation algorithms can be combined without much artifact creations to enhance the image quality. With these settings (low resolution 256 px and 0.05% laser power) lysosomes labelled with **FLCS1** can be recorded at for at least 100 z-stacks without losing on much intensity signal of the fluorescent labels.

These settings were used for the research presented in the next chapter where the movement patterns of copper(I) containing lysosomes was investigated by recording them in 3D over time before and after treatment of certain drugs that are under investigation to have positive effects for Parkinson's disease.

2.6. Materials and Methods

2.6.1. Simulated dataset

The simulated synthetic dataset was created using the ICY plugin from the 2014 ISBI particle tracking challenge.[150] The synthetic dataset consisted of "switching uniform" moving white particles in front of a black background including Brownian motion. The tracks provided from the ICY plugin were used as ground truth for the tracking benchmark comparisons. For the interpolation experiments in t-dimension between 1 to 12 images were removed from one time point to the next which gradually increased the distance of the travelled particles. For the multi-step interpolation experiment, the densely framed synthetic dataset was down-sampled, removing every second image in four repetitions (2x - 4x - 8x - 16x down-sampling), while keeping them as ground truth for comparison. The z-dimension interpolation dataset was created by gradually increasing the parameter for z-spacing (50-450) in the ICY image dataset generator while keeping the number of particles in the whole z-stack the same. The full set of parameters for the created simulated data can be found in Table 7 in the Appendix.

2.6.2. Particle tracking

Particle tracking was performed using the Fiji plugin TrackMate.[149,224] The detailed parameters for the particle tracking are provided in the Appendix **Table 8**(Table 8). The ground truth tracks for the real-life lysosomal data were evaluated as the track of the full image sequence without any removed images. For the synthetic datasets, the tracks were taken from the ICY plugin data generator. The evaluated tracks from TrackMate were exported in the ISBS challenge format and the down-sampled re-interpolated image sequences were compared to their ground truth tracks using the ISBI Challenge Tracking Batch Scoring plugin from ICY.[150]

2.6.3. Particle speed ground truth tracks generation

The ground truth tracks for the different particle movement speeds were generated in the following steps. First a big, simulated dataset (225 frames) was generated with the ICY data generator. This plugin provided an XML file with all the ground truth timepoints with precise particle point locations. This XML file was first converted into the ISBI XML format in the TrackMate interface and the relevant timepoints of this file were down-sampled the same way as the actual image sequence (where an increasing number of frames was removed between each timepoint). A developed python script selected just the timepoints and particle coordinates relevant for the specific movement speed and generated a new XML file containing just the locations of the particles for the selected frames in that speed option. These ground truth tracks were then compared with the TrackMate detected tracks of the BIL, BIC and the neural network tools interpolated image sequences. Then the five performance criteria from the ISBI particle tracking challenge[150] were evaluated with the associated ICY plugin by comparing the different tracking files.

The ground truth tracks for the real-life lysosomal data were evaluated as the TrackMate generated tracks of the full ground truth image sequence before removing images. The evaluated tracks from TrackMate were exported in the ISBS challenge format and the down-sampled and then re-interpolated image sequences were compared to their ground truth tracks using the ISBI Challenge Tracking Batch Scoring plugin from ICY.[150]

2.6.4. Network training

Zooming SlowMo with the options of 1x (no spatial resolution upscaling) and 2x image spatial resolution upscaling was first trained from scratch on the Vimeo90K-septuplet (82 GB) dataset in several steps of smaller 8-12 GB subsets for 3 days on Google Colab. Before using the networks for the interpolation task on a dataset both networks were fine-tuned with 0.5 to 3 GB of training data of the same imaging modality for 3-6 h. For the spatial resolution upscaling ZS was trained on the training data for 12 to 24 h.

2.6.5. Lysosome cell imaging

SH-SY5Y cells were cultured in Dulbecco's Modified Eagle Medium (DMEM, Invitrogen, Carlsbad, CA) supplemented with 10% Fetal Bovine Serum (FBS, Invitrogen), glutamine (2 mM), and penicillin/streptomycin (50 µg/mL, Invitrogen). All cells were grown in a 5%

CO_2 incubator at 37 °C. The cells were plated and grown on 8-well chamber slides (LabTekII Chamber Coverglass) in 250 µL of culture media at a plating density of 25,000 cells per well and allowed to grow for 24 h. Next the media was changed to a media containing lipofectamine 2000 (2 µl/ml) and the copper(I) probe, **FLCS1** (60 nM). The cells were incubated with the dye for 24 h. Prior to imaging the cell media was changed back to DMEM with 10% FBS (250 µl/well). The image acquisition was performed on a confocal microscope (Leica SP5) with a 63x magnification 1.4 NA oil immersion objective. 3D image (XYZT) time series were recorded for 15 min collecting 40 time points of 30 z-stack images at a resolution of 512 px (0.481 µm/px).

CHAPTER III

3.1. Introduction

The development of optical probes (Chapter I) and computational tools (Chapter II) allowed us to apply the new toolbox to specific biological problems. In particular, an investigation into the effects of Parkinson's disease (PD) drugs on the cellular movement of copper-containing lysosomes was a topic of interest. This chapter first provides a brief overview of the biology of lysosomes, it states a hypothesis of connecting lysosomal mobility with the health state of the cell, and it presents five drugs being investigated to treat PD that might influence the lysosomal activity and mobility. With this background in mind, preliminary investigations are presented where the new lysosome-selective fluorescent copper(I) probe has been used (**FLCS1** – see thesis Chapter I) together with the deep learning image enhancement tools (see thesis Chapter II) to investigate the lysosomal mobility changes upon treatment of SH-SY5Y cells with five drugs. This should serve as a case study for the new tools to be subsequently used for more detailed investigations of the lysosome mobility.

3.2. Theoretical Background

3.2.1. Lysosomes

As briefly mentioned in thesis Chapter I, lysosomes are intercellular membrane-enclosed organelles responsible for degrading biomacromolecules in mammalian cells and have therefore earned a reputation as the 'garbage disposal system' of the cell.[225] This degradative function is carried out by a vast number of luminal hydrolases specialized for certain

substrates. Those hydrolases contribute to the acidic lysosomal lumen pH of around 4.5-5.0. The lysosomal membrane consists of over 200 integral membrane proteins that regulate the proton-import to maintain the acidic pH of the lumen and control the luminal ion composition. Furthermore, there are multiple transporters that export products of degradation to the cytosol. Tethering factors and SNARE proteins are included to promote contact and fusion, respectively and a set of highly glycosylated lysosome-associated membrane proteins (LAMPs) protect the membrane from degradation by the acidic hydrolases inside the lysosomes. The lysosomal membrane that faces the cytosol serves as a platform for protein complexes that mediate interaction with the cytoskeleton and perform nutrient and stress signalling.[225] More recently, the garbage disposal perception of lysosomes has widened with the realization that they also participate in many other cellular processes such as killing of intruders and pathogens, plasma membrane repair, tumour invasion and metastasis, apoptosis, and gene regulation, among others (see Figure 97).[145] These findings sparked an increasing research interest in lysosomes and their multiple cellular functions.

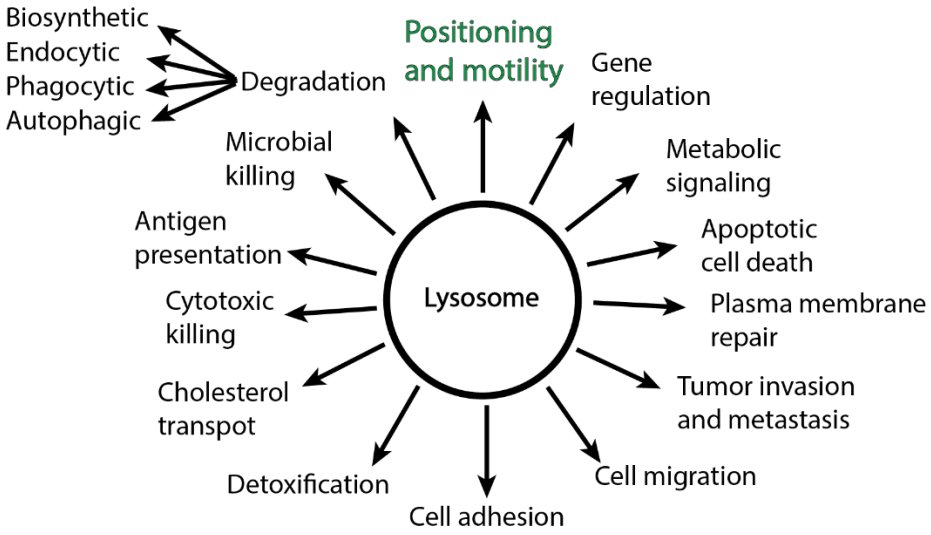

Figure 97: Multiple functions of lysosomes are influenced by their positioning and mobility.

3.2.1.1. Movement and location of lysosomes

The positioning of lysosomes is dependent on many factors. Usually they are broadly distributed throughout the cytoplasm, however in non-polarized cells they are mostly located in the so-called perinuclear cloud which is the central region surrounding the microtubule-organizing centre.[226] Lysosomes in polarized cells, such as neurons are also found in the cytoplasm of soma, axons and dendrites. Some of them are very mobile moving bidirectionally along microtubule tracks between the peripheral parts of the cells and the centre.[227] The movement of lysosomes is mostly mediated by kinesin (anterograde transport)

and dynein motors (retrograde transport).[228,229] Their movement can be seen as being not continuous but "stop-and-go"[230] which suggests that they are following a regulation mechanism. Interestingly the regulation mechanisms can be influenced under certain conditions such as cytosol acidification which leads to a lysosome dispersal of the perinuclear lysosome population. Alternatively alkalization leads to a cluster formation in central locations of the cell.[231,232] On the other hand, lysosomal dispersion can be induced by special stimuli such as treatment of macrophages or dendritic cells with bacterial lipopolysaccharides which simulate a bacterial infection. Other stimuli that lead to the perinuclear cluster formation of lysosomes are starvation,[233] drug-induced apoptosis,[234] or leucin-rich repeat kinase 2.[235] Sometimes, the lysosomal movement can be disturbed in a situation where both kinesin and dynein are pulling the lysosome in opposite directions.[236,237] Furthermore, lysosomal movement is also modulated by contacts with other organelles such as the endoplasmic reticulum (ER),[238,226] the trans-Golgi-network (TGN)[239] and peroxisomes.[240] In that way, lysosomes populate the entire cytosol in a regulated manner and perform their important cellular functions such as regulation of transition metal homeostasis, detoxification and recycling of proteins and cellular waste via autophagy during their travels. This highly controlled process of lysosomal movement is very important for the cell viability and miss-regulation of this intracellular transport is linked to several diseases such as neurodegenerative disorders (e.g. Parkinson's, Alzheimer's, and Huntington's disease),[241,242] diabetes, lysosomal storage disorders (LSDs) and many more.[243,244]

The causes for these diseases are very complex and under active investigation. One possible reason is an often age-related breakdown of cellular protein degradation pathways where lysosomes and autophagy play an important role.

3.2.1.2. Cellular degradation pathways and diseases

In eukaryotic cells there are two major protein internal degradation pathways in place. The first one is the ubiquitin-proteasome system (UPS) which is responsible for degrading short-lived proteins. The second one is the autophagy-lysosome pathway (ALP) where during autophagy signalling, autophagosomes fuse with lysosomes, forming the autolysosome which recycle long-lived and insoluble proteins.[245] In general autophagy is a self-degradative process that has a housekeeping role within a cell by removing misfolded or aggregated proteins and is responsible for balancing the energy and resources of a cell.[246]

The transcription factor EB (TFEB) plays very important regulatory roles influencing various processes including autophagy, lysosomal biogenesis and exocytosis, and lipid membrane repair catabolism amongst several others.[247–250] Furthermore, TFEB is part of the so called "coordinated lysosomal expression and regulation" (CLEAR) network,[251] which directly controls expression of genes linked to autophagy, lysosome and mitochondria biogenesis and mitochondrial quality control (MQC). The MQC is part in the defence mechanisms against ROS generation (see illustration in Figure 98).[247,252–254]

The mammalian target of rapamycin protein kinase complex 1 (mTORC1) is a key component that regulates the balance between energy and nutrient abundance with cell growth and proliferation.[248] It has been shown that inhibition of mTORC1 leads to an increased nuclear localization and activity of TFEB which in turn leads to increased autophagy and lysosome biogenesis.[248] Also N2a cells treated with GSK3 could regulate TFEB by phosphorylation, which controls its trafficking to the nucleus.[255] Therefore, targeting TFEB directly or via mTORC1 activation may represent an appealing therapeutic strategy to regulate cellular processes.[256]

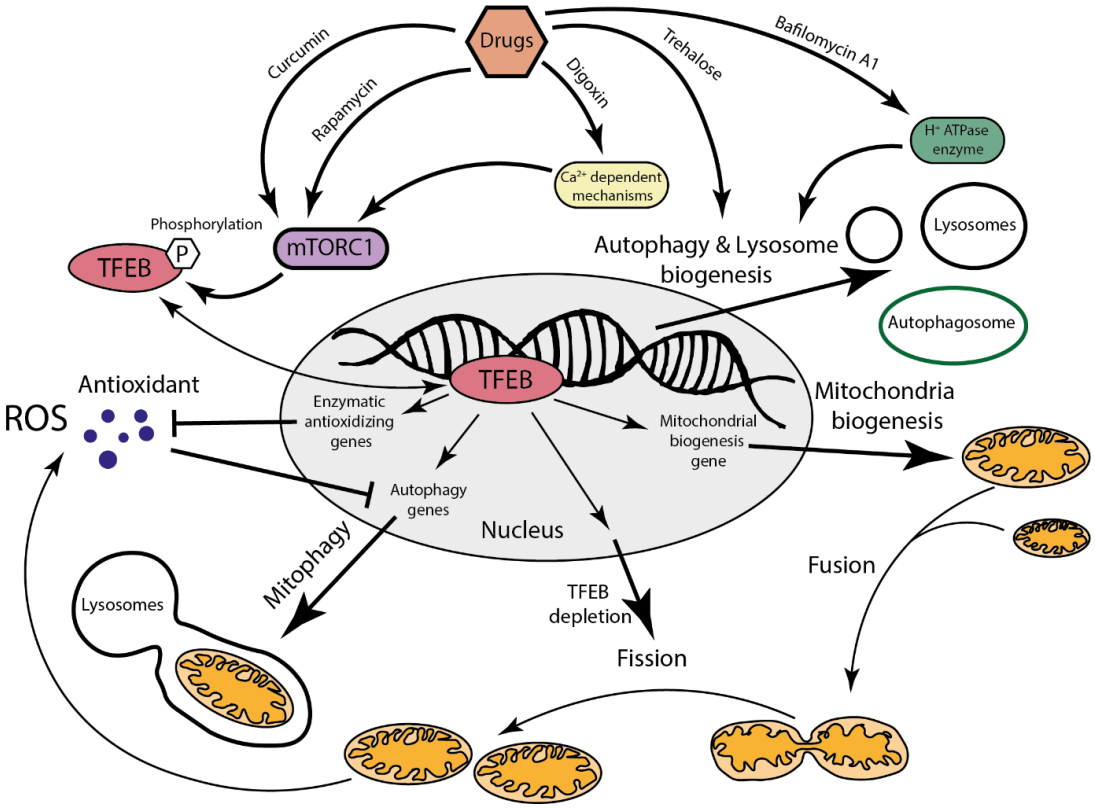

Figure 98: Visual illustration of TFEB gene regulation affecting processes such as lysosome biogenesis and MQC by activating mitophagy, regulating mitochondrial biogenesis, ROS clearance and balance of mitochondria fission-fusion cycle, *etc.* Targeting TFEB directly or via mTORC1 with certain drugs may represent an appealing therapeutic strategy to regulate MQC and other vital cellular processes.

The aging process and certain diseases cause a steady decline in autophagy.[257] Malfunction of the ALP results in impairments of the autophagosome-lysosome biogenesis process and causes increased levels of reactive oxygen species which can damage the cell. An enhanced TFEB activation improves the clearance mechanisms of deleterious macromolecules and defective or damaged organelles through autophagic and lysosomal degradation. It positively modulates the lipid catabolism, promotes longevity and has ameliorating effects for disease related to ALP dysfunction such as neurodegenerative diseases and lysosomal storage disorder amongst others.[251,258] An example for the positive effect of TFEB was observed by an overexpression of TFEB in *C. elegans* which significantly increased the lifespan through induction of macroautophagy.[258] Furthermore, lysosomal activity and mobility of *C. elegans* worms was investigated and a higher motility was found to be connected to a good organism health state and that aging resulted in a reduced activity of the lysosomes.[259]

Neurodegenerative diseases in particular are often caused by a loss of neurons due to an intracellular accumulation of aggregation-prone proteins, which in turn damage the protein degradation systems. The ALP pathways play an important role for the clearance process of intracellular misfolded protein aggregation to maintain a healthy homeostasis. Genetically, upregulation of TFEB has shown to lead to an attenuation of alpha-synuclein pathology in Parkinson's disease.[258,260]

Based on this evidence for the beneficial effects of TFEB up-regulation and the importance of a healthy lysosomal activity for cell health, many small molecules have been investigated for their use as TFEB activators or as supporters for lysosomal biogenesis. In general, any upregulation mechanism for lysosomal activity is thought to have beneficial effects on the clearance mechanisms and on the house keeping function of the cells. The potential therapeutic use of such compounds is seen as promising strategy for treating ALP dysfunction related diseases.

In the next section some of the compounds that have shown to have an influence on the ALP or/and the TFEB activity are presented.

1.3.5. Promising drug targets for autophagy and lysosomal regulation

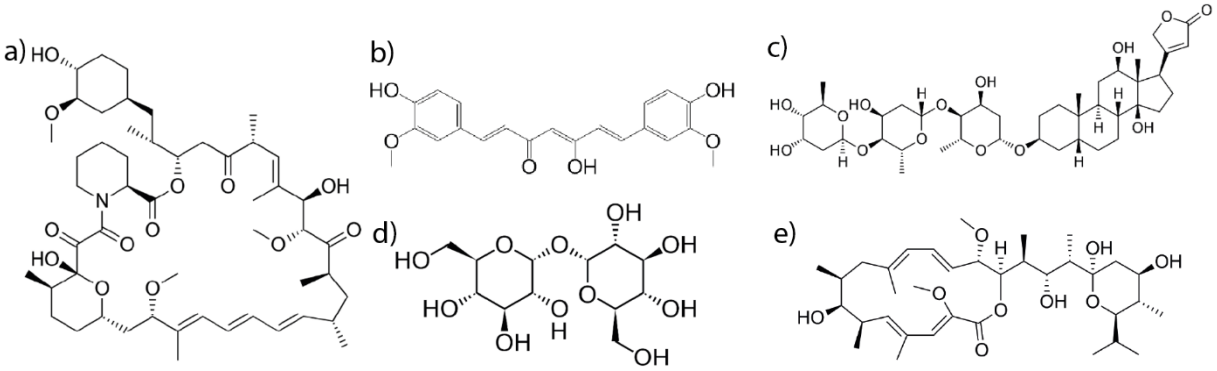

Figure 99: Chemical structures of a) rapamycin; b) curcumin; c) digoxin; d) trehalose; and e) bafilomycin A1

In the past many small molecules (such as those shown in Figure 99) have been investigated for their potential role on TFEB activation or for their support on lysosomal biogenesis. As shown in Figure 98, there are different proposed biological mechanisms of action. For this study five promising drugs were selected to investigate the lysosomal mobility after treatment of cells with those compounds. This could help to better understand the proposed mechanisms and their implications for cell health. Figure 99 presents the selected drug targets that have been used for this research. The first two compounds **rapamycin** and **curcumin** (see Figure 99a, b, respectively) both follow a TFEB activation process by influencing mTORC1 (see Figure 98).

Chemically, these compounds are clearly different. **Rapamycin** is a macrolide which belongs to a class of natural products that consist of a large macrocyclic lactone-ring, and it is commonly used as an immunosuppressant for human organ transplants. It is known to selectively bind to the protein complex mTORC1. It has been shown that influencing the activity of mTORC1 has some neuroprotective effects on several *in vivo* models for neurodegenerative diseases such as Parkinson's and Alzheimer's disease.[261] **Curcumin** on the other hand is a polyphenol that belongs to the family of curcuminoids. It has shown a wide range of positive effects such as a free radical scavenging activity, anti-inflammatory effects, it can cross the blood brain barrier and is neuroprotective.[262] These neuroprotective effects of curcumin have been tested on several neurotoxins or genetically induced PD models.[263] Furthermore, curcumin treatment has shown to enhance lysosomal function by increased lysosomal acidification and enzyme activity.

Both compounds are known to influence the TFEB activity via a mTORC1 inhibition pathway (see Figure 98).[264,265] Curcumin promotes TFEB nuclear translocation and reduces

the phosphorylation level of TFEB via a mTORC1 inhibition pathway and increases the transcriptional activity of TFEB.[266] Rapamycin is known to selectively bind and deactivate the protein complex mTORC1. The inactivation of mTORC1 by this drug leads to an enhanced TFEB gene expression which directly increases autophagy and lysosome biogenesis which is suspected to be the cause of its positive effects.[263]

The third compound with a slightly different TFEB activation mechanism is the drug **digoxin** (see Figure 99c). It is an organic compound that belongs to the category of cardiac glycosides and it can enhance the TFEB activation by increasing cytosolic Ca^{2+} levels (see Figure 98). The drug has been reported to extend the lifespan of *C. elegans* nematodes with this mechanism by increasing lysosomal activity and biogenesis.[267]

Alternatively, **trehalose** and **bafilomycin A1** (see Figure 98d, e, respectively) are two compounds that follow very different biological mechanisms compared to the previously mentioned ones but also induce lysosome biogenesis.

Trehalose is a nonreducing and naturally occurring sugar molecule consisting of two glucose molecules. It is widely produced in many different organisms such as bacteria, yeast, fungi, insects, invertebrates, and plants and it is used as a bioprotectant for cells from environmental conditions such as heat, cold, dehydration and oxidation.[268,269] Trehalose activates TFEB in an mTORC1-independent manner and enhances autophagy and lysosomal activity[270] which leads to an improved clearance of protein aggregates.[266] It has been found to provide many beneficial effects in the context of several different neurodegenerative diseases and decreases misfolded protein aggregates such as alpha-synuclein in PD cell models or tau accumulation in Alzheimer's mouse models,[271] amongst others.

On the other hand, **bafilomycins** belong to the family of macrolide antibiotics, which are produced by several different actinobacterias. These compounds have shown a wide range of biological activities such as anti-parasitic, anti-tumor, anti-fungal or immunosuppressant effects. In particular, bafilomycin A1 is known for its potent inhibition of cellular autophagy. Under normal conditions, autophagosomes fuse with lysosomes which facilitate the degradation process due to the lysosomal acidic pH and its available proteases.[272] When cells are treated with bafilomycin A1 it targets the vacuolare-type H^+-ATPase enzyme, which is a proton pump that acidifies lysosomes. This inhibits the acidification process, which stops the cascade of lysosome autophagosome fusion.

Taken together, the combination of the different drugs' positive health-related benefits with their different biological mechanisms and the lack of available literature of their effects on the

lysosomal mobility, makes the cellular effects of these drug interesting for investigation with the molecular and computational tools developed here.

3.3. Aims and Objectives

In this final part of the research project the different molecular (Chapter I) and computational (Chapter II) tools were used to investigate the movement of lysosomal compartments inside SH-SY5Y cells and explore the effects that different drugs have on the lysosomal mobility. This was planned as a case study for the utilization of the here developed tools and should serve as an exemplary workflow for future experiments that could investigate lysosomal mobility patterns in greater detail.

Based on the proposed biological functions of the five selected drug targets, which all somehow lead to an increase of lysosome biogenesis, it was hypothesized that treatment of cells with those compounds could lead to an increase in the activity and mobility of lysosomes. This was expected to provide a potential explanation for their positive effects reported in the literature. Since the mechanisms, of the first three compounds (rapamycin, curcumin, and digoxin) all follow mTORC1 dependent mechanisms, the activity and mobility changes of those compounds might follow a similar trend. On the other hand, trehalose and bafilomycin A1 with their mTORC1 independent mechanisms could display an alternative trend. Specifically, bafilomycin A1 with its ability to change the lysosomal pH was expected to show significant effects on the mobility behaviour of lysosomes since this compound has shown to have direct effects on the organelle of interest.

To investigate these hypotheses, cells were grown under normal conditions, labelled with the new **FLCS1** lysosomal copper(I) probe and z-stack recordings over long time periods were taken before and after the treatment of the cells with the corresponding drugs. The recorded image sequences were enhanced with the pixel resolution upscaling and image frame interpolation neural networks presented in thesis Chapter II. The movement patterns of the lysosomes were captured and analysed with the TrackMate plugin from Fiji.[149,224] Finally, the quantitative data from the lysosomal tracking studies after treatment, were analysed for anomalies and compared to the control baseline of untreated cells.

3.4. Results and Discussion

3.4.1. Case Study: Drug treatment comparison

The comparison of lysosomal mobility was carried out by recording cellular images with a confocal microscope over time in a z-stack mode at low laser powers (0.05%) and low resolution (256 px) to ensure a high frame sampling rate. Subsequently, the GMFN and DAIN network were applied increasing the resolution from 256 px to 512 px and increasing the frame density by a factor of 2x. After that the lysosomes were tracked using the TrackMate plugin. As expected, the untreated cells and cells treated with 0.1% DMSO in buffer (i.e., as a control since this amount was used to prepare the drug solutions), did not show significant changes in the mean particle speeds of the lysosomes before and after treatment.

Treatment of cells with digoxin and curcumin for 24 h significantly reduced the speed at which the lysosomes were moving. Treatment with bafilomycin A1 and trehalose also led to reduction on the lysosomes' speed, although this was less pronounced. Interestingly, treatment with rapamycin resulted in a small increase of lysosomal mobility. For the precise treatment protocols of the different drugs and concentrations see Materials and Methods Section 3.6. The average lysosomal speeds of the different conditions are shown in Figure 100a, overlayed recordings of the cells are shown in Figure 100c, and comparison videos are presented in the QR-code video link in Figure 100b.

These preliminary experiments suggest that the drugs digoxin and curcumin have a similar mobility reduction effect on lysosomes. Since curcumin and digoxin are following both a mTORC1-dependent mechanism for TFEB activation this could be the reason for these aligning effects. However, the increase of mobility of rapamycin, which does not follow the same trend contradicts this hypothesis. Generally, it was expected that these compounds would lead to a lysosomal mobility increase which could have indicated the reason for their positive effects in different disease models. An alternative explanation for the reduced mobility observed for digoxin and curcumin could be a drug induced apoptosis.[234] This is known to also reduce the mobility of lysosomes and lead to a lysosomal aggregation at the perinuclear region of the cell. However, this aggregation was not observed for the two investigated compounds in question.

The results on trehalose and bafilomycin A1 also showed a slight mobility reduction after the treatment but these were less pronounced compared to digoxin and curcumin.

Although all five compounds have previously been shown to either influence lysosome biogenesis and autophagy directly (trehalose, bafilomycin A1) or via indirect means by influencing the mTORC1 controlled TFEB location (rapamycin, curcumin, digoxin), their precise mechanisms are too different to draw mechanistic conclusions from these results. Since the results described above were only done in duplicate, more repeats and the effect of different drug concentrations need to be investigated before drawing definite conclusions of these findings. However, this observational case study provides the general workflow combining the different technologies to enable more thorough investigations into the precise biological mechanisms for these lysosomal speed reductions. Therefore, these preliminary results indicate that the selected drugs influence the lysosomal mobility to a certain extent, but more repeats and control experiments should be carried out to exclude other effects that could also play a role in lysosomal mobility.

Furthermore, the dose of the drugs and the treatment time (which has not been investigated in this research) could have an effect on the outcome of the studies. Since each drug used has a different mode of action on the cell metabolism more mechanistic experiments could also be beneficial to investigate the precise reason for the observed lysosomal mobility changes. Finally, specific autophagy staining with LC3 protein dye could be carried out in future experiments to distinguish lysosomes from autophagosomes.

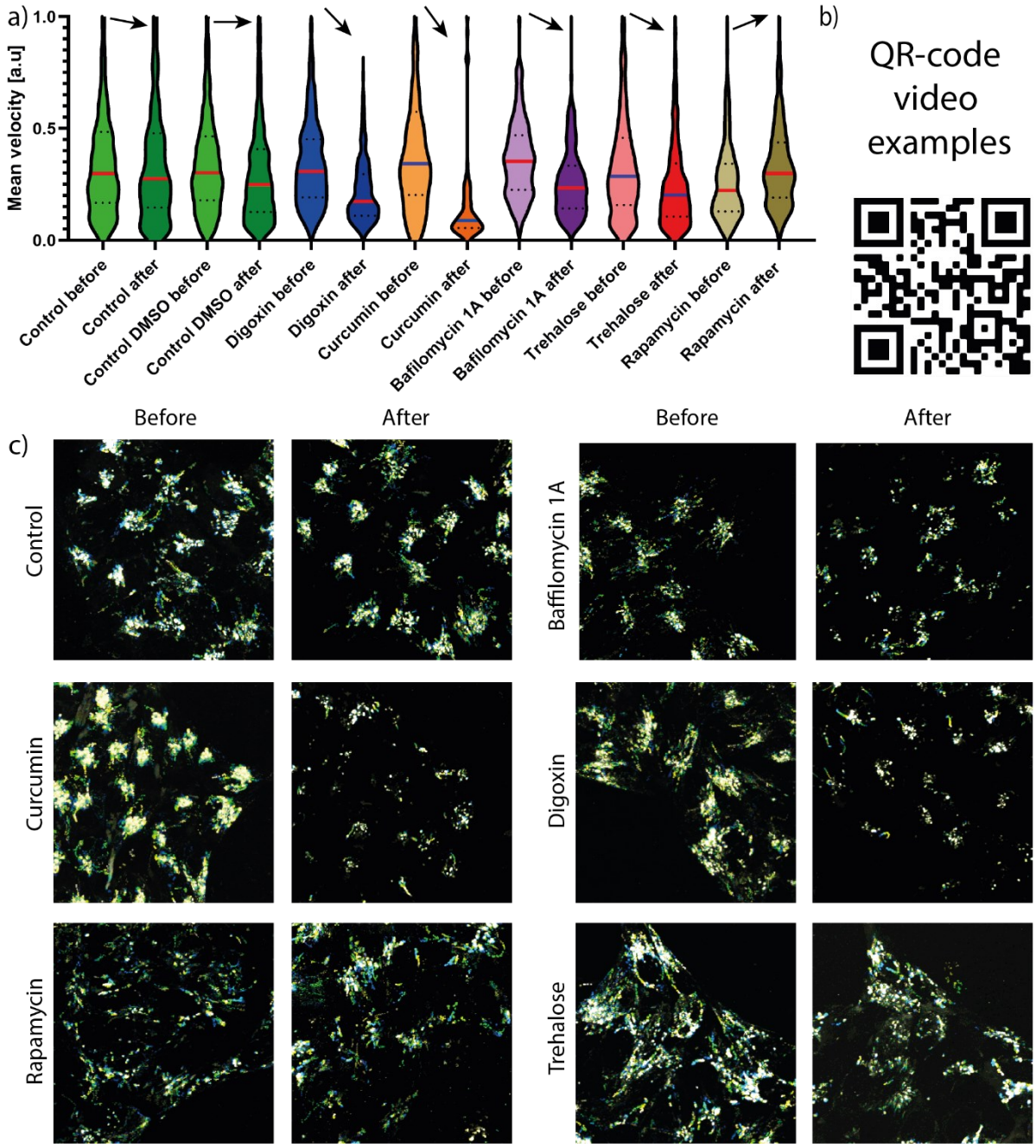

Figure 100: Lysosome drug treatment analysis. a) Lysosome movement speed distribution for the different before and after treatment conditions. b) QR-code video comparison examples for SH-SY5Y cells recorded in before and after treatment state for the different drugs. c) Overlayed image recordings over time of the different treatment conditions in the before and after state.

3.5. Conclusion

In this chapter preliminary drug treatment experiments on SH-SY5Y cells with rapamycin, digoxin, curcumin, trehalose and bafilomycin A1 were carried out to examine the lysosomal mobility changes compared to untreated cells. It was hypothesized that those drugs, which

have been shown to support the biogenesis of lysosomes, could also induce an increased activity and mobility of lysosomes. In contrast to the stated hypothesis the results suggested that only rapamycin showed a slight increase in lysosomal activity. Digoxin and curcumin induce a significant reduction on lysosome mobility while bafilomycin A1 and trehalose showed only a modest reduction effect. The results indicate that these drugs induce changes in the lysosomal movement behaviour, even though only one case showed the predicted increase. More experiments examining the effects of the drugs' dosage and more repeats need to be carried out to exclude other effects that could lead to the same observations. Furthermore, their precise mechanism should be investigated thoroughly before drawing definite conclusion on these results.

Despite the unexpected observations, the study presented in this chapter shows the applicability of the new optical probe and the computational tools to study the mobility of lysosomes in cells.

3.6. Materials and Methods

3.6.1. Treatment of SH-SY5Y cells

SH-SY5Y cells were grown in DMEM with 10% FBS, penicillin and streptomycin at 37 °C. Cells were plated on LabTek II coverslides at a seeding density of 20,000 cells per well and let grow for 48 h in the incubator. Then the media was changed to media containing 0.2% lipofectamine and 60 nM **FLCS1** and the cells were incubated for another 24 h. After that, the media was changed back to grow media and after 1 h the cells were imaged (this is the "before treatment" state) on a Leica SP7 confocal microscope at 630 nm excitation and a laser power of 0.05 % at a resolution of 256 px and in 4D z-stacks over time. Every z-stack took 15 sec, and the cells were recorded for 40 to 60 time points (10-15 min). The location of the cells was precisely recorded by measuring the distances of a set reference point of a cover glass impurity at the well corner. After the first imaging procedure the cells were treated with 370 nM digoxin, 250 nM rapamycin, 5 μM curcumin, 50 mM trehalose or 30 nM bafilomycin A1 in DMEM with its supplements and was incubated overnight for 24 h. For the second time point the same cells were searched based on the recorded coordinates and measured with the same microscopy settings as before (this is the "after treatment" state).

1.3.6. Particle tracking with TrackMate

Particle tracking was performed using the Fiji plugin TrackMate.[149,224] First the spatial pixel resolution of the recorded z-stack image sequence was upscaled with GMFN and the image frame interpolation along the t-dimension was carried out using the DAIN network. The enhanced image was then overlayed along the z-dimension and on this 2D+t dataset the particle tracking with TrackMate was performed. For detecting the particles, the LoG detector with an estimated blob diameter of 1 px and a threshold of 10-30 (depending on the intensity quality of the image) was used. The linking step was performed with the "Simple LAP tracker" with a linking distance of 3 µm, gap-closing of 3 µm and maximum frame gap of 2 frames. For the track selection a filter was set removing very short tracks with less than 7 frames to avoid flickering effects of partially detected lysosomal spots. The track statistics was saved and for the analysis the mean particle speed of each track in the image sequence was compared in the before and after treatment state of the same cells incubated with the drugs for 24 h.

CHAPTER VI

4.1. Summary and Outlook

4.1.1. Fluorescence copper(I) dye FLCS1

In this PhD research project, a new fluorescent copper(I) probe (**FLCS1**) was developed based on a BODIPY core structure connected with a NS_4 ligand that selectively bound to copper(I) based on *in vitro* experiments. The new probe showed superior photophysical properties and higher photostability to another BODIPY-based copper(I) probe (**CS3**) which is considered a 'gold standard'. **FLCS1** showed to detect copper(I) in lysosomes when live SH-SY5Y cells were imaged using FLIM. Further experiments with optically labelled alpha-synuclein confirmed colocalization of **FLCS1** with this protein inside lysosomes. In cellular experiments with this probe the copper transporter complex Cu-GTSM was used to demonstrate the ability to monitor changing levels of copper(I) in lysosomes using FLIM microscopy which is the first reported use of this technology for monitoring copper(I) levels in live cells.[273]

For future generations of copper(I) probes especially the binding affinity of the probe should be enhanced since the binding affinity of copper(I) in the cytosol exceeds the one from the **FLCS1** probe. This limits its application to only be able to detect copper(I) present in lysosomes, where due to the low pH, the probe is able to compete with other copper(I) binding sources. Furthermore, the dye could be made more water soluble which would potentially increase the likelihood to be able to directly treat the cells with the dye without the need of lipofectamine as a vehicle. This could be achieved by cleaving the allyl-ester groups

of the molecule or by modifying the BODIPY core structure with functional groups that increase the water solubility (e.g. SO_3^-, or COO^- groups)

4.1.2. Microscopy image enhancement strategies

The same copper(I) probe which localised in lysosomes was then used to perform lysosomal imaging to monitor the trafficking of the metal of this organelle inside cells. To overcome the limitations of the "eternal triangle of compromise" of point-scanning systems (speed, signal-to-noise ratio and spatial pixel resolution), several different neural networks were implemented tackling each of the corners of the triangle.

To improve the limitation of low image resolution, three neural networks were implemented (GMFN, SRFBN-S and Zooming SlowMo (ZS)) that could increase the pixel resolution of the recorded images by a factor of up to 4x. They were benchmarked against state-of-the-art mathematical upscaling methods (BIL and BIC), and it was shown that the deep learning resolution enhancement algorithms were better than the classical mathematical ones. Furthermore, ZS was compared with a previously reported neural network (PSSR) recently implemented for microscopy; ZS showed equivalent performance as this established network already used for microscopy.

To tackle the SNR problem an existing neural network called "Content-Aware Image Restoration" (in short CARE)[218] was used. This network showed promising results removing high levels of noise on a simulated dataset but also introduced some artefacts for 4D datasets where the intensity of the signal was sometimes not reconstructed correctly or caused flickering signals in the different z-stack slices.

Then, two state-of-the-art neural networks were implemented (DAIN and Zooming SlowMo) that could increase the image frame rate by interpolating images between two consecutive timepoints in the t- and z-dimension of 4D (TZXY) microscopy datasets. Those two interpolation networks were benchmarked against mathematical bilinear and bicubic interpolation techniques on simulated datasets and real-life microscopy data and showed significant improvements on the tracking performance of those datasets. All the mentioned image enhancement algorithms were implemented in Google Colab notebooks and were made available for the scientific community on the ZeroCostDL4Mic platform.

After establishing the functionality of each quality improvement technique, all three enhancement algorithms were tested in sequence on a synthetic dataset as well as on real experimental data. The low SNR, low resolution and low frame rate image sequences were

improved with CARE&ZS&ZS and CARE&GMFN&DAIN networks. Both workstreams showed large improvements over the low-quality images but the denoising network (CARE) produced artefacts that were amplified in the following enhancement steps. It was found that reducing the laser power made the CARE network redundant since the **FLCS1** probe showed good photostability while maintaining a good signal contrast at low laser powers. Therefore, just the resolution and frame rate enhancing algorithms were used for biological experiments. For future developments newer and more powerful algorithms could be implemented which potentially do not cause artefacts that are sometimes created by the frame interpolation networks. Also, the image spatial pixel resolution upscaling research is progressing quickly and could soon provide better and more powerful networks that could perform even better than the here implemented ones.

1.3.7. Effects of drug treatment on lysosomal mobility

Finally, the best performing neural network combination, i.e. GMFN and DAIN, was used to perform image enhancement on lysosomal movement datasets where the tracking results of copper-containing lysosomes before and after treatment with different drugs used in Parkinson's disease were compared. Treatment with digoxin and curcumin resulted in a significant reduced lysosomal activity and movement after incubation for 24 h. Trehalose and bafilomycin A1 also showed small reduction of lysosomal mobility while rapamycin showed a small lysosome movement speed increase. To confirm these observations more control experiments and repeats are needed, and some biological control experiments would be helpful to investigate the cause for the observations in more details. Furthermore, other movement parameters provided by the tracking algorithm can be considered to gain deeper insights into the effect of these drugs. The direction and lysosomal location over time in comparison to the nucleus could be investigated in more detail as well as the conditions of each individual cell could be considered. This would allow for a better understanding of yet unanswered question of, how individual lysosomes are organized spatially to coordinate and integrate their functions. More data and potentially even longer image recordings could be necessary to be able to carry out proper statistical evaluation of these results.

4.2. Publications & Conferences

Publications

1) Priessner M., Summers P. A., Lewis B. W., Sastre M., Ying L.,Kuimova M. K., Vilar R.,. Selective detection of Cu^{+} ions in live cells via fluorescence lifetime imaging microscopy. *Angew. Chemie Int. Ed.* - doi.org/10.1002/anie.202109349 (2021).

2) Priessner M., Gaboriau D. C.,Sheridan A., Lenn T., Chubb J., Manor U., Vilar R., Laine R. F., Deep Learning-based frame predictions for bioimaging, *bioRxiv*, doi.org/10.1101/2021.11.02.466664 / Nature Methods (submitted)

Academic Conference Presentations and Research Stays

03/07/2019: Poster presentation at Post Graduate Symposium at Imperial College London: *Developing a colocalization toolset for detecting copper(I) and alpha-synuclein in Parkinsons's Disease*

26/07/2018 – 29/07/2018: Conference poster presentation at the EMBO Workshop. In situ Methods in Cell Biology and Cellular Biophysics: *Developing a colocalization toolset for detecting copper(I) and alpha-synuclein in Parkinsons's Disease*

12/08/2019: Poster presentation at Post Graduate Symposium at Imperial College London**:** *Development of fluorescent probes for cellular imaging of copper(I) and colocalization studies with alpha-synuclein* (**Award**: 2nd best Poster Presentation)

12/08/2019 – 16/08/2019: Poster presentation at the International Conference on. Biological Inorganic Chemistry Conference**:** *Development of fluorescent probes for cellular imaging of copper(I) and colocalization studies with alpha-synuclein*

05/01/2020 – 29/02/2020: Research internship at Omnivoyant: *Using deep learning approaches for establishing colour constancy on social media images*

24/07/2020: Research talk at the Post Graduate Symposium at Imperial College London: *Investigation of Lysosomal Copper(I) Mobility in Cells relevant to Parkinsons's Disease using Deep Learning Strategies in Confocal Microscopy*

REFERENCES

1. Holm, R. H., Kennepohl, P. & Solomon, E. I. Structural and functional aspects of metal sites in biology. *Chem. Rev.* **96**, 2239–2314 (1996).
2. Waldron, K. J., Rutherford, J. C., Ford, D., *et al.* Metalloproteins and metal sensing. *Nature* **460**, 823–830 (2009).
3. Bolognin, S., Messori, L. & Zatta, P. Metal ion physiopathology in neurodegenerative disorders. *NeuroMolecular Med.* **11**, 223–238 (2009).
4. Williams, D. R. Metals, ligands, and cancer. *Chem. Rev.* **72**, 203–213 (1972).
5. Chen, Y. W., Yang, C. Y., Huang, C. F., *et al.* Heavy metals, islet function and diabetes development. *Islets* **1**, 169–176 (2009).
6. Wang, H., Wang, M., Wang, B., *et al.* The distribution profile and oxidation states of biometals in APP transgenic mouse brain: Dyshomeostasis with age and as a function of the development of Alzheimer's disease. *Metallomics* **4**, 289–296 (2012).
7. Uversky, V. N., Li, J. & Fink, A. L. Metal-triggered structural transformations, aggregation, and fibrillation of human α-synuclein: A possible molecular link between parkinson's disease and heavy metal exposure. *J. Biol. Chem.* **276**, 44284–44296 (2001).
8. Valeur, B. & Berberan-Santos, M. N. A brief history of fluorescence and phosphorescence before the emergence of quantum theory. *J. Chem. Ed.* **88**, 731–738 (2011).
9. Stockes, G. On the change of refrangibility of light. *Philos. Trans. R. Soc. London* **142**, 463–562 (1852).
10. Jabłoństski, A. Efficiency of anti-stokes fluorescence in dyes. *Nature* **131**, 839–840 (1933).
11. Kasha, M. Characterization of electronic transitions in complex molecules. *Discu. Fara. Soc.* **9**, 14–19 (1950).
12. Born, M. & Oppenheimer, R. Zur Quantentheorie der Molekeln. *Ann. Phys.* **389**, 457–484 (1927).
13. Tsukube, H. & Shinoda, S. Lanthanide complexes in molecular recognition and chirality sensing of biological substrates. *Chem. Rev.* **102**, 2389–2403 (2002).
14. Berezin, M. Y. & Achilefu, S. Fluorescence lifetime measurements and biological imaging. *Chem. Rev.* **110**, 2641–2684 (2010).

15. Bajzer, Z. & Prendergast, F. G. Maximum likelihood analysis of fluorescence data. *Meth. Enzy.* **210**, 200–237 (1992).
16. James, F. *Statistical methods in experimental physics*. (World Scientific Publishing Co., 2006).
17. Li, Y., Natakorn, S., Chen, Y., *et al.* Investigations on Average Fluorescence Lifetimes for Visualizing Multi-Exponential Decays. *Front. Phys.* **8**, 576862 (2020).
18. Sillen, A. & Engelborghs, Y. The Correct Use of 'Average' Fluorescence Parameters. *Photochem. Photobiol.* **67**, 475–486 (1998).
19. Olivares, M. & Uauy, R. Copper as an essential nutrient. *Am. J. Clin. Nutr.* **63**, 791S–6S (1996).
20. Verwilst, P., Sunwoo, K. & Kim, J. S. The role of copper ions in pathophysiology and fluorescent sensors for the detection thereof. *Chem. Commun.* 5556–5571 (2015).
21. Aron, A. T., Ramos-Torres, K. M., Cotruvo, J. A., *et al.* Recognition- and reactivity-based fluorescent probes for studying transition metal signaling in living systems. *Acc. Chem. Res.* **48**, 2434–42 (2015).
22. Ridge, P. G., Zhang, Y. & Gladyshev, V. N. Comparative Genomic Analyses of Copper Transporters and Cuproproteomes Reveal Evolutionary Dynamics of Copper Utilization and Its Link to Oxygen. *PLoS One* **3**, e1378 (2008).
23. Boal, A. K. & Rosenzweig, A. C. Structural Biology of Copper Trafficking. *Chem. Rev.* **109**, 4760–4779 (2009).
24. Ferguson-Miller, S. & Babcock, G. T. Heme/Copper Terminal Oxidases. *Chem. Rev.* **96**, 2889−2907 (1996).
25. Olivares, C. & Solano, F. New insights into the active site structure and catalytic mechanism of tyrosinase and its related proteins. *Pig. Cell Mel. Res.* **22**, 750–760 (2009).
26. Joe, M. & Fridovich, I. Superoxide Dismutase. *J. Biol. Chem.* **244**, 6049–6055 (1969).
27. Herranz, N. S., Dave, N. L., Millanes-Romero, A., *et al.* Lysyl Oxidase-like 2 Deaminates Lysine 4 in Histone H3. *Mol. Cell* **46**, 369–376 (2012).
28. Townsend, D. M., Tew, K. D. & Tapiero, H. The importance of glutathione in human disease. *Bio. Med. Pharmacother.* **57**, 145–155 (2003).
29. Meister, A. & Anderson, M. E. Glutathione. *Ann. Rev. Biochem* **52**, 711–60 (1983).
30. Cadet, J., Douki, T. & Ravanat, J.-L. Oxidatively generated base damage to cellular DNA. *Free Radic. Biol. Med.* **49**, 9–21 (2010).
31. Moreira, P. I., Nunomura, A., Nakamura, M., *et al.* Nucleic acid oxidation in Alzheimer disease. *Free Radic. Biol. Med.* **44**, 1493–1505 (2008).
32. Hyman, L. M. & Franz, K. J. Probing oxidative stress: Small molecule fluorescent sensors of metal ions, reactive oxygen species, and thiols. *Coord. Chem. Rev.* 2333–2356 (2012).
33. Halliwell, B. Oxidative stress and neurodegeneration: Where are we now? *J. Neurochem.* **97**, 1634–1658 (2006).
34. Winterbourn, C. C. Reconciling the chemistry and biology of reactive oxygen species. *Nat. Chem. Biol.* **4**, 278–286 (2008).
35. Murphy, M. P., Holmgren, A., Ran Larsson, N.-G., *et al.* Unraveling the Biological Roles of Reactive Oxygen Species. *Cell Metab.* **13**, 361–366 (2011).
36. Prousek, J. Fenton chemistry in biology and medicine. *Pure Appl. Chem* **79**, 2325–2338 (2007).
37. Hureau, C. Coordination of redox active metal ions to the amyloid precursor protein and to amyloid-β peptides involved in Alzheimer disease. Part 1: An overview. *Coord. Chem. Rev.* **256**, 2164–2174 (2012).

38. Lutsenko, S. Human copper homeostasis: a network of interconnected pathways. *Curr. Opin. in Chem. Biol.* **14**, 211–217 (2010).
39. Tsai, C. Y., Liebig, J. K., Tsigelny, I. F., *et al.* The copper transporter 1 (CTR1) is required to maintain the stability of copper transporter 2 (CTR2). *Metallomics* **7**, 1477–1487 (2015).
40. Zeid, C. A., Yi, L. & Kaler, S. G. Menkes Disease and Other Disorders Related to ATP7A. *Clin. Transl. Persp.on Wilson Diseas.* 439–447 (2019).
41. Polishchuk, E. V. & Polishchuk, R. S. The emerging role of lysosomes in copper homeostasis. *Metallomics* **8**, 853–862 (2016).
42. Robinson, N. J. & Winge, D. R. Copper metallochaperones. *Ann. Rev. Biochem.* **79**, 537–562 (2010).
43. Banci, L., Bertini, I., Ciofi-Baffoni, S., *et al.* Affinity gradients drive copper to cellular destinations. *Nature* **465**, 645–648 (2010).
44. Xiao, Z., Brose, J., Schimo, S., *et al.* Unification of the copper(I) binding affinities of the metallo-chaperones Atx1, Atox1, and related proteins: Detection probes and affinity standards. *J. Biol. Chem.* **286**, 11047–11055 (2011).
45. Xiao, Z., Gottschlich, L., Van Der Meulen, R., *et al.* Evaluation of quantitative probes for weaker Cu(I) binding sites completes a set of four capable of detecting Cu(I) affinities from nanomolar to attomolar. *Metallomics* **5**, 501–513 (2013).
46. Cotruvo, J. A., Aron, A. T., Ramos-Torres, K. M., *et al.* Synthetic fluorescent probes for studying copper in biological systems. *Chem. Soc. Rev.* 4400–4414 (2015).
47. Benítez, J. J., Keller, A. M., Huffman, D. L., *et al.* Relating dynamic protein interactions of metallochaperones with metal transfer at the single-molecule level. *Fara. Discu.* **148**, 71–82 (2011).
48. New, E. J. Tools to study distinct metal pools in biology. *Dalt. Trans.* **42**, 3210–3219 (2013).
49. Viguier, R. F. H. & Hulme, A. N. A sensitized europium complex generated by micromolar concentrations of copper(I): Toward the detection of copper(I) in biology. *J. Am. Chem. Soc.* **128**, 11370–11371 (2006).
50. Gitlin, J. D. Wilson Disease. *Gastroenterology* **125**, 1868–1877 (2003).
51. Concilli, M., Iacobacci, S., Chesi, G., *et al.* A systems biology approach reveals new endoplasmic reticulum-associated targets for the correction of the ATP7B mutant causing Wilson disease. *Metallomics* **8**, 920–930 (2016).
52. Das, S. K. & Ray, K. Wilson's disease: An update. *Nat. Clin. Pr. Neuro.* **2**, 482–493 (2006).
53. Gupta, A. & Lutsenko, S. Human copper transporters: Mechanism, role in human diseases and therapeutic potential. *Futur. Med. Chem.* **1**, 1125–1142 (2009).
54. Bisaglia, M. & Bubacco, L. Copper ions and Parkinson's disease: Why is homeostasis so relevant? *Biomolecules* **10**, 195 (2020).
55. Bagheri, S., Squitti, R., Haertlé, T., *et al.* Role of copper in the onset of Alzheimer's disease compared to other metals. *Front. Aging Neuro.* **9**, 446 (2018).
56. Fox, J. H., Kama, J. A., Lieberman, G., *et al.* Mechanisms of copper ion mediated Huntington's disease progression. *PLoS One* **2**, e334 (2007).
57. Lashuel, H. A., Overk, C. R., Oueslati, A., *et al.* The many faces of α-synuclein: from structure and toxicity to therapeutic target. *Nat. Rev. Neurosci.* **14**, (2013).
58. Rasia, R. M., Bertoncini, C. W., Marsh, D., *et al.* Structural characterization of copper(II) binding to α-synuclein: Insights into the bioinorganic chemistry of Parkinson's disease. *Proc. Natl. Acad. Sci. U. S. A.* **102**, 4294–4299 (2005).

59. Lee, H.-J., Patel, S. & Lee, S.-J. Intravesicular Localization and Exocytosis of -Synuclein and its Aggregates. *J. Neurosci.* **25**, 6016–6024 (2005).
60. El-Agnaf, O. M. A., Salem, S. A., Paleologou, K. E., *et al.* Alpha-Synuclein implicated in Parkinson's disease is present in extracellular biological fluids, including human plasma. *FASEB J.* **17**, 1945–1947 (2003).
61. Kowalik-Jankowska, T., Rajewska, A., Jankowska, E., *et al.* Products of Cu(II)-catalyzed oxidation of alpha-synuclein fragments containing M1-D2 and H50 residues in the presence of hydrogen peroxide. *Dalt. Trans.* 832–8 (2008).
62. Wright, J. A., Wang, X. & Brown, D. R. Unique copper-induced oligomers mediate alpha-synuclein toxicity. *FASEB J.* **23**, 2384–2393 (2009).
63. Becker, J. S., Matusch, A. & Wu, B. Bioimaging mass spectrometry of trace elements - recent advance and applications of LA-ICP-MS: A review. *Anal. Chim. Acta.* **835**, 1–18 (2014).
64. De Jonge, M. D. & Vogt, S. Hard X-ray fluorescence tomography-an emerging tool for structural visualization. *Curr. Opin. in Chem. Biol.* **20**, 606–614 (2010).
65. Vogt, S. & Ralle, M. Opportunities in multidimensional trace metal imaging: Taking copper-associated disease research to the next level. *Anal. Bioanal. Chem.* **405**, 1809–1820 (2013).
66. Hong-Hermesdorf, A., Miethke, M., Gallaher, S. D., *et al.* Subcellular metal imaging identifies dynamic sites of Cu accumulation in Chlamydomonas. *Nat. Chem. Biol.* **10**, 1034–1042 (2014).
67. Weiskirchen, S., Kim, P. & Weiskirchen, R. Determination of copper poisoning in Wilson's disease using laser ablation inductively coupled plasma mass spectrometry. *Ann. Transl. Med.* **7**, S72–S72 (2019).
68. Heuberger, D. M., Harankhedkar, S., Morgan, T., *et al.* High-affinity Cu(I) chelator PSP-2 as potential anti-angiogenic agent. *Sci. Rep.* **9**, 1–10 (2019).
69. Ackerman, C. M., Weber, P. K., Xiao, T., *et al.* Multimodal LA-ICP-MS and nanoSIMS imaging enables copper mapping within photoreceptor megamitochondria in a zebrafish model of Menkes disease. *Metallomics* **10**, 474–485 (2018).
70. Carter, K. P., Young, A. M. & Palmer, A. E. Fluorescent Sensors for Measuring Metal Ions in Living Systems. *Chem. Rev.* **114**, 4564−4601 (2014).
71. Qian, X. & Xu, Z. Fluorescence imaging of metal ions implicated in diseases. *Chem. Soc. Rev.* **44**, 4487–4493 (2015).
72. Lakowicz, J. R. Introduction to Fluorescence. *Principles of fluorescence spectroscopy* 1–26 (2006).
73. Treibs, A. & Kreuzer, F. -H. Difluorboryl-Komplexe von Di- und Tripyrrylmethenen. *Justus Liebigs Ann. Chem.* **718**, 208–223 (1968).
74. Culzoni, M. J., Muñoz De La Peña, A., MacHuca, A., *et al.* Rhodamine and BODIPY chemodosimeters and chemosensors for the detection of Hg^{2+}, based on fluorescence enhancement effects. *Analy. Meth.* **5**, 30–49 (2013).
75. Yuan, L., Lin, W., Zheng, K., *et al.* Far-red to near infrared analyte-responsive fluorescent probes based on organic fluorophore platforms for fluorescence imaging. *Chem. Soc. Rev* **42**, 622 (2013).
76. Ni, Y. & Wu, J. Far-red and near infrared BODIPY dyes: synthesis and applications for fluorescent pH probes and bio-imaging. *Org. Biomol. Chem.* **12**, 3774 (2014).
77. Sameiro, M. & Gonçalves, T. Fluorescent labeling of biomolecules with organic probes. *Chem. Rev.* **109**, 190–212 (2009).
78. Suzuki, K. New trends in Near-Infrared Fluorophores for Bioimaging. *Analy. Scie.* **30**, 327–349 (2014).

79. Zhang, W., Ahmed, A., Cong, H., *et al.* Application of multifunctional BODIPY in photodynamic therapy. *Dye. Pig.* **185**, 108937 (2021).
80. Kamkaew, A., Lim, S. H., Lee, H. B., *et al.* BODIPY dyes in photodynamic therapy. *Chem. Soc. Rev.* **42**, 77–88 (2013).
81. Chen, J. J., Conron, S. M., Erwin, P., *et al.* High-efficiency BODIPY-based organic photovoltaics. *App. Mat. Interf.* **7**, 662–669 (2015).
82. Aguiar, A., Farinhas, J., da Silva, W., *et al.* Simple BODIPY dyes as suitable electron-donors for organic bulk heterojunction photovoltaic cells. *Dye. Pigm.* **172**, 107842 (2020).
83. Ulrich, G., Ziessel, R. & Harriman, A. The chemistry of fluorescent bodipy dyes: Versatility unsurpassed. *Angew. Chem.* **47**, 1184–1201 (2008).
84. Wood, T. E. & Thompson, A. Advances in the chemistry of dipyrrins and their complexes. *Chem. Rev.* 1831–1861 (2007).
85. Atilgan, A., Eåik, E. T., Guliyev, R., *et al.* Near-IR-Triggered, Remote-Controlled Release of Metal Ions: A Novel Strategy for Caged Ions. *Angew. Chem.* **53**, 10678–10681 (2014).
86. Yang, Z., He, Y., Lee, J. H., *et al.* A self-calibrating bipartite viscosity sensor for mitochondria. *J. Am. Chem. Soc.* **135**, 9181–9185 (2013).
87. Yu, L., Muthukumaran, K., Sazanovich, I. V., *et al.* Excited-State Energy-Transfer Dynamics in Self-Assembled Triads Composed of Two Porphyrins and an Intervening Bis(dipyrrinato)metal Complex. *Inorg. Chem.* **42**, 6629–6647 (2003).
88. Wang, D., Fan, J., Gao, X., *et al.* Carboxyl BODIPY dyes from bicarboxylic anhydrides: One-pot preparation, spectral properties, photostability, and biolabeling. *J. Org. Chem.* **74**, 7675–7683 (2009).
89. Zhou, X., Yu, C., Feng, Z., *et al.* Highly Regioselective α-Chlorination of the BODIPY Chromophore with Copper(II) Chloride. *Org. Lett.* **17**, 4632–4635 (2015).
90. Poirel, A., De Nicola, A., Retailleau, P., *et al.* Oxidative coupling of 1,7,8-unsubstituted BODIPYs: Synthesis and electrochemical and spectroscopic properties. *J. Org. Chem.* **77**, 7512–7525 (2012).
91. Loudet, A. & Burgess, K. BODIPY Dyes and Their Derivatives: Syntheses and Spectroscopic Properties. *Chem. Rev.* **107**, 4891–4932 (2007).
92. Boens, N., Verbelen, B., Ortiz, M. J., *et al.* Synthesis of BODIPY dyes through postfunctionalization of the boron dipyrromethene core. *Coord. Chem. Rev.* **399** 213024 (2019).
93. Fahrni, C. J. Synthetic fluorescent probes for monovalent copper. *Curr. Opin. in Chem. Biol.* **17** 656–662 (2013).
94. Que, E. L., Domaille, D. W. & Chang, C. J. ChemInform Abstract: Metals in Neurobiology: Probing Their Chemistry and Biology with Molecular Imaging. *Chem. Inform.* **39**, 1517–1549 (2008).
95. Domaille, D. W., Que, E. L. & Chang, C. J. Synthetic fluorescent sensors for studying the cell biology of metals. *Nature Chem. Biol.* **4** 168–175 (2008).
96. Domaille, D. W., Zeng, L. & Chang, C. J. Visualizing ascorbate-triggered release of labile copper within living cells using a ratiometric fluorescent sensor. *J. Am. Chem. Soc.* **132**, 1194–1195 (2010).
97. Ueno, T., Urano, Y., Setsukinai, K., *et al.* Rational Principles for Modulating Fluorescence Properties of Fluorescein. *J. Am. Chem. Soc.* **126**, 14079–14085 (2004).
98. Yang, L., Mcrae, R., Henary, M. M., *et al.* Imaging of the intracellular topography of copper with a fluorescent sensor and by synchrotron x-ray fluorescence microscopy. *PNAS* **102**, 11179–11184 (2005).

99. Morgan, M. T., McCallum, A. & Fahrni, C. J. Rational Design of a Water-Soluble, Lipid-Compatible Fluorescent Probe for Cu(I) with Sub-Part-Per-Trillion Sensitivity. *Chem. Sci.* **7**, 1468–1473 (2016).
100. Zeng, L., Miller, E. W., Pralle, A., *et al.* A Selective Turn-On Fluorescent Sensor for Imaging Copper in Living Cells. *J. Am. Chem. Soc.* **128**, 10–11 (2006).
101. Dodani, S. C., Domaille, D. W., Nam, C. I., *et al.* Calcium-dependent copper redistributions in neuronal cells revealed by a fluorescent copper sensor and X-ray fluorescence microscopy. *Proc. Natl. Acad. Sci. U. S. A.* **108**, 5980–5 (2011).
102. Dodani, S. C., Leary, S. C., Cobine, P. A., *et al.* A targetable fluorescent sensor reveals that copper-deficient SCO1 and SCO2 patient cells prioritize mitochondrial copper homeostasis. *J. Am. Chem. Soc.* **133**, 8606–8616 (2011).
103. Hirayama, T., Van De Bittner, G. C., Gray, L. W., *et al.* Near-infrared fluorescent sensor for in vivo copper imaging in a murine Wilson disease model. *Proc. Natl. Acad. Sci.* **7**, 2228–2233 (2012).
104. Dodani, S. C., Firl, A., Chan, J., *et al.* Copper is an endogenous modulator of neural circuit spontaneous activity. *Proc. Nat. Acad. Sci.* **111**, 16280–16285 (2014).
105. Price, K. A., Hickey, J. L., Xiao, Z., *et al.* The challenges of using a copper fluorescent sensor (CS1) to track intracellular distributions of copper in neuronal and glial cells. *Chem. Sci.* **3**, 2748–2759 (2012).
106. Rae, T. D., Schmidt, P. J., Pufahl, R. A., *et al.* Undetectable intracellular free copper: The requirement of a copper chaperone for superoxide dismutase. *Science* **284**, 805–808 (1999).
107. Finney, L. A. & O'Halloran, T. V. Transition metal speciation in the cell: Insights from the chemistry of metal ion receptors. *Science* **300**, 931–936 (2003).
108. Wegner, S. V., Sun, F., Hernandez, N., *et al.* The tightly regulated copper window in yeast. *Chem. Commun.* **47**, 2571–2573 (2011).
109. Cooper, G. M. Lysosomes. *Cell A Mol. Approach. 2nd Ed.* (2000).
110. Blaby-Haas, C. E. & Merchant, S. S. Lysosome-related organelles as mediators of metal homeostasis. *J.Biol. Chem.* **289**, 28129–28136 (2014).
111. Polishchuk, E. V., Concilli, M., Iacobacci, S., *et al.* Wilson Disease Protein ATP7B Utilizes Lysosomal Exocytosis to Maintain Copper Homeostasis. *Dev. Cell* **29**, 686–700 (2014).
112. Lim, C. S., Han, J. H., Kim, C. W., *et al.* A copper(i)-ion selective two-photon fluorescent probe for in vivo imaging. *Chem. Commun.* **47**, 7146–7148 (2011).
113. Taki, M., Iyoshi, S., Ojida, A., *et al.* Development of highly sensitive fluorescent probes for detection of intracellular copper(I) in living systems. *J. Am. Chem. Soc.* **132**, 5938–5939 (2010).
114. Cao, X., Lin, W. & Wan, W. Development of a near-infrared fluorescent probe for imaging of endogenous Cu^{+} in live cellsw. *Chem. Commun.* **48**, 6247–6249 (2012).
115. Satriano, C., Trusso Sfrazzetto, G., Emanuela Amato, M., *et al.* A ratiometric naphthalimide sensor for live cell imaging of copper(i). *Chem. Commun.* **49**, 5565–5567 (2013).
116. Venetta, B. D. Microscope phase fluorometer for determining the fluorescence lifetimes of fluorochromes. *Rev. Sci. Instrum.* **30**, 450–457 (1959).
117. I. Bugiel, K. König & H. Wabnitz. Investigation of cells by fluorescence laser scanning microscopy with subnanosecond time resolution. *Laser Life Science* 47–53 (1989).
118. Wang, X. F., Uchida, T. & Minami, S. A Fluorescence Lifetime Distribution Measurement System Based on Phase-Resolved Detection Using an Image Dissector Tube: *Appl. Spectrosc.* **43**, 840–845 (1989).

119. Hötzer, B., Ivanov, R., Brumbarova, T., *et al.* Visualization of Cu^{2+} uptake and release in plant cells by fluorescence lifetime imaging microscopy. *FEBS J.* **279**, 410–419 (2012).
120. Paredes, J. M., Giron, M. D., Ruedas-Rama, M. J., *et al.* Real-time phosphate sensing in living cells using fluorescence lifetime imaging microscopy (FLIM). *J. Phys. Chem.* **117**, 8143–8149 (2013).
121. Szmacinski, H. & Lakowicz, J. R. Fluorescence lifetime-based sensing and imaging. *Sens. Actuat. B. Chem.* **29**, 16–24 (1995).
122. Sharma, D. K., Irfanullah, M., Basu, S. K., *et al.* An approach to estimate spatial distribution of analyte within cells using spectrally-resolved fluorescence microscopy. *Meth. Applic. Fluoresc.* **5**, 014003 (2017).
123. Peng, X., Yang, Z., Wang, J., *et al.* Fluorescence ratiometry and fluorescence lifetime imaging: Using a single molecular sensor for dual mode imaging of cellular viscosity. *J. Am. Chem. Soc.* **133**, 6626–6635 (2011).
124. Okabe, K., Inada, N., Gota, C., *et al.* Intracellular temperature mapping with a fluorescent polymeric thermometer and fluorescence lifetime imaging microscopy. *Nat. Commun.* **3**, 1–9 (2012).
125. Suhling, K., Hirvonen, L. M., Levitt, J. A., *et al.* Fluorescence lifetime imaging (FLIM): Basic concepts and some recent developments. *Med. Phot.* **27**, 3–40 (2015).
126. Hickey, J. L., James, J. L., Henderson, C. A., *et al.* Intracellular Distribution of Fluorescent Copper and Zinc Bis(thiosemicarbazonato) Complexes Measured with Fluorescence Lifetime Spectroscopy. *Inorg. Chem* **54**, 9556–9567 (2015).
127. Waghorn, P. A., Jones, M. W., Theobald, M. B. M., *et al.* Shining light on the stability of metal thiosemicarbazonate complexes in living cells by FLIM. *Chem. Scie.* **4**, 1430–1441 (2013).
128. Grüter, A., Hoffmann, M., Müller, R., *et al.* A high-affinity fluorescence probe for copper(II) ions and its application in fluorescence lifetime correlation spectroscopy. *Analy. Bioanal. Chem.* **411**, 3229–3240 (2019).
129. McCranor, B. J., Szmacinski, H., Zeng, H. H., *et al.* Fluorescence lifetime imaging of physiological free Cu(II) levels in live cells with a Cu(II)-selective carbonic anhydrase-based biosensor. *Metallomics* **6**, 1034–1042 (2014).
130. Sofi, C., Pascu, I., James, T. D., *et al.* Ditopic boronic acid and imine-based naphthalimide fluorescence sensor for copper(II). *Chem. Commun.* **50**, 11771–11966 (2014).
131. Amat-Guerri, F., Liras, M., Carrascoso, M. L., *et al.* Methacrylate-tethered Analogs of the Laser Dye PM567-Synthesis, Copolymerization with Methyl Methacrylate and Photostability of the Copolymers. *Photochem. Photobio.* **77**, 577–584 (2007).
132. Gabe, Y., Ueno, T., Urano, Y., *et al.* Tunable design strategy for fluorescence probes based on 4-substituted BODIPY chromophore: Improvement of highly sensitive fluorescence probe for nitric oxide. *Anal. Bioanal. Chem.* **386**, 621–626 (2006).
133. Kozlowski, H., Luczkowski, M., Remelli, M., *et al.* Copper, zinc and iron in neurodegenerative diseases (Alzheimer's, Parkinson's and prion diseases). *Coord. Chem. Rev.* **256**, 2129–2141 (2012).
134. De Silva, A. P., Gunaratne, H. Q. N., Gunnlaugsson, T., *et al.* Signaling recognition events with fluorescent sensors and switches. *Chem. Rev.* **97**, 1515–1566 (1997).
135. Matsui, A., Umezawa, K., Shindo, Y., *et al.* A near-infrared fluorescent calcium probe: A new tool for intracellular multicolour Ca^{2+} imaging. *Chem. Commun.* **47**, 10407–10409 (2011).

136. Ishikawa, J., Sakamoto, H. & Wada, H. Synthesis and silver ion complexation behavior of fluoroionophores containing a benzothiazolyl group linked to an N-phenylpoly-thiazaalkane moiety. *J. Chem. Soc.* **2**, 1273–1279 (1999).
137. Ozturk, T., Klymchenko, A. S., Capan, A., *et al.* New 3-hydroxyflavone derivatives for probing hydrophobic sites in microheterogeneous systems. *Tetrahedron* **63**, 10290–10299 (2007).
138. Cao, X., Lin, W. & Wan, W. Development of a near-infrared fluorescent probe for imaging of endogenous Cu^{+} in live cells. *Chem. Commun.* **48**, 6247–6249 (2012).
139. Morgan, M. T., Yang, B., Harankhedkar, S., *et al.* Stabilization of Aliphatic Phosphines by Auxiliary Phosphine Sulfides Offers Zeptomolar Affinity and Unprecedented Selectivity for Probing Biological Cu(I). *Angew. Chem.* **57**, 9711–9715 (2018).
140. Radunz, S., Kraus, W., Bischoff, F. A., *et al.* Temperature- And Structure-Dependent Optical Properties and Photophysics of BODIPY Dyes. *J. Phys. Chem. A* **124**, 1787–1797 (2020).
141. Morgan, M. T., Bagchi, P. & Fahrni, C. J. Designed To Dissolve: Suppression of Colloidal Aggregation of Cu(I)-Selective Fluorescent Probes in Aqueous Buffer and In-Gel Detection of a Metallochaperone. *J. Am. Chem. Soc.* **133**, 15906–15909 (2011).
142. Ding, W. Q. & Lind, S. E. Metal ionophores - An emerging class of anticancer drugs. *IUBMB Life* **61**, 1013–1018 (2009).
143. Morgan, M. T., Bourassa, D., Harankhedkar, S., *et al.* Ratiometric two-photon microscopy reveals attomolar copper buffering in normal and Menkes mutant cells. *Proce. Nat. Acad. Scie.* **116**, 12167–12172 (2019).
144. Settembre, C., Fraldi, A., Medina, D. L., *et al.* Signals from the lysosome: A control centre for cellular clearance and energy metabolism. *Nat. Rev. Mol. C. Biol.* **14**, 283–296 (2013).
145. Ballabio, A. The awesome lysosome. *EMBO Mol. Med.* **8**, 73–76 (2016).
146. Donnelly, P. S., Caragounis, A., Du, T., *et al.* Selective intracellular release of copper and zinc ions from bis(thiosemicarbazonato) complexes reduces levels of Alzheimer disease amyloid-β peptide. *J. Biol. Chem.* **283**, 4568–4577 (2008).
147. Smith, R. M. & Martell, A. E. Critical Stability Constants. (1989).
148. Manzo, C. & Garcia-Parajo, M. F. A review of progress in single particle tracking: From methods to biophysical insights. *Reports Prog. Phys.* **78**, 124601 (2015).
149. Tinevez, J. Y., Perry, N., Schindelin, J., *et al.* TrackMate: An open and extensible platform for single-particle tracking. *Methods* **115**, 80–90 (2017).
150. Chenouard, N., Smal, I., de Chaumont, F., *et al.* Objective comparison of particle tracking methods. *Nat. Meth.* **11**, 281–289 (2014).
151. Minsky, M. Microscopy apparatus. *United States Patent Office* (1961).
152. Light, F., Author, M., White, J. G., *et al.* An Evaluation of Confocal versus Conventional Imaging of Biological Structures by. *J. Cell Biol.* **105**, 41–46 (1987).
153. Airy, G. B. On the Diffraction of an Object-glass with Circular Aperture. *Transactions of the Cambridge Philosophical Society,* ***5***, 283–291 (1835).
154. Airy disk - Wikipedia. https://en.wikipedia.org/wiki/Airy_disk. (Accessed 2021-08-19)
155. Ferrand, A., Schleicher, K. D., Ehrenfeuchter, N., *et al.* Using the NoiSee workflow to measure signal-to-noise ratios of confocal microscopes. *Sci. Reports* **9**, 1–12 (2019).
156. Waters, J. C. Accuracy and precision in quantitative fluorescence microscopy. *J. Cell Biol.* **185**, 1135–1148 (2009).
157. Conchello, J. A. & Lichtman, J. W. Optical sectioning microscopy. *Nat. Meth.* **2** 920–931 (2005).

158. Ntziachristos, V. Going deeper than microscopy: The optical imaging frontier in biology. *Nat. Meth.* **7**, 603–614 (2010).
159. Cheong, W. F., Prahl, S. A. & Welch, A. J. A Review of the Optical Properties of Biological Tissues. *IEEE J. Quantum Electron.* **26**, 2166–2185 (1990).
160. Egner, A., Schrader, M. & Hell, S. W. Refractive index mismatch induced intensity and phase variations in fluorescence confocal, multiphoton and 4Pi-microscopy. *Opt. Commun.* **153**, 211–217 (1998).
161. Shotton, D. M. Electronic light microscopy: present capabilities and future prospects. *Histochem. Cell Biol.* **104**, 97–137 (1995).
162. Gómez-Gaviro, M. V., Sanderson, D., Ripoll, J., *et al.* Biomedical Applications of Tissue Clearing and Three-Dimensional Imaging in Health and Disease. *iScience* **23**, (2020).
163. Icha, J., Weber, M., Waters, J. C., *et al.* Phototoxicity in live fluorescence microscopy, and how to avoid it. *BioEssays* **39**, 1700003 (2017).
164. Fischer, R. S., Wu, Y., Kanchanawong, P., *et al.* Microscopy in 3D: A biologist's toolbox. *Tre. Cell Biol.* **21**, 682–691 (2011).
165. Carlton, P. M., Boulanger, J., Kervrann, C., *et al.* Fast live simultaneous multiwavelength four-dimensional optical microscopy. *Proc. Nat. Acad. Sci.* **107**, 16016–16022 (2010).
166. Stephens, D. J. & Allan, V. J. Light microscopy techniques for live cell imaging. *Science,* **300**, 82–86 (2003).
167. Dittrich, P., Malvezzi-Campeggi, F., Jahnz, M., *et al.* Accessing molecular dynamics in cells by fluorescence correlation spectroscopy. *Biol. Chem.* **382**, 491–494 (2001).
168. Hoebe, R. A., Van Der Voort, H. T. M., Stap, J., *et al.* Quantitative determination of the reduction of phototoxicity and photobleaching by controlled light exposure microscopy. *J. Microsc.* **231**, 9–20 (2008).
169. Prewitt, J. M. S. & Mendelsohn, M. L. The Analysis of Cell Images. *Ann. New York Acad. Sci.* **128**, 1035–1053 (1966).
170. Hounsfield, G. N. Computerized transverse axial scanning (tomography): I. Description of system. *Br. J. Radiol.* **46**, 1016–1022 (1973).
171. Mansberg, H. P., Saunders, A. M. & Groner, W. The Hemalog D white cell differential system. *J. Histochem. Cytochem.* **22**, 711–724 (1974).
172. Lecun, Y., Bengio, Y. & Hinton, G. Deep learning. *Nature* **521**, 436–444 (2015).
173. Ciregan, D., Meier, U. & Schmidhuber, J. Multi-column deep neural networks for image classification. *IEEE CCVPR* 3642–3649 (2012).
174. Shelhamer, E., Long, J. & Darrell, T. Fully Convolutional Networks for Semantic Segmentation. *IEEE TPAMI* **39**, 640–651 (2017).
175. Li, M., Zuo, W. & Zhang, D. Convolutional Network for Attribute-driven and Identity-preserving Human Face Generation. *arXiv*:1608.06434 (2016).
176. Ronneberger, O., Fischer, P. & Brox, T. U-net: Convolutional networks for biomedical image segmentation. *LNCS* **51**, 234–241 (2015).
177. WU, Y., RIVENSON, Y., ZHANG, Y., *et al.* Extended depth-of-field in holographic image reconstruction using deep learning based auto-focusing and phase-recovery. *arXiv*: **5,** 704–710 (2018).
178. Nehme, E., Weiss, L. E., Michaeli, T., *et al.* Deep-STORM: Super-resolution single-molecule microscopy by deep learning. *arXiv*: **5,** 458–464 (2018).
179. Ouyang, W., Aristov, A., Lelek, M., *et al.* Deep learning massively accelerates super-resolution localization microscopy. *Nat. Biotechnol.* **36**, 460–468 (2018).

180. Fang, L., Monroe, F., Novak, S. W., *et al.* Deep learning-based point-scanning super-resolution imaging. *Nat. Meth.* **18**, 406–416 (2021).
181. Helgadottir, S., Argun, A. & Volpe, G. Digital video microscopy enhanced by deep learning. *arXiv* **6**, 506–513 (2018).
182. Xing, F., Xie, Y., Su, H., *et al.* Deep Learning in Microscopy Image Analysis: A Survey. *IEEE TNNLS* **29**, 4550–4568 (2018).
183. El Naqa, I. & Murphy, M. J. What Is Machine Learning? *Mach. Lear. Rad. Onc.* 3–11 (2015).
184. Olshausen, B. A. & Field, D. J. Emergence of simple-cell receptive field properties by learning a sparse code for natural images. *Nature* **381**, 607–609 (1996).
185. Bengio, Y., Lee, D.-H., Bornschein, J., *et al.* Towards Biologically Plausible Deep Learning. *CIFAR* 1–9 (2015).
186. Marblestone, A. H., Wayne, G. & Kording, K. P. Toward an integration of deep learning and neuroscience. *Front. Comput. Neurosci.* **10**, 94 (2016).
187. Hu, J., Niu, H., Carrasco, J., *et al.* Voronoi-Based Multi-Robot Autonomous Exploration in Unknown Environments via Deep Reinforcement Learning. *IEEE Trans. Veh. Technol.* **69**, 14413–14423 (2020).
188. Krizhevsky, A., Sutskever, I. & Hinton, G. E. ImageNet Classification with Deep Convolutional Neural Networks. *NeurIPS Proceed.* 1–9 (2009).
189. Google's AlphaGo AI wins three-match series against the world's best Go player – TechCrunch. https://techcrunch.com/2017/05/24/alphago-beats-planets-best-human-go-player-ke-jie/amp/?guccounter=1. (Accessed 2021-07-20)
190. Schmidhuber, J. Deep Learning in Neural Networks: An Overview. *Neural Networks* **61**, 85–117 (2014).
191. Bengio, Y., Courville, A. & Vincent, P. Representation Learning: A Review and New Perspectives. *IEEE TPAMI* **35**, 1798–1828 (2012).
192. Khan, A., Sohail, A., Zahoora, U., *et al.* A Survey of the Recent Architectures of Deep Convolutional Neural Networks. *Arti. Intelli. Rev.* **53**, 5455–5516 (2020).
193. Utgoff, P. E., Cussens, J., Kramer, S., *et al.* Inductive Transfer. *Ency. Mach. Lear.* 545–548 (2011).
194. Falk, T., Mai, D., Bensch, R., *et al.* U-Net: deep learning for cell counting, detection, and morphometry. *Nat. Meth.* **16**, 67–70 (2019).
195. Lateef, F. & Ruichek, Y. Survey on semantic segmentation using deep learning techniques. *Neurocomputing* **338**, 321–348 (2019).
196. Long, F. Microscopy cell nuclei segmentation with enhanced U-Net. *BMC Bioinf.* **21**, 1–12 (2020).
197. Goodfellow, I. J., Pouget-Abadie, J., Mirza, M., *et al.* Generative Adversarial Nets. *Adv. Neur. Inf. Proc. Sys.* **27**, 1–9 (2014).
198. Yadav, A., Shah, S., Xu, Z., *et al.* Stabilizing Adversarial Nets With Prediction Methods. *arXiv:* 1705.07364 (2017).
199. Ounkomol, C., Seshamani, S., Maleckar, M. M., *et al.* Label-free prediction of three-dimensional fluorescence images from transmitted-light microscopy. *Nat. Meth.* **15**, 917–920 (2018).
200. Mao, X.-J., Shen, C. & Yang, Y.-B. Image Restoration Using Very Deep Convolutional Encoder-Decoder Networks with Symmetric Skip Connections. *Adv. Neural Inf. Process. Syst.* 2810–2818 (2016).
201. Kingma, D. P. & Ba, J. L. Adam: A method for stochastic optimization. *ICLR 2015 - Conf. Tr. Proc.* 1–15 (2015).

202. Glasner, D., Bagon, S. & Irani, M. Super-Resolution from a Single Image. *IEEE ICCV* 1–8 (2009).
203. Jia, Y., Yang, W., Gao, Y., *et al.* Image super resolution via visual prior based digital image characteristics. *LNCS* 168–177 (2013).
204. Zhang, K., Gao, X., Tao, D., *et al.* Single image super-resolution with non-local means and steering kernel regression. *IEEE Image Process.* **21**, 4544–4556 (2012).
205. Li, Q., Li, Z., Lu, L., *et al.* Gated Multiple Feedback Network for Image Super-Resolution. *CVPR,* arXiv: 1907.04253 (2019).
206. Li, Z., Yang, J., Liu, Z., *et al.* Feedback Network for Image Super-Resolution. *CVPR,* arXiv: 1903.09814 (2019).
207. Niklaus, S., Mai, L. & Liu, F. Video Frame Interpolation via Adaptive Separable Convolution. *CVPR,* arXiv: 1708.01692 (2017).
208. Ancuti, C., Haber, T., Mertens, T., *et al.* Video enhancement using reference photographs. *Vis. Comp.* **24**, 709–717 (2008).
209. Bao, W., Lai, W. S., Ma, C., *et al.* Depth-aware video frame interpolation. *IEEE CVPR,* 3698–3707 (2019).
210. Chen, W., Fu, Z., Yang, D., *et al.* Single-Image Depth Perception in the Wild. *Adv. Neural Inf. Process. Syst.* 730–738 (2016).
211. Sun, D., Yang, X., Liu, M. Y., *et al.* PWC-Net: CNNs for Optical Flow Using Pyramid, Warping, and Cost Volume. *IEEE CVPR,* 8934–8943 (2018).
212. He, K., Zhang, X., Ren, S., *et al.* Deep residual learning for image recognition. *IEEE CCVPR,* 770–778 (2016).
213. Xiang, X., Tian, Y., Zhang, Y., *et al.* Zooming Slow-Mo: Fast and Accurate One-Stage Space-Time Video Super-Resolution. *IEEE CCVPR,* 2002.11616 (2020).
214. Chen, H., He, X., Qing, L., *et al.* Real-World Single Image Super-Resolution: A Brief Review. *IVP,* arXiv: 2103.02368 (2021).
215. Hyndman, R. J. & Koehler, A. B. Another look at measures of forecast accuracy. *Int. J. Forecast.* **22**, 679–688 (2006).
216. Pontius, R. G., Thontteh, O. & Chen, H. Components of information for multiple resolution comparison between maps that share a real variable. *Environ. Ecol. Stat.* **15**, 111–142 (2008).
217. Willmott, C. J. & Matsuura, K. On the use of dimensioned measures of error to evaluate the performance of spatial interpolators. *Int. J. Geogr. Inf. Sci.* **20**, 89–102 (2006).
218. Weigert, M., Schmidt, U., Boothe, T., *et al.* Content-aware image restoration: pushing the limits of fluorescence microscopy. *Nat. Meth.* **15**, 1090–1097 (2018).
219. Son, S., Lee, J., Nah, S., *et al.* AIM 2020 Challenge on Video Temporal Super-Resolution. *LNCS,* 23–40 (2020).
220. Culley, S., Albrecht, D., Jacobs, C., *et al.* Quantitative mapping and minimization of super-resolution optical imaging artifacts. *Nat. Meth.* **15**, 263–266 (2018).
221. Xiang, X., Tian, Y., Zhang, Y., *et al.* Zooming SlowMo: An Efficient One-Stage Framework for Space-Time Video Super-Resolution. *IEEE CCVPR,* 2104.07473 (2021).
222. Nah, S., Son, S., Timofte, R., *et al.* AIM 2019 challenge on video temporal super-resolution: Methods and results. *ICCVW,* 3388–3398 (2019).
223. Chamier, v. L., Laine, R. F., Jukkala, J., *et al.* Democratising deep learning for microscopy with ZeroCostDL4Mic. *Nat. Comm.* **12**, 2276 (2021).
224. Schindelin, J., Arganda-Carreras, I., Frise, E., *et al.* Fiji: An open-source platform for biological-image analysis. *Nat. Meth.* **9**, 676–682 (2012).

225. Pu, J., Guardia, C. M., Keren-Kaplan, T., *et al.* Mechanisms and functions of lysosome positioning. *J .Cell Sci.* **129**, 4329–4339 (2016).
226. Jongsma, M. L. L. M., Berlin, I., Wijdeven, R. H. H. M., *et al.* An ER-Associated Pathway Defines Endosomal Architecture for Controlled Cargo Transport. *Cell* **166**, 152–166 (2016).
227. Matteoni, R. & Kreis, T. E. Translocation and clustering of endosomes and lysosomes depends on microtubules. *J. Cell Biol.* **105**, 1253–1265 (1987).
228. Harada, A., Takei, Y., Kanai, Y., *et al.* Golgi vesiculation and lysosome dispersion in cells lacking cytoplasmic dynein. *J. Cell Biol.* **141**, 51–59 (1998).
229. Hollenbeck, P. J. & Swanson, J. A. Radial extension of macrophage tubular lysosomes supported by kinesin. *Nature* **346**, 864–866 (1990).
230. Jordens, I., Fernandez-Borja, M., Marsman, M., *et al.* The Rab7 effector protein RILP controls lysosomal transport by inducing the recruitment of dynein-dynactin motors. *Curr. Biol.* **11**, 1680–1685 (2001).
231. Heuser, J. Changes in lysosome shape and distribution correlated with changes in cytoplasmic pH. *J. Cell Biol.* **108**, 855–864 (1989).
232. Parton, R. G., Dotti, C. G., Bacallao, R., *et al.* pH-induced microtubule-dependent redistribution of late endosomes in neuronal and epithelial cells. *J. Cell Biol.* **113**, 261–274 (1991).
233. Korolchuk, V. I., Saiki, S., Lichtenberg, M., *et al.* Lysosomal positioning coordinates cellular nutrient responses. *Nat. Cell Biol.* **13**, 453–462 (2011).
234. Yu, L., Wu, W. K. K., Gu, C., *et al.* Obatoclax impairs lysosomal function to block autophagy in cisplatin-sensitive and -resistant esophageal cancer cells. *Oncotarget* **7**, 14693–14707 (2016).
235. Dodson, M. W., Zhang, T., Jiang, C., *et al.* Roles of the Drosophila LRRK2 homolog in Rab7-dependent lysosomal positioning. *Hum. Mol. Genet.* **21**, 1350–1363 (2012).
236. Mrakovic, A., Kay, J. G., Furuya, W., *et al.* Rab7 and Arl8 GTPases are Necessary for Lysosome Tubulation in Macrophages. *Traffic* **13**, 1667–1679 (2012).
237. Li, X., Rydzewski, N., Hider, A., *et al.* A molecular mechanism to regulate lysosome motility for lysosome positioning and tubulation. *Nat. Cell Biol.* **18**, 404–417 (2016).
238. Raiborg, C., Wenzel, E. M., Pedersen, N. M., *et al.* Repeated ER-endosome contacts promote endosome translocation and neurite outgrowth. *Nature* **520**, 234–238 (2015).
239. Wang, T. & Hong, W. Interorganellar regulation of lysosome positioning by the Golgi apparatus through Rab34 interaction with Rab-interacting lysosomal protein. *Mol. Biol. Cell* **13**, 4317–4332 (2002).
240. Chu, B. B., Liao, Y. C., Qi, W., *et al.* Cholesterol transport through lysosome-peroxisome membrane contacts. *Cell* **161**, 291–306 (2015).
241. Fraldi, A., Klein, A. D., Medina, D. L., *et al.* Brain Disorders Due to Lysosomal Dysfunction. *Annu. Rev. Neurosci.* **39**, 277–295 (2016).
242. Parenti, G., Andria, G. & Ballabio, A. Lysosomal storage diseases: From pathophysiology to therapy. *Annu. Rev. Med.* **66**, 471–486 (2015).
243. Aridor, M. & Hannan, L. A. Tarffic jam: A compendium of human diseases that affect intracellular transport processes. *Traffic* **1**, 836–851 (2000).
244. Aridor, M. & Hannan, L. A. Traffic Jams II: An update of diseases of intracellular transport. *Traffic* **3**, 781–790 (2002).
245. Klionsky, D. J., Eskelinen, E.-L. & Deretic, V. Autophagosomes, phagosomes, autolysosomes, phagolysosomes, autophagolysosomes… Wait, I'm confused. *Autophagy* **10**, 549 (2014).

246. Wang, S. F., Wu, M. Y., Cai, C. Z., *et al.* Autophagy modulators from traditional Chinese medicine: Mechanisms and therapeutic potentials for cancer and neurodegenerative diseases. *J. Ethnopharmac.* **194**, 861–876 (2016).
247. Settembre, C., Di Malta, C., Polito, V. A., *et al.* TFEB links autophagy to lysosomal biogenesis. *Science,* **332**, 1429–1433 (2011).
248. Martina, J. A., Chen, Y., Gucek, M., *et al.* MTORC1 functions as a transcriptional regulator of autophagy by preventing nuclear transport of TFEB. *Autophagy* **8**, 903–914 (2012).
249. Settembre, C., Zoncu, R., Medina, D. L., *et al.* A lysosome-to-nucleus signalling mechanism senses and regulates the lysosome via mTOR and TFEB. *EMBO J.* **31**, 1095–1108 (2012).
250. Roczniak-Ferguson, A., Petit, C. S., Froehlich, F., *et al.* The transcription factor TFEB links mTORC1 signaling to transcriptional control of lysosome homeostasis. *Sci. Signal.* **5**, (2012).
251. Sardiello, M., Palmieri, M., Ronza, A. Di, *et al.* A gene network regulating lysosomal biogenesis and function. *Science,* **325**, 473–477 (2009).
252. Settembre, C., De Cegli, R., Mansueto, G., *et al.* TFEB controls cellular lipid metabolism through a starvation-induced autoregulatory loop. *Nat. Cell Biol.* **15**, 647–658 (2013).
253. Medina, D. L., Di Paola, S., Peluso, I., *et al.* Lysosomal calcium signalling regulates autophagy through calcineurin and TFEB. *Nat. Cell Biol.* **17**, 288–299 (2015).
254. Settembre, C., Zoncu, R., Medina, D. L., *et al.* A lysosome-to-nucleus signalling mechanism senses and regulates the lysosome via mTOR and TFEB. *EMBO J.* **31**, 1095–1108 (2012).
255. Parr, C., Carzaniga, R., Gentleman, S. M., *et al.* Glycogen Synthase Kinase 3 Inhibition Promotes Lysosomal Biogenesis and Autophagic Degradation of the Amyloid-β Precursor Protein. *Mol. Cell. Biol.* **32**, 4410 (2012).
256. Zhang, W., Li, X., Wang, S., *et al.* Regulation of TFEB activity and its potential as a therapeutic target against kidney diseases. *Cell Death Discov. 2020 61* **6**, 1–10 (2020).
257. Barbosa, M. C., Grosso, R. A. & Fader, C. M. Hallmarks of Aging: An Autophagic Perspective. *Front. Endocrinol.* **9**, (2018).
258. Lapierre, L. R., De Magalhaes Filho, C. D., McQuary, P. R., *et al.* The TFEB orthologue HLH-30 regulates autophagy and modulates longevity in Caenorhabditis elegans. *Nat. Commun.* **4**, (2013).
259. Sun, Y., Li, M., Zhao, D., *et al.* Lysosome activity is modulated by multiple longevity pathways and is important for lifespan extension in C. Elegans. *Elife* **9**, 1–28 (2020).
260. Hogan, P. G., Chen, L., Nardone, J., *et al.* Transcriptional regulation by calcium, calcineurin, and NFAT. *Genes and Development* **17** 2205–2232 (2003).
261. Johnson, S. C., Yanos, M. E., Kayser, E. B., *et al.* MTOR inhibition alleviates mitochondrial disease in a mouse model of Leigh syndrome. *Science,* **342**, 1524–1528 (2013).
262. Farooqui, A. A. & Farooqui, T. Therapeutic potentials of curcumin in parkinson's disease. *Curcumin for Neurological and Psychiatric Disorders: Neurochemical and Pharmacological Properties* 333–344 (2019).
263. Nguyen, T. T., Vuu, M. D., Huynh, M. A., *et al.* Curcumin effectively rescued Parkinson's disease-like phenotypes in a novel Drosophila melanogaster model with dUCH knockdown. *Oxid. Med. Cell. Longev.* **2018**, (2018).
264. Zhang, J., Wang, J., Xu, J., *et al.* Curcumin targets the TFEB-lysosome pathway for induction of autophagy. *Oncotarget* **7**, 75659 (2016).

265. J, H., XY, P., Y, X., *et al.* Curcumin induces autophagy to protect vascular endothelial cell survival from oxidative stress damage. *Autophagy* **8**, 812–825 (2012).
266. Xu, J., Zhang, X. Q. & Zhang, Z. Transcription factor EB agonists from natural products for treating human diseases with impaired autophagy-lysosome pathway. *Chin. Med.* **15**, 1–17 (2020).
267. Wang, C., Niederstrasser, H., Douglas, P. M., *et al.* Small-molecule TFEB pathway agonists that ameliorate metabolic syndrome in mice and extend C. elegans lifespan. *Nat. Comm.* **8**, (2017).
268. Khalifeh, M., Barreto, G. E. & Sahebkar, A. Trehalose as a promising therapeutic candidate for the treatment of Parkinson's disease. *B. J. Pharmac.* **176**, 1173–1189 (2019).
269. Chen, Q. & Haddad, G. G. Role of trehalose phosphate synthase and trehalose during hypoxia: From flies to mammals. *J. Exp. Biol.* **207**, 3125–3129 (2004).
270. Rusmini, P., Cortese, K., Crippa, V., *et al.* Trehalose induces autophagy via lysosomal-mediated TFEB activation in models of motoneuron degeneration. *Autophagy* **15**, 631 (2019).
271. Khalifeh, M., Read, M. I., Barreto, G. E., *et al.* Trehalose against Alzheimer's Disease: Insights into a Potential Therapy. *BioEssays* **42**, (2020).
272. Shacka, J. J., Klocke, B. J. & Roth, K. A. Autophagy, Bafilomycin and Cell Death: The 'A-B-Cs' of Plecomacrolide-Induced Neuroprotection. *Autophagy* **2**, 228–230 (2006).
273. Priessner, M., Summers, P. A., Lewis, B., *et al.* Selective detection of Cu^{+} ions in live cells via fluorescence lifetime imaging microscopy. *Angew. Chem.* **60**, 23148–23153 (2021).

APPENDIX

Appendix Chapter I

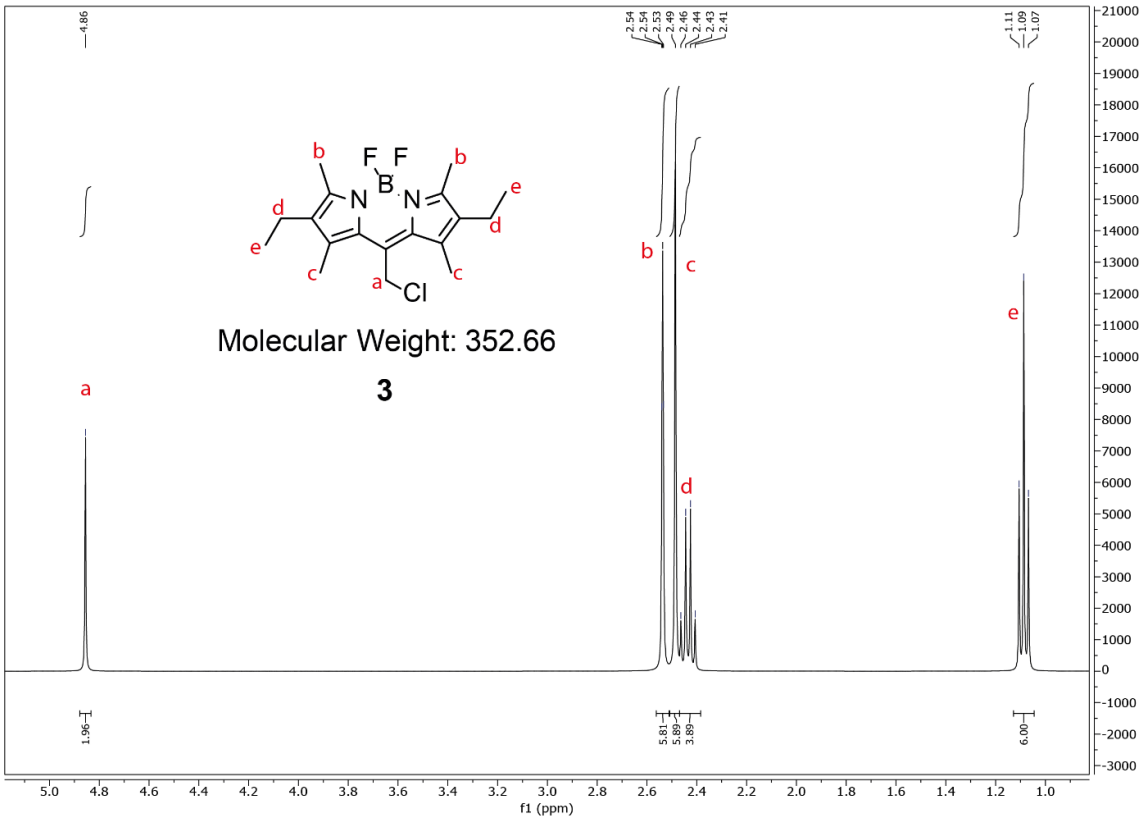

Figure 101: ^{1}H NMR spectrum (in $CDCl_3$, 400 MHz) of compound **3**.

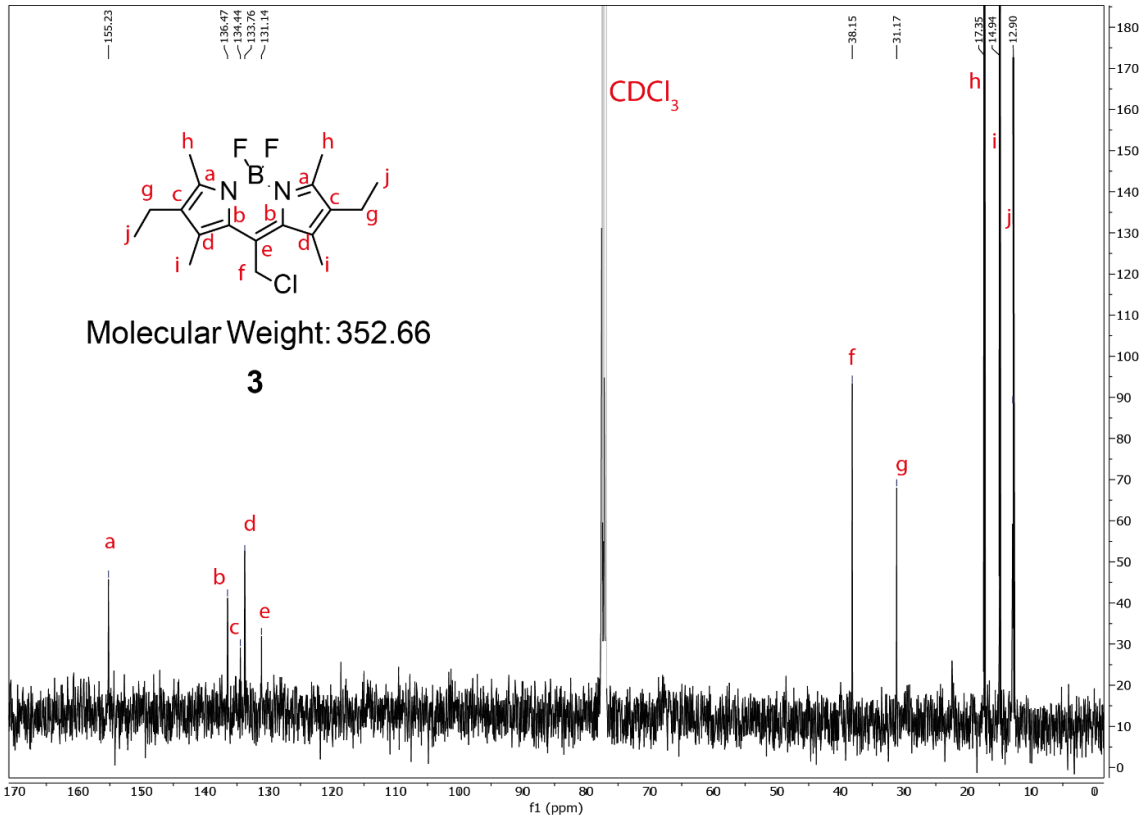

Figure 102: ^{13}C NMR spectrum (in $CDCl_3$, 100 MHz) of compound **3**.

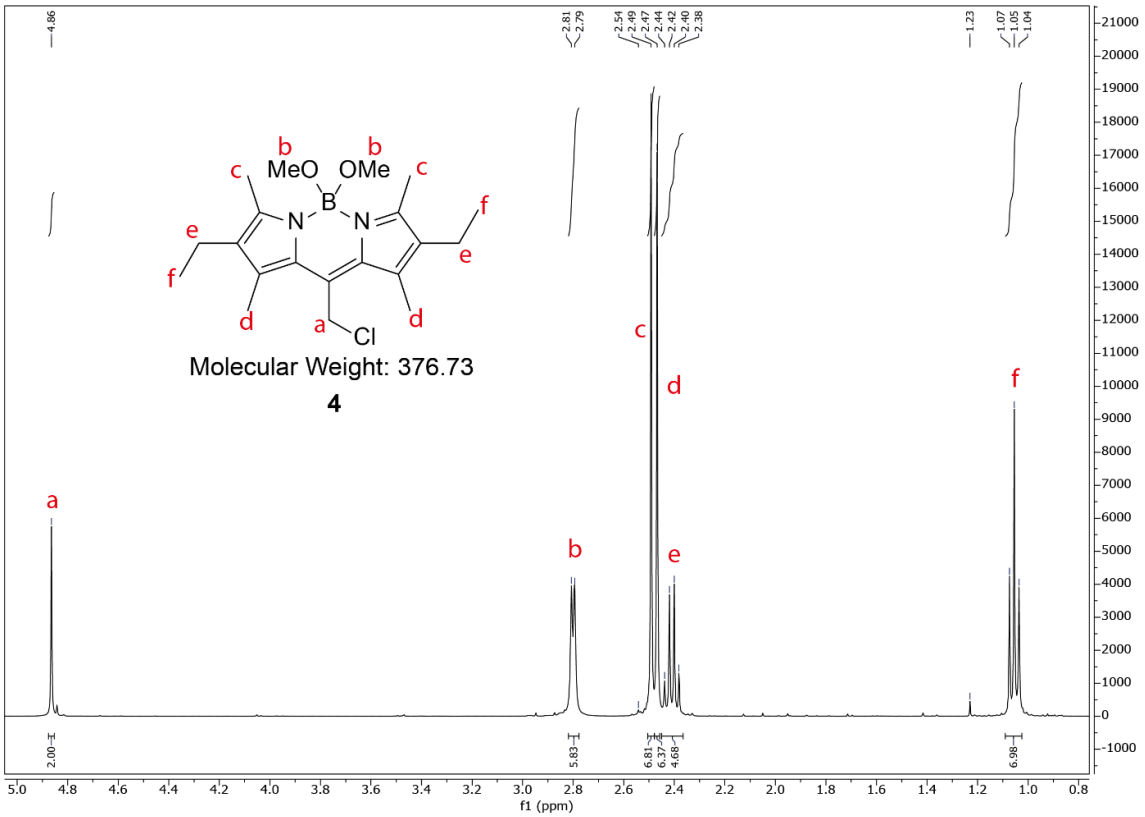

Figure 103: ^{1}H NMR spectrum (in $CDCl_3$, 400 MHz) of compound **4**.

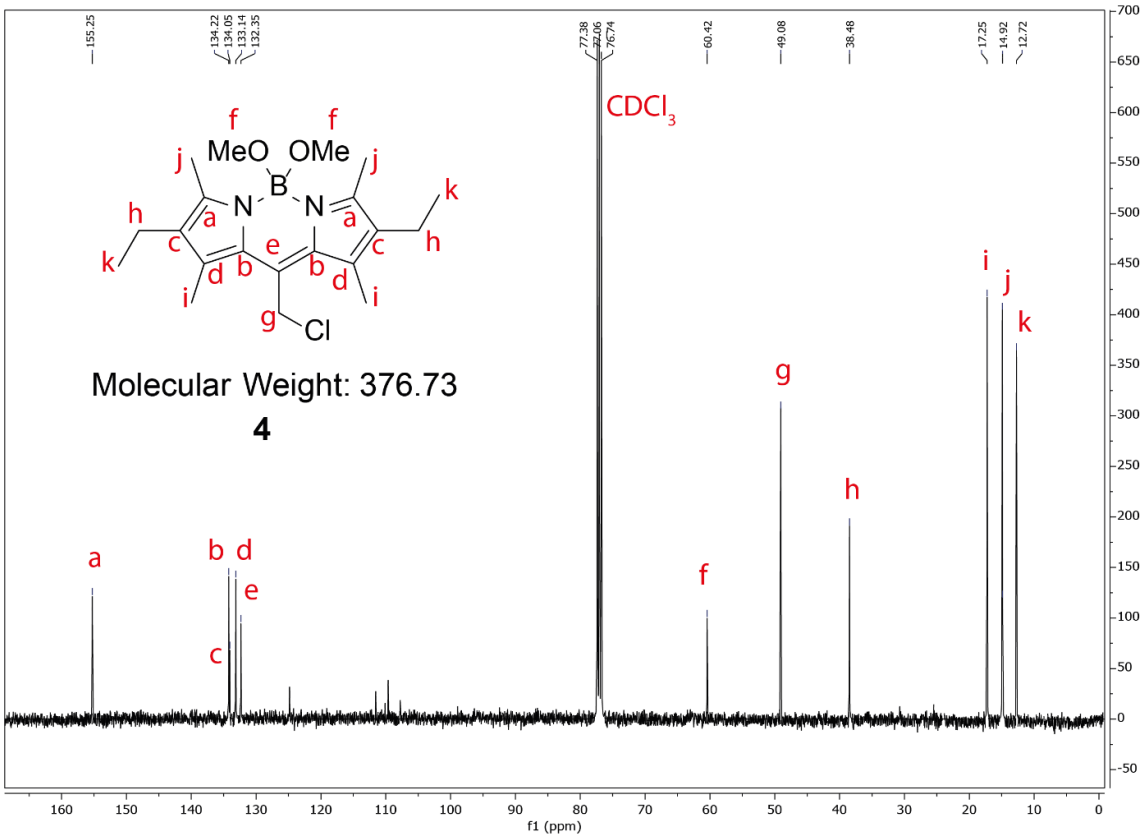

Figure 104: ^{13}C NMR spectrum (in $CDCl_3$, 400 MHz) of compound **4**.

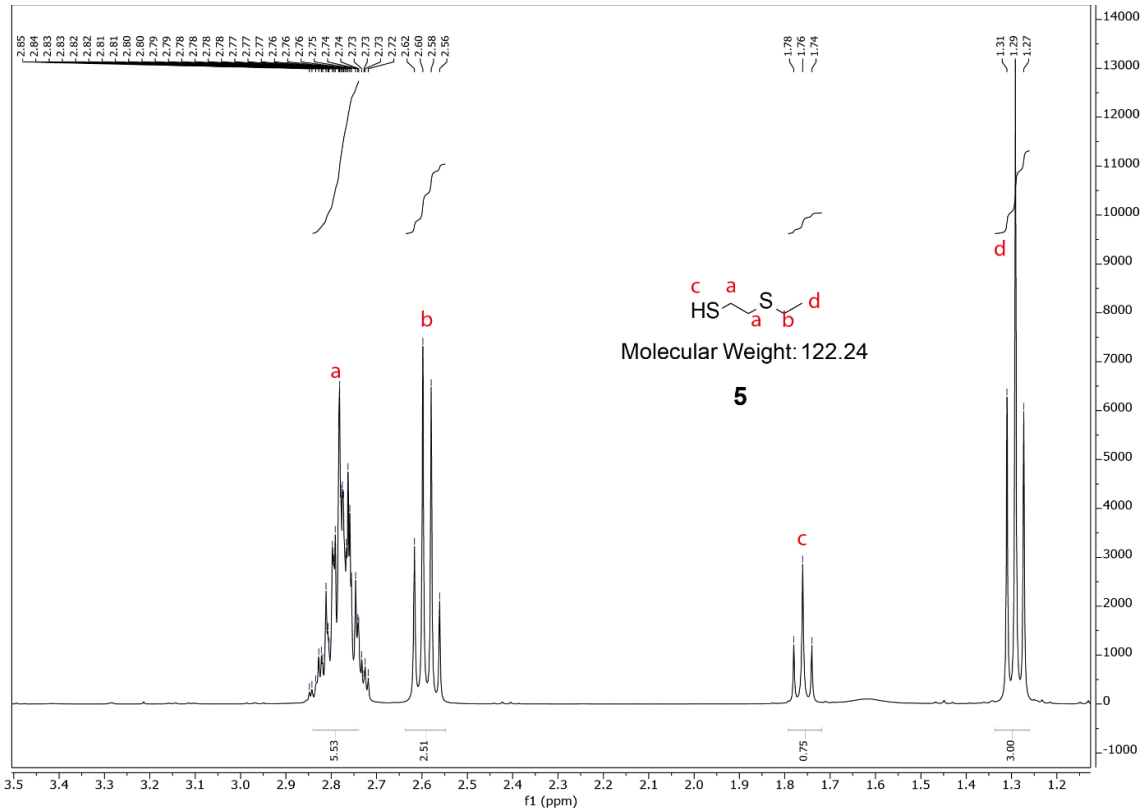

Figure 105: ^{1}H NMR spectrum (in $CDCl_3$, 400 MHz) of compound **5**.

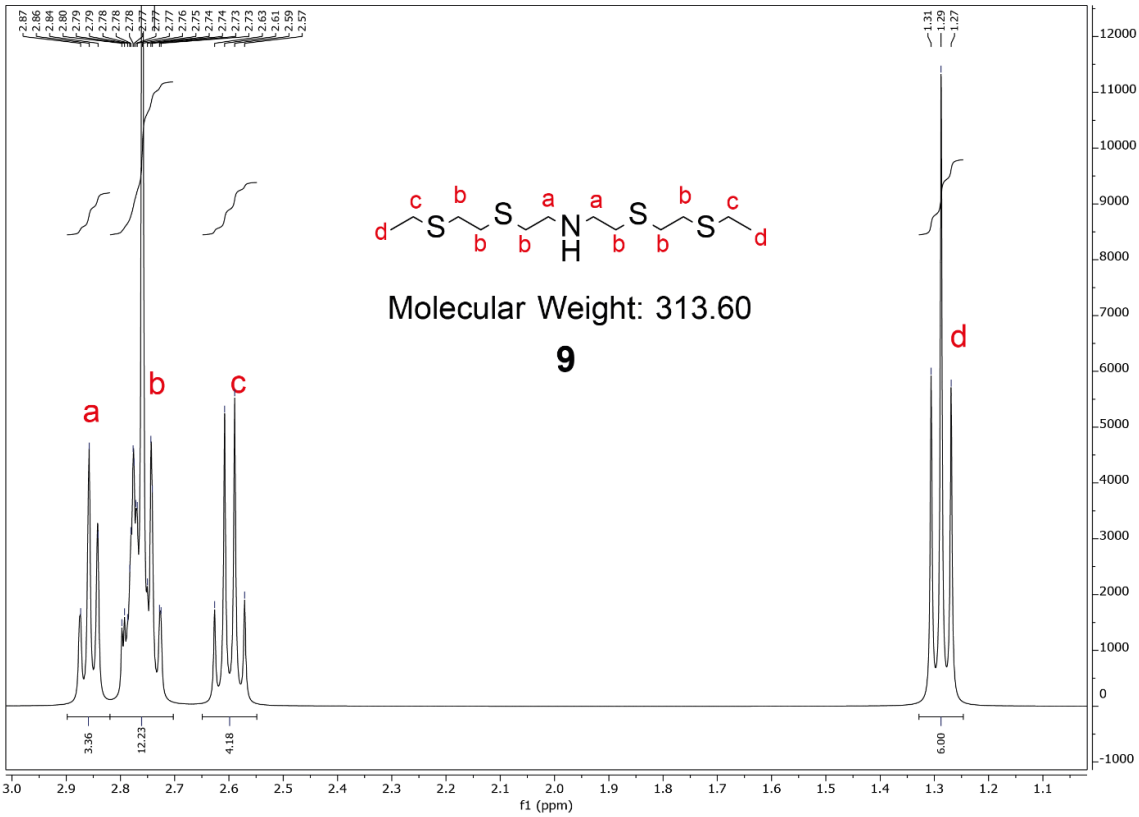

Figure 106: ^{1}H NMR spectrum (in $CDCl_3$, 400 MHz) of compound **9**.

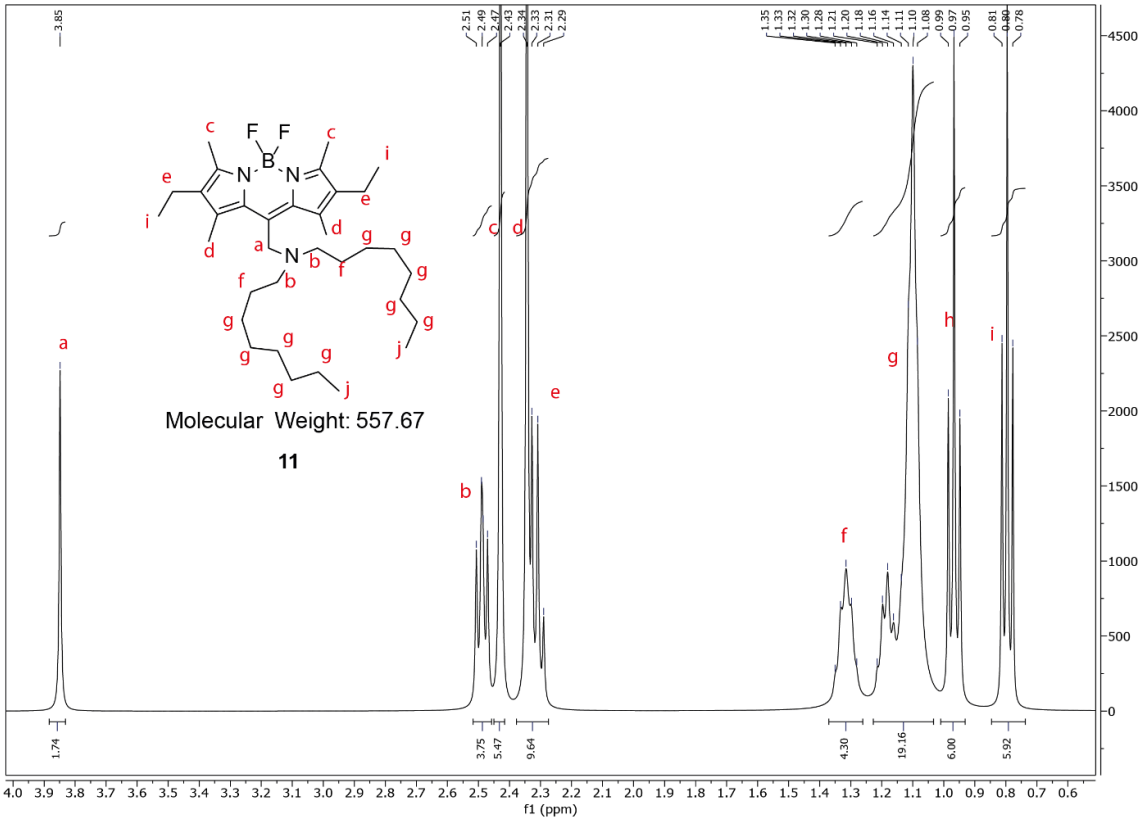

Figure 107: ^{1}H NMR spectrum (in $CDCl_3$, 400 MHz) of compound **11**.

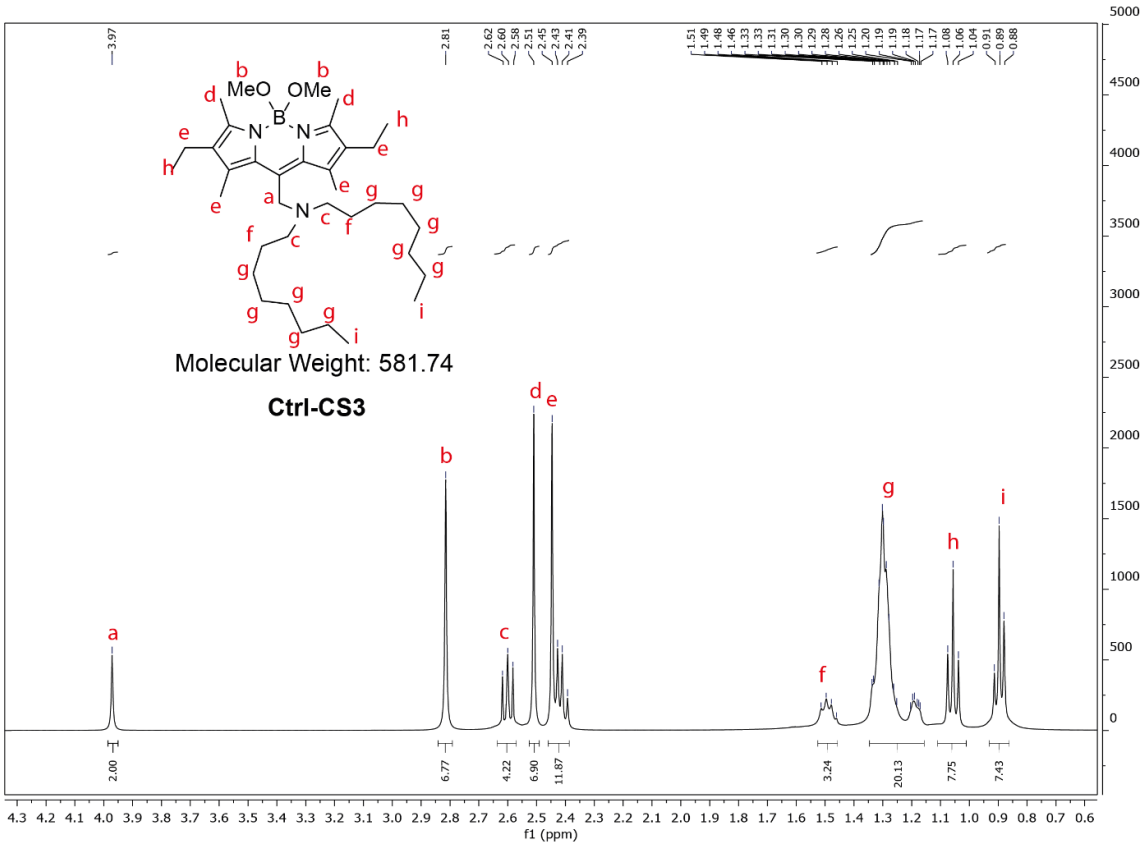

Figure 108: ^{1}H NMR spectrum (in $CDCl_3$, 400 MHz) of compound **Ctrl-CS3**.

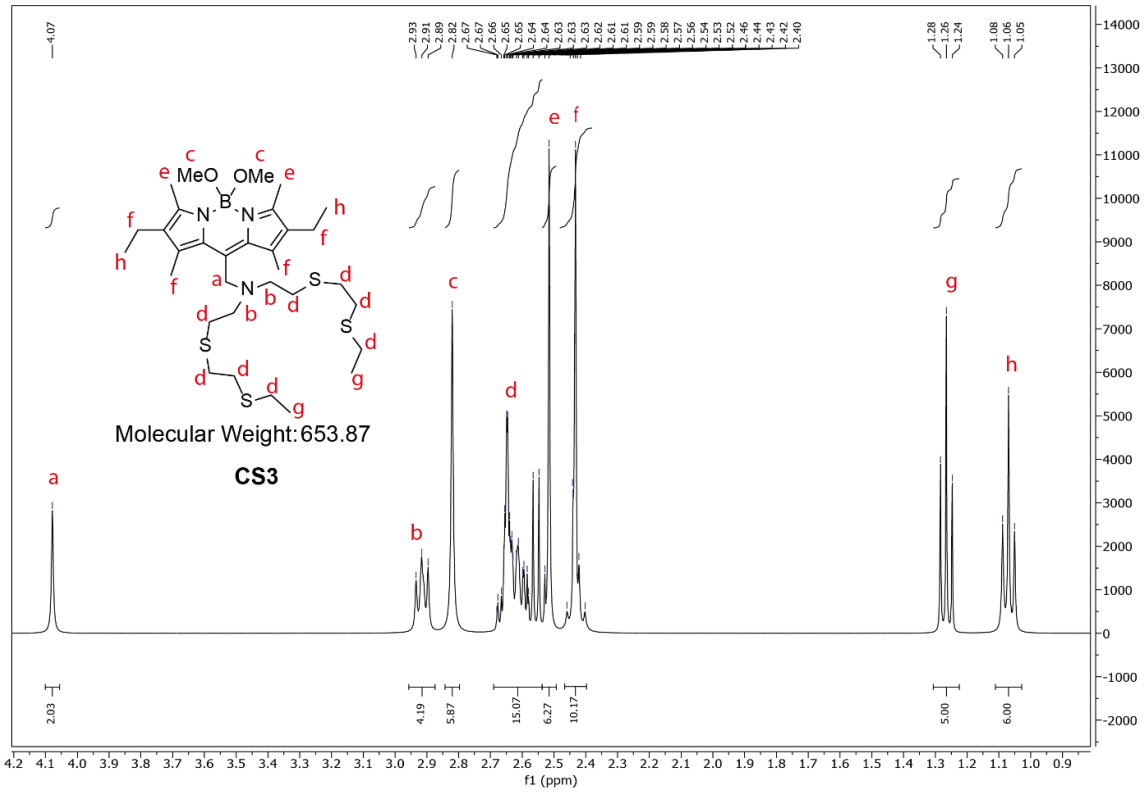

Figure 109: ^{1}H NMR spectrum (in $CDCl_3$, 400 MHz) of compound **CS3**.

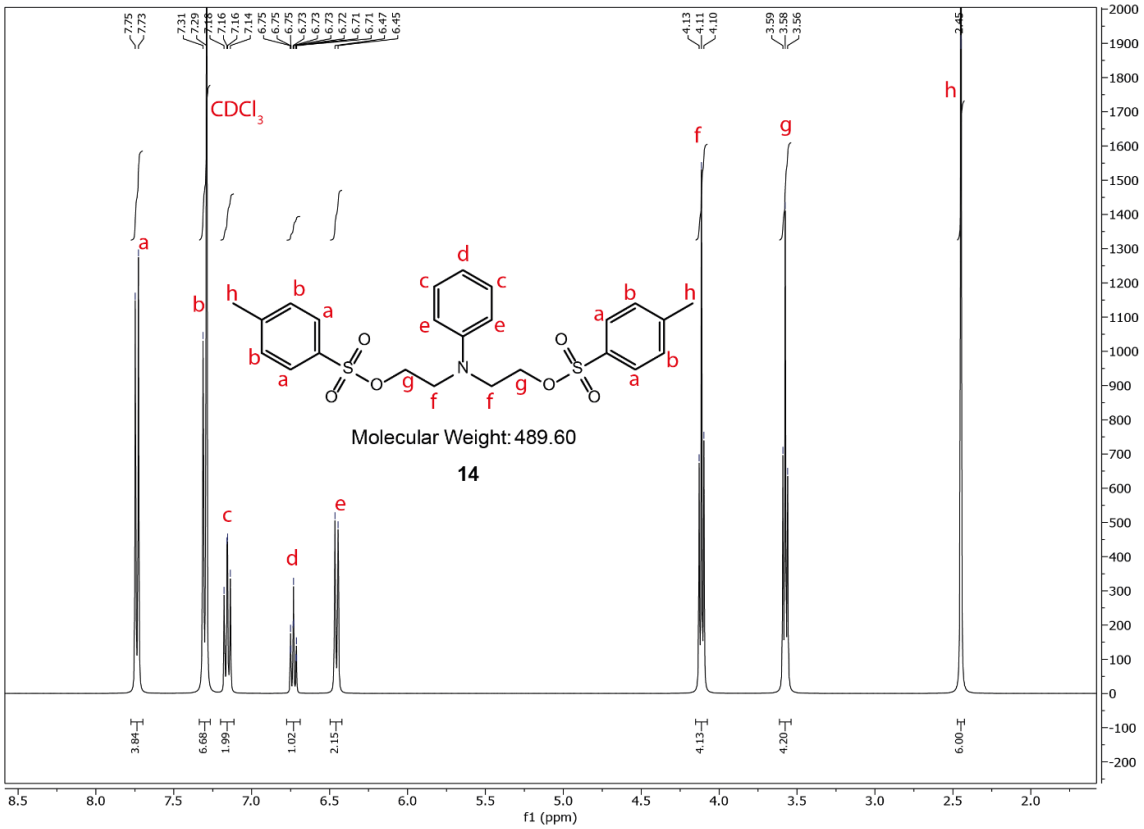

Figure 110: ^{1}H NMR spectrum (in $CDCl_3$, 400 MHz) of compound **14**.

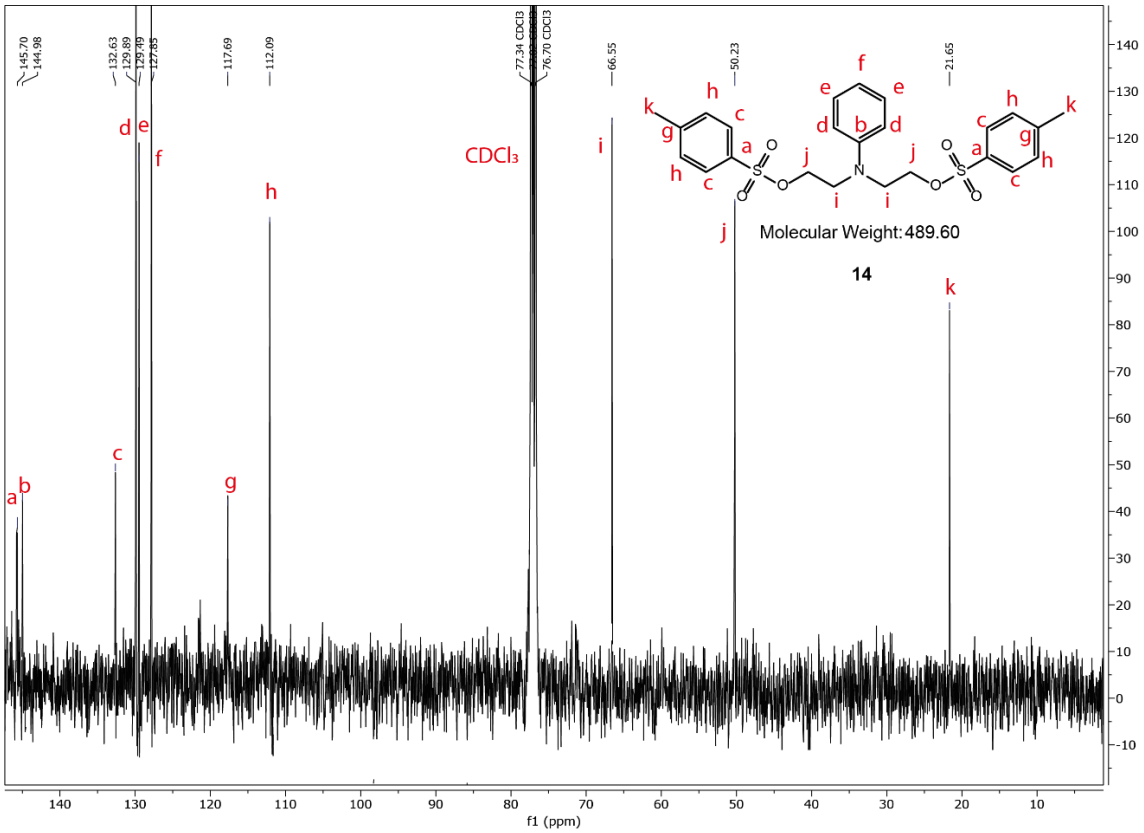

Figure 111: ^{13}C NMR spectrum (in $CDCl_3$, 100 MHz) of compound **14**.

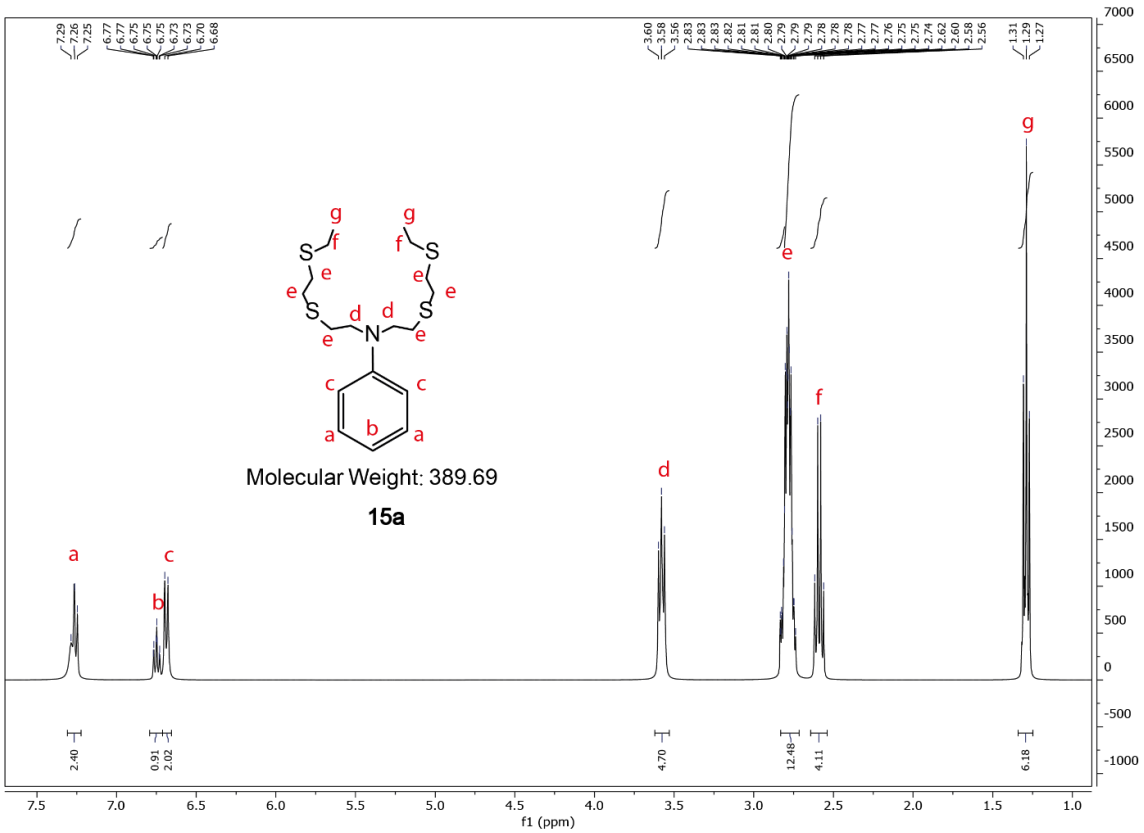

Figure 112: ^{1}H NMR spectrum (in $CDCl_3$, 400 MHz) of compound **15a**.

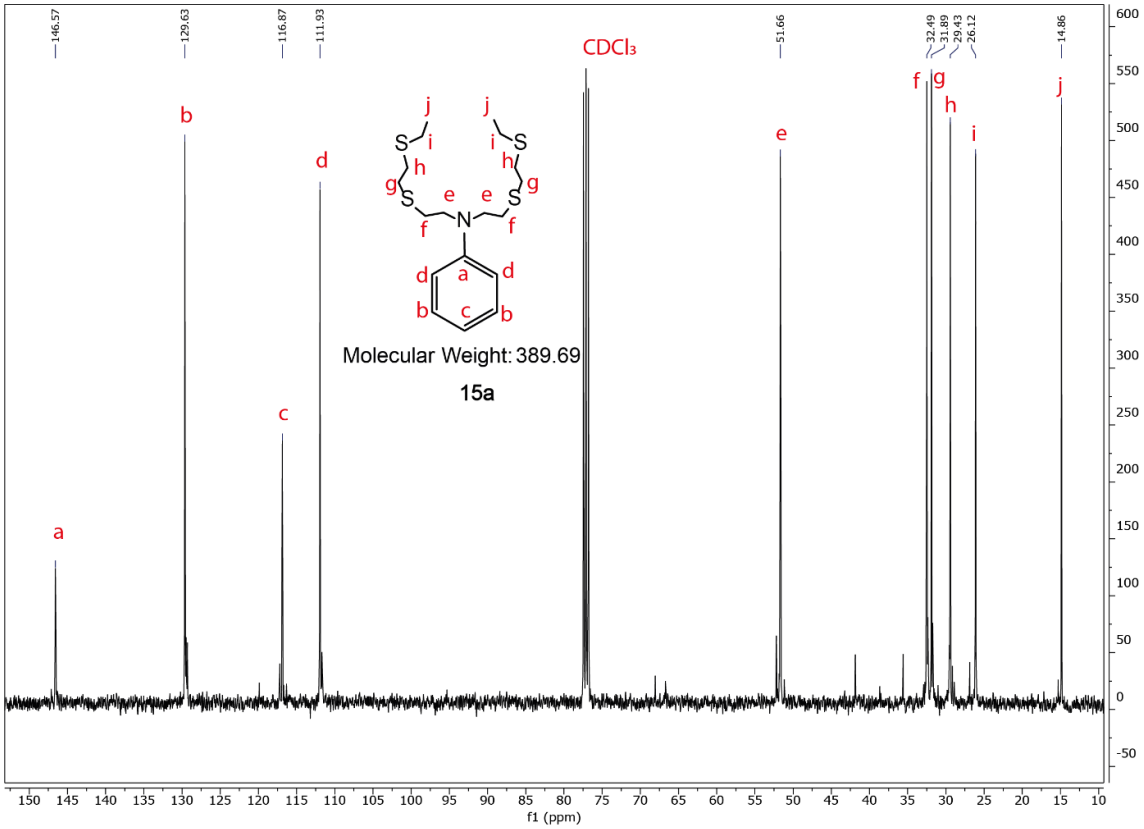

Figure 113: ^{13}C NMR spectrum (in $CDCl_3$, 100 MHz) of compound **15a**.

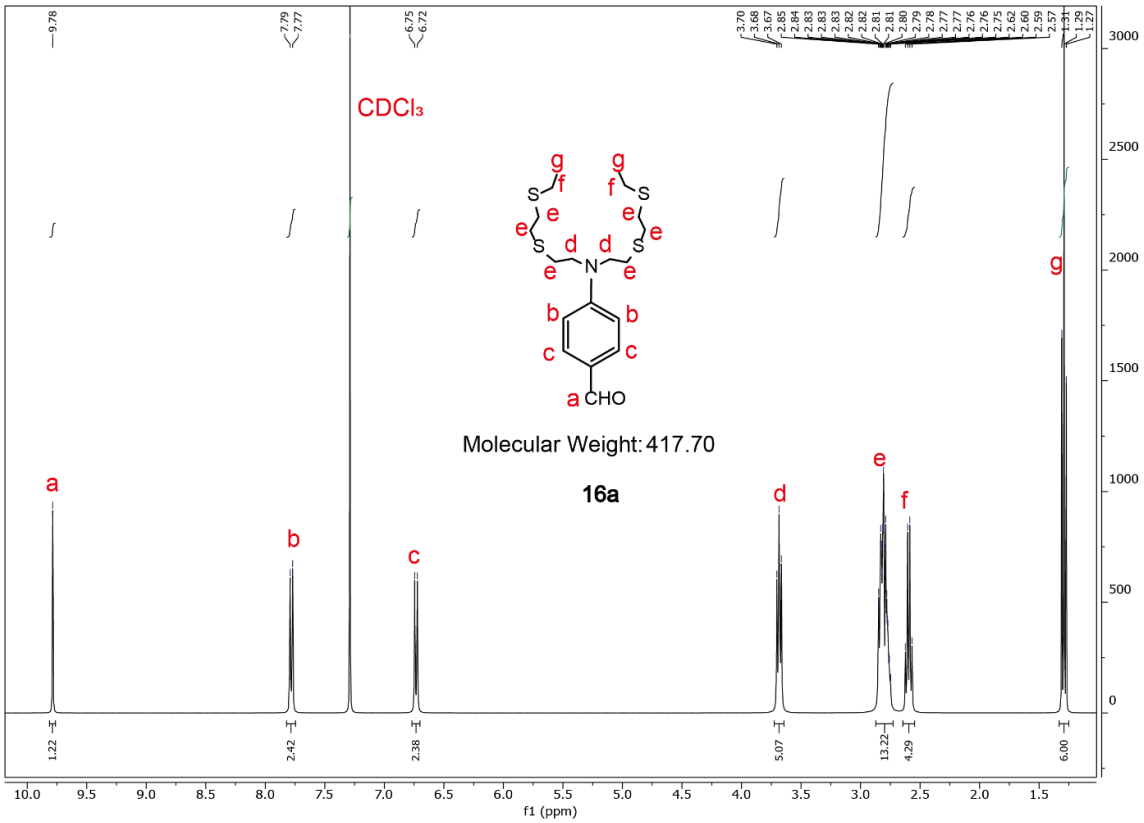

Figure 114: ^{1}H NMR spectrum (in $CDCl_3$, 400 MHz) of compound **16a**.

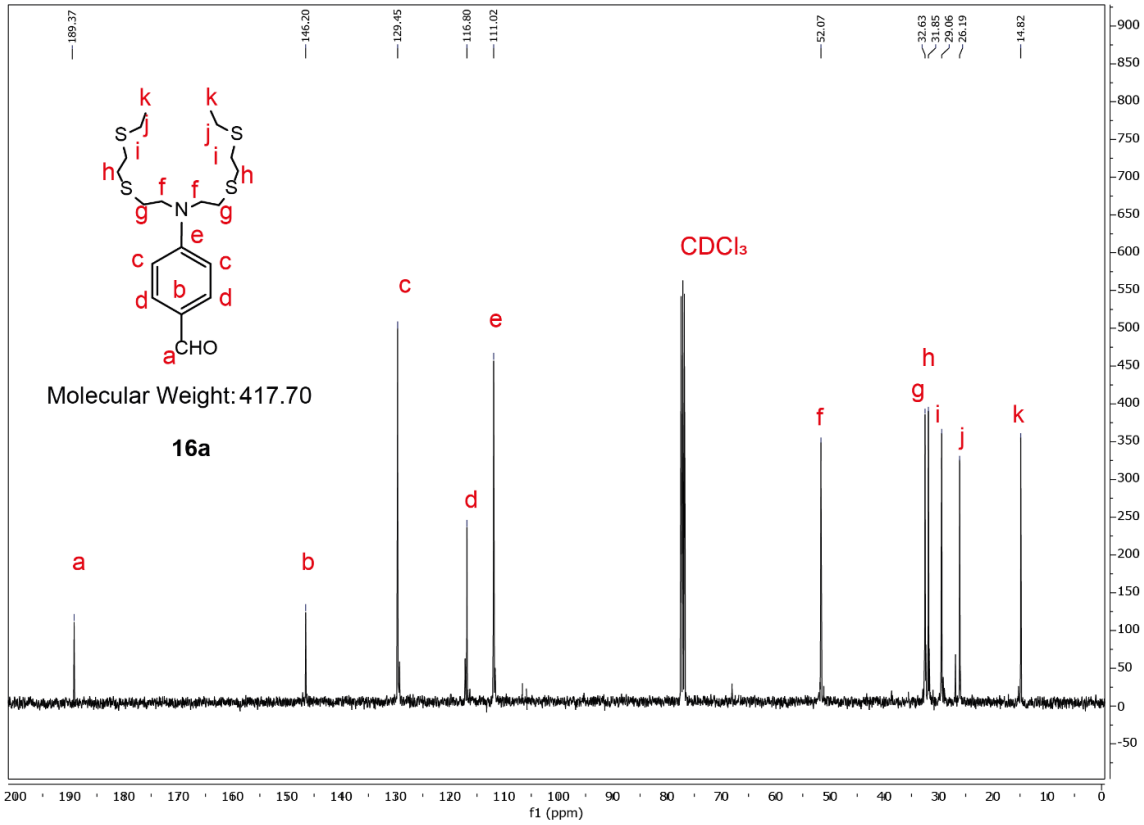

Figure 115: ^{13}C NMR spectrum (in $CDCl_3$, 100 MHz) of compound **16a**.

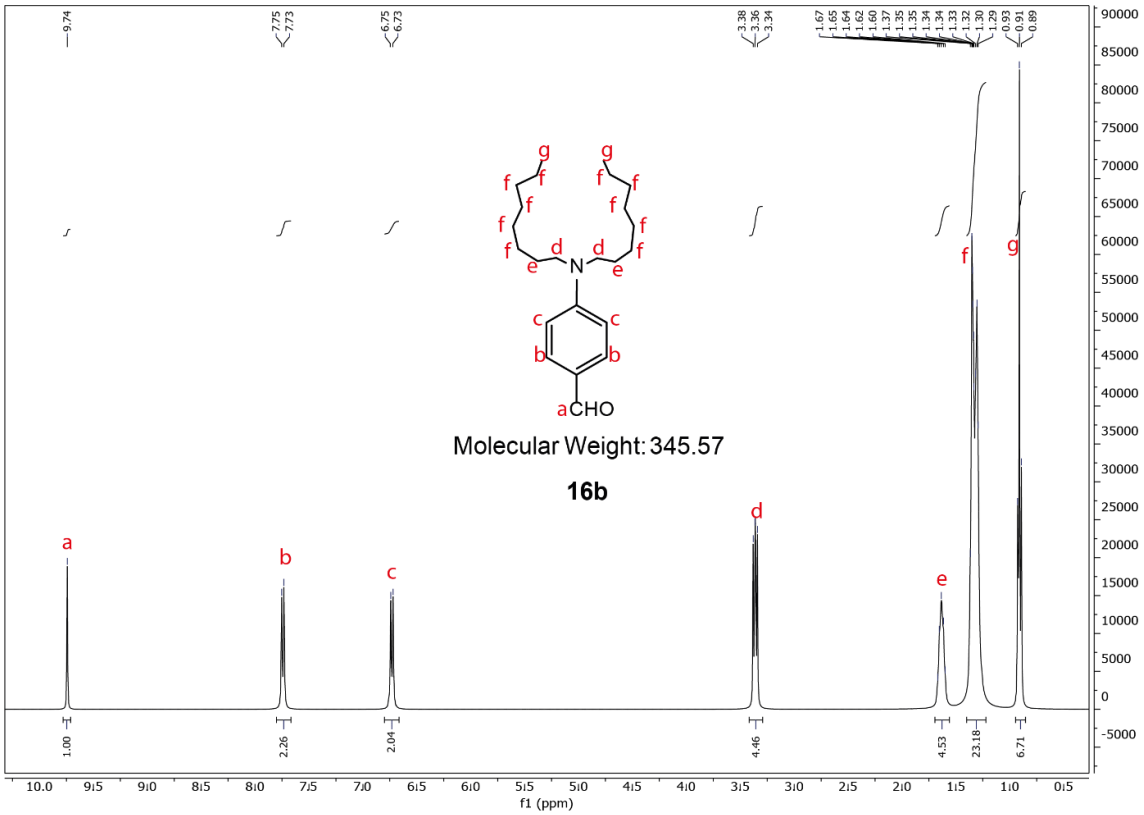

Figure 116: ^{1}H NMR spectrum (in $CDCl_3$, 400 MHz) of compound **16b**.

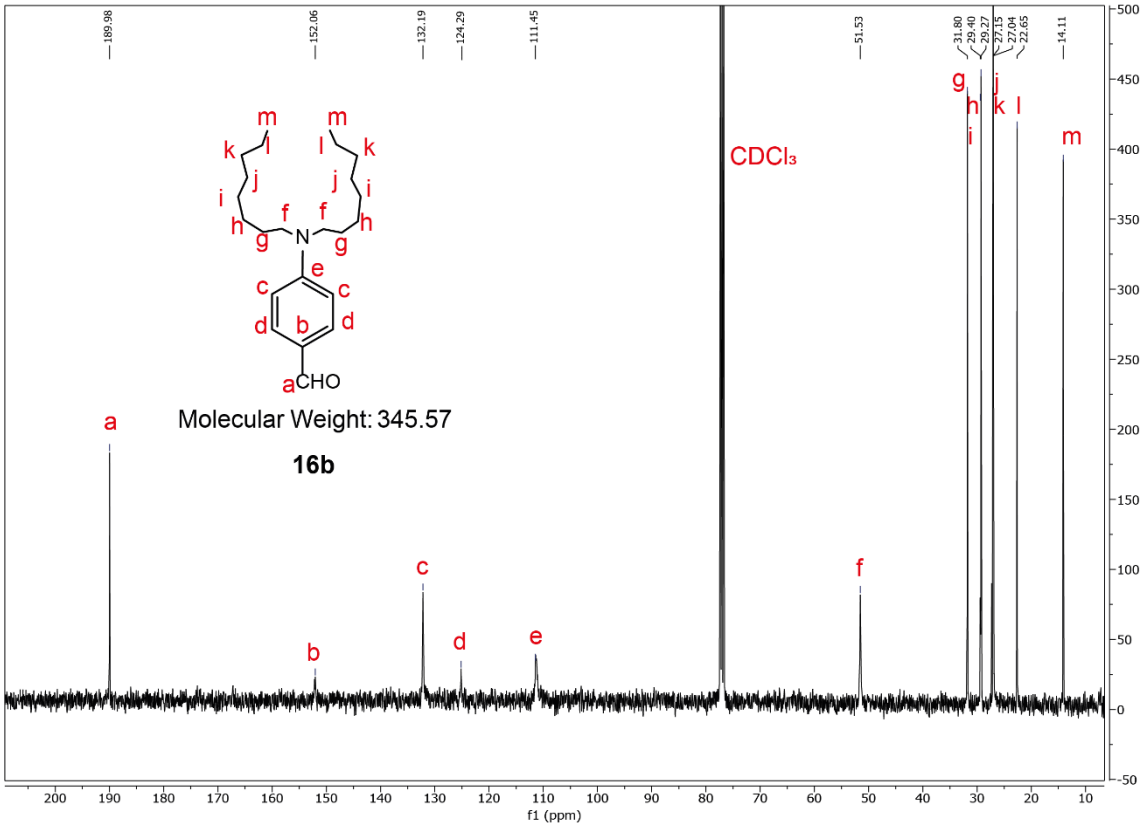

Figure 117: ^{13}C NMR spectrum (in $CDCl_3$, 100 MHz) of compound **16b**.

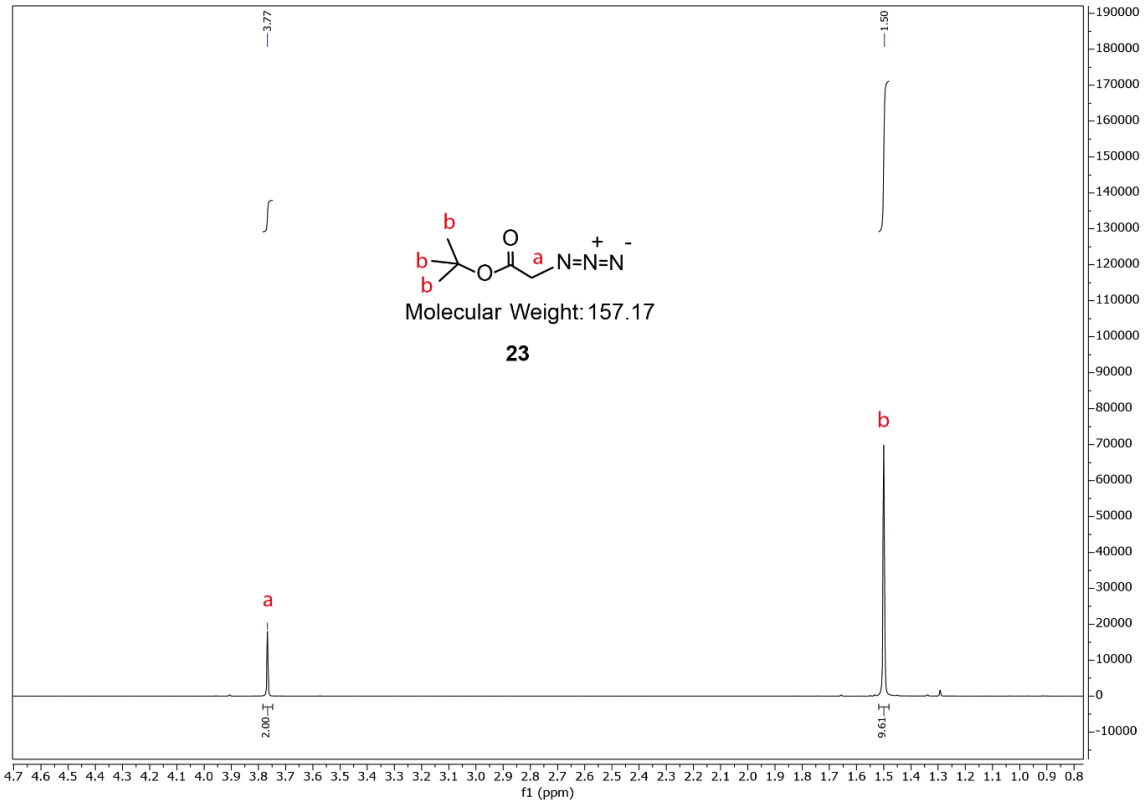

Figure 118: ^{1}H NMR spectrum (in DMSO, 400 MHz) of compound **23**.

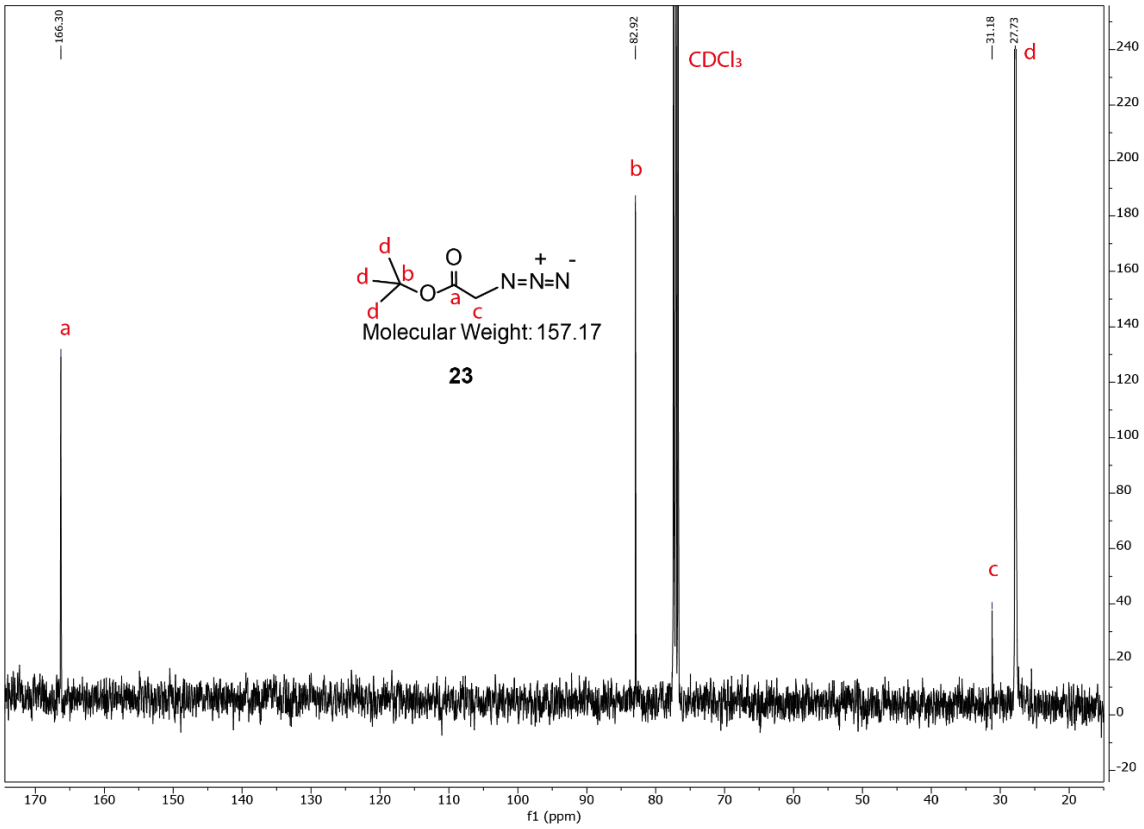

Figure 119: ^{13}C NMR spectrum (in $CDCl_3$, 100 MHz) of compound **23**.

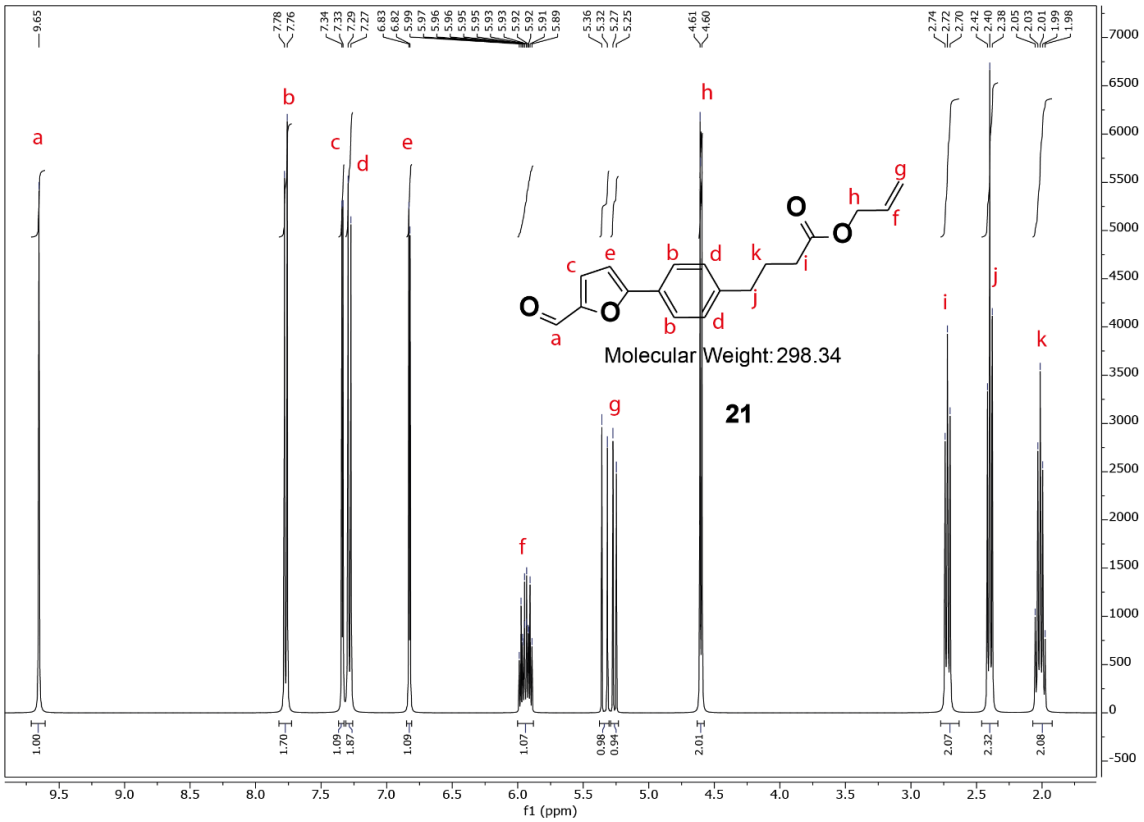

Figure 120: ^{1}H NMR spectrum (in $CDCl_3$, 400 MHz) of compound **21**.

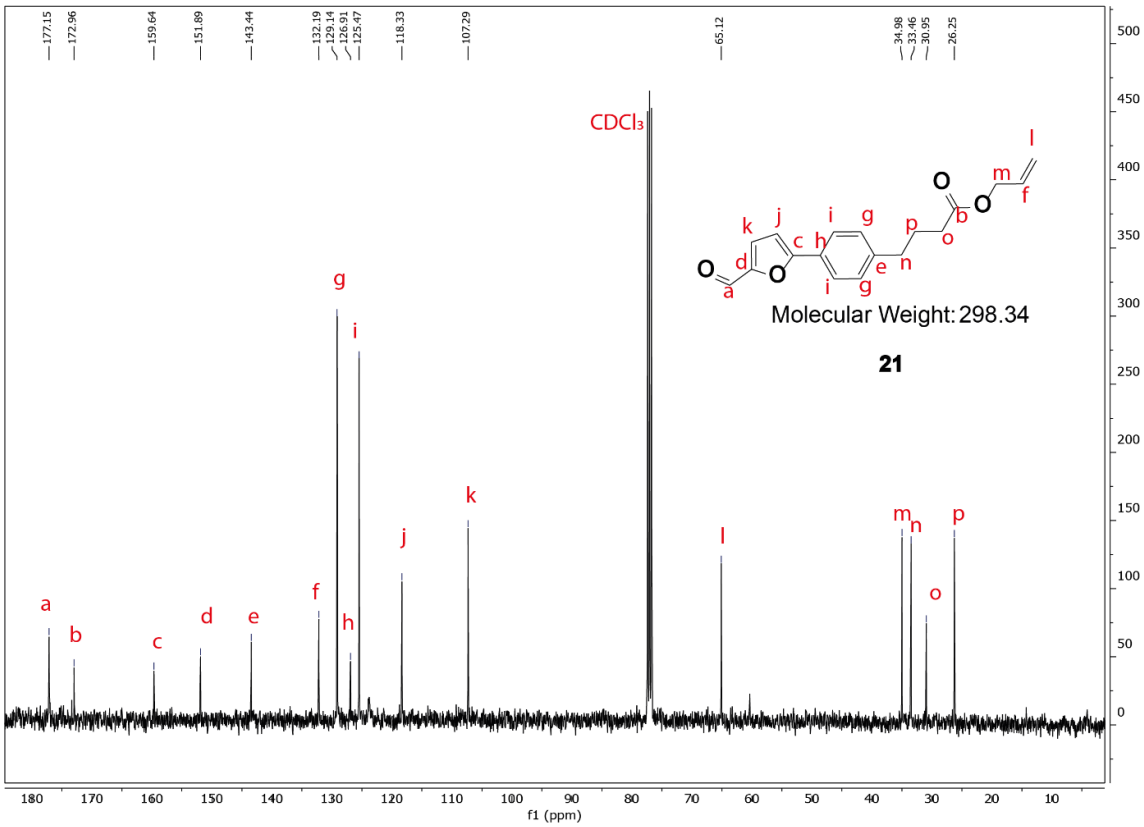

Figure 121: ^{13}C NMR spectrum (in $CDCl_3$, 100 MHz) of compound **21**.

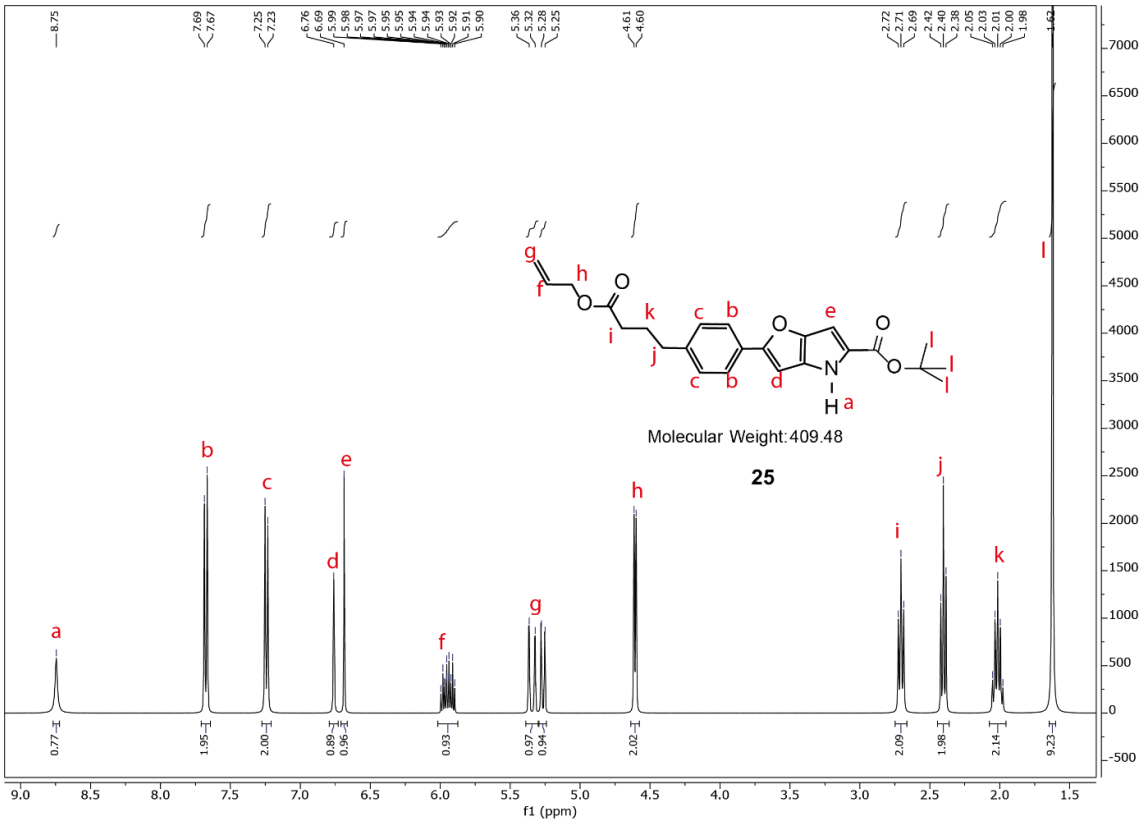

Figure 122: ^{1}H NMR spectrum (in $CDCl_3$, 400 MHz) of compound **25**.

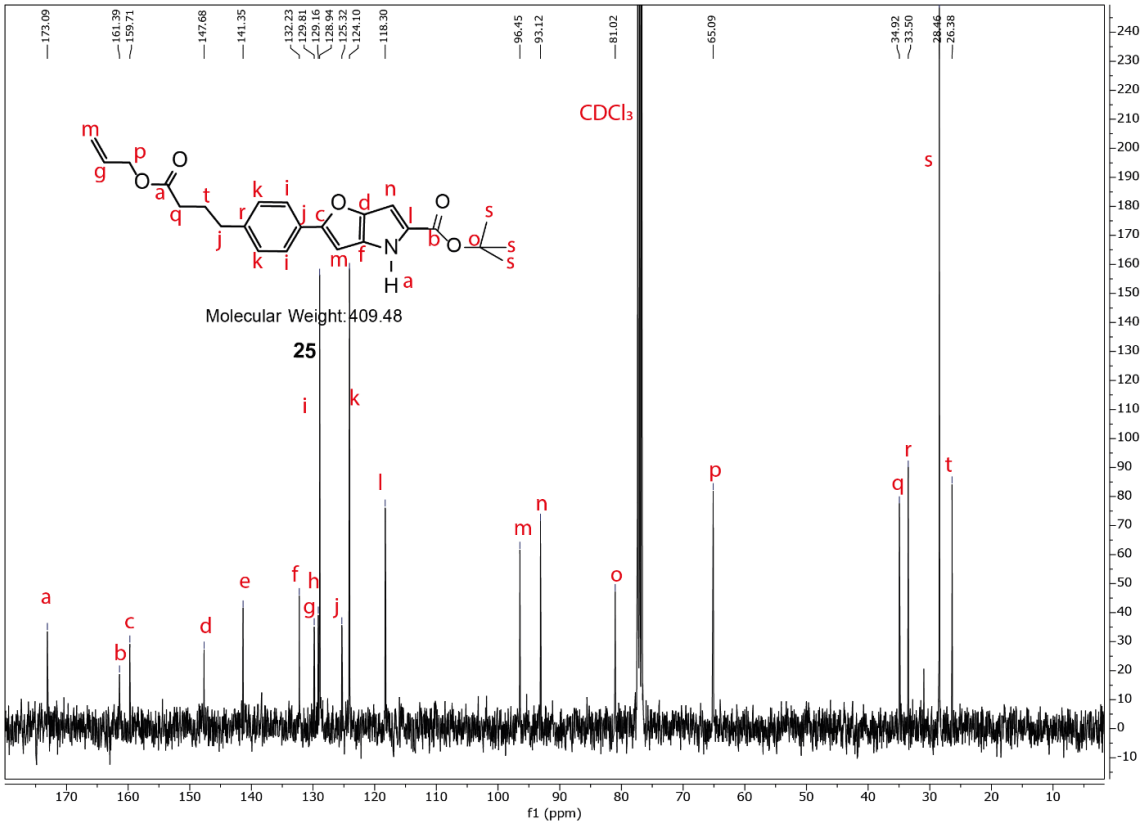

Figure 123: ^{13}C NMR spectrum (in $CDCl_3$, 100 MHz) of compound **25**.

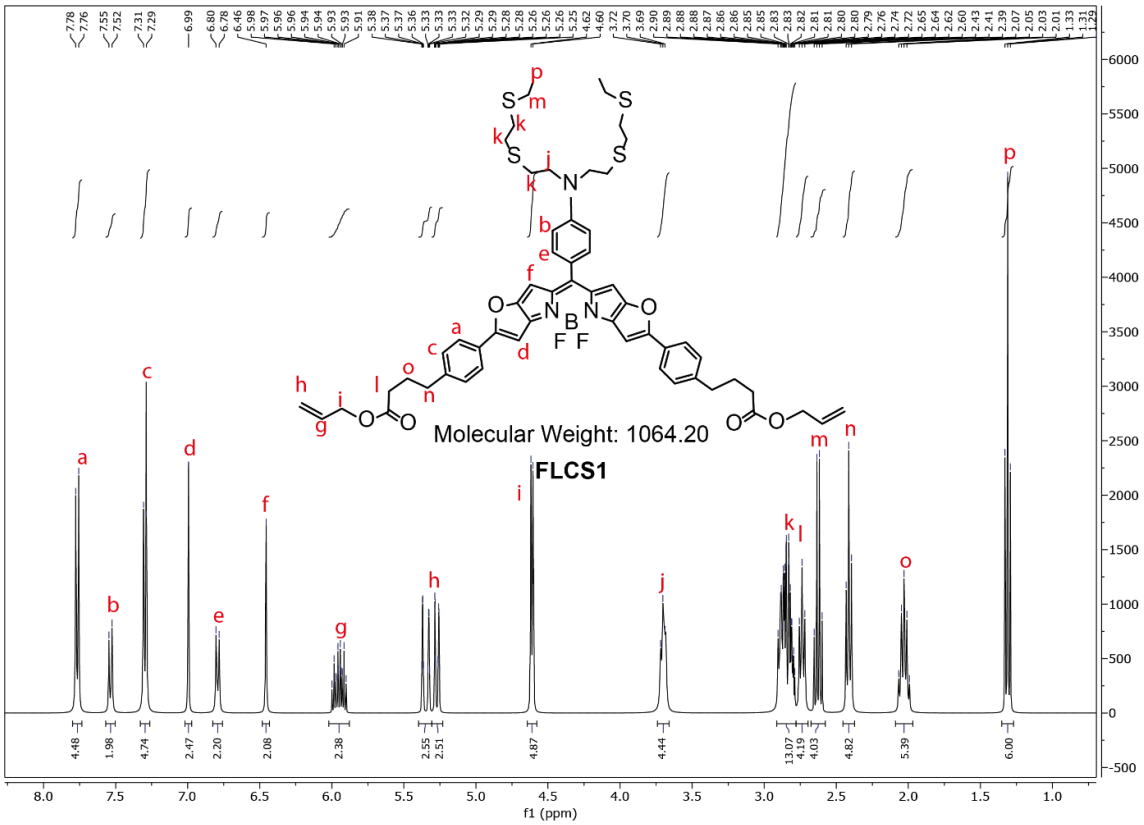

Figure 124: ^{1}H NMR spectrum (in $CDCl_3$, 400 MHz) of compound **FLCS1**

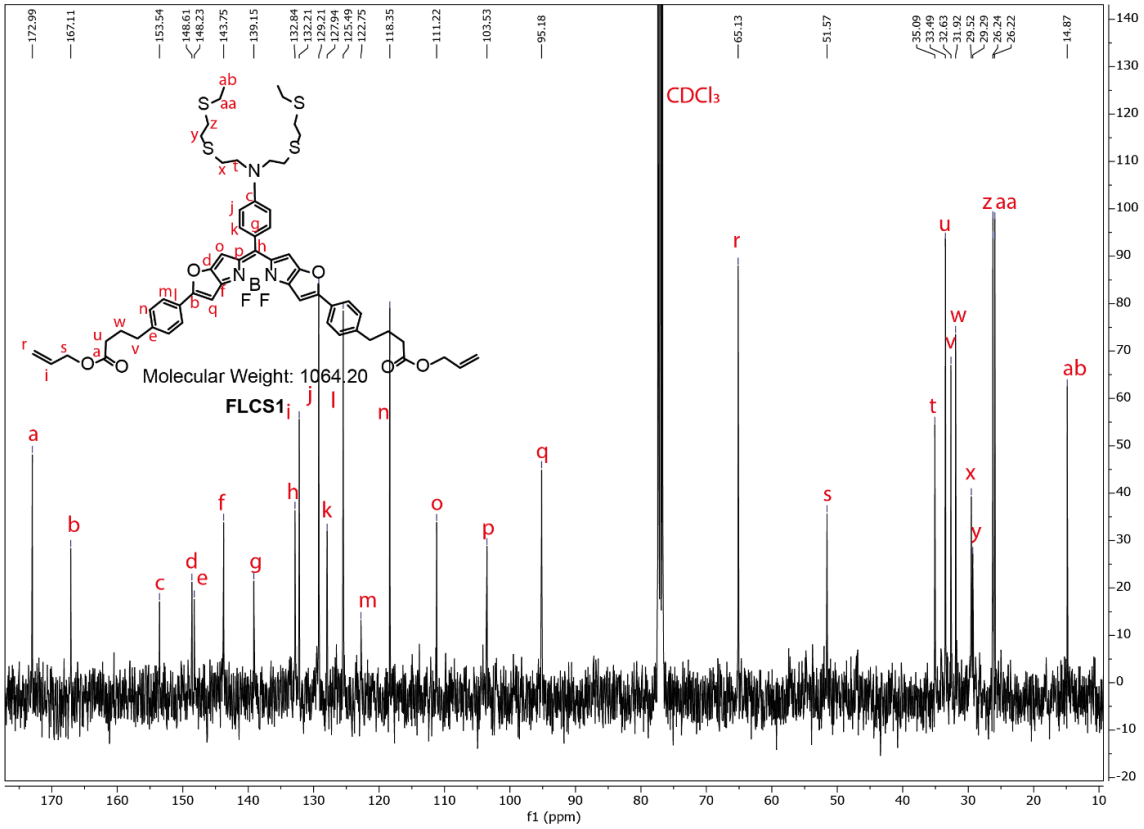

Figure 125: ^{13}C NMR spectrum (in $CDCl_3$, 100 MHz) of compound **FLCS1**.

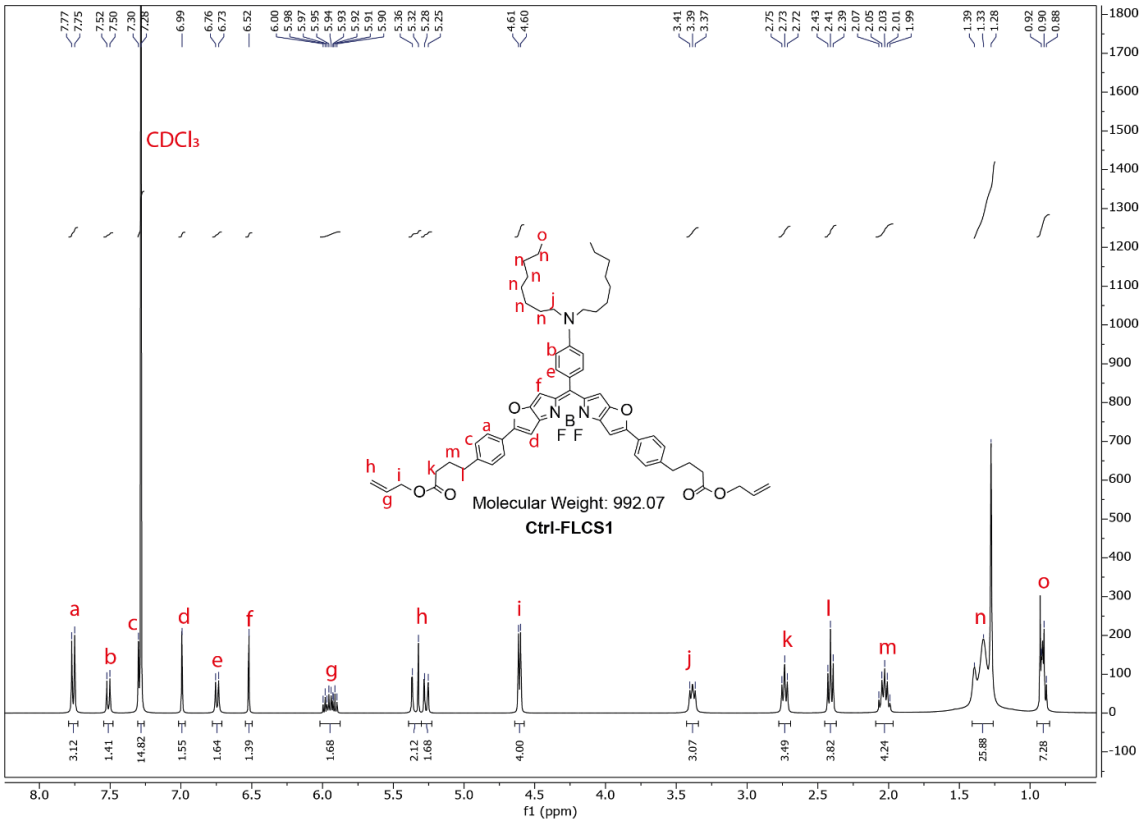

Figure 126: ^{1}H NMR spectrum (in $CDCl_3$, 400 MHz) of compound **Ctrl-FLCS1**

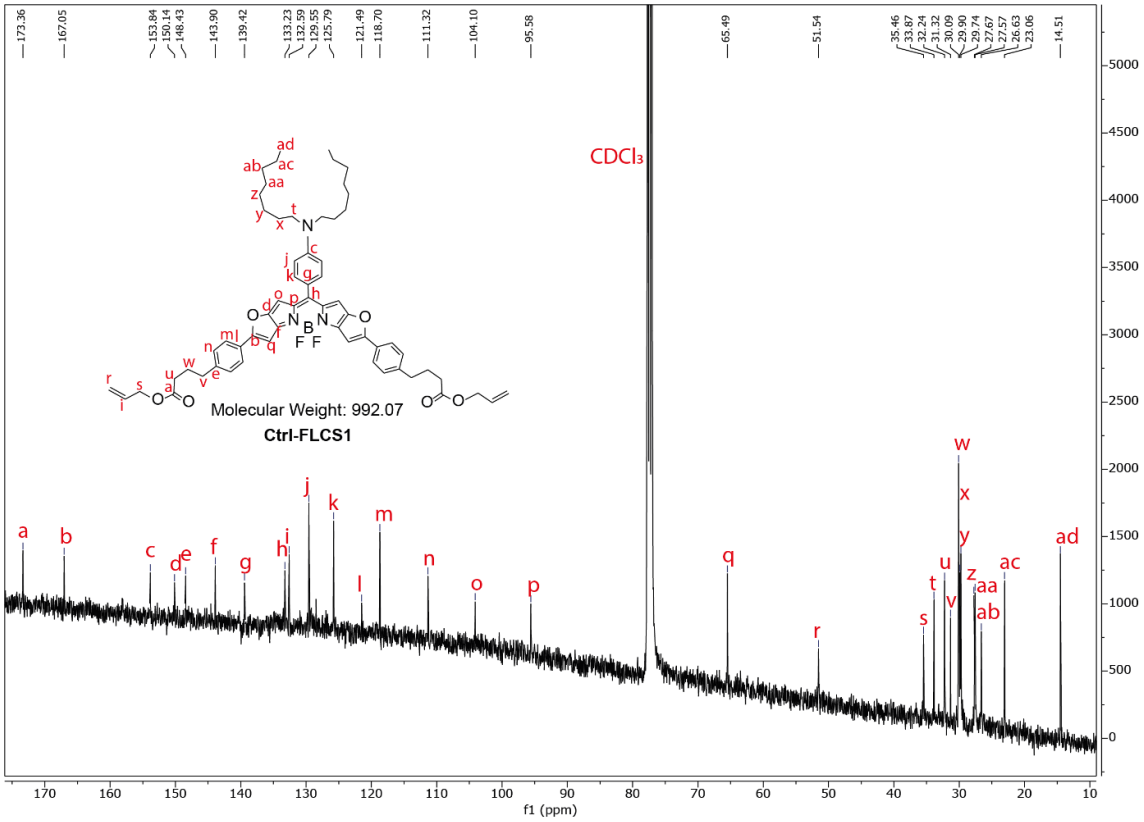

Figure 127: ^{13}C NMR spectrum (in $CDCl_3$, 100 MHz) of compound **Ctrl-FLCS1**

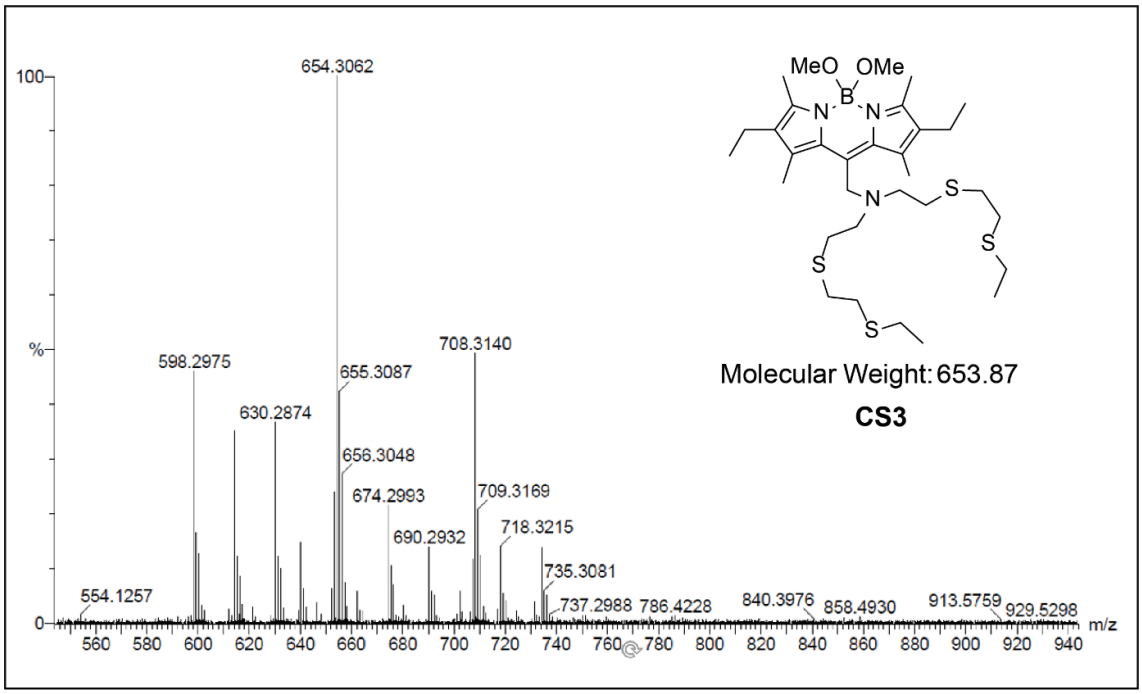

Figure 128: ESI-MS spectrum of **CS3** in MeOH.

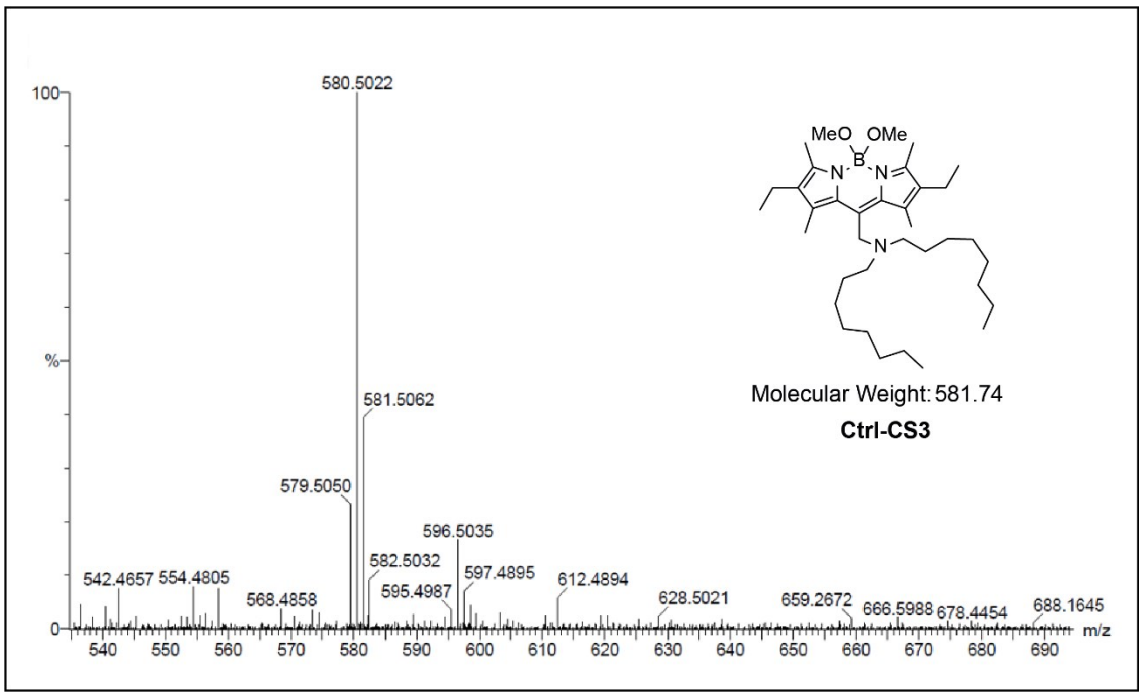

Figure 129: ESI-MS spectrum of **Ctr-CS3** in MeOH.

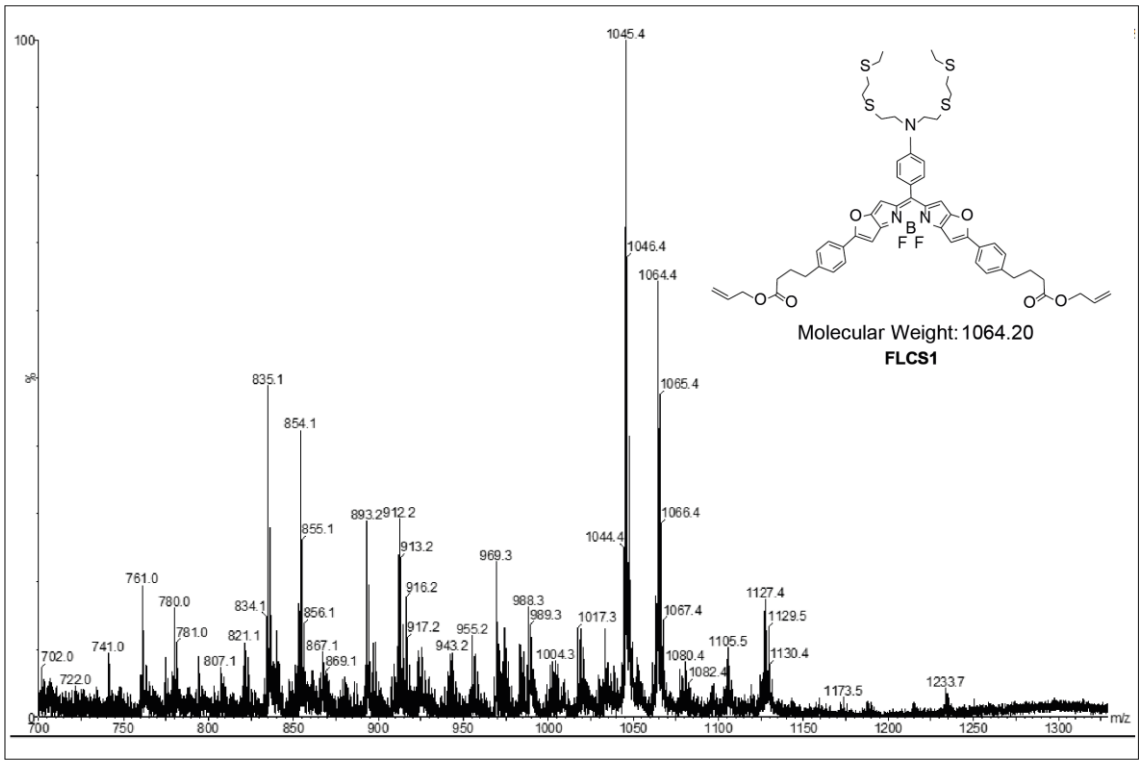

Figure 130: MALDI-TOF MS spectrum of **FLCS1**.

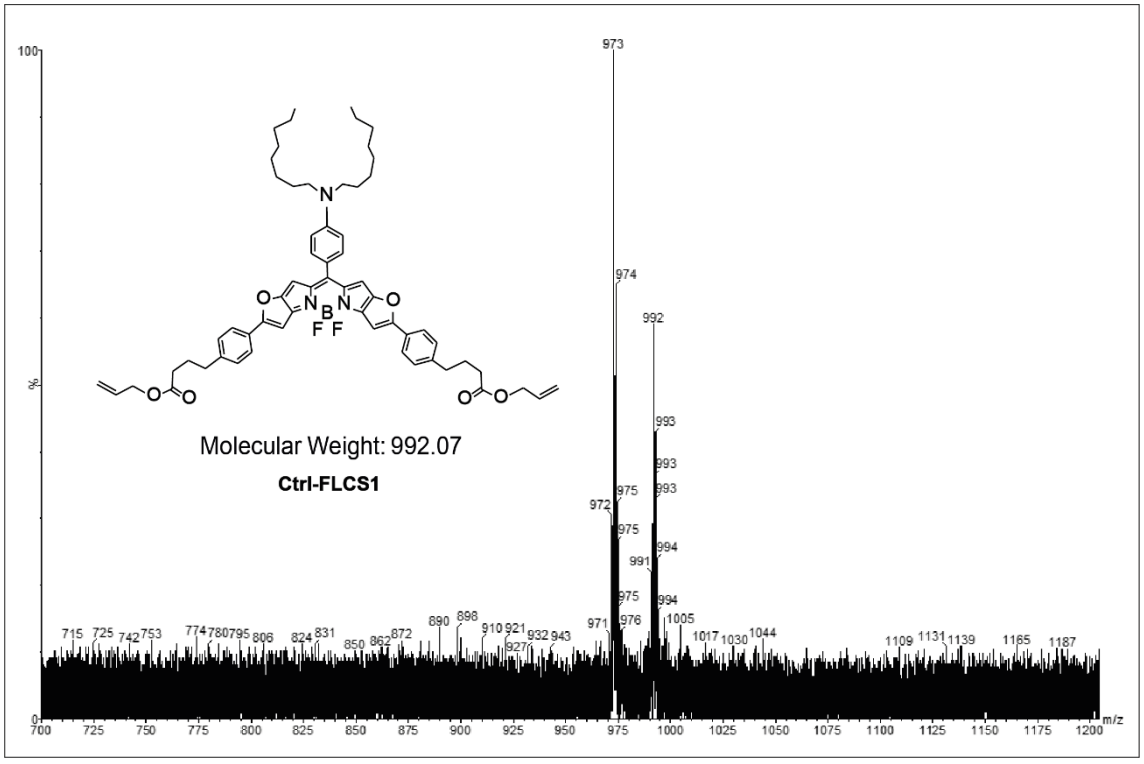

Figure 131: MALDI-TOF MS spectrum of **Ctrl-FLCS1**.

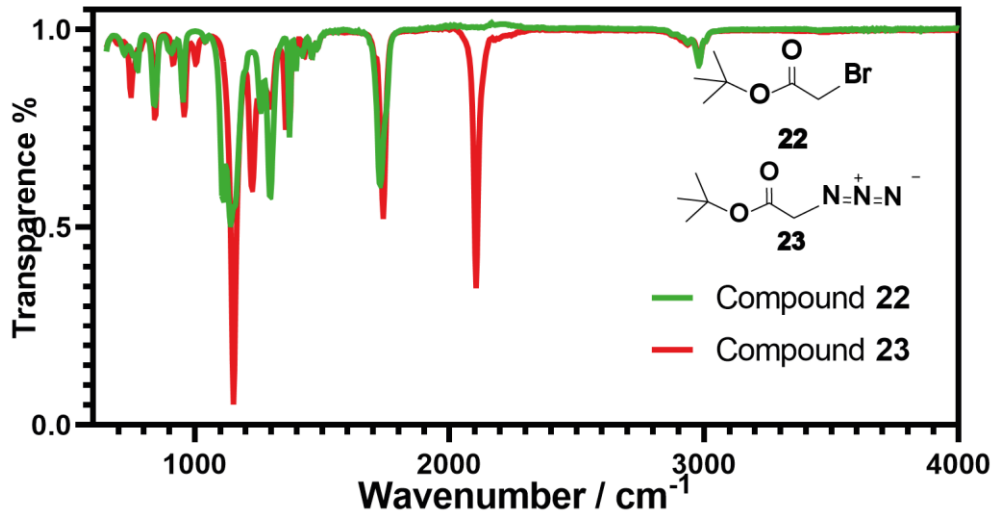

Figure 132: Comparison of IR spectra of compound **22** and compound **23** showing azide band appearing at 2105 cm^{-1}.

Table 5: TCSPC titration parameters. TCSPC fitting parameters of titration of copper(I) to **CS3** (5 µM) in methanol; biexponential fit with fixed values for τ_1 = 0.97±0.02 ns and τ_2 = 6.58±0.04 ns.

	a_1	a_2	τ_{avg}	χ^2
CS3 0.0 eq copper(I)	0.913±0.000	0.087±0.000	3.183±0.011	1.506
CS3 0.1 eq copper(I)	0.916±0.000	0.084±0.000	3.119±0.010	1.640
CS3 0.2 eq copper(I)	0.916±0.000	0.084±0.000	3.130±0.011	1.386
CS3 0.3 eq copper(I)	0.891±0.000	0.109±0.000	3.513±0.012	1.409
CS3 0.4 eq copper(I)	0.885±0.001	0.115±0.001	3.604±0.012	1.454
CS3 0.5 eq copper(I)	0.868±0.001	0.132±0.001	3.819±0.013	1.392
CS3 0.6 eq copper(I)	0.863±0.001	0.137±0.001	3.884±0.014	1.321
CS3 0.7 eq copper(I)	0.843±0.001	0.157±0.001	4.109±0.014	1.399
CS3 0.8 eq copper(I)	0.838±0.001	0.162±0.001	4.161±0.015	1.299
CS3 0.9 eq copper(I)	0.816±0.001	0.184±0.001	4.365±0.016	1.349
CS3 1.0 eq copper(I)	0.796±0.001	0.204±0.001	4.534±0.017	1.315
CS3 1.1 eq copper(I)	0.786±0.001	0.214±0.001	4.616±0.018	1.296
CS3 1.2 eq copper(I)	0.757±0.001	0.243±0.001	4.817±0.019	1.361
CS3 1.4 eq copper(I)	0.744±0.001	0.256±0.001	4.903±0.020	1.379
CS3 1.6 eq copper(I)	0.739±0.001	0.261±0.001	4.936±0.021	1.366
CS3 1.8 eq copper(I)	0.736±0.001	0.264±0.001	4.951±0.021	1.340
CS3 2.0 eq copper(I)	0.709±0.002	0.291±0.002	5.100±0.022	1.352
CS3 3.0 eq copper(I)	0.699±0.002	0.301±0.002	5.157±0.023	1.376
CS3 4.0 eq copper(I)	0.674±0.002	0.326±0.002	5.274±0.024	1.400

Table 6: TCSPC titration parameters. TCSPC fitting parameters of titration of copper(I) to **FLCS1** (1 μM) in methanol; biexponential fit with fixed values for τ_1 = 0.39±0.00 ns and τ_2 = 3.09±0.01 ns.

	a_1	a_2	τ_{avg}	χ^2
FLCS1 0 eq Cu(I)	0.982±0.000	0.018±0.000	0.732±0.000	1.947
FLCS1 0.1 eq Cu(I)	0.957±0.000	0.043±0.000	1.092±0.000	1.602
FLCS1 0.2 eq Cu(I)	0.908±0.000	0.092±0.000	1.594±0.000	1.535
FLCS1 0.3 eq Cu(I)	0.897±0.000	0.103±0.000	1.674±0.000	1.371
FLCS1 0.4 eq Cu(I)	0.862±0.000	0.138±0.000	1.898±0.000	1.383
FLCS1 0.5 eq Cu(I)	0.823±0.000	0.177±0.000	2.089±0.000	1.328
FLCS1 0.6 eq Cu(I)	0.782±0.000	0.218±0.000	2.247±0.000	1.359
FLCS1 0.7 eq Cu(I)	0.741±0.000	0.259±0.000	2.371±0.001	1.436
FLCS1 0.8 eq Cu(I)	0.696±0.000	0.304±0.001	2.481±0.000	1.459
FLCS1 0.9 eq Cu(I)	0.652±0.001	0.348±0.001	2.571±0.001	1.495
FLCS1 1.0 eq Cu(I)	0.607±0.001	0.392±0.001	2.645±0.001	1.530
FLCS1 1.2 eq Cu(I)	0.531±0.001	0.469±0.001	2.749±0.001	1.625
FLCS1 1.4 eq Cu(I)	0.490±0.001	0.510±0.001	2.794±0.001	1.590
FLCS1 1.6 eq Cu(I)	0.461±0.002	0.539±0.002	2.823±0.002	1.643
FLCS1 1.8 eq Cu(I)	0.454±0.002	0.546±0.002	2.830±0.002	1.640
FLCS1 2.0 eq Cu(I)	0.459±0.002	0.541±0.002	2.825±0.002	1.524

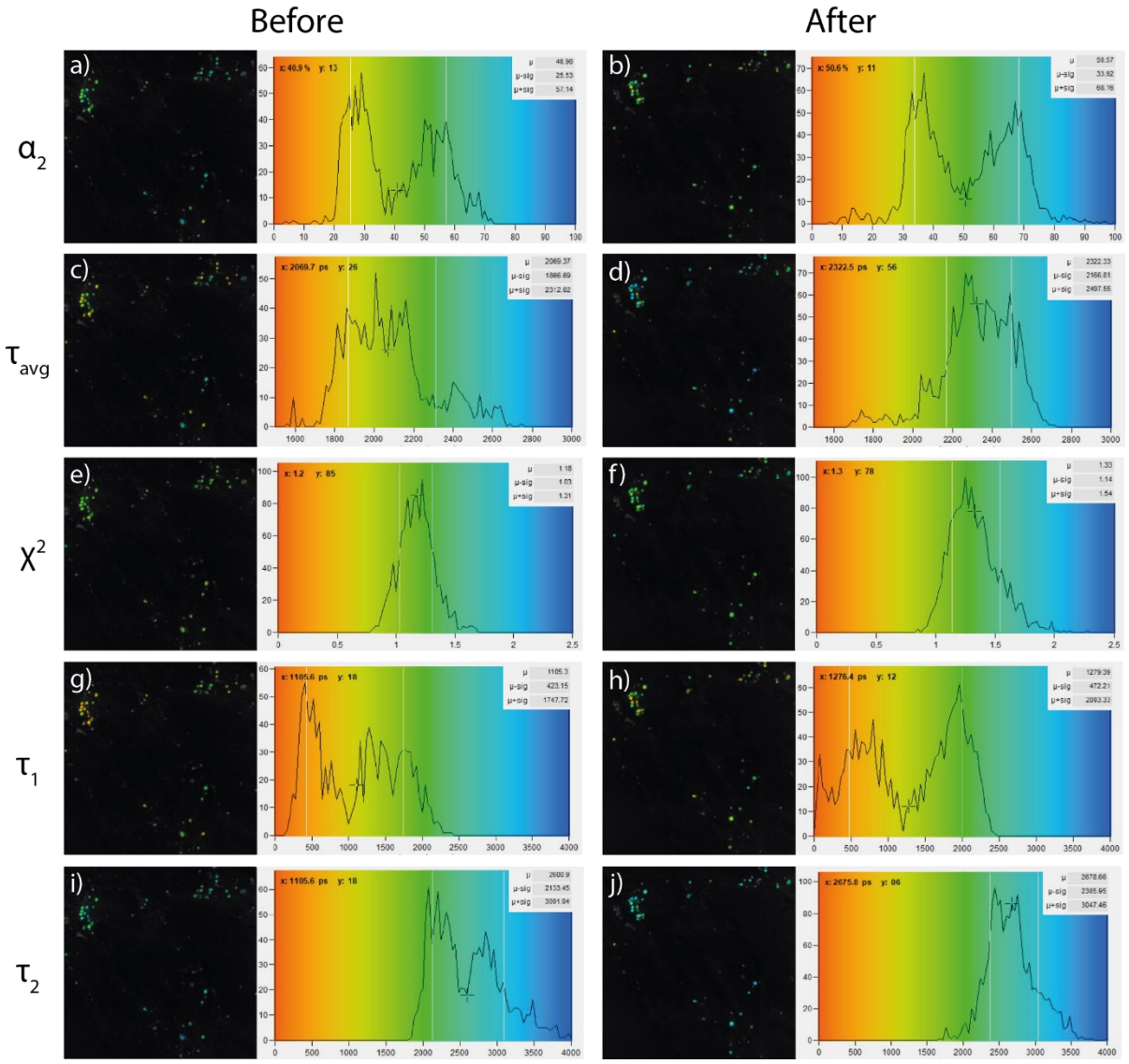

Figure 133: FLIM imaging with variable lifetime values. Example FLIM images and corresponding histograms of parameter distributions for **FLCS1** in SH-SY5Y cells showing a, b) α_2; c, d) τ_{avg}; e, f) χ^2; g, h) τ_1 and g, h) τ_2 signal at variable values for τ_1 and τ_2 before and after 20 min treatment of Cu-GTSM.

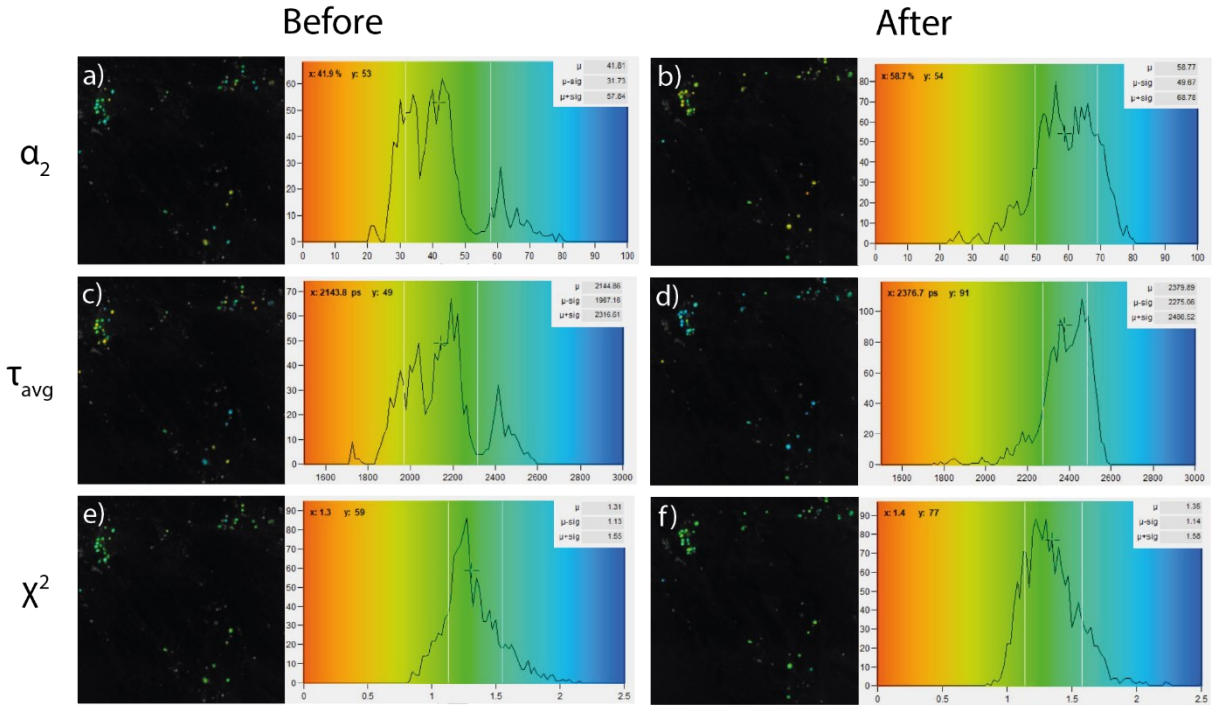

Figure 134: FLIM imaging with fixed lifetime values. Example FLIM images and corresponding histograms of parameter distributions for **FLCS1** in SH-SY5Y cells showing a, b) α_1; c, d) τ_{avg}; e, f) χ^2; at fixed values for τ_1 =0.7 ns and τ_2 =2.7 ns before and after 20 min treatment of Cu-GTSM.

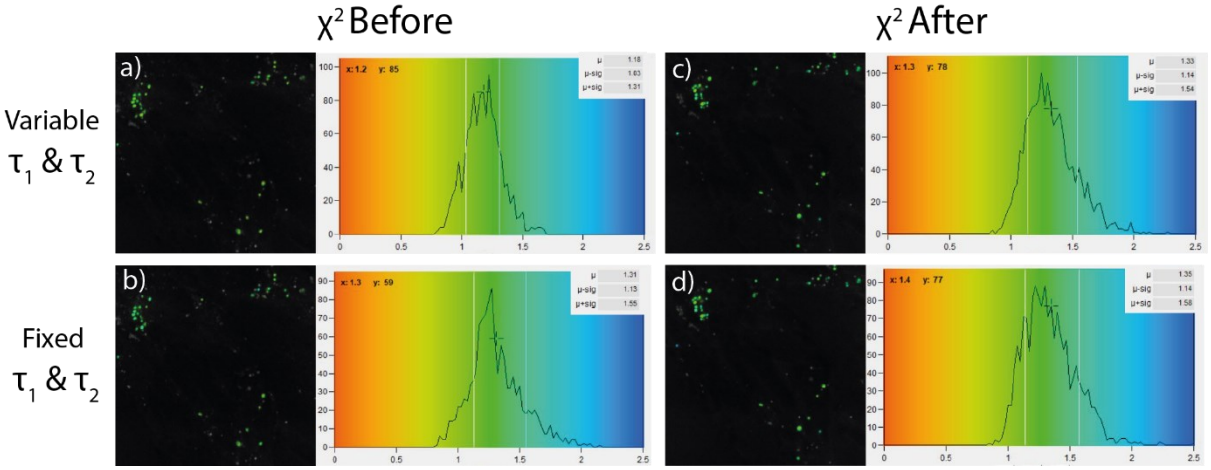

Figure 135: FLIM χ^2 comparison. Example FLIM image of **FLCS1** in SH-SY5Y cells showing χ^2 value with variable τ_1 and τ_2 values a) before and c) after and for values fixed at τ_1 =0.7 ns and τ_2 =2.7 ns, b) before and d) after 20 min treatment of Cu-GTSM; histograms of χ^2 value distributions are also shown.

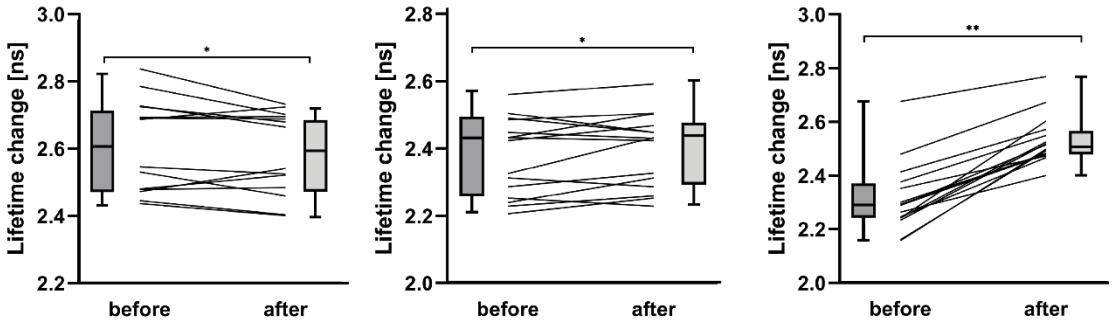

Figure 136: FLIM image analysis. Effect of 20 min incubation of 1% DMSO in DMEM (left), effect of repeated laser exposure (middle), effect of Cu-GTSM (2.5 µM) in DMEM on **FLCS1** fluorescence lifetime signal in cells (right). * $p > 0.5$ shows no statistical significance ** $p < 0.0005$ shows statistical significance with student t-test.

Appendix Chapter II

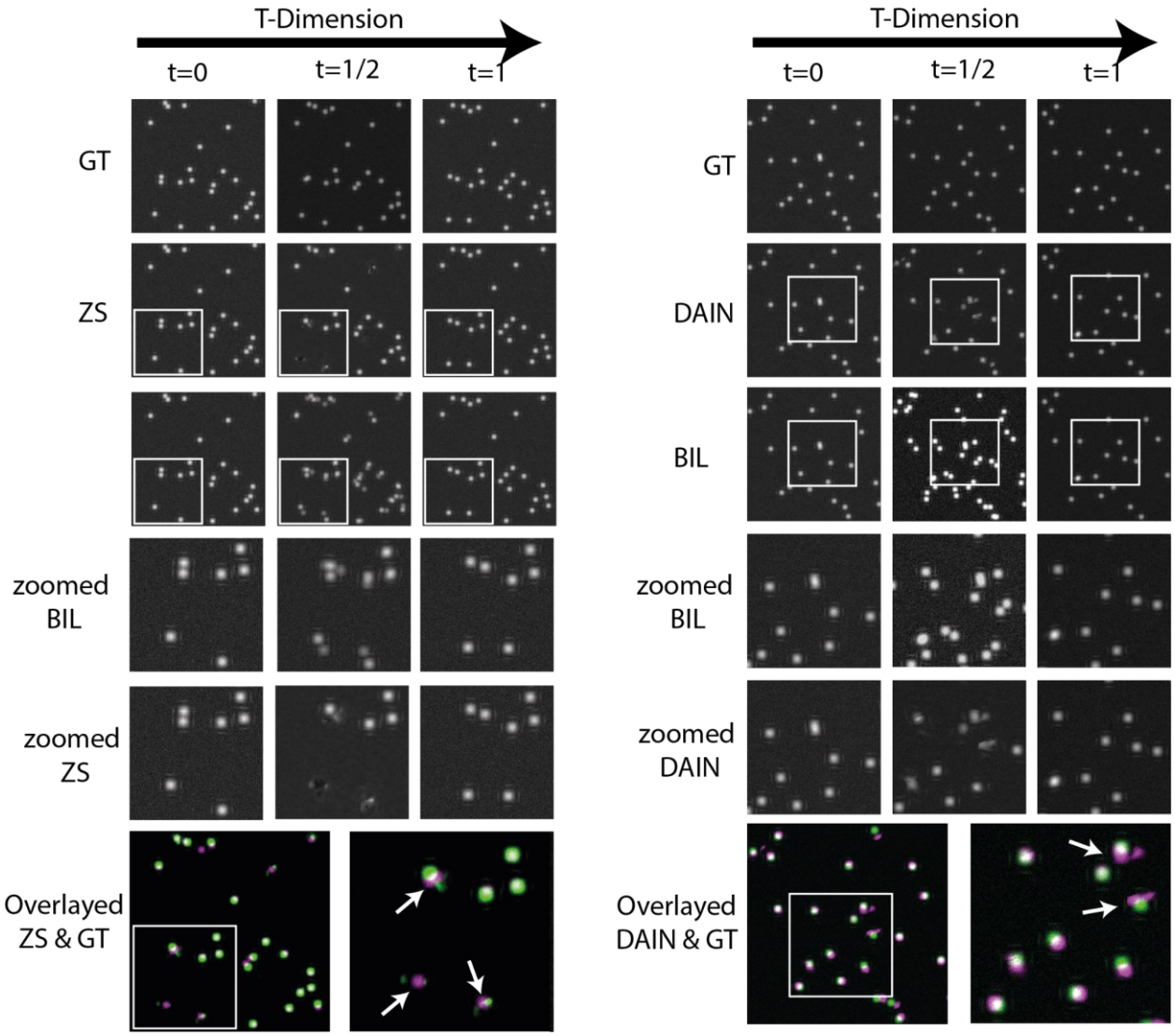

Figure 137: Visual artefacts of DAIN and ZS image frame interpolation results in comparison to the ground truth of a simulated dataset at particle speed V7. Overlayed images show ground truth particles in green and interpolated location of particles in magenta.

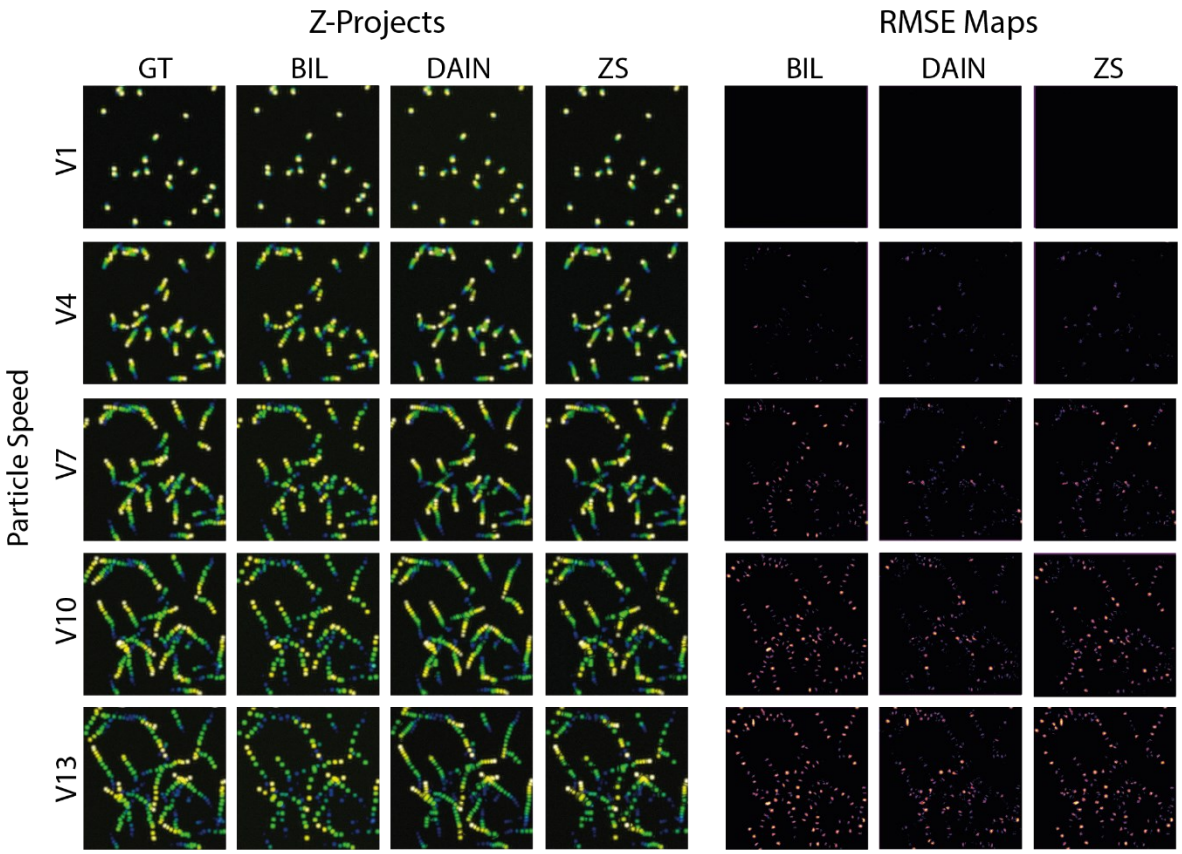

Figure 138: t-Project of the different image frame interpolation methods of the particle movements at different speeds.

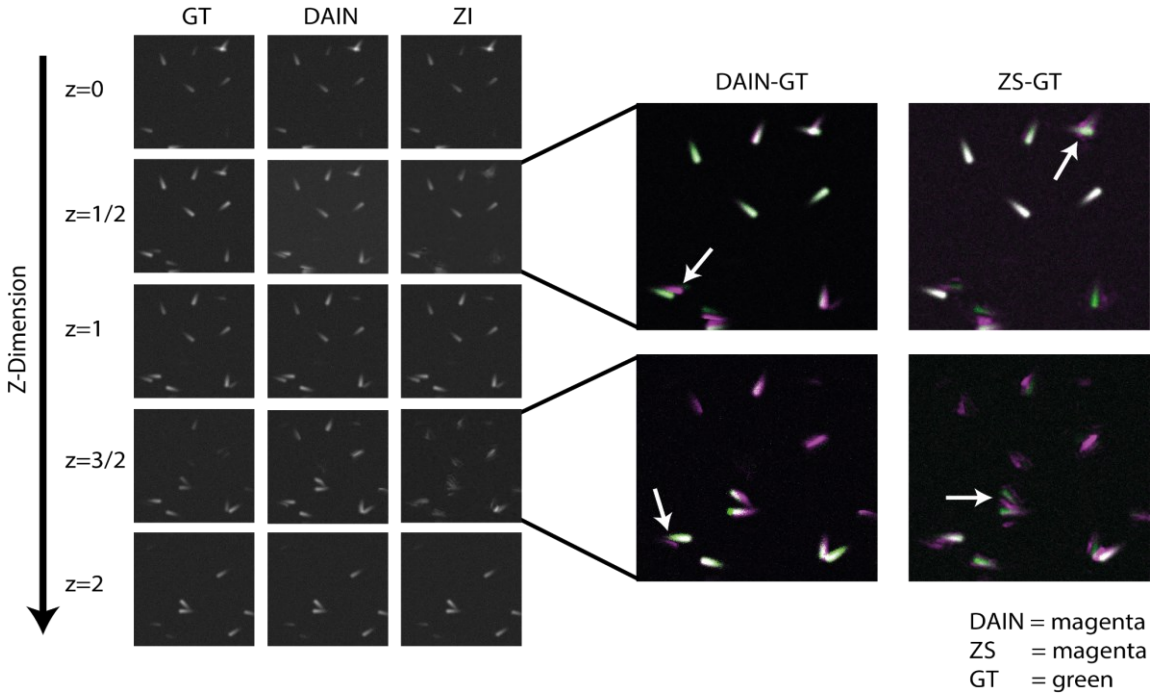

Figure 139: Visual comparison of DAIN and ZS for z-stack image frame interpolation to the ground truth at slice distance 300.

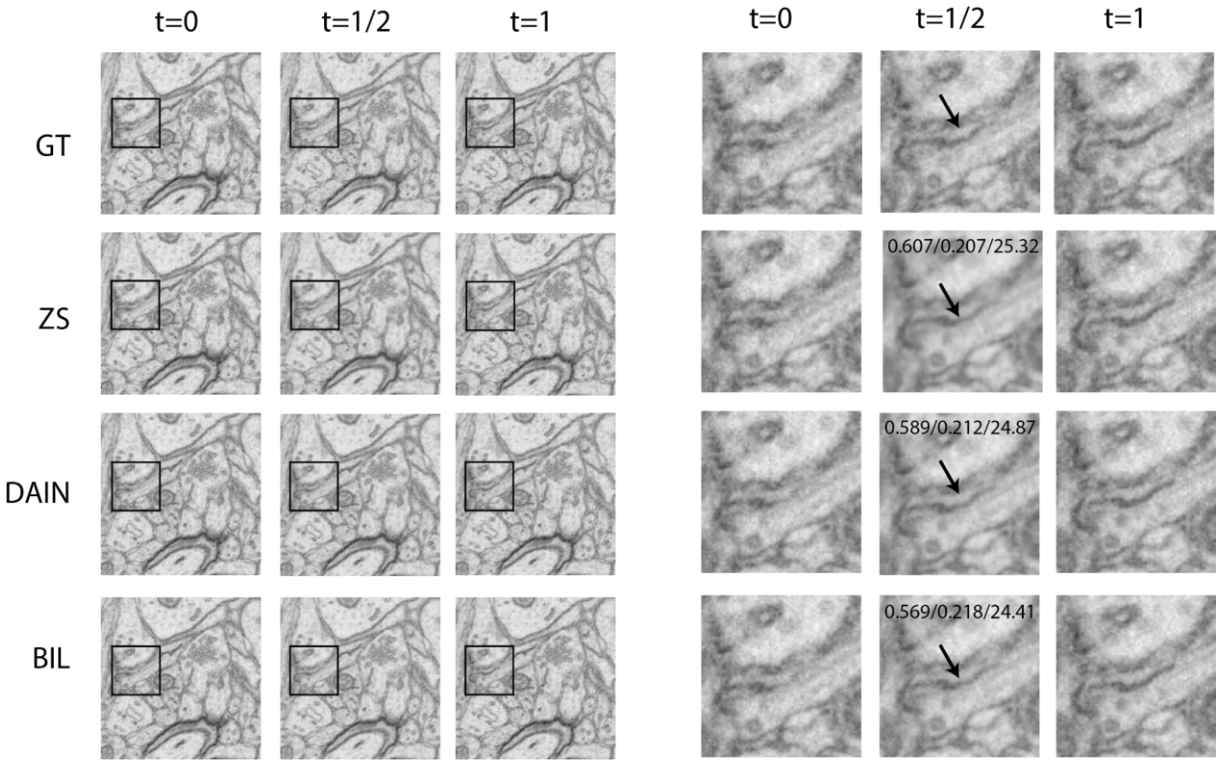

Figure 140: 2x image frame interpolation of ZS and DAIN on EM dataset. ZS produces better quality results than DAIN. ZS creates smoother transitions of an imaged dendrite (see red arrow in zoomed sections).

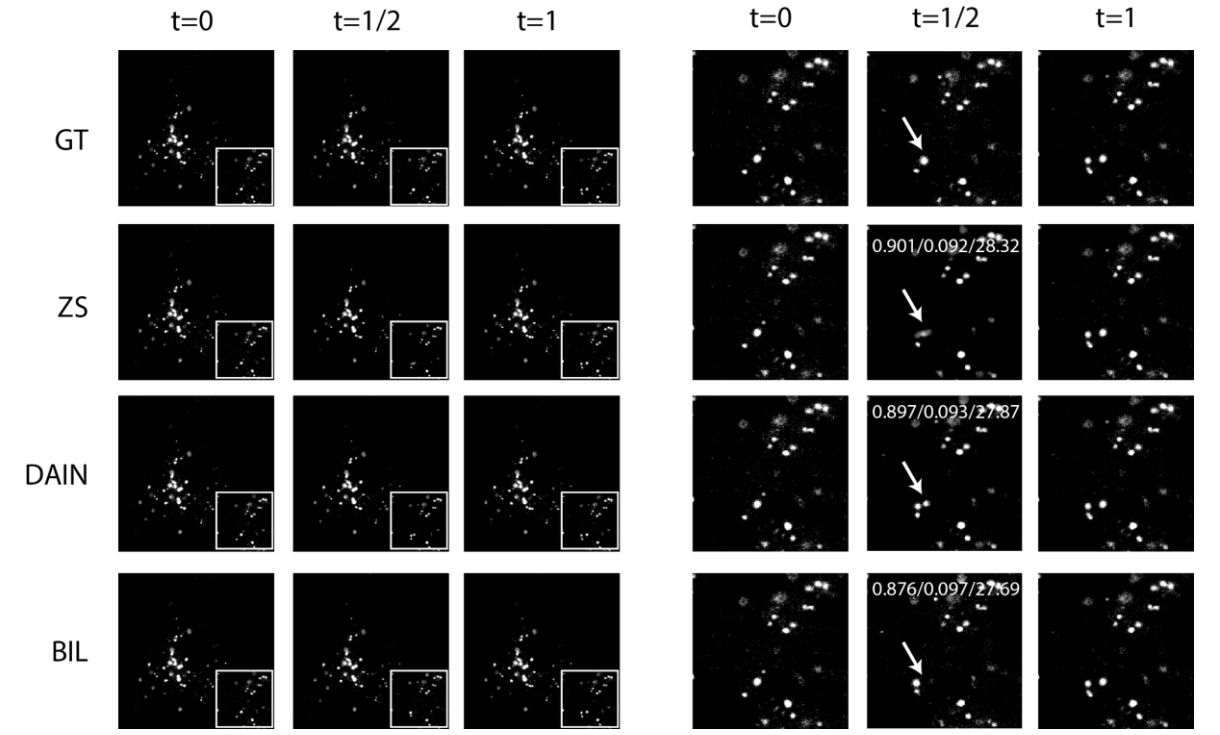

Figure 141: 2x image frame interpolation of ZS and DAIN of lysosomes on a confocal microscope. DAIN produces slightly better-quality results than ZS. ZS misses faster moving lysosomes while DAIN is able to capture these organelles well (example highlighted with white arrow in zoomed sections).

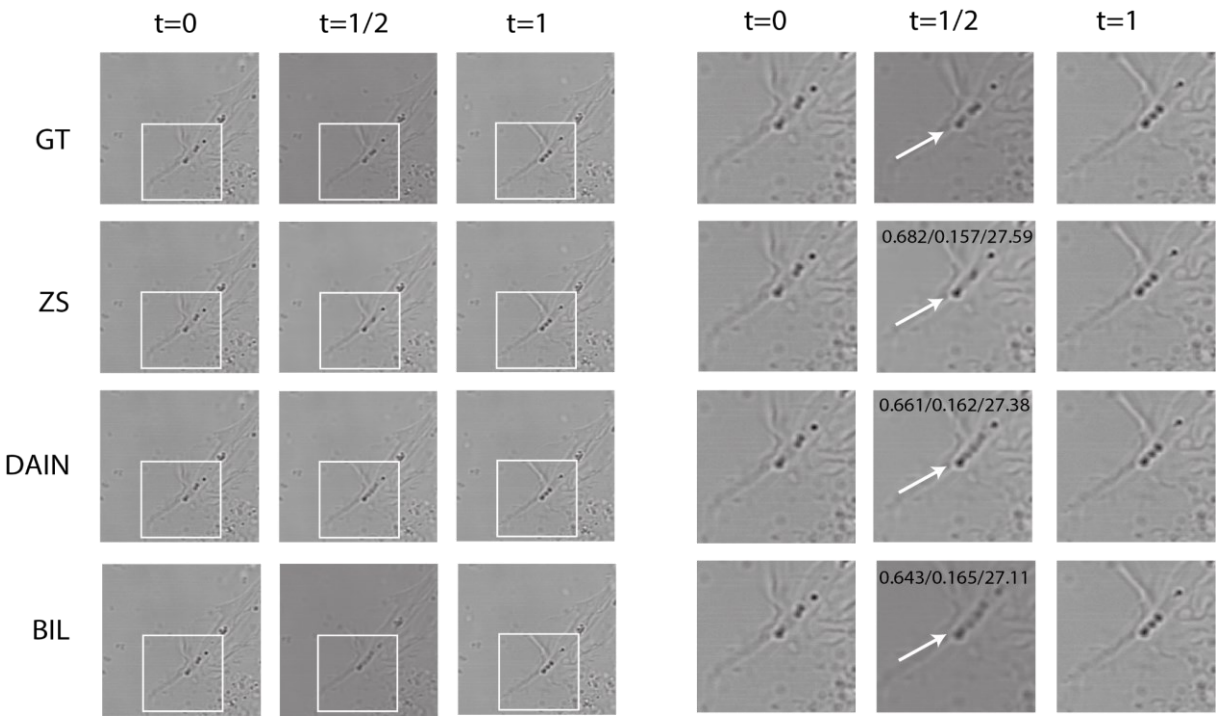

Figure 142: 2x image frame interpolation of ZS and DAIN of SH-SY5Y cells in brightfield microscope. ZS produces slightly better-quality results than DAIN. DAIN creates visual artefacts for fast moving lipid droplets while ZS manages to capture the movement better (see white arrow in zoomed sections).

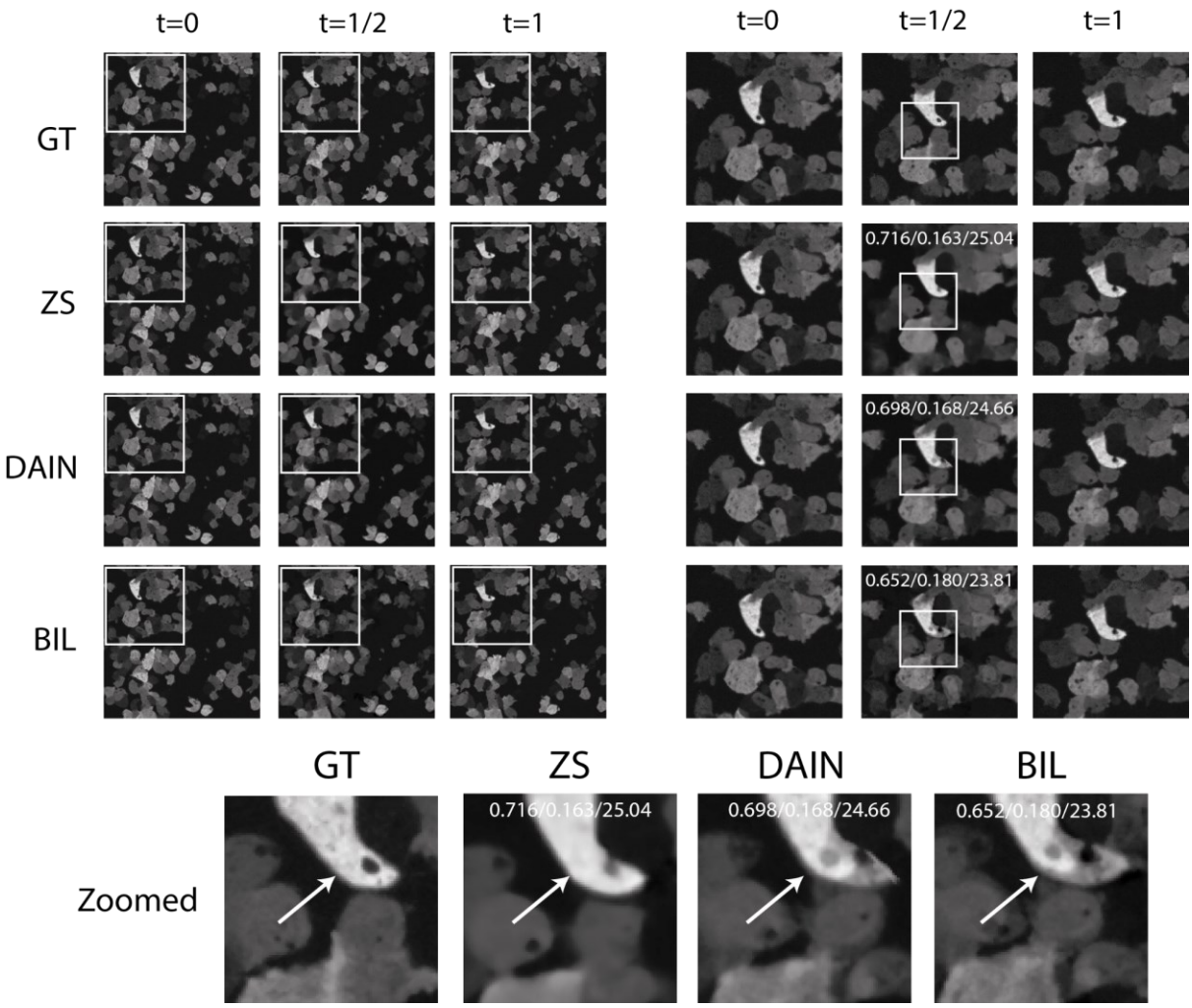

Figure 143: 2x image frame interpolation of ZS and DAIN on spinning disk confocal microscopy dataset. ZS creates smoother transitions and better-quality interpolation results than DAIN (see white arrows in zoomed sections).

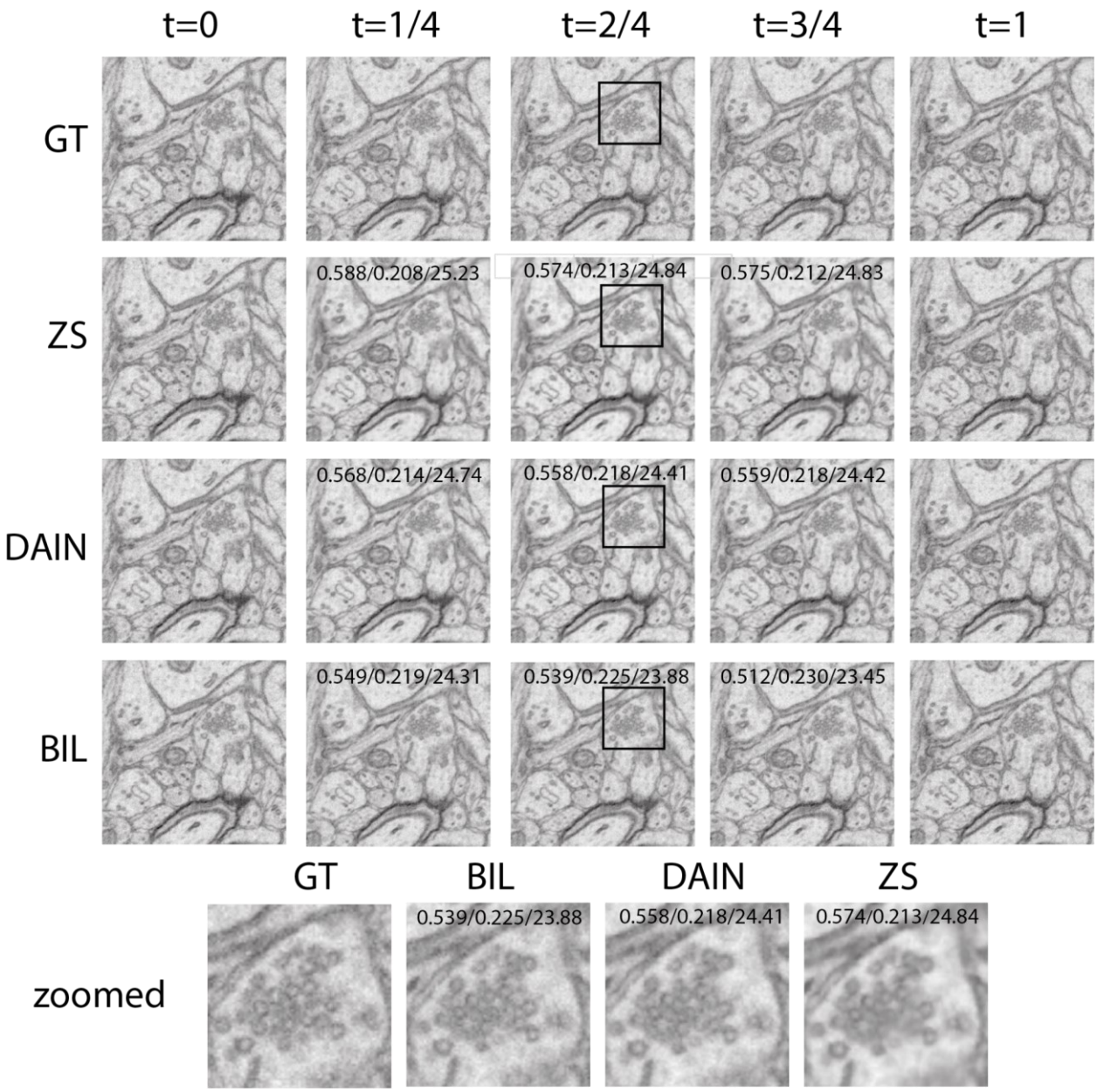

Figure 144: 4x image frame interpolation of ZS and DAIN on EM dataset. DAIN produces better quality results than ZS. ZS creates strong visual artefacts especially for the synaptic vesicles (see zoomed sections).

QR-code video examples of interpolated datasets

Figure 145: QR-code video example of 2x and 4x image frame interpolation.

Table 7: Parameter for creation of synthetic dataset with ICY plugin.[150]

ICY (ISBI Challenge Track Generator)		
	T-dimension Dataset	**Z-dimension Dataset**
SNR:	10	30
Density:	40	50
Image width:	512	512
Image height:	512	512
Image depth:	1	17
Sequence length:	225	1
MinTrackLength:	52	1
Warmup length:	50	50
Extinction rate:	0.003	0.05
x borders simu:	50	100
y borders simu:	50	100
z borders simu:	20	20
xy pixel size:	15	15
Slice spacing:	250	50 -450
Creator types:	SWITCHING_UNIFORM	DIRECTED_MIX
Sigma Brownian:	1	/
q1:	2	1
V min:	2	16
V max:	2	16
Probe directed Brownian:	0.3	/
Probe Brownian directed:	0.3	/

Table 8: Parameters for tracking particles with Fiji TrackMate plugin.[149,224]

TrackMate Parameters Simulated Dataset	
Estimated blob diameter:	10 µm
Threshold:	2
Selected Tracker:	Simple LAP tracker
Linking max distance:	15 (V1-6); 20 (V7-10); 25 (V11-12)
Gap-closing max distance:	15 (V1-6); 20 (V7-10); 25 (V11-12)
Gap-closing max frame gap:	2

TrackMate Parameters Life Dataset	
Estimated blob diameter:	3 µm
Threshold:	10
Selected Tracker:	Simple LAP tracker
Quality particles	Number calibrated to GT number
Linking max distance:	8
Gap-closing max distance:	8
Gap-closing max frame gap:	2

Table 9: Training data and time information for fine-tuning DAIN and ZS networks for the image interpolation task with the different datasets.

Training / fine tuning for image frame interpolation					
Dataset	**Test dimension**	**Pixel dimension**	**Size**	**Fine tune DAIN**	**Fine tune ZS**
VIMEO video dataset	T	488x256	82 GB	provided	72 h
Mitochondria dataset	T	512x512	14 GB	5 h	5 h
Lightsheet CF dataset	T	512x512	500 MB	5 h	5 h
BF dataset	T	512x512	3.6 GB	12 h	12 h
Synthetic dataset	T	512x512	450 MB	5 h	5 h
Synthetic dataset	Z	512x512	350 MB	5 h	5 h
CF Lysosomal dataset	T	512x512	5.2 GB	12 h	12 h
CF Fibronectin dataset	T	512x512	800 MB	5 h	5 h
Actin dataset	Z	512x512	500 MG	5 h	5 h
EM dataset	Z	512x512	1 GB	12 h	12 h

Table 10: Training data and time information for fine-tuning DAIN and ZS networks for the image spatial pixel resolution upscaling task for the different datasets.

Training / fine tuning for pixel upscaling					
Dataset	**upscale factor**	**LR pixel dimension**	**HR pixel dimension**	**Size HR**	**Fine tune ZS**
VIMEO video dataset	**2x**	488x256	244x128	82 GB	72 h
VIMEO video dataset	**4x**	488x256	122x64	82 GB	provided
BF dataset	**2x**	1024x1024	512x512	3.6 GB	24 h
BF dataset	**4x**	1024x1024	512x512	3.6 GB	24 h
Lightsheet CF dataset	**2x**	512x512	256x256	4.3 GB	24 h
Lightsheet CF dataset	**4x**	512x512	128x128	4.3 GB	24 h
EM dataset	**2x**	512x512	256x256	12.1 GB	24 h
EM dataset	**4x**	512x512	128x128	12.1 GB	24 h
CF Lysosomal dataset	**2x**	512x512	256x256	5.2 GB	24 h
CF Lysosomal dataset	**4x**	512x512	128x128	5.2 GB	24 h